Curso 2009/10
CIENCIAS Y TECNOLOGÍAS/41
I.S.B.N.: 978-84-7756-990-9

JUAN ANTONIO FERNÁNDEZ ONTIVEROS

Núcleos de galaxias activas a escalas de parsecs

Directores
ALMUDENA PRIETO ESCUDERO
JOSÉ ANTONIO ACOSTA PULIDO

SERVICIO DE PUBLICACIONES
UNIVERSIDAD DE LA LAGUNA

SOPORTES AUDIOVISUALES E INFORMÁTICOS
Serie Tesis Doctorales

A mis abuelos.

Resumen

El centro de nuestra Vía Láctea, así como el de las galaxias más cercanas, constituye un excelente laboratorio para estudiar el entorno de agujeros negros supermasivos con una resolución espacial muy alta, del orden de unos pocos parsecs. Entender cómo funcionan estos objetos tan cercanos es el primer paso para identificar los mecanismos principales que operan en las galaxias más lejanas. En la región central de una galaxia solemos encontrar, además del agujero negro supermasivo, diversas componentes de distinta naturaleza: desde regiones de formación estelar, pasando por fuentes puntuales muy brillantes con un origen no-estelar como son los núcleos de galaxias activas (AGN, por sus siglas en inglés), hasta la población estelar subyacente de la propia galaxia. Todas estas componentes contribuyen de forma significativa a la energía total liberada en la región central de la galaxia (Galliano et al. 2005; Reunanen et al. 2010; Schödel et al. 2010), unas veces compitiendo de forma directa entre ellas en un determinado intervalo del espectro y otras de forma indirecta dominando en diferentes rangos en longitud de onda. En este contexto, la distribución espectral de energía (SED) es una herramienta que refleja la naturaleza de estos objetos, de origen térmico en el caso de las poblaciones estelares (tanto jóvenes como viejas), y como emisión no-térmica en el caso de los núcleos activos. Sin embargo, estos últimos también producen emisión térmica al calentar el gas y polvo de su entorno, mientras que las poblaciones estelares jóvenes contribuyen al continuo no-térmico tras la muerte de las primeras estrellas masivas y la aparición de las primeras remanentes de supernova.

Una de las mejores formas de afrontar el estudio de estos sistemas consiste en construir SEDs cubriendo el rango más amplio posible del espectro electromagnético (desde radio hasta rayos-X pasando por el óptico e infrarrojo), a partir de observaciones hechas con técnicas de alta resolución espacial. El tamaño típico que esperamos para el toroide –la estructura de gas y polvo que envuelve y alimenta al agujero negro– es del orden de unos pocos parsecs (Jaffe et al. 2004; Tristram et al. 2007). Por otra parte, los elementos básicos que componen las regiones de formación estelar parecen

ser cúmulos estelares muy jóvenes y compactos, con tamaños en el rango de 0.5 a 20 pc, edades en torno a ~ 10 Maño y masas en torno a $\gtrsim 10^4\,M_\odot$ (Portegies Zwart et al. 2010). Por lo tanto, para llevar a cabo un estudio en profundidad de la región nuclear en las galaxias más cercanas es vital resolver espacialmente estas componentes individualmente en un amplio rango del espectro. Sin embargo, disponer de la SED de cada uno de estos elementos cubriendo los rangos de radio, infrarrojo (IR), óptico, ultravioleta (UV) y rayos-X no es sencillo, especialmente si queremos una resilución espacial uniforme. Un tamaño angular de $0\farcs1$ corresponde a ~ 2 pc a una distancia de 4 Mpc, y a ~ 10 pc a 20 Mpc. Alcanzar estas resoluciones implica la necesidad de utilizar telescopios espaciales en el óptico y UV, óptica adaptativa desde tierra en los rangos óptico e infrarrojo, e interferometría en los rangos de radio, milimétrico y submilimétrico. Para el rango de altas energías la mejor resolución disponible nos la proporciona el telescopio espacial *Chandra*, con $\sim 1''$, pero este valor es todavía un orden de magnitud superior a la resolución necesaria. No obstante, en el caso de los núcleos activos esta resolución aún nos permite extender el estudio de la SED a este rango, ya que suelen ser fuentes bastante brillantes y dominan sobre la contribución de la galaxia anfitriona, especialmente por encima de $\gtrsim 6$ keV. En este contexto, la tesis parte del estudio de una muestra de seis galaxias cercanas con diferentes niveles de actividad nuclear, tanto en términos de formación estelar como actividad de origen no-estelar. Como ejemplo del primer caso está NGC 253, una de las galaxias starburst más cercanas y conocidas, mientras que en el segundo tenemos a NGC 7469, una galaxia Seyfert cuyo brillo es equiparable al de los quásares más débiles, incluida en el primer estudio de galaxias Seyferts presentado por Seyfert (1943). Para estos objetos estudiamos, de forma independiente, las propiedades de la formación estelar y del núcleo activo.

En primer lugar, la estructura interna de un AGN, y por tanto su distribución espectral de energía, parecen venir determinadas en gran parte por parámetros relacionados con la energía total que libera el núcleo activo o la eficiencia en el proceso de acreción (Elitzur & Shlosman 2006; Hönig & Beckert 2007; Kuraszkiewicz et al. 2009). Por lo tanto, una de las primeras preguntas que surgen es, precisamente, de qué manera cambia la forma de la SED con la luminosidad de la fuente central. En el caso de AGNs muy brillantes, como los quásares, la resolución espacial no es determinante, ya que la contribución de la galaxia anfitriona es prácticamente despreciable, y la SED intrínseca del núcleo activo se conoce con detalle en casi todo el rango espectral. Sin embargo, el dominio de bajas luminosidades presenta muchas más dificultades, principalmente debido a la contribución de dicha galaxia anfitriona. Para estudiar la distribución de energía de AGNs de baja luminosidad (LLAGNs) construímos una SED representativa a partir de los objetos de nuestra muestra con estas características, incluyendo LINERs y galaxias Seyfert débiles. Por primera vez utilizamos datos con alta resolución espacial en infrarrojo medio (MIR) en un estudio de este tipo, lo que nos

permite caracterizar la SED de estos objetos en el rango donde domina la componente de polvo y gas que envuelve al núcleo activo. Ésta parece ser, precisamente, una de las componentes más sensibles a los cambios estructurales que se producen a distintas luminosidades.

Por otra parte estudiamos la formación estelar que se produce en torno a estos núcleos activos. Los cúmulos estelares jóvenes (YSCs) que constituyen estas regiones de formación estelar, mencionados anteriormente, tienen muchas propiedades en común con los cúmulos globulares (GCs). Como consecuencia, el origen de estos últimos suele asociarse a la evolución de los primeros (Portegies Zwart et al. 2010). Ambos son similares en términos de masa y edad, aunque sus funciones de masas difieren notablemente, especialmente en el extremo de masas más bajas (Fall & Zhang 2001). Galaxias en interacción y starbursts suelen estar plagadas de cúmulos jóvenes que cubren un amplio rango en brillo y masa, por lo que se convierten en excelentes laboratorios para estudiar la evolución temprana de estos candidatos a "cúmulos globulares jóvenes". En este estudio encontramos formación estelar reciente en forma de cúmulos compactos en el núcleo de todas las galaxias de la muestra, incluso en la galaxia elíptica NGC 1052. Las principales propiedades de estos cúmulos se compararán, incluyendo su brillo, tamaño, edad, masa y forma de la SED. A partir de los cúmulos resueltos en el núcleo de NGC 253, construiremos una SED representativa para regiones extragalácticas de formación estelar que cubre los rangos de radio, infrarrojo medio y cercano, y el rango óptico. La SED representativa de estas regiones muestra claramente un exceso de emisión en el infrarrojo cercano que se interpreta como la contribución energética de objetos protoestelares muy jóvenes pertenecientes a estos cúmulos estelares. La naturaleza de esta emisión estaría asociada en este caso a polvo muy caliente ($\gtrsim 1000\,\mathrm{K}$) cerca de las estrellas en formación que constituyen cada cúmulo.

Conclusiones

Las aportaciones principales de esta tesis son:

- Se presenta un nuevo alineamiento desde el rango de radio hasta el óptico para la región central de las galaxias NGC 253 y NGC 1386, con una precisión por debajo de $\sim 0\farcs12$, basado en los datos en infrarrojo de VLT/NaCo. En el caso de NGC 253, la extensión de dicho alineamiento al rango de rayos-X utilizando imágenes del telescopio espacial *Chandra* ha cambiado completamente el enfoque sobre la naturaleza del núcleo de esta galaxia.

- Se demuestra que la posición de TH2, la fuente más brillante en radio en el núcleo de NGC 253, no es compatible con X-1, la fuente más brillante

descubierta en la banda de rayos-X duros. Esta última muestra un brillo y una pendiente espectral en rayos-X que la identifican como "hidden AGN".

- Se presenta una distribución espectral de energía (SED) promedio a partir de AGNs de baja luminosidad (LLAGNs), partiendo de datos con alta resolución espacial en los rangos de radio, MIR, NIR, óptico y rayos-X. La forma de la SED promedio desde el infrarrojo medio hasta el óptico revela la carencia del exceso ultravioleta, presente en los quásares y las galaxias Seyfert de tipo 1. Sin embargo, esta ausencia no se produce por un oscurecimiento directo del núcleo activo, como es el caso de las galaxias Seyfert de tipo 2.

- Se construye una SED representativa de cúmulos estelares jóvenes a partir de datos en los rangos de radio, infrarrojo y óptico para las regiones de formación estelar en el núcleo de NGC 253. Ésta distribución muestra un claro exceso en el infrarrojo cercano (1–2 μm) que se interpreta como la emisión de polvo caliente ($\gtrsim 1000\,\mathrm{K}$) asociado a los objetos protoestelares en formación que hay en el interior de estos cúmulos.

- Se encuentra, por primera vez, formación estelar muy reciente ($\lesssim 10\,\mathrm{Maño}$) en forma de cúmulos estelares compactos en la región central de una galaxia elíptica, NGC 1052 en este caso. La presencia de estas regiones se interpreta como el último brote de formación estelar residual tras una fusión que sucedió aparentemente hace $\sim 1\,\mathrm{Gaño}$.

- Para cada región de formación estelar se proporcionan distribuciones espectrales de energía en un amplio rango en longitud de onda. También se proporcionan estimaciones del brillo, tamaño, anchura equivalente de Hα, masa fotométrica, extinción y tasa de formación estelar de cada región. Se concluye que estas regiones son cúmulos estelares jóvenes y compactos (YSCs) similares a los más masivos que se encuentran en la Vía Láctea (como los casos de NGC 1386 y NGC 1052), o a los cúmulos compactos que se forman en galaxias en interacción o con formación estelar muy intensa (como los casos de NGC 253, NGC 1097, NGC 7582 y NGC 7469).

- La función de masas para los cúmulos estelares jóvenes en NGC 253 y NGC 7469 muestra un comportamiento en forma de ley de potencias, similar al que se encuentra en regiones de formación estelar en la Vía Láctea –con un índice de $\gamma \sim 2$–, en el caso de NGC 253, o en entornos de formación estelar más activos ($\gamma > 2$), como en el caso de NGC 7469.

- En cambio, la función de masas para los cúmulos estelares detectados en NGC 1097 muestra un truncamiento en torno a $\sim 2.1 \times 10^5\,\mathrm{M}_\odot$. Este hecho

se interpreta como la destrucción selectiva de los cúmulos de masas más bajas que produce la evolución dinámica en este sistema.

Abstract

THE centres of the Milky Way and nearby galaxies represent excellent laboratories to explore the physics of supermassive black holes (SMBH) at spatial resolutions of the order of parsecs. Understanding these systems is essential to interpret the results obtained for more distant objects. However, when we look inside the central region of galaxies, it is frequent to find a number of different sources: star-forming regions, active galactic nuclei (AGN) as a point-like source not linked with stellar processes, and the population of the underlying galaxy. All of them contribute to the total nuclear output with comparable energies (Galliano et al. 2005; Reunanen et al. 2010; Schödel et al. 2010), sometimes in the same wavelength range and sometimes in different part of the spectrum. The mentioned components are reflected in the integrated spectral energy distribution (SED) of the galactic central region, usually in the form of thermal emission, as in the case of stellar populations (both old and young), and non-thermal emission in the case of active nuclei. However, AGNs also contribute to the thermal emission by heating the surrounding gas and dust, and supernova remnants (SNRs) become important non-thermal emitters shortly after a star-formation burst.

One of the best approaches to unravel these phenomena is to investigate their energy output from radio to infrared (IR), optical, ultraviolet (UV) and X-rays using high-spatial resolution techniques. The typical size expected for the reservoir material of gas and dust that surrounds and feeds a SMBH is about a few parsecs (Jaffe et al. 2004; Tristram et al. 2007). On the other hand, the building blocks of star-forming regions appear to be young and very compact stellar clusters with sizes in the range 0.5–20 pc, ages around ~ 10 Myr and masses of about $\gtrsim 10^4\,M_\odot$ (Portegies Zwart et al. 2010). Therefore, resolving these components over a wide range in wavelength is mandatory to perform a comprehensive analysis of the nuclear region of nearest galaxies. In this context, sampling the SEDs with a high-spatial resolution is an excellent tool to investigate the nature of the energy output of these sources, but built them for a wide wavelength range is not straightforward. An angular resolution of $0\farcs1$ corresponds to ~ 2 pc at a distance of 4 Mpc, and ~ 10 pc at 20 Mpc. Achieving spatial

resolutions of this order requires the use of space telescopes and/or ground-based AO facilities in the optical, UV and IR, and interferometry at radio, millimetre and submillimetre wavelengths. At high energies the *Chandra* space observatory provides the best resolution with $\sim 1''$, although this is still an order of magnitude higher than the required resolution. Nevertheless, we still have a chance for active nuclei, as these are bright X-ray sources and usually do not have rivals in their host galaxies above $\gtrsim 6\,\mathrm{keV}$. This thesis is focused on a sample of six nearby galaxies with different levels of activity in terms of star-formation and non-stellar activity. NGC 253 is an example of the former, one of the closer and well-known starbursts, while NGC 7469 is representative of the bright quasar-like Seyferts, included in the original study by Seyfert (1943). For all the objects in the sample we study separately the properties of the star-formation and the SED of the active nuclei.

First of all, the internal structure of AGNs, and thus their SEDs, seems to be largely determined by both the accretion efficiency and the amount of energy released by the central engine (Elitzur & Shlosman 2006; Hönig & Beckert 2007; Kuraszkiewicz et al. 2009). Thus, one of the first questions to answer is related with the changes in the shape of the SED with the luminosity of the central source. In the case of very bright AGNs, i.e. quasars, the spatial resolution is not crucial, as the contribution from the host galaxy to the integrated SED is negligible. However, the low-luminosity regime is more problematic as the integrated SED reflects that of the host galaxy. To study these nuclei we construct a median SED for low-luminosity AGNs (LLAGNs), from the individual distributions of LINERs and faint Seyferts in the sample. For the first time, we include high-spatial resolution data in the MIR, which permit us to identify significant changes in the SED of LLAGNs when compared with quasars and bright Seyferts. These variations are associated with internal changes in the structure of the central engine at different luminosities.

On the other hand, we study the circumnuclear star-forming regions that surround these active nuclei. These are resolved in young stellar clusters (YSCs), mentioned above, which share many properties with globular clusters (GCs). As a consequence, the origin of the latter seem to be connected somehow with the evolution of the former (Portegies Zwart et al. 2010). Their masses and sizes are in agreement, although their mass functions look different, specially at the low-mass end of this distribution (Fall & Zhang 2001). Interacting and starburst galaxies are crowded of young clusters spanning a wide range in luminosity and mass, thus becoming excellent laboratories to study the early properties and evolution of these candidates for being "young globular clusters". In this context, we found recent star formation in the form of compact clusters in the central parsecs of all the galaxies in the sample, including the elliptical NGC 1052. Their main properties are compared, including their brightness, size, age, mass and shape of their SEDs. A representative template for extragalactic star-forming regions is obtained including the radio, IR and optical ranges, from the YSCs

resolved in the starburst NGC 253. This template for YSCs clearly shows a near-infrared excess when compared with stellar population models, which is interpreted as the contribution from protostellar objects still embedded in their dust cocoons inside these clusters. This emission would be associated with hot dust ($\gtrsim 1000\,\mathrm{K}$) very close to the protostars.

Contents

1

Introduction

DUE to its proximity (~ 8.3 kpc, Reid 1993), the centre of our Milky way permits us to achieve the highest spatial resolution in the study of nearby nuclei. However, the main difficulties come from the very high extinction in the line of sight towards the Galactic Centre, which basically limits the high-spatial resolution studies in this region to the IR and radio ranges. For nearby galaxies, the picture of the central part is much clear but the spatial resolution, e.g. using ground-based adaptive optics (AO), usually drops to a few parsecs at $D \sim 5$ Mpc or tens of parsecs at ~ 20 Mpc. However, despite of these limitations, the local universe offers us a wide range of nuclei in terms of luminosity, star-formation activity and morphology of the host galaxies.

In this Chapter we will review previous studies of AGNs covering a wide spectral range, i.e. from radio to IR, optical/UV and X-rays (Section 1.1). We will compare the results obtained in previous studies using low-spatial resolution data with recent works using the highest-spatial resolution facilities available in each spectral range (*Chandra*, *HST*, VLT, VLA and VLBA/VLBI). In the second part of this Chapter we will review recent studies related with the formation and evolution of YSC systems, from the Milky Way to starburst and interacting galaxies (Section 1.2). In Section 1.3 we present the motivations and main goals for this thesis. Finally, we provide a brief description of this work in Section 1.4.

1.1 A multiwavelength view of the nearest AGNs

Broadly speaking, the term "active galactic nucleus" or AGN, refers to the existence of energetic phenomena in the central region of galaxies which cannot be linked directly with a stellar origin. These sources can release a great amount of energy in a very small

region, and thus some of the fundamental questions about these objects are related with the mechanism that powers the central engine. Although we do not have direct proofs, there are many evidences pointing towards gravitational accretion of matter by the SMBH as the source of energy in AGNs. The common picture consists on infalling material heated to high temperatures in a dissipative accretion disk that surrounds the black hole (see Koratkar & Blaes 1999, and references therein).

Leaving aside exotic objects, there is a clear segregation of AGNs depending on their total or bolometric luminosity (L_{bol}). Quasi-stellar objects (QSOs), or quasars, are typically more than 100 times brighter than their host galaxy ($L_{bol} \sim 10^{46}\,\mathrm{erg\,s^{-1}}$), Seyfert nuclei show a brightness comparable to their host galaxy ($L_{bol} \sim 10^{44}\,\mathrm{erg\,s^{-1}}$) and low-luminosity AGNs (LLAGNs) present usually a very low activity level and are not easily distinguishable within their hosts ($L_{bol} \lesssim 10^{42}\,\mathrm{erg\,s^{-1}}$). Nevertheless, the most common characteristic to all AGNs is that they are usually luminous X-ray sources (Elvis et al. 1978). Low-ionization nuclear emission-line regions (LINERs) are examples of LLAGNs, showing relatively strong intensity in their low-ionization lines (e.g. [O I] at 6300 Å and [N II] at 6548 Å, 6583 Å). LINERs are very common, since they appear to be present in nearly half of all spiral galaxies (Ho et al. 1994).

Another important division considers two AGN types depending on the characteristics of the emission lines in their spectra. Type 1 AGNs have two different sets of emission lines superposed on one another, while type 2 AGNs only show one of them (Khachikian & Weedman 1974). The common set of lines to both AGN types is characteristic of low-density ionized gas (electron density $n_e \sim 10^3$–$10^6\,\mathrm{cm^{-3}}$) and exhibit widths corresponding to velocities of $\lesssim 900\,\mathrm{km\,s^{-1}}$, known as the "narrow lines". A second set of lines present only in type 1 AGNs is formed by broad components but only in the permitted lines, showing widths of up to $10^4\,\mathrm{km\,s^{-1}}$ for these "broad lines". The absence of broad-forbidden lines indicates that the broad-line gas is of high density ($n_e \gtrsim 10^9\,\mathrm{cm^{-3}}$), and thus non-electric-dipole transitions are collisionally suppressed (see Peterson 1997, and references therein).

Furthermore, AGNs are variable across the whole wavelength range, not only in the continuum but in the broad emission lines as well (Matthews & Sandage 1963; Smith & Hoffleit 1963; Peterson 1993; Collier et al. 1998; Kaspi et al. 2000). Many QSOs were found to vary about 0.3–0.5 mag in the optical range over a few months. Some of them were even found to vary on time scales as short as a few days. This fact, on the basis of coherence arguments, implies that the radiation must come from a region with a size not larger that a few light-days in size, i.e. a region not larger than the Solar System is emitting hundreds of times as much energy as the whole galaxy.

At first order, the SED of an AGN can be described as a power law of the form $\nu F_\nu \propto \nu^{-\alpha+1}$, with α usually in the $0 \leq \alpha \leq 1$ range (Peterson 1997). Nevertheless, at radio wavelengths we can discern two types of AGNs depending on their relative

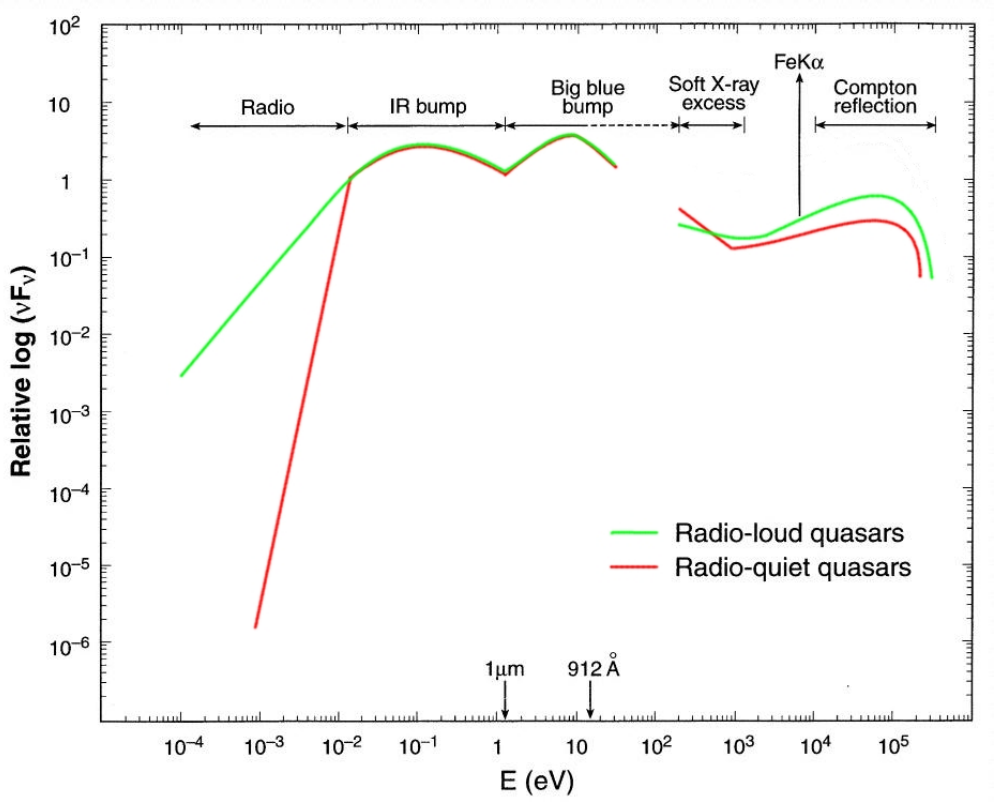

FIGURE 1.1— Schematic representation of the broadband continuum spectral energy distribution for radio-quiet (red colour) and radio-loud (green) AGNs. The main components of a typical AGN are indicated in the figure. Adapted from Koratkar & Blaes (1999).

power in radio: radio-loud and radio-quiet. Fig. 1.1 shows a schematic view of the typical SED of radio-loud and radio-quiet quasars. The former are much brighter at radio wavelengths and present a flatten slope in this range when compared with the latter, which are in turn 10–20 times more numerous. Broad-line radio galaxies (BLRGs) and narrow-line radio galaxies (NLRGs) are the radio-loud analogs of type 1 and type 2 Seyferts, although they appear to occur in elliptical galaxies rather than spirals. However, radio-quiet does not mean that these sources are silent at radio wavelengths, i.e. the majority of them show compact radio cores in their nuclei (Slee et al. 1994; Sadler et al. 1995). The rest of the SED is much more similar for both types and shows a nearly flat power distribution (constant νF_ν), as mentioned before, with a number of interesting features when we look in detail. In the optical/UV we find the Big Blue Bump (BBB), associated with the main energy production mechanism which is most likely an accretion disk. Longwards, the infrared bump is thought to

arise from reprocessing of the UV emission by dust at different temperatures in a range of distances. In the X-ray range the emission is interpreted as the high-energy continuation of the BBB, together with a Comptonized power law with fluorescence and reflection from "cold" material (Koratkar & Blaes 1999).

For an average Seyfert galaxy, the central black hole has a typical mass around $10^7\,M_\odot$, which corresponds to a Schwarzschild radius of $R_S \sim 10^{13}$ cm, i.e. slightly larger than half of the distance from the Sun to the Earth (~ 0.7 AU). Again, from the time scale of the variable flux at certain wavelength ranges, one can also estimate the spatial scale associated with the different parts of the SED (Peterson 1997). In this sense, the X-rays are produced in a region not farther than a few times R_S from the SMBH, and the UV/optical continuum emission released by the accretion disk comes from a region smaller than $\sim 10^{15}$ cm (~ 70 AU). The variability in the broad lines points towards a size of about 10^{16} cm for the BLR (~ 4 light-days). Moreover, most of the IR continuum emission is produced at radius $\gtrsim 10^{17}$ cm ($\gtrsim 0.1$ light-years), i.e. farther than the dust sublimation limit (Barvainis 1987). Finally, we find the NLR at $\gtrsim 10^{18}$ cm ($\gtrsim 0.3$ pc). With these scales in mind, we will introduce in the next Section the most widespread picture considered nowadays to explain the internal structure and the differences among the different types of AGNs: the unified model. Further Sections will be focused on the main contributions derived from the exploration of nearby active galaxies at high-spatial resolution and the main differences when compared with low-spatial resolution studies.

1.1.1 The unified model for AGNs

In the nearest AGNs, the NLR extends up to kiloparsec scales forming an ionization bicone out of the main body of the host galaxy, suggesting that they show an axial rather than a spherical symmetry. In those AGNs with a radio jet, the axis of the jet also appears to be located within the opening angle of the ionization cone. On the other hand, the discovery for some of the prototypical Sy2s of broad-permitted lines in their polarized (Antonucci & Miller 1985) or infrared spectra (Blanco et al. 1990), as it was the case of NGC 1068, suggested the presence of an anisotropic obscuring structure that partially covers the central engine. This is also supported by the fact that Sy2s are systematically more obscured than Sy1s (Risaliti et al. 1999). Thus, the unified model is based on the existence of an optically thick obscuring torus that permits the radiation to escape only through a certain solid angle around its axis. This model was described by Antonucci (1993) to explain the differences observed between type 1 and type 2 Seyferts (hereafter Sy1 and Sy2, respectively). The analogous model for radio-loud galaxies was elaborated by Urry & Padovani (1995). In this context, all the AGNs present a similar structure as in Fig. 1.2, and therefore it is our relative orientation with

regard to the geometry of the system that discriminates whether we find a type 1, for uncovered solid angles, or an obscured type 2 AGN.

Fig. 1.2 shows a schematic picture of the unified model divided in two sides corresponding to radio-quiet (left) and radio-loud (right) galaxies. The SMBH lies at the centre of the accretion disk, and both are surrounded by the obscuring torus. For radio-loud objects the model also consider the formation of a jet along the axis of the disk. Close to the SMBH, the BLR (red dots in Fig. 1.2) represents a system of fast rotating clouds producing the broad emission lines in the spectra of type 1 AGNs. Along the ionization cone, the interstellar clumpy media in the host galaxy is also

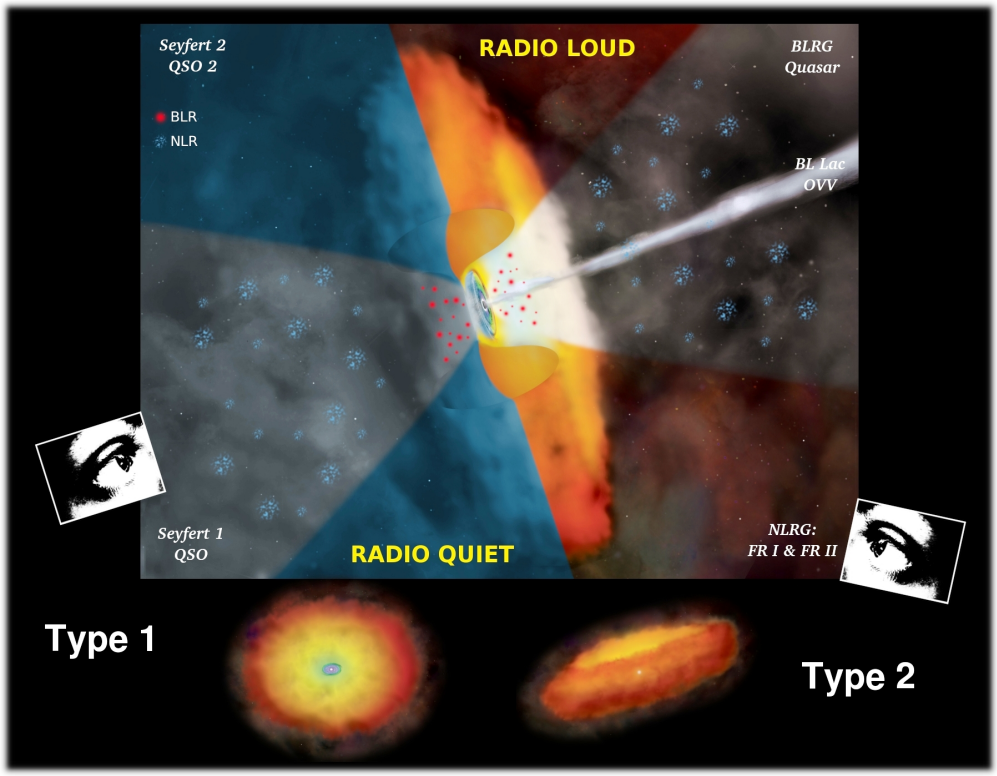

FIGURE 1.2— Unified model for AGNs according to Antonucci (1993). Labels for the diverse kinds of AGNs found in the literature are placed according to their proper orientation within the unified model. BLRG stands for broad-line radio galaxies, while NLRG corresponds to narrow-line radio galaxies. The latter are divided in two types: Fanaroff-Riley I (or FR I), with radio jets brighter towards the central core, and Fanaroff-Riley II (or FR II), brighter towards the lobes at the far end of the jet (Fanaroff & Riley 1974). BL Lac objects and optically violent variables (OVVs), also known as "blazars", correspond to radio-loud AGNs with their jets oriented in the direction of our line of sight (for a detailed taxonomy of AGNs see Peterson 1997, and references therein).

illuminated, forming the NLR (blue clouds in Fig. 1.2).

1.1.2 Low-spatial resolution studies

Some of the first studies obtaining average SEDs for AGNs were presented by Sanders et al. (1989) and Elvis et al. (1994) for the case of radio-loud and radio-quiet quasars, which are very similar to the schematic SEDs shown in Fig. 1.1. Despite of the spatial resolution, the templates in these cases are representative of the nuclear source, since this is two orders of magnitude brighter than the host galaxy. However, even for bright Seyferts it is usual to have a strong contribution in the IR from the host galaxy, e.g. the nuclear starburst ring in NGC 7469 dominates this range with two thirds of the bolometric luminosity, for apertures of $\sim 4''$ (Wilson et al. 1991). In general, the energy released by a Seyfert nuclei is comparable to the contribution of the galaxy from radio to the soft X-rays, and thus measurements in this range with a beam larger than the central core will be blended with the light from their host. As expected, the case of LLAGNs is even more critical as they are faintest active nuclei.

Schmitt et al. (1997) presented average SEDs for spiral, elliptical, starbursts, Sy2s and LINERs based on data with a spatial resolution around $10''$–$20''$. Their sample is based on the catalogue of *IUE* (*International Ultraviolet Explorer*) spectra from Kinney et al. (1993) and Kinney et al. (1996), including a total of 59 objects: 6 non-active spirals, 6 non-active ellipticals plus one spiral bulge, 26 star-forming galaxies, 15 Sy2s and 5 LINERs. Starburst are also divided at the value of $E(B-V) = 0.4$ between those with a lower reddening (SBL) and those with a higher reddening (SBH). The individual SEDs were normalized before the average to the flux at 7000 Å, which is representative of the contribution from the old stellar population. These authors find that ellipticals and spirals present very similar SEDs over the whole range, and both are fainter than the rest (Fig. 1.3). Starbursts are quite similar across the whole SED, although SBL are stronger in the UV and fainter in the IR when compared with SBH. LINERs are quite similar to starburst and Sy2s in the NIR-to-optical range, but fainter at other wavelengths. Nevertheless, they are stronger in the MIR when compared with normal spirals and ellipticals. Finally, Sy2s are similar to starbursts from radio to the NIR, fainter in the optical-UV range but stronger in the X-rays.

However, the average energy distributions of both LINERs and Sy2s still reflect the stellar contribution in the visual range, with a remarkable peak at $\sim 0.9\,\mu$m ($\log \nu \sim 14.5$ in Fig. 1.3). In the MIR, Sy2s are suspiciously similar to starbursts, a fact that could be produced by a coupling between nuclear activity and star formation, i.e. Sy2s frequently show circumnuclear starbursts since both phenomena are feed by large amounts of molecular material in the central region (González Delgado et al. 2001). This argument can be extrapolated to radio wavelengths, since the SNRs left after a

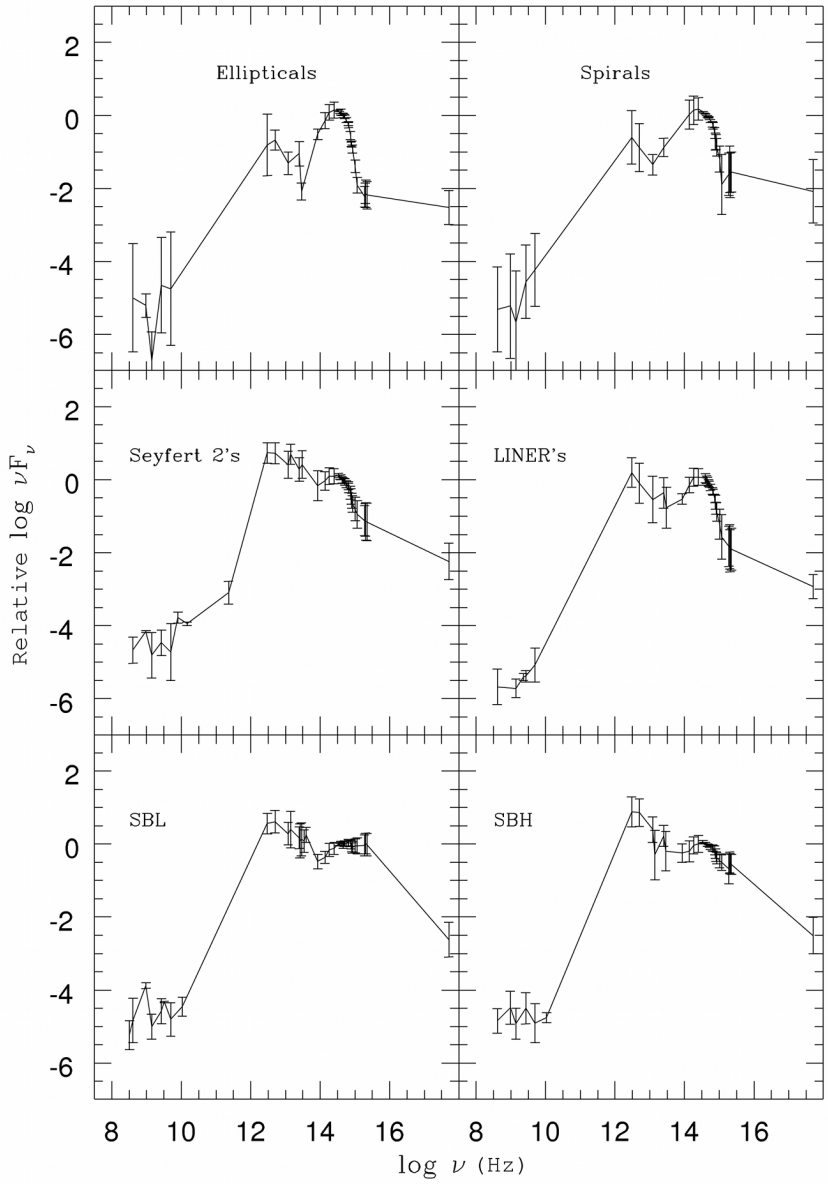

FIGURE 1.3— Average SEDs by Schmitt et al. (1997) for a sample of 6 spiral galaxies, 6 ellipticals plus one spiral bulge, 11 low-reddening starbursts (SBL), 15 high-reddening starburst (SBH), 15 Sy2s and 5 LINERs. Individual SEDs were normalized to their flux at 7000 Å before the average. The division between low and high-reddening starburst is made at $E(B-V) = 0.4$. Adapted from Schmitt et al. (1997).

star-formation episode contribute mostly to this range. Interestingly, when compared with radio-loud and radio-quiet quasars by Sanders et al. (1989), the SED of the latter presents a slope at radio wavelengths quite similar to the cases of Sy2s, LINERs and starbursts.

Polletta et al. (2007) presented a set of SEDs for 117 AGNs detected at hard X-rays ($F_{2-10\,\mathrm{keV}} > 10^{-14}\,\mathrm{erg\,cm^{-2}\,s^{-1}}$), including data from *XMM–Newton*, VLT/VIMOS and the Canada-France-Hawaii Telescope in the optical, UKIRT in the NIR, *Spitzer* in the IR and VLA at radio wavelengths. These authors classify their sample in three types depending on the similarity of their SEDs to that of a quasar-like source (AGN1s, $\sim 32\%$ of the sources), either a type 2 AGN or composite type 2 plus star-formation (AGN2s, $\sim 50\%$) and a star-forming template similar to spiral or starburst galaxies (SF, $\sim 18\%$). For each of these classes, average rest-frame SEDs were obtained from the MIR to X-rays, normalizing the SEDs at 1 μm before the average. This wavelength represents the sublimating radius for the dust and therefore divides the emission from the accretion disk, in the optical/UV, from the dust in the IR (Elvis et al. 1994).

Overall, the resulting average SEDs become increasingly blue in the NIR to optical range ($\lambda < 1\,\mu\mathrm{m}$), red towards the IR ($1 < \lambda < 10\,\mu\mathrm{m}$) and soft in the X-rays from the SFs to AGN2s and AGN1s (see Fig. 5 in Polletta et al. 2007, also Fig. 1.4). This means that SEDs for AGN1s are the bluest shortwards of 1 μm, the reddest in the 1–10 μm range and the softest ones at X-rays. However, in the optical they are still redder than the quasar templates given by Elvis et al. (1994). In contrast, the average SEDs for SF and AGN2s are quite similar and significantly redder in this range when compared with AGN1s, suggesting that the optical emission in most of the SF and AGN2s might be dominated by the light of the host galaxy. In the NIR and MIR, AGN1s and AGN2s are very similar and redder than SFs. In the X-rays, SFs seem to be the strongest absorbed sources, followed by AGN2s and AGN1s in this order. Moreover, Polletta et al. (2007) also investigated the variations of the average SEDs with the AGN intrinsic luminosity. Each class (AGN1, AGN2 and SF) is separated in three groups depending on their absorption-corrected broadband X-ray luminosity: $L^{corr}_{0.5-10\,\mathrm{keV}} < 10^{44}\,\mathrm{erg\,s^{-1}}$, $10^{44} < L^{corr}_{0.5-10\,\mathrm{keV}} < 10^{44.64}\,\mathrm{erg\,s^{-1}}$ and $L^{corr}_{0.5-10\,\mathrm{keV}} > 10^{44.64}\,\mathrm{erg\,s^{-1}}$. Fig. 1.4 shows the average SEDs for each case, grouping them by their X-ray luminosity (left column) or by their class (right column). The radio-quiet quasar template from Elvis et al. (1994) is also shown for comparison.

At low luminosities (Fig. 1.4*a*), the host galaxy dominates the emission and the different classes are consistent within the 1σ dispersion, although their SEDs show some differentiated features. For intermediate-luminosity sources (Fig. 1.4*c*) these differences are significant in the optical shortwards of $\sim 0.4\,\mu\mathrm{m}$, with AGN1s becoming bluer, and also in the IR longwards of 2 μm, with AGN1s and AGN2s becoming redder. The most luminous AGN1s in Fig. 1.4*e* are considerably brighter

in the X-rays than the rest, with an optical-to-IR SED quite similar to the quasar template. Therefore, the optical/UV emission can be interpreted as the signature of

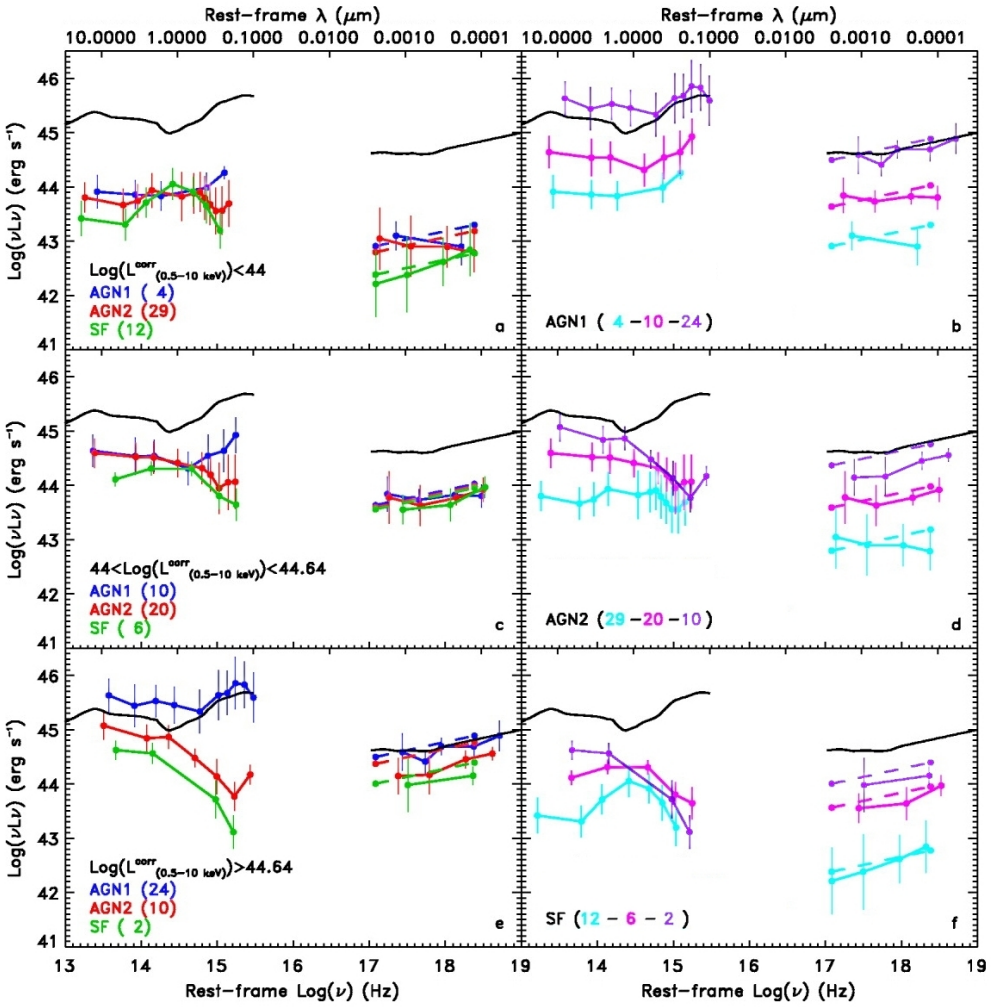

FIGURE 1.4— *Left column:* average SEDs for AGN1s (blue colour), AGN2s (red) and SFs (green) grouped by their absorption-corrected broadband X-ray luminosity ($L^{corr}_{0.5-10\,\mathrm{keV}}$) are represented by filled circles in *a)* $< 10^{44}\,\mathrm{erg\,s^{-1}}$, *c)* 10^{44}–$10^{44.64}\,\mathrm{erg\,s^{-1}}$ and *e)* $> 10^{44.64}\,\mathrm{erg\,s^{-1}}$, considering observed (solid-lines) and absorption-corrected 0.5–10 keV X-ray luminosities (dashed-lines). *Right column:* filled circles show average SEDs for AGN1s (*b*), AGN2s (*d*) and SFs (*f*) separated by their absorption-corrected broadband X-ray luminosity, i.e. $< 10^{44}\,\mathrm{erg\,s^{-1}}$ (cyan), 10^{44}–$10^{44.64}\,\mathrm{erg\,s^{-1}}$ (magenta) and $> 10^{44.64}\,\mathrm{erg\,s^{-1}}$ (purple). Solid and dashed-lines as in left column. The number of sources used to derive the average SEDs in both columns is annotated. The black-solid line represents the template for radio-quiet quasars from Elvis et al. (1994). Figure adapted from Polletta et al. (2007).

the BBB produced by the accretion disk. AGN2s and SF show a similar SED shape with an offset in luminosity. Nevertheless, changes with the intrinsic luminosity within each class are highlighted in the right column of the figure. The panel *b* in Fig. 1.4 shows that the average SED shape of AGN1s is very consistent at all luminosities. The AGN2s (Fig. 1.4*d*) become redder with increasing X-ray luminosities, probably due to the rising contribution from hot dust associated with the active nucleus. Their X-ray spectra become also slightly harder with increasing luminosity. SFs vary in a similar way as AGN2s (Fig. 1.4*f*), i.e. their SEDs become redder with increasing luminosity, although their NIR luminosity remains approximately the same.

Summarizing, templates obtained from data with low-spatial resolution (tens of arcseconds or larger), are representative of the nuclear core only at high-luminosities ($\gtrsim 10^{45}\,\mathrm{erg\,s^{-1}}$), i.e. for quasars and bright Seyferts. However, the uncertainty remains below $L \sim 10^{44}\,\mathrm{erg\,s^{-1}}$. Moreover, at very low luminosities ($\lesssim 10^{42}\,\mathrm{erg\,s^{-1}}$) we expect significant changes in the internal structure of the torus, and therefore in the nature of the AGN emission (Elitzur & Shlosman 2006; Hönig & Beckert 2007).

1.1.3 High-spatial resolution studies

In the last 20 years, the *HST* in the optical/UV range together with the use of high-spatial resolution techniques in 8-meter class telescopes (i.e. AO and interferometry), in the NIR, allowed us to access the inner parsecs of the nearest galaxies. For active galaxies this means that we are able to almost isolate the light from the central engine to the starlight of the galaxy at these spectral ranges, something that is already possible since a long time at radio wavelengths using very-long baseline interferometry (VLBI). As mentioned before, the lack of resolution at high energies is not so harmful, specially in the hard X-rays. Thanks to these improvements, interferometric studies in the IR have revealed the presence of dusty structures with sizes of a few parsecs around Seyfert nuclei similar to the proposed torus in the unified model (Jaffe et al. 2004; Tristram et al. 2007; Beckert et al. 2008; Burtscher et al. 2009; Pott et al. 2010), although it seems that this structure is not universally present (Meisenheimer et al. 2007).

However, interferometric observations in the IR are subject to bright sources, limiting the number of objects that can be covered. Some recent works have collected high-spatial resolution images in the UV/optical and/or the IR ranges for a larger number of objects, loosing spatial resolution with regard to interferometry data but gaining a wider coverage in wavelength with a very consistent spatial resolution. For example, the recent work by Ramos Almeida et al. (2009) explores the IR range with high-spatial resolution, deriving an average template for Sy2s in the 1–20 μm range. Ho (1999) and Eracleous et al. (2010) collect the SED of LINERs from sets of high-spatial resolution data in the X-ray, optical/UV and radio ranges. In this context, one

of the most complete studies in terms of wavelength coverage was presented by Prieto et al. (2010) for a sample of Sy1s and Sy2s including X-ray, optical, IR and radio data with a consistent spatial resolution in the 5–20 pc range. Finally, fitting all these data to state-of-the-art torus models permits to constrain the physical properties of the material that hides the central engine (Hönig et al. 2006; Schartmann et al. 2008; Nenkova et al. 2008; Ramos Almeida et al. 2009).

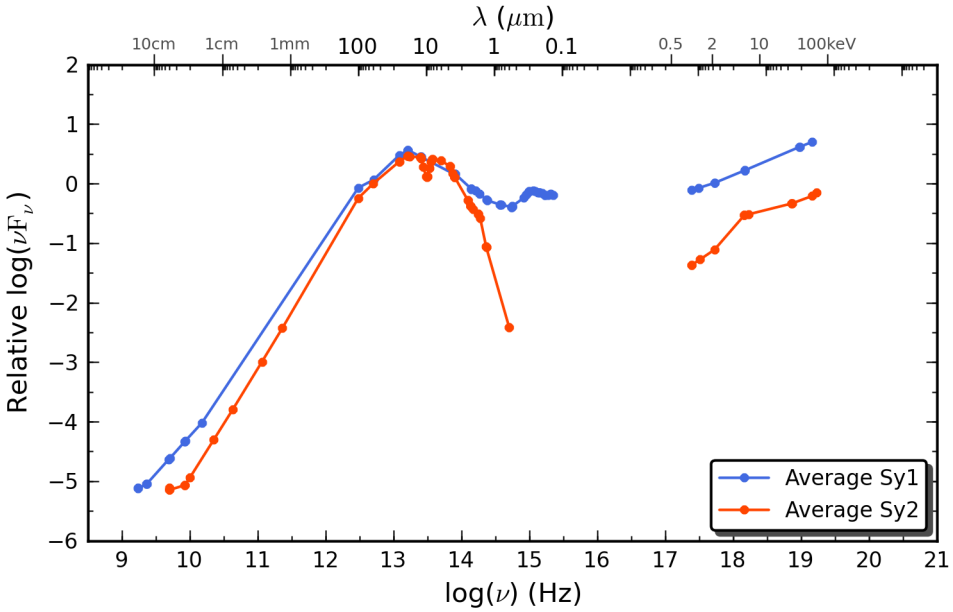

FIGURE 1.5— Average SEDs for Sy1s (blue dots) and Sy2s (red dots). Adapted from Prieto et al. (2010).

High-spatial resolution SEDs from 1 to 18 μm for a sample of local Seyferts (Ramos Almeida et al. 2009) show that their MIR spectra decreases more steeply towards the NIR with regard to fluxes measured from larger apertures ($\gtrsim 1.5''$). These authors also found that the fall of the SED in the IR is more pronounced for types 2 ($\alpha \sim 3$) rather than for intermediate types ($\alpha \sim 1.6$–2). A similar result can be derived from the average SEDs presented by Prieto et al. (2010), shown in Fig. 1.5. In this work, a mean distribution for both Seyfert types[1] was obtained from high-spatial resolution data including three Sy1s (NGC 3783, NGC 1566 and NGC 7469) and four Sy2s (Circinus, NGC 1068, NGC 5506 and NGC 7582). Before averaging, the

[1] http://www.iac.es/project/parsec/main/seyfert-SED-template.php

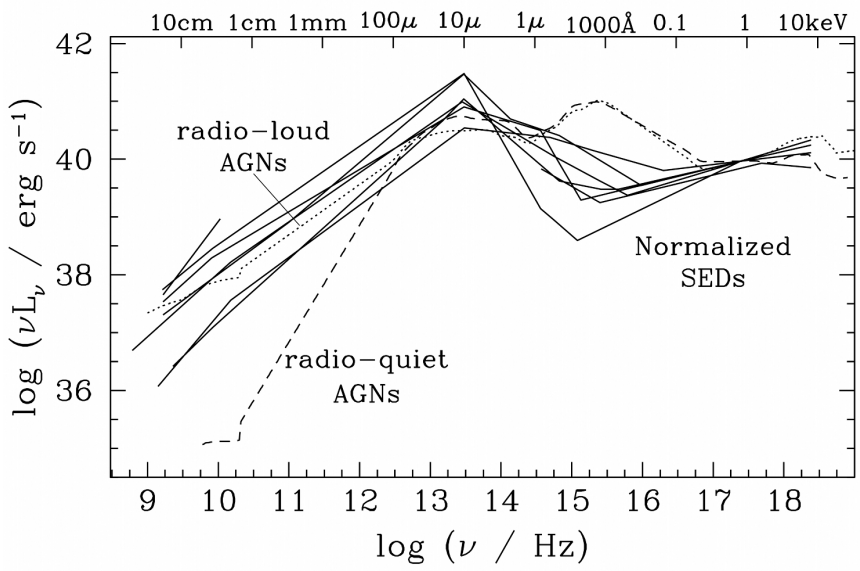

FIGURE 1.6— A compilation of LINER SEDs normalized at 1 keV (solid lines) by Ho (1999). Objects included are: NGC 3031 (M81), NGC 4261 (3C 270), NGC 4374 (M84), NGC 4486 (M87), NGC 4579 (M58), NGC 4594 (M104) and NGC 6251. The fluxes rely on HSR data except in the IR, where the photometry apertures are larger than $\gtrsim 3''$–$10''$ in the NIR and MIR and $\gtrsim 1'$ in the FIR. Normalized distributions for radio-loud (dotted line) and radio-quiet quasars (dashed line) from Elvis et al. (1994) are also plotted for comparison. Adapted from Ho (1999).

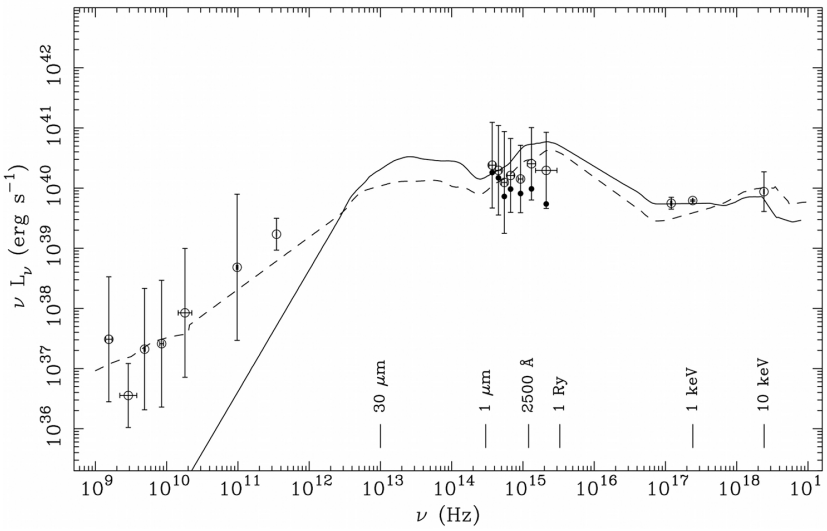

FIGURE 1.7— Average SED for a sample of 24 LINERs. Open circles represent the average after extinction corrections, while the filled circles show the average before any extinction corrections were applied (in the range 0.1–1 μm only). The vertical error bars indicate the standard deviation in $\log(\nu L_\nu)$. The horizontal error bars represent the frequency bands within which measurements were averaged. Overplotted are the average SEDs of radio-quiet (solid lines) and radio-loud (dashed lines) quasars from Elvis et al. (1994), normalized to the same X-ray luminosity as the average LINER SED. Adapted from Eracleous et al. (2010).

rest-frame SEDs were normalized to the mean value of its power distribution (νF_ν). Fig. 1.5 shows two clear similarities for both types: the broad IR bump in the 2–10 μm range and the rise towards higher energies in the X-rays ($\sim$ 1–200 keV). The slope at radio wavelengths is also quite similar for both distributions. Shortwards of 2 μm, Sy2s show a deep absorption-like profile which almost or totally hides the nuclei in the optical and UV ranges. In contrast, Sy1s show and upturn in their SEDs around 1 μm and a secondary bump in the optical/UV, which reminds to the the BBB usually found in quasars (see Fig. 1.1). Furthermore, the luminosity associated with the IR bump represents $\gtrsim 70\%$ of the total energy output, complemented mostly by the energy released shortwards of 20 keV. When compared with the SED obtained with lower-spatial resolution data (e.g. IR satellites), the shape of the SED can be strongly affected by the light contribution from the host galaxy. For many of the brightest Seyferts, $L \gtrsim 10^{44}\,\mathrm{erg\,s^{-1}}$, this is a minor problem as the AGN component dominates the SED. However, in the case of the faintest ones the situation is quite dramatic since the low-spatial resolution SED is sampling, at certain wavelength ranges, the energy distribution of the host galaxy rather than that of the active nucleus itself.

Ho (1999) presented the SEDs of a sample of 7 low-luminosity AGNs, using high-spatial resolution data ($\lesssim 1''$) in the X-ray, optical/UV and radio ranges (Fig. 1.6). These SEDs look very different when compared with classical luminous AGNs, with the absence of an ultraviolet excess (i.e. the big blue bump) associated with the accretion disk. These authors also propose that this is an intrinsic property to the SEDs of LINERs, and not an artifact of strong dust extinction. In a recent study by Eracleous et al. (2010) the statistics are improved with the SEDs of 35 LINERs, using a similar dataset. In this case, individual SEDs were normalized (arbitrarily) to an integrated X-ray luminosity in the 2–10 keV range of $10^{40}\,\mathrm{erg\,s^{-1}}$ (11 LINERs were rejected at this stage due to their non-detection at X-rays). The average SED was then obtained from the mean of the $\log(\nu L_\nu)$, i.e. the geometric mean of the power distribution, in different frequency bins. In the range between 0.1 and 1 μm this process was repeated before and after applying extinction corrections. Fig. 1.7 shows that the average LINER SED has a very similar slope at X-rays when compared with the quasars templates by Eracleous et al. (2010), although the slope at radio wavelengths resembles to that of radio-loud quasars.

1.2 Star-formation in the centre of galaxies

Star formation appears to occur almost exclusively within molecular clouds, sufficiently dense and shielded against the interstellar ultraviolet radiation. The highest fraction of molecular gas is usually found also in those parts of the galactic disks with the highest total gas surface densities, although this value can increase up to 90% for

the entire galaxy in the case of the most active star-forming galaxies (Iono et al. 2005). This molecular material is organized into giant molecular clouds (GMCs), which have masses in the 10^4–$10^7\,M_\odot$ range (Klessen et al. 2009). In this environment, stars are formed in the densest regions within a cloud, and thus only a small fraction of the material in the cloud become stars. The mass function (also called mass spectrum) of the molecular clouds seems to be well described by a power law:

$$\frac{dN}{dM} \propto M^{-\gamma} \tag{1.1}$$

with $1.3 \lesssim \gamma \lesssim 1.8$, apparently without any characteristic mass or a turnover for the mass function in the 1–$10^3\,M_\odot$ range, i.e. as the Jeans mass, which represents the lower limit for gravitationally-bound clouds (Kramer et al. 1998). Interestingly, this distribution changes slightly when considering the protostellar cores of these clouds. In this case, the mass function resembles a double power law with $\gamma \sim 2.5$ above $0.5\,M_\odot$ and $\gamma \sim 1.5$ for lower masses, very similar to the stellar IMF (Motte et al. 1998; Johnstone et al. 2001, 2006; Lada et al. 2008). Therefore, the molecular cloud complexes tend to induce a "clustered" star formation mode, to the point that the isolated star formation is quite unusual (Lada & Lada 2003). As an example, it seems that less than 4% of the O-type stars in the Milky Way have formed outside a clustered environment (Schilbach & Röser 2008).

The formation of compact and massive clusters with thousand of stars is very rare in our neighbourhood: the Orion Nebula Cluster is located at $\sim 410\,$pc and shows a few O–B stars, NGC 3603 is found in the Carina region ($\sim 7\,$kpc) and is about ten times more massive than the Orion Nebula Cluster with a dozen O stars. The latter is also considered as the closest "starburst knot" (Moffat et al. 2002). Farther away, if we look at the Large Magellanic Cloud (LMC, $\sim 55\,$kpc), we can find clusters with ages comparable to those of many open clusters in the Milky Way, but their masses and core densities exceed those of the latter. In the LMC, the giant star-forming region 30 Doradus –also known as the Tarantula Nebula or NGC 2070– is a big extragalactic H II region with roughly ten times more mass than NGC 3603 and more than 400 O stars (Walborn & Blades 1997). At the centre of 30 Doradus, the cluster R 136 represents a very good example of a young stellar cluster (YSC). Due to the compactness of its core, this was once believed to be an extraordinary single stellar object with $\sim 2000\,M_\odot$ and $10^8\,L_\odot$, until Weigelt & Baier (1985) resolved it into individual stars. Actually, it is formed by a total of $\sim 10^5$ young stars within a region of only $\sim 10\,$pc in size (Campbell et al. 2010). Nevertheless, with its total mass of about $\sim 2 \times 10^4\,M_\odot$, R 136 is still at the lower end of the YSCs mass range (Walborn et al. 2002). The "bluish knots" and "super-star clusters" (SSCs) forming the giant H II regions in starburst and merging galaxies, like M82 or the Antennae, are also identified as YSCs or groups of them (Kennicutt & Chu 1988; Portegies Zwart et al. 2010). The

mean densities of some of these starbursts approach those found in the core of GMCs, but the dense gas in the former extends over regions with a few kiloparsecs in size. Thus, these regions can reach a projected SFR per unit area as high as the maximum limit observed for nearby stellar clusters and associations (Meurer et al. 1997).

As mentioned before, most of the stars form in clusters, which appear to be specially ubiquitous in starburst and interacting galaxies. However, apart from the youngest ones, only a small fraction of stars are currently found inside clusters, suggesting that the latter have short lives. In line with this, open clusters in the Galaxy are dissolved on time scales of $\sim 250\,\mathrm{Myr}$, comparable to the median age of those in the solar neighbourhood (Kharchenko et al. 2005). Moreover, observations of massive clusters in the Antennae (Fall et al. 2005) and M51 (Bastian et al. 2005) find an excess of clusters with ages around 10 Myr, when compared with what would be expected by assuming a constant cluster formation rate (Bastian & Gieles 2006). This suggests that a high percentage of clusters might be disrupted after the first $\sim 10\,\mathrm{Myr}$ (Mengel et al. 2005). This "infant mortality" can be even higher than 95% (Fall & Zhang 2001). In this context, the lifetime of a YSC is determined at first order by its evaporation time (τ_{ev}), i.e. the time that it takes for internal stellar encounters to eject all of its members. This is, in turn, largely determined by N, the number of stars in the system (Lada & Lada 2003):

$$\tau_{ev} \propto \frac{N}{\ln N} \tag{1.2}$$

Therefore, the more massive a cluster is, the larger the number of stars and so the lifetime of the cluster. YSCs with masses of about $\gtrsim 10^5\,\mathrm{M}_\odot$ have expected lifetimes comparable to the age of the universe and are promising candidates for being "young globular clusters", i.e. evolving toward globular clusters (GCs) in the future. However, this evolution is not just a matter of aging, since there are important differences in the internal structure and the mass function of both systems (Portegies Zwart et al. 2010). With regard to the latter, the mass distribution of YSCs found in interacting and starburst galaxies usually follow a power law with $\gamma \sim 2$ in the 10^4–$10^6\,\mathrm{M}_\odot$ range (Whitmore et al. 1999; Zhang & Fall 1999), thus similar to the mass spectra of molecular clouds (Rosolowsky 2005), while GCs show a lognormal mass distribution with a turnover at a characteristic mass of $\approx 2 \times 10^5\,\mathrm{M}_\odot$ and a dispersion of $\sigma(\log M) \sim 0.5$ (see Fig. 1.8, Harris 1991). In further Sections we will go from the nearest resolved clusters in the Milky Way and the Magellanic Clouds to the more numerous but barely resolved populations of young clusters found in nearby galaxies, trying to understand how a recently formed YSC system may or not evolve into an old population of GCs.

1.2.1 Resolved young stellar clusters

There are basically two types of clusters depending on their content of interstellar matter (Portegies Zwart et al. 2010): standard open clusters with little or no interstellar matter, and "embedded clusters" which are fully or partially surrounded by interstellar gas and dust. Most of the latter are invisible in the optical range and are usually detected in the IR. Embedded clusters are considered as protoclusters, becoming standard open clusters or YSCs when they emerge from their natal clouds. In fact, because of the strong and variable obscuration affecting these regions, no truly massive clusters were known to exist in our Galaxy until the Arches and Quintuplet clusters were identified by Figer et al. (1999a) at IR wavelengths in the Galactic Centre. Fig. 1.9 shows how the complex structure of the Galactic Centre difficults

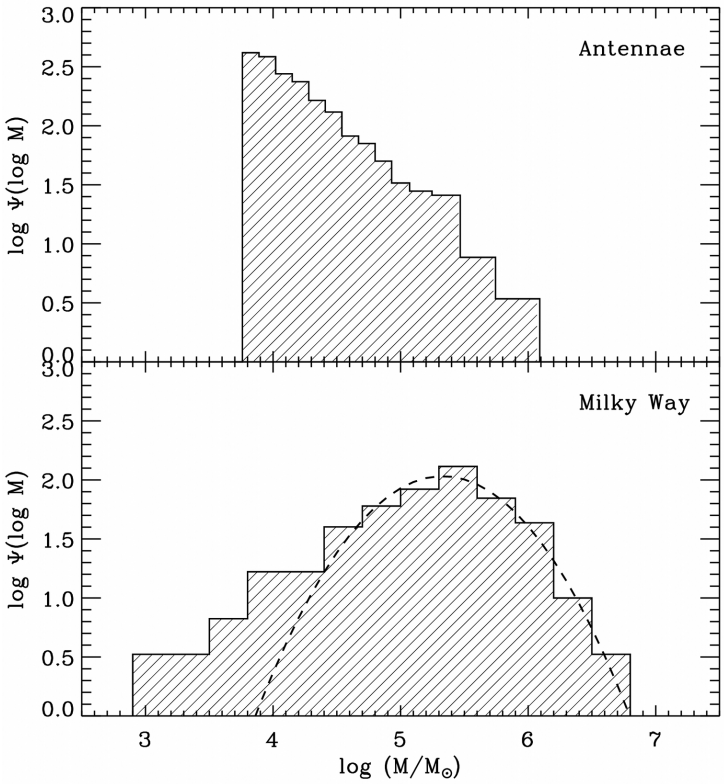

FIGURE 1.8— Mass distribution for YSCs in the Antennae (Zhang & Fall 1999) and the GCs in the Milky Way (Harris 1996). The dashed line represents a lognormal mass function with a peak at $M_* = 2\times10^5\,\mathrm{M}_\odot$ and a dispersion of $\sigma(\log M) = 0.5$, which corresponds to a Gaussian distribution of absolute magnitudes with $M_V = -7-3$ and $\sigma(M_V) = 1.2$ (for $M/L_V = 3$). Adapted from Fall & Zhang (2001).

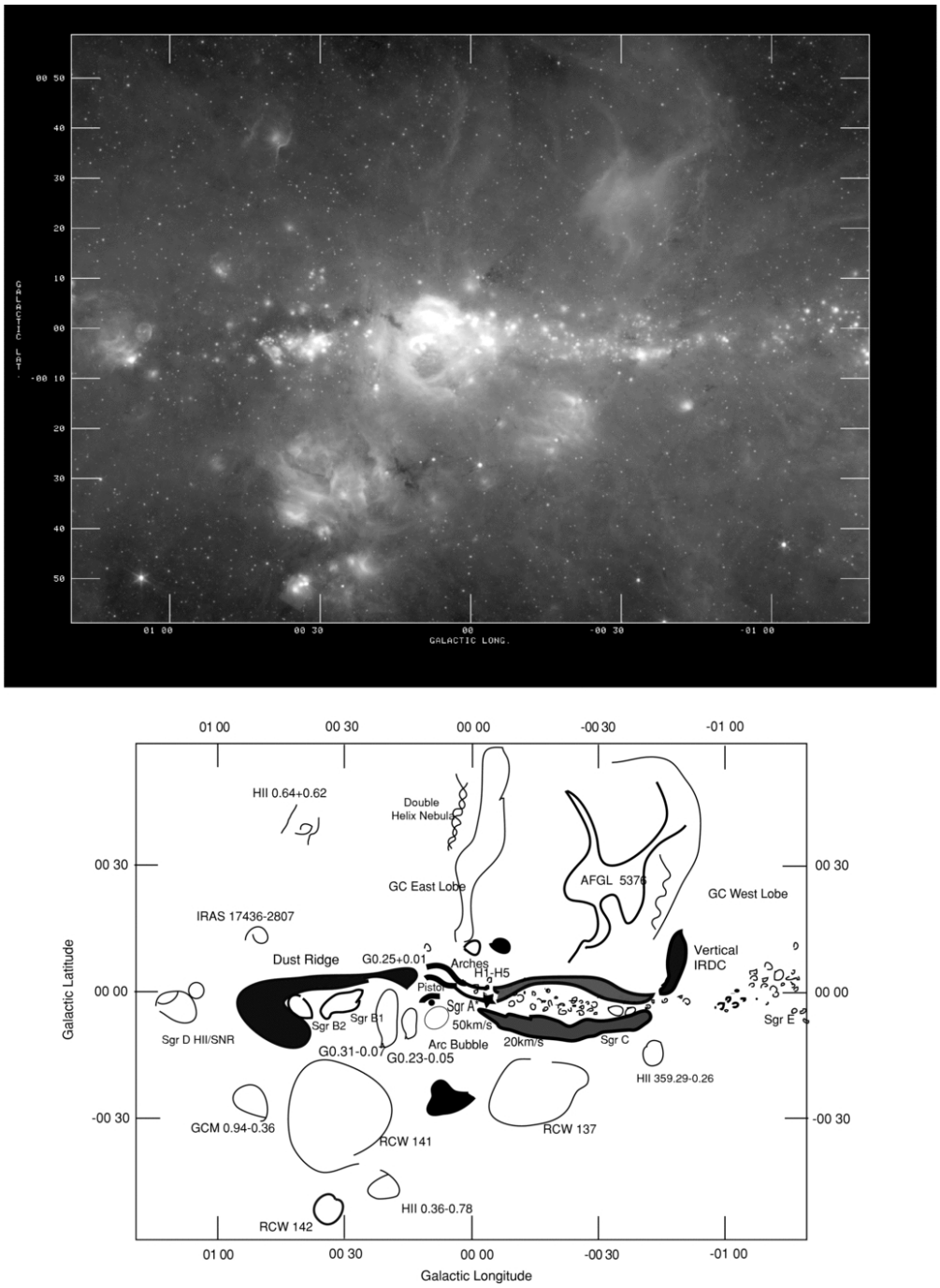

FIGURE 1.9— *Upper panel:* central $2.^{\circ}5 \times 2^{\circ}$ of the Galaxy showing the prominent H II complexes (Sgr A*–E) at 24 µm. *Lower panel:* schematic diagram of prominent features seen in the upper panel. Adapted from Yusef-Zadeh et al. (2009).

the identification of YSCs in this region. However, since the discovery of these clusters a larger population of similar objects has been found in our Galaxy (Figer 2008; Portegies Zwart et al. 2010). Tables 2 and 3 in Portegies Zwart et al. (2010) show a compilation of YSCs for the Milky Way, SMC and LMC, together with their main properties (including age, mass and size). Arches is a very young cluster with 1–2 Myr, a total mass of $\sim 2 \times 10^4\,\mathrm{M}_\odot$ and it is also highly obscured by $A_V \sim 30$ mag (Figer et al. 2002). The Quintuplet cluster is ~ 4 Myr old and has a mass of $\gtrsim 10^4\,\mathrm{M}_\odot$, with a similar obscuration as the Arches cluster (Figer et al. 1999b). However, the most massive YSC in the Milky Way is currently Westerlund 1 ($\sim 6 \times 10^4\,\mathrm{M}_\odot$) which has an age of about 3.5 Myr and is obscured "only" by $A_V \sim 10$ mag (Clark et al. 2005).

Due to their vicinity, YSCs in the Small and Large Magellanic Clouds (SMC and LMC, respectively) can also be resolved into individual stars. By resolving nearby clusters we can also study their internal structure and compare it with that of local GCs, which are proposed as the older-age counterparts of YSCs. As an example, another difference emerges between them when we consider the surface brightness distribution: the brightness profile for GCs is usually well described by a King profile (King 1966), while that of YSCs is best represented by a power law with a core (see Elson et al. 1987).

IR and radio observations of embedded clusters suggest that the early stages of YSCs may be very similar to those of compact H II regions containing a single protostar, even showing similarities in their SEDs (see Johnson 2004, 2005, and references therein). Fig. 1.10 depicts the parallel evolution of a massive star and a young and massive SSC. Formed from molecular cloud condensations, both seem to spend the first 10–20% of their lives in an embedded stage very similar to ultra-compact H II regions (Kobulnicky & Johnson 1999). During this period, almost all the luminosity is reprocessed by the surrounding dust shell or "cocoon" and radiated from MIR to submillimetre wavelenghts. When young stars have just emerged from these "cradles", we usually detect a hot dust component associated with debris material or a circumstellar protoplanetary disk (Faustini et al. 2009). On the other hand, evidences for hot dust emission in very young stellar clusters have been also detected (Johnson et al. 2004), although it is not clear whether this component comes from the individual protostars, i.e. as the sum of all the light emitted by disks, or from the intracluster medium.

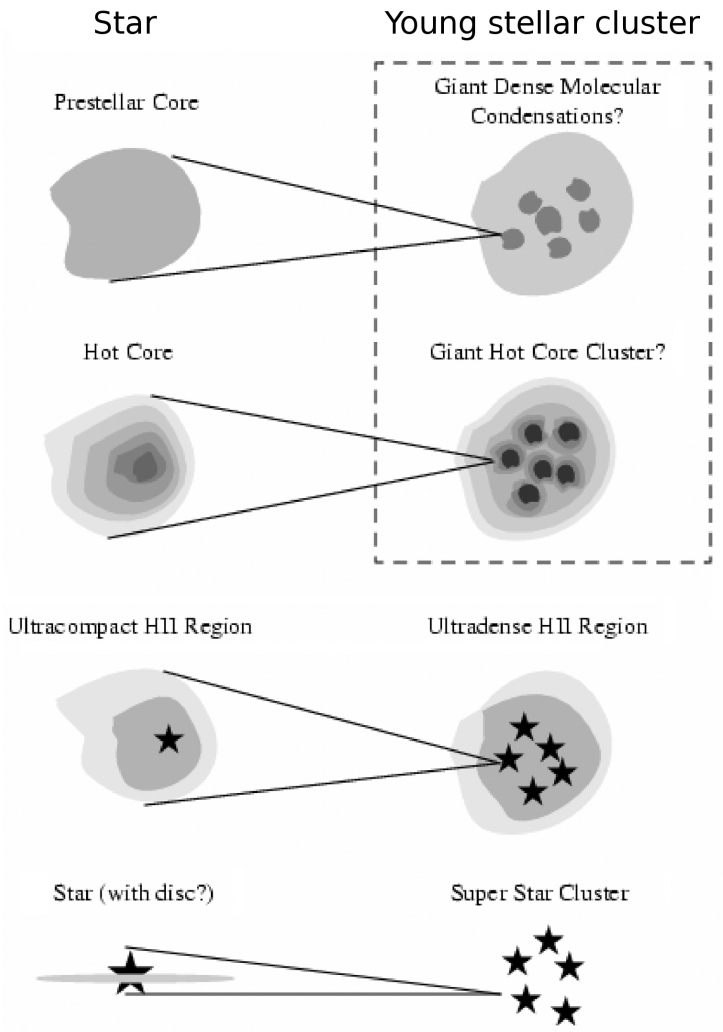

FIGURE 1.10— Scheme of the parallel evolutionary sequence for individual massive stars (left) and massive stellar clusters (right). Stages within the dash-line box have not been observationally identified. Adapted from Johnson (2005).

1.2.2 Extragalactic young stellar clusters

Unlike their relatives in the Milky Way and the Magellanic clouds, stellar clusters in nearby galaxies are barely or not resolved. Nonetheless, they span a much wider range in their age and mass distributions, becoming excellent laboratories to study the star formation process in very different environments. The study of these systems with high-spatial resolution techniques has shed light on the matter of the YSC mass

distribution. Recent works show significant results for "normal" spiral galaxies like M31 (Caldwell et al. 2009; Vansevičius et al. 2009; Perina et al. 2010) or M81 (Santiago-Cortés et al. 2010), circumnuclear rings in spirals like NGC 1512 and NGC 5248 (Maoz et al. 2001), starbursts like NGC 5253 (Vanzi & Sauvage 2004) or M82 (McCrady & Graham 2007), and interacting galaxies like M51 (Bik et al. 2003; Hwang & Lee 2010), or the Antennae (Whitmore et al. 1999; Zhang & Fall 1999). The latter exhibit more than 10^3 young clusters visible in the optical, and this even increase when we look at IR wavelengths (Gilbert et al. 2000). Table 4 in Portegies Zwart et al. (2010) collect the main properties for a number of YSCs found outside the Local Group.

As mentioned at the beginning of this Section, the mass distribution of YSC

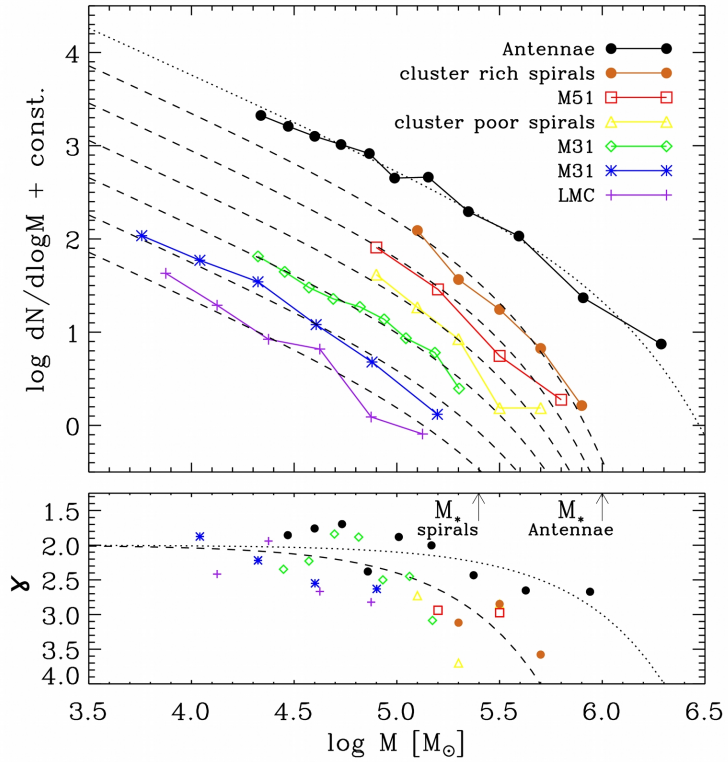

FIGURE 1.11— *Upper panel:* Comparison of mass functions for clusters younger than ~ 1 Gyr in different galaxies. The cluster mass functions in spirals are compared to a Schechter function with $M_* = 2.5 \times 10^5\,\mathrm{M}_\odot$ (dashed lines), and $M_* = 10^6\,\mathrm{M}_\odot$ for the case of the Antennae (dotted line). *Lower panel:* logarithmic slopes corresponding to the mass and the Schechter functions shown in the upper panel. Adapted from Portegies Zwart et al. (2010).

systems usually follows a power-law behaviour with a slope close to ~ -2. However, some studies have also found evidences for a truncation of this power-law at the high-mass end (Gieles et al. 2006b; Larsen 2009; Vansevičius et al. 2009). In this context, the YSC mass function is better represented by the Schechter (1976) distribution:

$$\psi(M) \equiv \frac{dN}{dM} \propto \left(\frac{M}{M_*}\right)^{-\gamma} \exp\left(-\frac{M}{M_*}\right) \tag{1.3}$$

where $\gamma \sim 2$ and M_* is the characteristic mass at which the distribution deviates from the power-law behaviour. The latter is found to be $\sim 2 \times 10^5\,\mathrm{M}_\odot$ for spiral galaxies similar to the Milky Way and circumnuclear starburst rings (Gieles et al. 2006b; Larsen 2009; van de Ven & Chang 2009) and $\gtrsim 10^6\,\mathrm{M}_\odot$ for interacting and luminous infrared galaxies (Bastian 2008). Fig. 1.11 shows a comparison of the mass distribution measured for YSCs younger than 1 Gyr in nearby galaxies, suggesting that the value of M_* depends on the local environment, i.e. on the host galaxy.

On the other hand, GCs usually show a lognormal mass distribution with a turnover at a characteristic mass of $\approx 2 \times 10^5\,\mathrm{M}_\odot$ with a dispersion of $\sigma(\log M) \sim 0.5$ (Fig. 1.8, Harris 1991). One explanation for this preferred mass scale is that the environment where the actual GCs were born, i.e. the ancient galaxies, favoured the formation of objects with masses around 10^5–$10^6\,\mathrm{M}_\odot$, but these special conditions do not persist in the local universe where the new clusters are forming. An alternative explanation is that clusters at the low-mass tail of the mass distribution are preferentially destroyed through dynamical evolution (Vesperini & Heggie 1997).

In this regard, we should mention that YSCs are relatively weak bound systems and thus are easily disrupted by different mechanisms (Fall & Zhang 2001). First, stellar evolutionary processes remove mass from clusters on short timescales ($\lesssim 100\,\mathrm{Myr}$) via supernova explosions and stellar winds. On longer timescales, gravitational encounters within the clusters (two-body relaxation) and tidal forces induced by the gravitational potential as the clusters orbit around the galaxy (gravitational shocks) strip the stars away from the clusters. More precisely, the inner $\sim 1\,\mathrm{kpc}$ of a galaxy is a specially dangerous place for YSCs. However, the disruption via supernova explosions and stellar winds seems to be roughly independent of mass, i.e. the infant mortality process disrupts clusters independently of their mass, and thus preserves the shape of the initial mass function. In line with this, Fall et al. (2005) find that the shape of the mass function for YSCs in the Antennae is nearly independent of age. On the other hand, if the mass function were strongly affected by gravitational shocks, its shape should depends on the radius within a galaxy and also vary from one galaxy to another, in contrast with observations which show very little variations within and among different galaxies (Harris 1991). Finally, analytical modelling by Fall & Zhang (2001) suggests the importance of two-body relaxation processes in the disruption of clusters at the

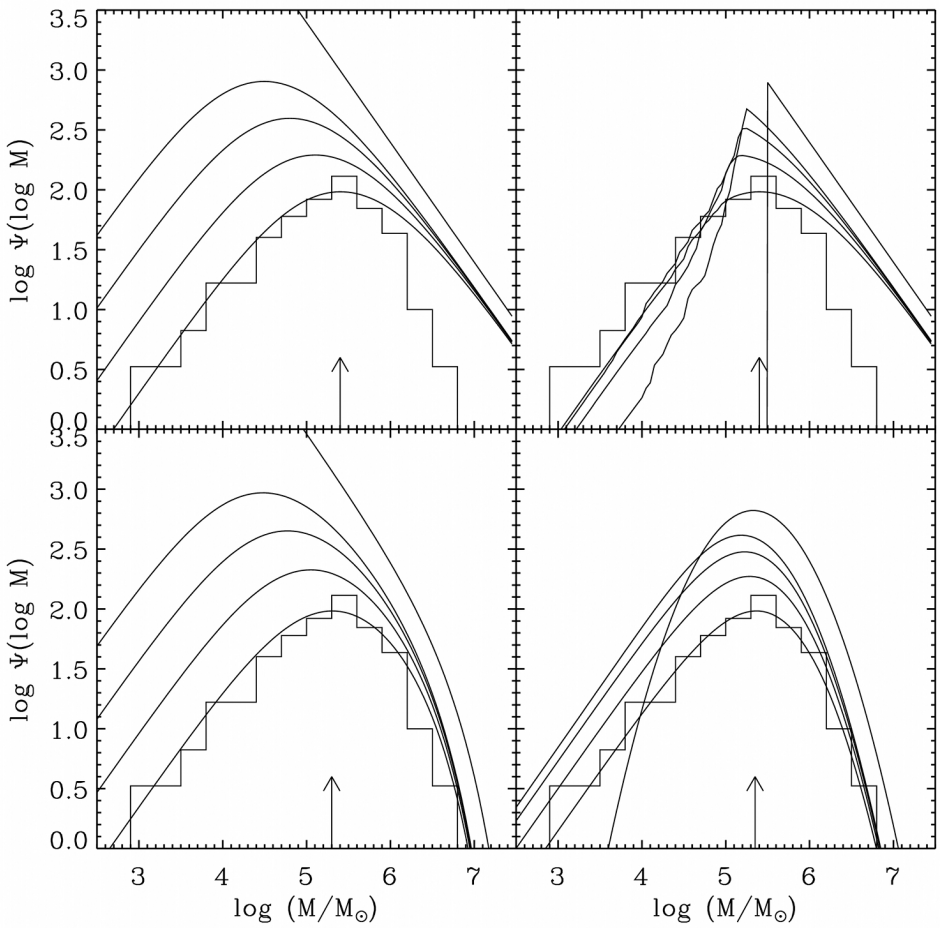

FIGURE 1.12— Evolution of different theoretical IMFs for YSCs. These are: a power law of index $\gamma = 2$ (upper left), the same power law truncated at $3 \times 10^5\,M_\odot$ (upper right), a Schechter function with $\gamma = 2$ and $M_* = 5 \times 10^6\,M_\odot$ (lower left) and a lognormal function with a maximum at $2 \times 10^5\,M_\odot$ and $\sigma(\log M) = 0.5$ (lower right). Each mass function is plotted at $t = 0, 1.5, 3, 6$ and 12 Gyr. The arrows indicated the peak of the distribution at 12 Gyr. The histograms represent the empirical mass function of GCs in the Milky Way. Adapted from Fall & Zhang (2001).

low-mass tail of the mass distribution, while high-mass clusters are mainly affected by stellar evolution and gravitational shocks. As a result, for a variety of different initial mass functions similar to those found in strong star-forming environments (starbursts and interacting galaxies), the theoretical distribution develops a turnover around a characteristic mass of $M_* \sim 2 \times 10^5\,M_\odot$ after ~ 12 Gyr, when the evaporation by two-body relaxation has disrupted most of the low-mass clusters (see Fig. 1.12). In other

words, the disruption erase, after a Hubble time, all the information of the initial shape at the low-mass tail of the cluster IMF. In contrast, the high-mass end remains nearly invariant in all cases. In this scenario, the outliving clusters should look like old GCs at the end of this process.

1.3 Motivation and main goals

1.3.1 Background

Part of this work is an extension of the project initiated during the stay of A. Prieto, K. Tristram and N. Neumayer at the Max-Planck Institut für Astronomie in Heidelberg and published in Prieto et al. (2010). This is one of the first attempts to characterize the SED of nearby Seyferts from radio to X-rays with a quite uniform high-spatial resolution ($\lesssim 10\,$pc) over the whole spectral range. Its comparison with large aperture data shed light on the role of the host galaxy emission when we consider templates with low-spatial resolution. However, although the number of objects is quite limited (three Sy1s and four Sy2s), this is imposed by the number of nearby and brightest active galaxies ($\lesssim 20\,$Mpc) and the need of very different facilities (*HST*, 8–10 m class telescopes, *Chandra*, VLA and VLBA/VLBI) to sample the SED at parsecs scales across the whole wavelength range. Among the possible configurations for the VLA, the A-array provides the best resolution ($\lesssim 1''$). We try to use data from this array when available, although preference is given to VLBA or VLBI interferometry data. Previous studies with high-spatial resolution (parsec scales) have been performed for the nearby galaxies NGC 1068, Circinus, Centaurus A or NGC 4151 (Jaffe et al. 2004; Prieto et al. 2004; Tristram et al. 2007; Häring-Neumayer et al. 2006; Meisenheimer et al. 2007; Hönig et al. 2008; Ramos Almeida et al. 2009; Pott et al. 2010).

1.3.2 Starting point

In this regard, this work explores particularly the range corresponding to low-luminosity AGNs (LLAGNs), i.e. LINERs and faint Seyferts ($L \lesssim 10^{42}\,\mathrm{erg\,s^{-1}}$), for which we expect significant differences in their internal structure when compared with brighter AGNs. Specifically, when compared with the sample of LINER SEDs by Ho (1999) and Eracleous et al. (2010), our data additionally cover the NIR to MIR range. This part of the spectrum is particularly interesting as it contains the emission reprocessed by the dust in the proposed torus, a structure that is predicted to vanish for the luminosities exhibited by the LLAGNs in our sample (Elitzur & Shlosman 2006; Hönig & Beckert 2007).

Another important aspect of this thesis is the star formation in the nucleus of galaxies. These are violent environments that challenge the scenarios considered by current theories of star formation, i.e. the high tidal shear from the black hole should

disrupt the molecular clouds in the inner parsecs (Bonnell & Rice 2008; Graham & Spitler 2009). Nevertheless, the formation of massive stellar clusters ($\gtrsim 10^4\,M_\odot$) is usually related with strong starburst episodes in the nucleus of galaxies. The birth and evolution of these massive clusters is of special interest since they are nowadays the main candidates for being "young globular clusters", i.e. evolving toward globular clusters in the future. Their main observable properties span very similar ranges (Portegies Zwart et al. 2010), with a consistent size distribution for both of them (Maíz-Apellániz 2001). However, their luminosity and mass functions present important differences (Harris 1991; Larsen 2002; Fall & Zhang 2001). In this context, we focused our study in the characterization of young stellar clusters (YSCs) found in the nucleus of the galaxies in the sample (size, brightness, colour, age, mass and star-formation rate). The high-spatial resolution permits us to identify individual clusters in crowded environments as nuclear starbursts, and thus sample the faint end of the mass function which is particularly affected by disruption processes (Fall & Zhang 2001).

1.3.3 Goals

Therefore, the main goals of this thesis are:

- To collect a high-spatial resolution database from radio to IR, optical and X-rays for nearby but relatively less bright AGNs.
- To obtain a representative energy distribution for low-luminosity AGNs at parsec scales and compare it with those corresponding to bright Seyferts and quasars.
- To characterize the main properties and the SEDs of young stellar clusters found in the centre of all the AGNs so far studies by us: brightest Seyferts and less bright LINERs, with a particular emphasis on the nature of the IR emission.
- To provide a SED template at parsec scales for these young stellar clusters including the information at radio, IR and optical wavelengths.
- To build the luminosity and mass functions of these young stellar clusters and compare them with those obtained for merging/starburst galaxies and the young and globular cluster systems in the Milky Way.
- To investigate special cases: a possible hidden AGN in the nucleus of NGC 253 and star formation in the centre of the elliptical galaxy NGC 1052.

Future facilities like ALMA, in the millimetre/submillimetre range, and the ELT and JWST in the optical/NIR ranges will be of special interest to extend this study to more distant galaxies $\lesssim$ 80–100 Myr. Particularly, ALMA will have a key role in the high-spatial resolution studies since the millimetre/submillimetre range is currently

unknown at resolutions bellow $\sim 1''$. Nevertheless, this facility is characterized not only by its high-spatial resolution, but also by its high sensitivity. Both aspects will permit us, for example, to resolve the torus in the nearest AGNs and trace cold molecular gas maps for star-forming regions at a comparable or even better resolution than the *HST*, VLT plus AO, VLBI and VLA/A-array data that will be shown along this thesis.

1.4 A brief description of the thesis

In Chapter 2 we introduce the dataset in which this thesis is based. The main characteristics of the data and the facilities used in the different spectral ranges are described in Section 2.2. In Section 2.3 we describe in detail the methods used in the reduction, calibration, alignment and photometry of these data.

In Chapter 3 we review the main properties of the galaxies in the sample, including wide field images at different wavelengths with an indication of the FOV covered by our high-spatial resolution images. A preliminary analysis is presented together with the photometry of compact sources in the central parsecs of the galaxies in the sample.

Chapter 4 is focused on the sample of active galactic nuclei, organized by their bolometric luminosity, comparing high and low-spatial resolution SEDs. A representative template is obtained for the AGNs with relatively lower luminosity in the sample. In addition, we discuss the case of the nucleus of NGC 253.

Chapter 5 deals with the star-forming clusters found in the central parsecs of the sample of AGNs. A representative template for extragalactic young stellar clusters is presented in Section 5.2. Resolved star-formation in the form of young stellar clusters is found in the central $2 \times 2\,\mathrm{kpc}^2$ of NGC 1052 (Section 5.3). Finally, we compare the global properties of these young clusters among the galaxies in the sample, including their size, brightness, colour, age, mass, SFR, SED, luminosity and mass functions (Sections 5.4 and 5.5).

In Chapter 6 we summarize briefly the main results and present the conclusions of this study. Some indications for possible research lines based on results from this thesis that can be accomplished with future facilities are given.

2

Data

We present a high-spatial resolution dataset from radio to infrared and optical for the central parsecs of some of the nearest and brightest Seyfert galaxies accessible from the Southern Hemisphere. The main characteristics of the sample and the data reduction, as well as the alignment and photometry methods, are explained through this Chapter.

2.1 Introduction

THIS thesis is based on a multiwavelength high-spatial resolution dataset covering the radio, infrared and optical ranges for a sample of nearby active galaxies. These are selected from the sample of Seyfert nuclei obtained by Prieto et al. (2010) and Reunanen et al. (2010), which covers some of the nearest and brightest Seyfert nuclei accessible from the Southern Hemisphere, plus the well-known starburst galaxy NGC 253. The high-spatial resolution data permit us to examine precisely the central parsecs of NGC 253, NGC 1052, NGC 1097, NGC 1386, NGC 7469 and NGC 7582, allowing us to disentangle the star-formation activity and the active nuclei, mixed in most of the previous studies. Section 2.2 includes a summary with the main characteristics of the sample, the observational techniques handled and the spatial resolution achieved in the optical/IR range. In Section 2.3 we describe the reduction, alignment and photometry extraction processes, relating minutely the cases of NGC 253 and NGC 1386, for which a new and precise registration was found between the radio and IR/optical datasets, compared with previous studies in the literature. Finally, we compile all the MIR, NIR and optical data in the Table 2.2.

2.2 The dataset

The dataset in which this thesis is based consist mainly on a compilation of high-spatial resolution images acquired with the Very Large Telescope (VLT), an 8-meter class facility including four telescopes located in Cerro Paranal, Chile. The images cover the near (NIR) and mid-infrared (MIR) ranges for a sample of six nearby active galaxies, from 4 to 65 Mpc. Table 2.1 shows the main characteristics of the sample including equatorial coordinates, size, distance, the morphological type of the galaxy and the classification of the active nucleus. These observations were completed with the highest-spatial resolution data available in the optical range from the *Hubble Space Telescope* (*HST*), radio from the Very Large Array (VLA) and Very Long Baseline Interferometry (VLBI) observations and X-rays (*Chandra X-ray Observatory*), making it one of the most complete datasets at parsec scales for this sample of active galaxies.

TABLE 2.1— Main characteristics of the observed sample. R.A. and Dec correspond to the position of the active nucleus according to *HST* astrometry, except for the case of NGC 253, whose R.A. and Dec. correspond to the coordinates of the knot used for alignment purposes.

Name	**R.A.** [HH MM SS]	**Dec.** [DD MM SS]	**Size**	**D** [Mpc]	**1″** [pc]	**Type**	**Class**
NGC 253	00 47 33.267	−25 17 14.05	27.′5×6.′8	3.94[a]	19.1	SAB(s)c	Starburst
NGC 1052	02 41 04.737	−08 15 20.80	3.′0×2.′1	18.0[b]	87.3	E4	LINER 1.9
NGC 1097	02 46 18.962	−30 16 29.45	9.′3×6.′3	14.5[c]	70.3	SB(r′l)b	LINER 1
NGC 1386	03 36 46.253	−35 59 58.64	3.′4×1.′3	15.3[b]	74.2	SB(s)a	Sy 2
NGC 7469	23 03 15.609	+08 52 26.29	1.′5×1.′1	65.2[d]	316.1	(R′)SAB(rs)a	Sy 1.2
NGC 7582	23 18 23.628	−42 22 13.25	5.′0×2.′1	19.9[e]	96.5	SB(s)ab	Sy 2

[a] Karachentsev et al. (2003)
[b] Jensen et al. (2003)
[c] Tully (1988)
[d] $v_{hel} = 4892 \pm 2\,\mathrm{km\,s^{-1}}$ (Keel 1996); $H_0 = 75\,\mathrm{km\,s^{-1}\,Mpc^{-1}}$
[e] Terry et al. (2002)

The optical and NIR images comprise a number of broad and intermediate-band filters together with a set of narrow-band filters centred on Hydrogen emission lines such as Hα+[N II], Paα or Brα and their adjacent continuum. In those cases where the corresponding narrow-band continuum image was not acquired, the closest broad-band filter was assumed as the reference for the continuum. In the following sections we will describe the main characteristics of the ground-based IR observations and the data compiled from the scientific archives in the optical, radio and X-rays. Detailed information about the optical and IR data is provided at the end of this chapter in

Table 2.2, such as filter, central wavelength and bandwidth, pixel scale, integration time, wavefront sensor, Seeing, photometric zero point, magnitude and size of the active nucleus, spatial resolution in arc-seconds (if available) and date of observation. Moreover, Fig. 2.1 shows the spatial resolution achieved as a function of frequency and wavelength for the *HST*, VLT/NaCo and VLT/VISIR data.

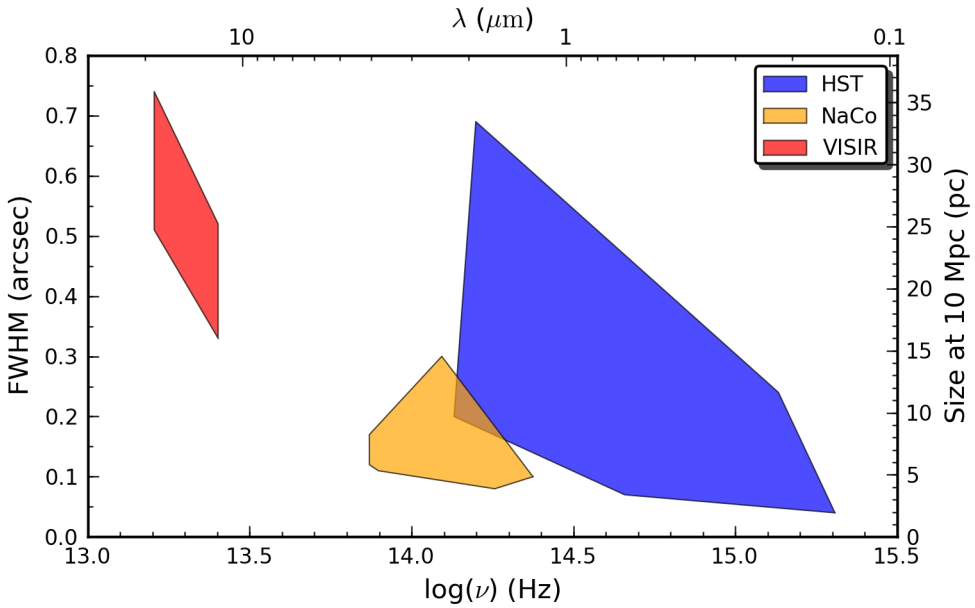

FIGURE 2.1— Spatial resolution (FWHM) according to frequency and wavelength for *HST* (blue), VLT/NaCo (orange) and VLT/VISIR (red) data. The physical scale corresponds to a source located at 10 Mpc.

2.2.1 Ground-based IR observations (VLT)

Near-infrared images were obtained with the adaptive optics (AO) assisted instrument NaCo[1], located at the VLT facility in Paranal Observatory, Chile. NaCo sets out for NAOS (Nasmyth Adaptive Optics System) plus CONICA, a near-infrared spectro-imaging camera (Lenzen et al. 2003; Rousset et al. 2003), installed at the Nasmyth B focus on UT4. NaCo provides adaptive optics assisted imaging, imaging polarimetry, coronography and spectroscopy in the 1–5 μm range, in which CONICA contains several cameras allowing diffraction limited sampling with a spatial resolution of about $0\farcs06$ in the *Ks*-band. The adaptive optics system is equipped with both

[1] http://www.eso.org/sci/facilities/paranal/instruments/naco/

visible and infrared wavefront sensors and five dichroic filters which split the light from the telescope between CONICA and one of the NAOS wave-front sensors. The Field of View (FOV) covers $27\farcs7 \times 27\farcs7$ and $13\farcs5 \times 13\farcs5$ for the $0\farcs0271\,\mathrm{px}^{-1}$ and $0\farcs01326\,\mathrm{px}^{-1}$ modes, respectively.

The active nucleus was used as reference for the adaptive optics system due to the lack of a natural guide star close enough to the science objects, except for the NaCo narrow-band images of NGC 7582, where the nucleus is almost obscured and the wavefront sensing was performed in the optical. In this case, the wave-front sensor closed the loop of the AO system using one of the star-forming point-like regions located very close to the position of the active nucleus ($\lesssim 5''$). In other cases, the IR dichroic filter was used when the nucleus was strongly obscured in the optical range. Specifically, the strongest IR source in the field was employed for wave-front sensing in the case of NGC 253. For most of the galaxies, data was collected on the *J*, *H*, *Ks* and *L'* bands, using the *jitter* technique (Devillard 1999), although observations for some of the objects were acquired with the IB_2.06, IB_2.12, NB_2.12, IB_2.42, IB_2.48 and NB_4.05 bands. The latter are intermediate (IB) and narrow-band (NB) filters including some emission lines or their adjacent continuum in the IR: He I at 2.059 μm for IB_2.06, H_2 1–0$S(1)$ transition at 2.1218 μm for IB_2.12 and NB_2.12, the [Si VII] coronal line at 2.48 μm and Brα for the NB_4.05 band.

Mid-Infrared images

The MIR images were taken with VISIR[2] (VLT Imager and Spectrometer for mid-InfraRed), located at the Cassegrain focus on UT3 (Lagage et al. 2004). This instrument provides diffraction limited imaging and spectroscopy in the two MIR atmospheric windows, with a spatial resolution of about $0\farcs3$ in the *N*-band (8–13 μm) and $0\farcs5$ in the *Q*-band (16.5–24.5 μm). It is equipped with a $256 \times 256\,\mathrm{px}^2$ detector covering a FOV of about $19\farcs2 \times 19\farcs2$ for the $0\farcs075\,\mathrm{px}^{-1}$ pixel scale and $32\farcs3 \times 32\farcs3$ for the $0\farcs127\,\mathrm{px}^{-1}$ mode. The observations were performed using the chopping plus nodding technique with the PAH2_2 and Q2 bands, hereafter *N* and *Q*-bands, respectively.

2.2.2 Hubble Space Telescope data

The IR observations were complemented with additional data from the Hubble Space Telescope (*HST*). The images, taken directly from the scientific archive, were acquired with the Wide-Field Planetary Camera 1 (WFPC1[3]), Wide-Field Planetary Camera 2

[2] http://www.eso.org/sci/facilities/paranal/instruments/visir/
[3] http://www.stsci.edu/hst/wfpc

(WFPC2[4]), Advanced Camera for Surveys (ACS[5]), Near Infrared Camera and Multi-Object Spectrometer (NICMOS[6]), the Faint Object Camera (FOC[7]) and the Space Telescope Imaging Spectrograph (STIS[8]).

As in the case of the ground-based observations, the optical set comprises a number of broad band filters, some of them very similar to bands in the Johnson–Kron–Cousins, Strömgren and Gunn–Thuan systems: F330W (u-band), F435W (B-band), F547W and F550M (y-band), F555W and F606W (V-band), F675W (R-band), F814W (I-band), F850LP (z-band), F110W (J-band), F160W (H-band), F222M (K-band). The narrow-band images are centred on emission lines such as Hα+[N II] (F656N, F658N, FR656N_2 and FR680N), Paα (F187N and F190N), [S II]$_{\lambda 6716}$ (F673N), [S III]$_{\lambda 9532}$ (F953N), [O III]$_{\lambda 5007}$ (F502N and FR533N).

2.2.3 Radio data

The radio set consist on a compilation of data taken from the literature plus archival VLA/VLBA data (Orienti & Prieto 2010). To achieve the adequate spatial resolution enough to resolve the nuclear structure, we considered observations carried out when the VLA was in one of the extended configurations (array A or B) at frequencies ranging between 1.4 and 14.9 GHz, when available. We considered data sets either at frequencies lacking information or for which data presented in the literature were found to be unsatisfactory.

2.2.4 X-ray data

NGC 253 data, presented in Müller-Sánchez et al. (2010), was taken from the ACIS instrument and extracted from the *Chandra* archive[9] (ObsID 3931) and observed in 2003 September 16. *Chandra* data include information about the photon energies and positions that were used to obtain energy-filtered images, and to carry out sub-pixel resolution spatial analysis. Although the default pixel size of the *Chandra*/ACIS detector is $0\farcs492$, smaller spatial scales are accessible as the image moves across the detector pixels during the telescope dither, therefore sampling pixel scales smaller than the default pixel of the *Chandra*/ACIS detector.

[4] http://www.stsci.edu/hst/wfpc2
[5] http://www.stsci.edu/hst/acs
[6] http://www.stsci.edu/hst/nicmos
[7] http://www.stsci.edu/hst/foc
[8] http://www.stsci.edu/hst/stis
[9] http://cda.harvard.edu/chaser

2.3 Methods: reduction, alignment and photometry

In this section we describe the techniques used in data reduction and calibration (Section 2.3.1), image registration from optical to radio wavelengths (Section 2.3.2) and photometry of compact sources found in the images (Section 2.3.4).

2.3.1 Data reduction

Reduction of ground-based IR data consisted basically on sky subtraction, registration and combination of frames corresponding to each dataset using tools provided by ESO (European Organization for Astronomical Research in the Southern Hemisphere), ECLIPSE and ESOREX packages for the NIR and MIR images, respectively. Further analysis of the data was performed using IRAF (Image Reduction and Analysis Facility), IDL (Interactive Data Language) and the *Python Programming Language*[10].

The estimation of photometric zero points was based on observations of calibrators selected from the lists of Persson et al. (1998) (VIS and N20C80 dichroics) and van der Bliek et al. (1996) (N90C10 dichroic) for the *J*, *H* and *Ks* filters; Leggett et al. (2003) for the *L'* and *M*-bands; Cohen et al. (1999) for the *N* and *Q*-bands. These values are in agreement with those given by the "Quality control and data processing group" at ESO. Conversion factors from counts per second to flux units were derived using the photometric zero points and the FUV to IR Vega spectra from Bohlin (2007).

In the optical range, reduced and calibrated images were taken directly from the *HST* archive. Prior to the image registration process, we corrected geometric distortions for the WFPC2 and the ACS images using *MultiDrizzle* package in PyRAF (Koekemoer et al. 2002).

The radio data reduction was carried out in Orienti & Prieto (2010) following the standard procedures for the VLA implemented in the NRAO AIPS[11] package. Images were produced after a phase-only calibration iterations. In order to obtain an accurate flux density at 1.4 GHz, it was necessary to image several confusing sources falling within the primary beam. Uncertainties in the determination of flux density are dominated by amplitude calibration errors, which are between 3% and 5%., being worse at 14.9 GHz. The rms noise level (1σ) on the image plane is usually below 0.1 mJy, being irrelevant for our targets, with the exception of NGC 1097 for which it is comparable to the amplitude calibration errors.

The X-ray data reduction was carried out in Müller-Sánchez et al. (2010) using the CIAO 4.0[12] data analysis system and the *Chandra* calibration database (CALDB 4.0.0[13]). The exposure time was processed to exclude background flares, using the

[10] http://python.org
[11] http://www.aips.nrao.edu/
[12] http://asc.harvard.edu/ciao
[13] http://cxc.harvard.edu/caldb

task LC_CLEAN.SL[14] in source-free sky regions of the same observation. The net exposure time after the flare removal is 76 ksec, and the nucleus did not present a significant pileup.

We made $0\farcs125\,\mathrm{pixel}^{-1}$ images with a FWHM resolution of $\sim 0\farcs5$ in two bands: 0.5–2 keV (hereafter the soft X-ray band) and 2–10 keV (the hard X-ray band). The absolute astrometric accuracy of *Chandra* is $1''$ rms. Moreover, we applied smoothing techniques to detect the low contrast diffuse emission. We applied the adaptive smoothing CIAO tool CSMOOTH, based on the algorithm developed by Ebeling et al. (2006). CSMOOTH is an adaptive smoothing tool for images containing multiscale complex structures, preserving the spatial signatures and the associated counts as well as significance estimates. A minimum and maximum significance S/N level of 3 and 4, and a scale maximum of 2 pixels were used.

2.3.2 Image registration

The detailed study of a complex system in a wide wavelength range, such as the nuclear region of an active galaxy, requires a very fine registration across the whole range. One of the principal difficulties is the inability to use the same sources from radio to optical and X-rays. The optical range is very sensitive to the presence of dust –most of the sources fade out completely when the extinction becomes higher than $A_V > 5$ mag–, while hot dust ($T > 200$ K) emission is detected in the MIR range. In short, we need a consistent registration across the whole spectrum, but the fact of observing different processes at different wavelengths forces us to divide the dataset in a few main blocks (e.g. radio, IR and optical) and perform consistent alignments for the images inside each block. Finally, we search for point-like sources or common structures among different blocks to complete the registration of the whole set.

Most of the galaxies in our sample evince large quantities of dust in their nucleus and, in some cases, this is combined with the effect of a high inclination angle for the object. As a consequence, the morphology of the galaxy suffers a strong variation with wavelength. In particular, the active nuclei of NGC 7582 and NGC 1386 and the strongest IR source in NGC 253 are completely hidden in the optical, and thus were avoided for alignment purposes in this range. In order to obtain a reliable image registration in these cases, we searched for point-like regions or *knots* detected in the majority of the filters. The final alignment was found by minimizing the variance of the knots' positions among different wavelengths. However, in some cases, the active nucleus is the only source detected longwards of *K*-band and thus the registration in the *L*, *N* and *Q*-bands is based on its position. In the majority of the cases, VLA radio data and *Chandra* X-ray data registration is also based on the position of the active nucleus, since it is by far the most bright source in the FOV.

[14] http://cxc.harvard.edu/ciao/download/scripts

A proof of consistency in all cases is the similarity of the low-luminosity contours found across the whole wavelength range. Furthermore, for some of the galaxies the alignment provides new radio and hard X-ray counterparts for optical/IR knots that were previously unrelated. We further explain the alignment in detail for the illustrative cases of NGC 253 and NGC 1386, where the new registration defines a different scenario when compared with previous publications.

NGC 253

The IR set for NGC 253 was aligned using the brightest source, which is an outstanding feature at all wavelengths: knot #4 in Fig. 2.2, labelled as M1 in Galliano et al. (2005). Since this source vanishes in the optical range, we use the second in brightness,

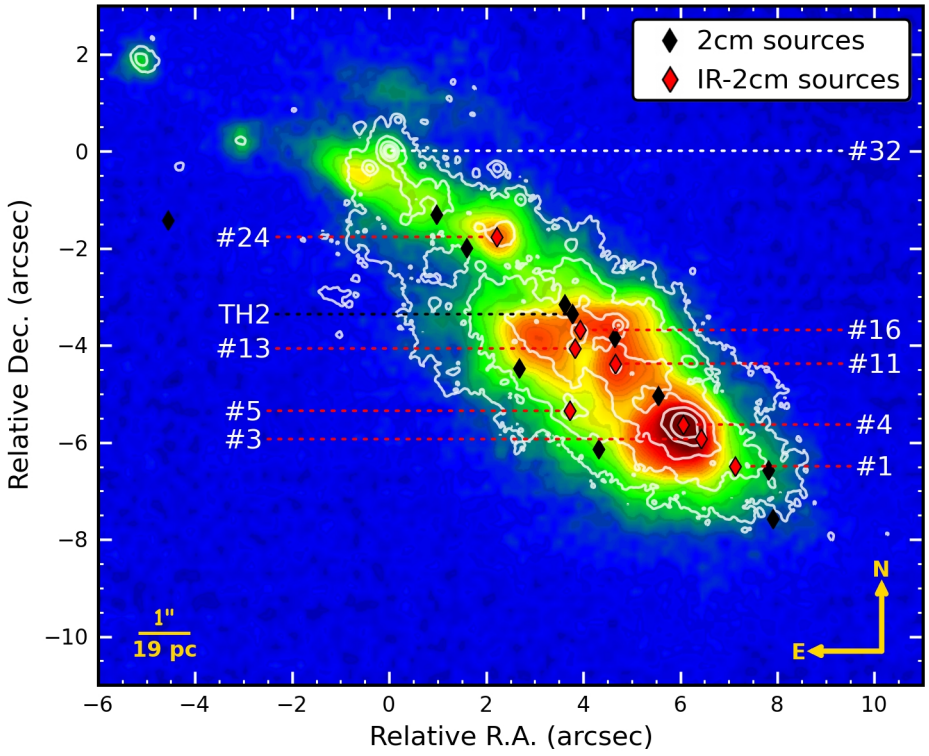

FIGURE 2.2— *Q*-band image with *L*-band contours and VLA 2cm source positions overlapped (diamonds). Sources with IR counterpart are marked in red. The labels for the regions correspond to their IR counterparts (see Table 3.1). TH2 is the strongest compact radio source (Ulvestad & Antonucci 1997).

knot #32 (Fig. 2.2), to align the optical and IR sets. Finally, more than 10 NIR knots with *HST*/WFPC2 counterparts are found, with also a good correspondence between the diffuse emission morphologies seen in both spectral ranges. The key alignment, however, is between IR and VLA radio data from the literature.

The availability of the VLT/NaCo adaptive optics *L*-band image with spatial resolution (0.″13) comparable to that of the 2 cm VLA map (beam 0.″20 × 0.″10; Ulvestad & Antonucci 1997) allowed us to settle a very precise source identification in the NGC 253 nuclear region (Fig. 2.3). A first, visual alignment using point-like sources permitted us to find eight common knots. The final registration was obtained

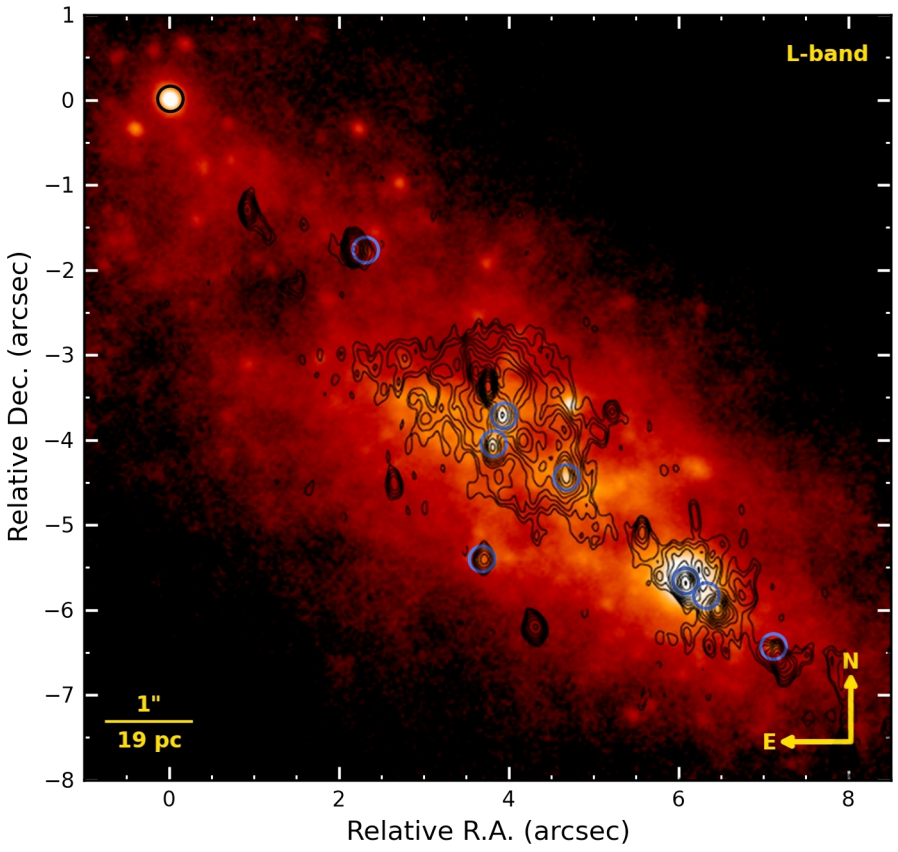

FIGURE 2.3— L'-band image with VLA 2 cm contours overplotted. Blue circles indicate the position of the eight IR knots with a counterpart at radio wavelengths. The black circle corresponds to knot #32, which provided the alignment between optical and NIR data.

after distance minimization between *L*-band and 2 cm positions (red circles in Fig. 2.3), with a positional accuracy of about 0.″03, based on the variations of the knots' positions between both ranges.

This alignment was cross-checked with the *Q*-band (Fig. 2.2), in which it was found that the low-brightness contours reproduce equivalent ones in the *L*-band and the radio maps (e.g. when compared with 2 cm map in Fig. 2.3). Previous alignments are based on either an absolute or "blind" registration between radio and optical/IR (e.g. Forbes et al. 2000) or lower resolution MIR images (e.g. Galliano et al. 2005).

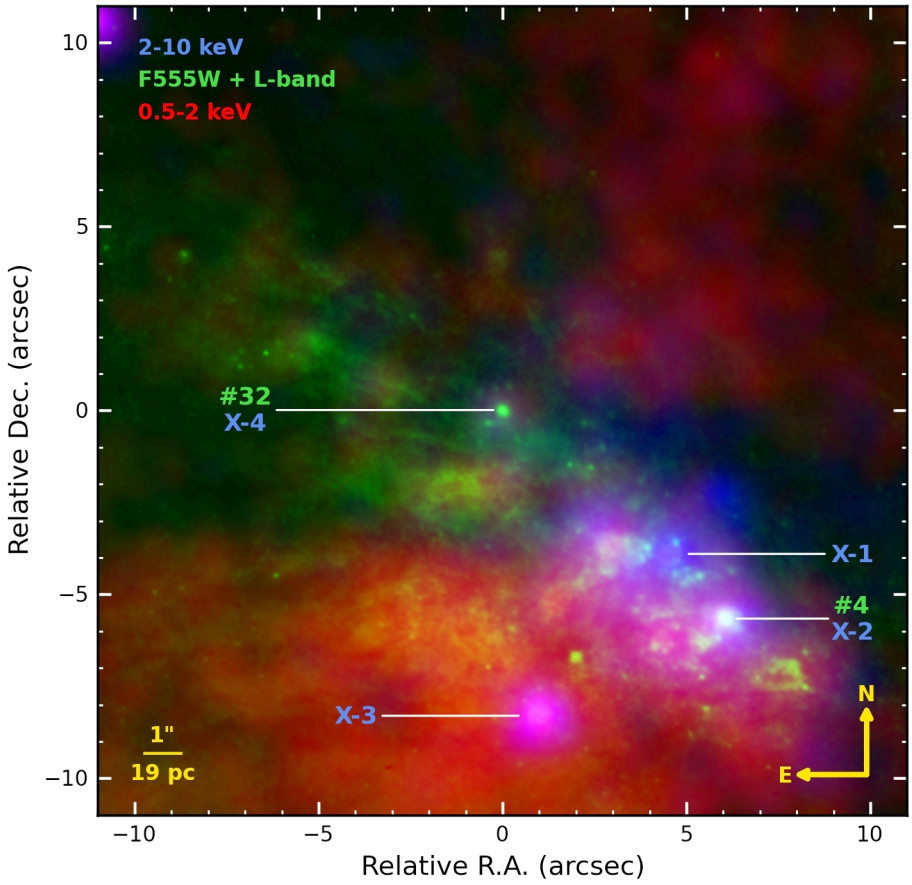

FIGURE 2.4— Alignment of the *Chandra* X-ray data for the central region of NGC 253 based on the position of the optical/IR knots #4 and #32 and the X-ray knots X-1 and X-4. Green colour corresponds to a composition of the *HST*/F555W filter and the VLT/NaCo *L*-band, whereas red and blue colours correspond to the soft (0.5–2.0 keV) and hard (2–10 keV) X-ray bands, respectively.

The strongest IR peak (knot #4), which lacks a radio counterpart in these alignments, is now the counterpart of the thermal radio emitter TH7 in Turner & Ho (1985), also called 5.63–41.3 in Ulvestad & Antonucci (1997). Remarkably, the strongest radio source in the field, TH2 or 5.79–39.1, which has been proposed as an AGN (Ulvestad & Antonucci 1997; Lenc & Tingay 2006; Rodríguez-Rico et al. 2006), is undetected at optical or IR wavelengths. This will be further studied in Section 4.5.

Finally, we registered the optical, IR and radio set with the *Chandra* X-ray data. The soft X-ray image shows several knots of emission embedded in a diffuse component which originates in the nuclear starburst and extends south-west in an apparent cone of ionization (Strickland et al. 2000; Müller-Sánchez et al. 2010). In the hard X-ray image, the emission is more compact and consist on three individual point-like sources (X-1, X-2 and X-3) plus a more extended and isolated region (X-4). The first step in the registration process was based on the *Chandra* absolute astrometry, which has an accuracy of $\sim 1''$ rms. This approximation was improved through the identification of common sources: two of the hard X-ray knots were found to have possible *L*-band counterparts in knots #32 and #4 (IR peak), based on their relative positions. The presence of these reference objects allowed us to tie the X-ray and IR images and achieve $\sim 0\farcs5$ relative position accuracy in searching for radio and IR counterparts to the X-ray sources. A three colour composite image of the central $22'' \times 22''$ ($420 \times 420\,\mathrm{pc}^2$) is shown in Fig. 2.4. Green colour corresponds to *HST*/WFPC2 F555W band plus VLT/NaCo *L*-band, red colour to the soft X-ray emission (0.5–2.0 keV) and blue colour to the hard X-ray emission (2–10 keV). The alignment was confirmed by the similar morphology exhibited by both the strong winds detected south-east of the nuclear starburst in the F555W image and the soft X-rays image (Fig. 2.4). Furthermore, the most prominent dust lane running north-west alongside the starburst is spatially coincident in both images. Surprisingly, a strong hard X-ray source (X-1) lies in the centre of this galaxy without any clear counterpart at optical, IR or radio wavelengths. TH2, the historically proposed AGN, and the source X-1 are not each other counterparts. The latter is located $\sim 1\farcs1$ south-west from the former, well beyond the error of $\sim 0\farcs5$ in the registration of the images. We will go deeply into this in Section 4.5.

NGC 1386

The alignment of *HST*/optical and NaCo *J* and *K*-bands in the case of NGC 1386 was based on the position of the three knots encircled in Fig. 2.5 (top panel). Although the nuclear region in this object is very bright when compared with the starburst ring around, the active nucleus is only detected as a point-source longwards of *K*-band and cannot be used for the registration. Furthermore, its position changes $\sim 0\farcs5$ from optical to *K*-band with regard to the knots (bottom panel in Fig. 2.5). Thus, NICMOS

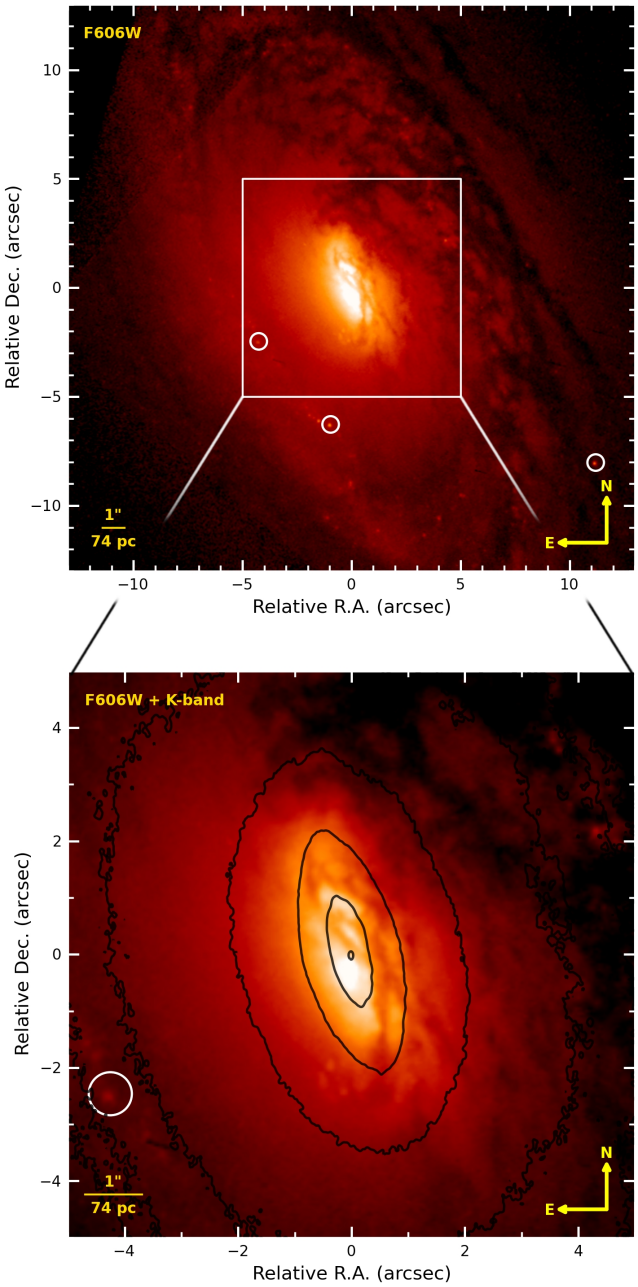

FIGURE 2.5— Top panel: *HST* F606W image with the three knots used for the alignment between optical and NIR images (white circles). Bottom panel: Zoom on the central $10'' \times 10''$ with NaCo *Ks*-band contours overlaid in black colour. The optical peak is located $\sim 0.''5$ south of the *Ks*-band peak.

images (which field of view does not include the knots), NaCo *L* and NB_4.05 bands, VISIR *N* and *Q*-bands and VLA 8.4 GHz data were aligned using the active nucleus.

A special case is the narrow-band filter F502N, which includes the contribution of the [O III]$_{\lambda 5007}$. The knots are not detected in this filter and, as the line contribution dominates the emission, the nuclear morphology is completely distorted when compared with the broad-band filters. The alignment in this case was obtained by cross-correlation with the F658N image, which includes Hα+[N II] and shows both a similar nuclear morphology and the three knots used in the optical-NIR alignment.

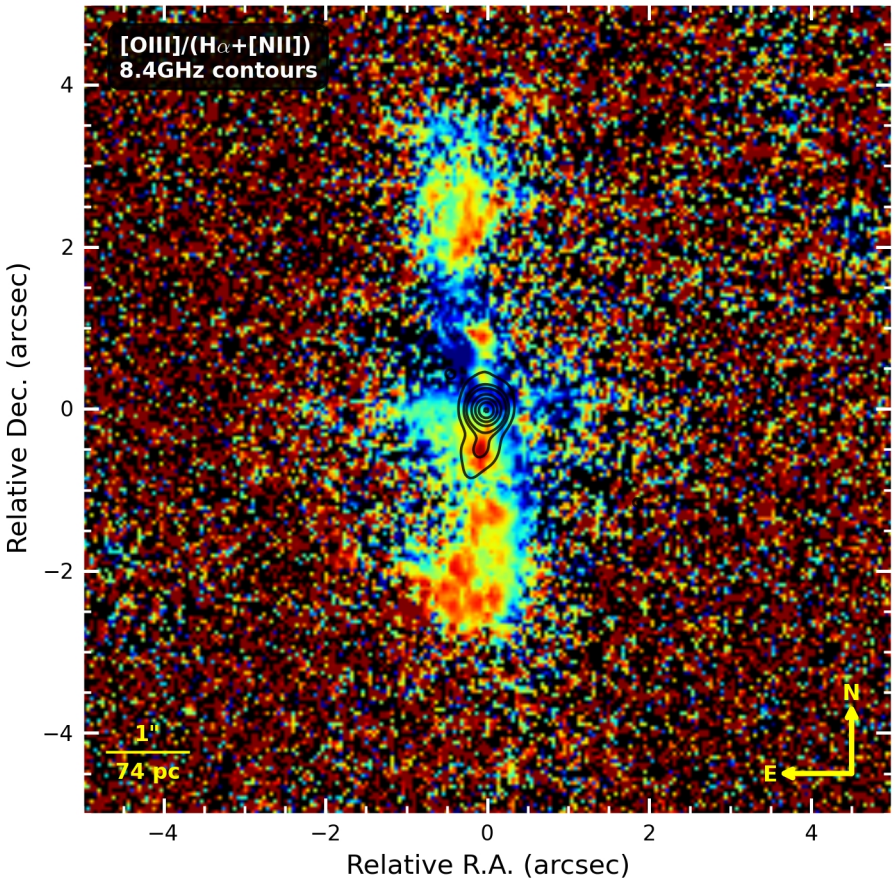

FIGURE 2.6— [O III]/(Hα+[N II]) line ratio with 8.4 GHz contours overlaid. A local maximum in the emission-line ratio map coincides with the jet-like extended emission south of the radio nucleus at 8.4 GHz. This is assumed to be coincident with the position of the AGN in the *Ks*-band.

For this object, the new registration permitted us to identify a counterpart in the [O III]/(Hα+[N II]) emission line ratio image from Ferruit et al. (2000) for the jet-like radio extension detected south of the nucleus (Nagar et al. 1999). Fig. 2.6 shows that a local maximum in the emission line ratio map coincides fairly well with the tiny jet at 8.4 GHz. A previous alignment by Mundell et al. (2009) could not establish a direct association between the radio and optical components.

2.3.3 Identification of compact sources

As a reference for each object, we select the optical or NIR image with the highest-spatial resolution containing the larger number of knots. This image was then explored using the DAOPHOT finding algorithm (Stetson 1987) to look for point-like sources or knots over a 3σ threshold. Once localized, we assume that these positions are fixed for the rest of the filters. This method was adopted to find knots in the central parsecs of NGC 253 or NGC 1097, using the VLT/NaCo *L*-band in the first case and the *HST*/ACS FR656N_2 in the second as a reference. For NGC 7469 this procedure was also used to complete the original sample of 30 knots found by Díaz-Santos et al. (2007) up to a total of 59 knots, using the *HST*/ACS F550M filter.

However, this technique could not be directly applied, in some cases due to the faintness of the knots when compared with the background light of the galaxy, in other due to the presence of gradients in the same background over the field of view. To amend these effects and improve the efficiency of the finding algorithm we applied the unsharp-masking technique (Heisler & Vader 1994; Sofue et al. 1994; Pogge & Martini 2002) in the cases of NGC 1052 (*Ks*-band) and NGC 7582 (IB_2.06 filter) before the identification of knots (Figs 3.8 and 2.7, respectively). Although this method consists on dividing an image by a smoothed mask of itself, we opted for the difference between the image and the mask. The main reason for this change is that the subtraction does not produce noise in those regions with low signal to noise (S/N). As a smoothing kernel we selected a median circular filter with $r \sim 0\farcs3$, wide enough to preserve the larger knots but small in size when compared with the extended light distribution. At last, the unsharp-mask image enhances point-like sources and removes most of the background. In the case of NGC 7582 (Fig. 2.7), the strong IR point-like nucleus was removed prior to the smoothing process using a 2D Gaussian plus Sèrsic components (Peng et al. 2002), as a safeguard against the light spread in the surroundings of this bright source.

Still, in the case of NGC 1386, a visual inspection of the *HST*/WFPC2 F606W and F658N images and the VLT/NaCo *Ks*-band was required to identify the majority of the knots present in the circumnuclear ring of this galaxy.

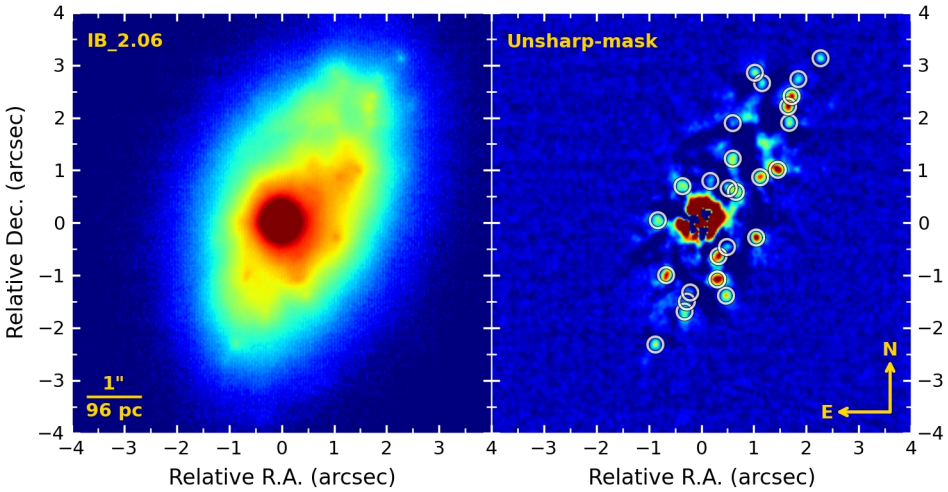

FIGURE 2.7— NGC 7582 IB_2.06 band (left panel) and the corresponding unsharp-mask image obtained from a nucleus-subtracted original using a median filter of 0.″3 ($\sim$ 29 pc, right panel).

2.3.4 Photometry of compact sources

The photometry of the nucleus and the identified knots for all the galaxies was extracted from a circular aperture with a radius of $r \approx$ FWHM in each band, using the FWHM listed in Table 2.2, which represents 96% of the flux for a perfect bidimensional Gaussian. For those filters were the active nuclei dominate the emission, the aperture selected for this source was a bit wider in order to include all the light from the AGN, since the background contribution was negligible in those cases. The local background was subtracted in all cases by subtracting the value of the mode measured in a ring around ($r \approx$ [2–4] FWHM). This permits us to remove the contribution from the diffuse light to the emission from the knots, and thus balance the variations in the photometry due to different spatial resolution among different filters and objects. Measurements in those filters where some of the knots are not detected provide us an upper limit on the flux. Fluxes for the active nuclei and all the knots detected in each galaxy are shown in Section 3.2. In the case of NGC 253, the nuclear flux corresponds to the strongest source detected in the IR, since the assumed nucleus in the literature is undetected at optical or IR wavelengths.

Extinction values at each knot were derived for all the objects with a measured Hα/Paα or Hα/Brα ratio, i.e. NGC 253, NGC 1097 and NGC 7469 (see Tables 3.1, 3.2 and 3.6). The visual extinction was derived, assuming the extinction law by Cardelli et al. (1989), by comparing the measured ratio with the estimate given by Osterbrock (1989), case B ($T = 10^4$ K, $N_e = 10^4$ cm^{-3}). Line fluxes were determined,

after continuum subtraction, from the narrow-band filters F656N, F658N, FR656N_2 and FR680N (Hα+[N II]), F187N and F190N (Paα) and NB_4.05 (Brα). The continuum was inferred from: *i)* a narrow-band continuum filter adjacent to the line filter, *ii)* by interpolating between two broad-band filters at both sides of the line or *iii)* by scaling the continuum in a broad-band filter to that of the narrow-band filter containing the line. The latter is the case for Brα, where we used the *L*-band to estimate the continuum of the NB_4.05 filter. The scaling factor was determined by measuring the emission ratio between both filters in a number of inter-knot regions, and thus not affected by strong line emission. However, there is still a possible contamination by diffuse Brα emission, which is the main uncertainty in the scaling factor. In such case, the Brα flux would be underestimated, and therefore the derived extinction would be a lower limit. We estimate the error magnitude to be $A_V \sim 0.3$ mag, based on the scatter of the *L*-band/NB_4.05 ratio values. Nevertheless, this error is of the same order as those derived from the photometry extraction and does not affect our results qualitatively. The Hα flux was corrected in all cases by the [N II] contribution in the filter assuming that to be 40% of the total (Baldwin et al. 1981). Reducing the [N II] contribution to 20% lowers individual A_V by 0.5 mag. As these values are derived assuming screen extinction, they must be always considered as lower limits because of possible internal extinction.

Using the Hα and continuum fluxes measured before, we derived the Hα equivalent width for each knot (W(Hα)), which gives us an estimate for the age of the knots by assuming instantaneous star-formation (e.g. Leitherer et al. 1999). Finally, we compiled the fluxes measured for all the knots in each galaxy in Tables 3.1, 3.2, 3.3, 3.4, 3.5 and 3.6.

TABLE 2.2— Optical (*HST*) and IR (VLT) dataset for the sample of galaxies. The columns correspond to: telescope/instrument, filter name, central wavelength and full-width at half-maximum of the filter ($\lambda - \Delta\lambda$), pixel scale, integration time, Wave-Front Sensor dichroic (WFS), Seeing, zero point magnitude (ZP), Vega magnitude of the nucleus, Full-Width at Half-Maximum (FWHM) measured on the most compact object found in each image and on the active nucleus (FWHM*), and observation date. The active nucleus was the reference for the adaptive optics system except in NGC 7582 narrow-band images. In the case of NGC 253, M_{nucl} and FWHM* correspond to the brightest IR knot. Values for the ZP marked with * are based on calibration data taken on a different date than the object data.

Instrument	**Filter**	$\lambda - \Delta\lambda$ [μm]	**Scale** [$''$px^{-1}]	**Exposure** [s]	**WFS**	**Seeing**	**ZP** [mag]	$\mathbf{M_{nucl} \pm Err}$ [mag]	**FWHM**	**FWHM***	**Date** [DD MM YYYY]
					NGC 253						
HST/WFPC2	F555W	0.544 – 0.123	0.0455	400	.....		21.8	$\cdots \pm \cdots$[a]	0.″16	...[a]	29 05 1994
HST/WFPC2	F656N	0.656 – 0.013	0.1	1200	.....		17.4	15.4 ± 0.4	0.″24	1.″03	17 09 1994
HST/WFPC2	F675W	0.672 – 0.087	0.1	102.5	.....		22.1	17.8 ± 0.2	0.″23	3.″22	17 09 1994
HST/WFPC2	F673N	0.673 – 0.007	0.1	700	.....		18.8	17.8 ± 0.7	0.″25	3.″35	02 01 1996
HST/WFPC2	F814W	0.800 – 0.152	0.0455	205	.....		20.9	17.4 ± 0.2	0.″11	0.″20	29 05 1994
HST/WFPC2	F850LP	0.911 – 0.102	0.0455	300	.....		19.3	16.3 ± 0.3	0.″11	0.″16	09 07 1997
HST/WFPC2	F953N	0.954 – 0.005	0.0455	1300	.....		16.0	14.1 ± 0.5	0.″11	0.″45	09 07 1997
VLT/NaCo	J	1.265 – 0.250	0.0271	540	N90C10	0.″7	20.95*	14.52 ± 0.06	0.″29	0.″29	04 12 2005
VLT/NaCo	Ks	2.18 – 0.35	0.0271	500	N90C10	0.″7	19.92*	12.47 ± 0.04	0.″24	0.″28	04 12 2005
VLT/NaCo	L′	3.80 – 0.62	0.0271	4.375	JHK	0.″6	21.89*	9.33 ± 0.01	0.″13	0.″15	02 12 2005
VLT/NaCo	NB_4.05	4.051 – 0.020	0.0271	8.75	JHK	0.″7	18.66*	8.39 ± 0.01	0.″14	0.″16	02 12 2005
VLT/VISIR	PAH2_2	11.88 – 0.37	0.127	2826.24	...	0.″8	13.16	1.89 ± 0.01	0.″40	0.″40	01 12 2004
VLT/VISIR	Q2	18.72 – 0.88	0.127	6237	...	0.″8	12.10*	−0.20 ± 0.01	0.″74	0.″74	09 10 2005
					NGC 1052						
HST/ACS-HRC	F250W	0.272 – 0.056	0.025	300	.....		22.3	20.0 ± 0.3	0.″16	0.″16	18 10 2002
HST/ACS-HRC	F330W	0.336 – 0.041	0.025	300	.....		22.9	19.6 ± 0.2	0.″12	0.″12	18 10 2002
HST/WFPC1	F555W	0.545 – 0.120	0.044	1000	.....		23.1	18.9 ± 0.2	0.″20	0.″66	21 07 1992
HST/WFPC2	F658N	0.659 – 0.007	0.0455	1900	.....		18.2	15.0 ± 0.3	0.″10	0.″16	16 06 1996
HST/STIS	F28X50LP	0.722 – 0.268	0.051	60	.....		24.95	16.79 ± 0.03	0.″12	0.″15	02 01 1999
HST/NIC2	F160W	1.600 – 0.277	0.075	639.85	.....		21.80	13.72 ± 0.03	0.″18	0.″37	26 09 1998
VLT/NaCo	J	1.265 – 0.250	0.0271	900	VIS	0.″9	24.13*	14.94 ± 0.02	0.″26	0.″98	03 12 2005
VLT/NaCo	Ks	2.18 – 0.35	0.0271	400	VIS	0.″7	23.10*	14.26 ± 0.02	0.″12	0.″12	03 12 2005
VLT/NaCo	L′	3.80 – 0.62	0.0271	5.25	VIS	1.″0	22.08	11.36 ± 0.01	0.″12	0.″12	03 12 2005

[a]The strongest IR source in NGC 253 was not detected in this image.

NGC 1097											
HST/WFPC2	F218W	0.221 – 0.041	0.1	1200	.....		17	18 ± 2	0.″24	0.″26	28 06 1999
HST/WFPC1	F555W	0.545 – 0.120	0.044	1000	.....		23.1	18.9 ± 0.2	0.″12	0.″14	30 09 1992
HST/ACS-HRC	FR656N_2	0.640 – 0.011	0.025	1250	.....		22.4	17.9 ± 0.1	0.″07	0.″08	24 01 2004
HST/ACS-WFC	F658N	0.658 – 0.009	0.05	700	.....		22.42	16.03 ± 0.06	0.″13	0.″14	05 06 2004
HST/ACS-HRC	FR656N_1	0.659 – 0.011	0.025	1250	.....		22.34	16.76 ± 0.08	0.″07	0.″07	24 01 2004
HST/ACS-WFC	F814W	0.806 – 0.154	0.05	120	.....		25.51	16.62 ± 0.02	0.″13	0.″19	05 06 2004
HST/NIC3	F187N	1.875 – 0.016	0.2	960	.....		18.07	12.05 ± 0.07	0.″70	0.″70	05 06 2007
HST/NIC3	F190N	1.900 – 0.015	0.2	960	.....		18.29	12.24 ± 0.07	0.″69	0.″69	05 06 2007
VLT/NaCo	J	1.265 – 0.250	0.0271	80	VIS	0.″6	24.05	15.23 ± 0.02	0.″21	0.″29	19 08 2002
VLT/NaCo	H	1.66 – 0.33	0.0271	40	VIS	0.″6	23.95	14.39 ± 0.01	0.″18	0.″20	19 08 2002
VLT/NaCo	Ks	2.18 – 0.35	0.0271	80	VIS	0.″5	22.99	13.77 ± 0.02	0.″13	0.″15	19 08 2002
VLT/NaCo	L′	3.80 – 0.62	0.0271	5.6	VIS	1.″1	22.10	12.74 ± 0.02	0.″16	0.″16	18 01 2005
VLT/VISIR	PAH2_2	11.88 – 0.37	0.075	3060.35	...	0.″7	16.2	7.9 ± 0.1	0.″52	0.″55	03 09 2006
VLT/VISIR	Q2	18.72 – 0.88	0.075	3974.4	...	0.″6	12.26	6.00 ± 0.08	0.″51	0.″53	04 09 2006
NGC 1386											
HST/WFPC2	F502N	0.501 – 0.011	0.0455	800	.....		18.0	15.5 ± 0.3	0.″11	0.″64	28 06 1997
HST/WFPC2	F547M	0.548 – 0.048	0.0455	360	.....		21.7	17.8 ± 0.2	0.″09	0.″98	1997–1999[b]
HST/WFPC2	F606W	0.600 – 0.150	0.0455	160	.....		22.90	17.09 ± 0.08	0.″11	0.″64	14 06 1995
HST/WFPC2	F658N	0.659 – 0.007	0.0455	2000	.....		18.2	14.8 ± 0.2	0.″12	0.″34	1997–1999[b]
HST/WFPC2	F791W	0.787 – 0.122	0.0455	80	.....		21.5	16.5 ± 0.1	0.″11	1.″01	28 06 1997
HST/WFPC2	F814W	0.800 – 0.152	0.0455	80	.....		21.6	16.4 ± 0.1	0.″11	1.″01	25 02 1999
HST/NIC1	F110M	1.103 – 0.139	0.043	512	.....		21.05	15.60 ± 0.09	0.″14	0.″94	01 04 1998
HST/NIC2	F110W	1.128 – 0.384	0.075	32	.....		22.48	14.38 ± 0.03	0.″14	0.″89	01 04 1998
HST/NIC2	F160W	1.600 – 0.280	0.075	256	.....		21.84	13.33 ± 0.03	0.″16	0.″96	01 04 1998
VLT/NaCo	J	1.265 – 0.250	0.0271	1200	VIS	0.″8	24.14	15.78 ± 0.03	0.″21	0.″32	28 11 2005
VLT/NaCo	IB_2.12	2.12 – 0.06	0.0271	648	VIS	0.″7	21.01	14.31 ± 0.05	0.″17	0.″85	17 11 2004
VLT/NaCo	NB_2.12	2.122 – 0.022	0.0271	648	VIS	0.″7	20.11	14.00 ± 0.07	0.″20	0.″60	17 11 2004
VLT/NaCo	Ks	2.18 – 0.35	0.0271	600	VIS	0.″9	23.06	14.02 ± 0.02	0.″09	0.″16	28 11 2005
VLT/NaCo	IB_2.42	2.42 – 0.06	0.0271	600	VIS	1.″4	19.58	13.22 ± 0.06	0.″30	0.″30	23 12 2002
VLT/NaCo	IB_2.48	2.48 – 0.06	0.0271	600	VIS	1.″4	19.30	12.53 ± 0.05	0.″28	0.″28	23 12 2002
VLT/NaCo	L′	3.80 – 0.62	0.0271	5.25	VIS	1.″1	22.12	11.78 ± 0.01	0.″16	0.″16	03 12 2005
VLT/NaCo	NB_4.05	4.051 – 0.020	0.0271	8.75	VIS	1.″0	19.20	10.05 ± 0.02	0.″16	0.″16	03 12 2005
VLT/NaCo	NB_4.05	4.051 – 0.020	0.0271	8.75	VIS	0.″8	19.20*	10.27 ± 0.02	0.″17	0.″17	04 12 2005
VLT/VISIR	PAH2_2	11.88 – 0.37	0.075	1083.3	...	0.″7	15.47	5.02 ± 0.01	0.″36	0.″36	16 08 2006
VLT/VISIR	Q2	18.72 – 0.88	0.075	1987.2	...	1.″0	11.54	3.23 ± 0.02	0.″58	0.″58	15 08 2006

NGC 7469										
HST/FOC	F130M	0.148 – 0.066	0.01435	995.9	.....	16.3	13.4 ± 0.3	0.″04	0.″04	09 11 1991
HST/FOC	F152M	0.180 – 0.093	0.01435	995.9	.....	17.8	13.9 ± 0.2	0.″04	0.″04	09 11 1991
HST/FOC	F170M	0.195 – 0.069	0.01435	995.9	.....	18.3	13.8 ± 0.1	0.″04	0.″04	09 11 1991
HST/WFPC2	F218W	0.221 – 0.040	0.1	1200	.....	16.6	16.6 ± 0.3	0.″19	0.″19	28 06 1999
HST/ACS-HRC	F330W	0.336 – 0.041	0.025	1200	.....	22.91	14.17 ± 0.02	0.″07	0.″09	20 11 2002
HST/ACS-WFC	F435W	0.432 – 0.069	0.05	1260	.....	25.79	··· ± ···[c]	0.″12	...[c]	12 06 2006
HST/WFPC2	FR533N	0.509 – 0.006	0.1	160	.....	17.8	14.2 ± 0.2	0.″19	0.″19	13 05 2000
HST/WFPC2	F547M	0.548 – 0.048	0.0455	12	.....	20.93	15.28 ± 0.08	0.″10	0.″10	13 05 2000
HST/ACS-HRC	F550M	0.558 – 0.039	0.025	2220	.....	24.40	15.77 ± 0.02	0.″07	0.″08	09 07 2006
HST/WFPC2	F606W	0.600 – 0.150	0.0455	500	.....	20.9	··· ± ···[c]	0.″13	...[c]	10 06 1994
HST/WFPC2	FR680N	0.667 – 0.008	0.1	48	.....	18.36	12.70 ± 0.08	0.″19	0.″19	13 05 2000
HST/WFPC2	F814W	0.800 – 0.152	0.0455	7	.....	20.89	14.41 ± 0.06	0.″09	0.″09	13 05 2000
HST/ACS-WFC	F814W	0.806 – 0.154	0.05	720	.....	25.51	··· ± ···[c]	0.″16	...[c]	12 06 2006
HST/WFPC1	F785LP	0.883 – 0.141	0.044	180	.....	21.51	15.26 ± 0.06	0.″12	0.″12	21 09 1992
HST/NIC2	F110W	1.128 – 0.384	0.075	351.66	.....	22.48	12.77 ± 0.01	0.″12	0.″12	10 11 1997
HST/NIC2	F160W	1.606 – 0.277	0.075	351.66	.....	21.80	11.55 ± 0.01	0.″15	0.″15	10 11 1997
HST/NIC3	F187N	1.875 – 0.016	0.2	1343.76	.....	18.07	11.43 ± 0.05	0.″36	0.″36	31 05 2007
HST/NIC3	F190N	1.900 – 0.015	0.2	959.77	.....	18.29	11.19 ± 0.04	0.″34	0.″34	31 05 2007
HST/NIC2	F222M	2.218 – 0.121	0.075	479.55	.....	20.22	10.41 ± 0.01	0.″20	0.″20	10 11 1997
VLT/NaCo	J	1.265 – 0.250	0.01326	64	N20C80 0.″7	23.46	13.86 ± 0.01	0.″10	0.″10	18 11 2002
VLT/NaCo	H	1.66 – 0.33	0.01326	32	N20C80 0.″7	23.45	12.63 ± 0.01	0.″08	0.″08	18 11 2002
VLT/NaCo	Ks	2.18 – 0.35	0.01326	24	N20C80 0.″7	22.55	11.93 ± 0.01	0.″13	0.″13	18 11 2002
VLT/NaCo	L′	3.80 – 0.62	0.0271	5.075	VIS 0.″9	21.93	8.95 ± 0.01	0.″11	0.″11	22 12 2005
VLT/NaCo	NB_4.05	4.051 – 0.020	0.0271	8.75	VIS 0.″7	19.23	8.68 ± 0.01	0.″12	0.″12	03 12 2005
VLT/VISIR	PAH2_2	11.88 – 0.37	0.075	1083.3	... 0.″6	15.45	4.66 ± 0.01	0.″33	0.″33	13 07 2006
VLT/VISIR	Q2	18.72 – 0.88	0.075	1987.2	... 0.″5	11.31	2.74 ± 0.02	0.″50	0.″50	06 08 2006

[b] Combined images for NGC 1386 from the F547M and F658N datasets adquired in 28 06 1997 (80 s and 800 s) and 25 02 1999 (280 s and 1200 s).
[c] The nuclear source in NGC 7469 saturated the detector in these cases.

NGC 7582											
HST/WFPC2	F606W	0.600 – 0.150	0.0455	560	.....		25.4	22.5 ± 0.3	0.″14	0.″14	25 07 2001
HST/NIC2	F160W	1.606 – 0.277	0.075	639.9	.....		21.82	11.93 ± 0.01	0.″16	0.″16	15 12 1997
VLT/NaCo	IB_2.06	2.06 – 0.06	0.0271	100	VIS	0.″6	20.83	11.01 ± 0.01	0.″16	0.″16	22 05 2003
VLT/NaCo	IB_2.12	2.12 – 0.06	0.0271	100	VIS	0.″7	20.59	10.96 ± 0.01	0.″15	0.″15	18 06 2003
VLT/NaCo	IB_2.48	2.48 – 0.06	0.0271	20	VIS	1.″2	19.74	10.10 ± 0.01	0.″10	0.″10	15 10 2002
VLT/NaCo	L′	3.80 – 0.62	0.0271	6.3	JHK	1.″2	21.95	8.23 ± 0.01	0.″12	0.″12	06 12 2005
VLT/NaCo	NB_4.05	4.051 – 0.020	0.0271	8.75	VIS	1.″1	19.01	7.83 ± 0.01	0.″13	0.″13	02 12 2005
VLT/VISIR	PAH2_2	11.88 – 0.37	0.075	1444.40	...	0.″8	15.47	4.85 ± 0.01	0.″33	0.″33	06 08 2006
VLT/VISIR	Q2	18.72 – 0.88	0.075	4104	...	0.″7	11.20	3.25 ± 0.04	0.″74	0.″74	16 06 2006

3

A first glimpse at parsec scales

In this chapter we introduce the sample of galaxies studied in this thesis. First, we briefly discuss previous works already published in the literature for each object, focusing on those results obtained with high-spatial resolution data. Then, we perform a preliminary analysis of the high-spatial resolution images, with special attention to the properties of point-like sources found in the central parsecs of each galaxy: size, brightness, luminosity, line emission and visual extinction. Star-forming regions in NGC 1097 display very low W(Hα) values. In contrast, a total of 15 knots in the elliptical NGC 1052 exhibit Hα emission.

3.1 Introduction

THIS thesis is based on a sample of active galaxies: NGC 253, NGC 1052, NGC 1097, NGC 1386, NGC 7469 and NGC 7582. Six is a quite limited sample, but so is the number of nearby active galaxies that can be studied at parsec scales. Moreover, to built a multiwavelength archive with the highest-spatial resolution data available for each of the objects requires a big effort. First of all, we need different facilities for each range of the spectra (e.g. *Chandra*, *HST*, VLT, VLA). At this point, the use of scientific archives is remarkably useful. Then we have to review and collect the measurements in the literature, in order to alleviate the task of applying for observing time at the mentioned facilities. On the other hand, there is always a bit of inconsistency between results for different epochs or authors. More precisely, it was challenging to obtain a unique SED for NGC 7469 which is a highly variable AGN, specially in the optical/UV range. Nevertheless, although we have only six nuclei for a very wide sample in terms of intrinsic luminosity and host galaxy type (see Section 3.2), we can trace the main variations driven by the luminosity, in the case of the nuclear SED, and by the environment, in the case of the star-formation.

Recent publications in the field also present either a limited number of objects (~ 10) or a more limited coverage in wavelength (Ramos Almeida et al. 2009; Prieto et al. 2010; Eracleous et al. 2010). Therefore, the results from this study will be discussed in context with previous work and the data will be of public domain for future studies.

Aside of the AGN, in all cases the high-spatial resolution images reveal a number of point-like regions in the surroundings of the active nuclei. These are identified with young stellar clusters (see Chapter 5), and, as mentioned in Section 1.2, their origin seems to be highly related with the environment. Thus, our sample offer the possibility to resolve the nuclear star-forming regions and take a glance at the possible variation of their properties for different host galaxies.

The structure of this Chapter is organized as follows. The main results published in the literature for each galaxy in the sample are summarized in Section 3.2, accompanied by a set of wide-field images in the UV, optical, and IR from *GALEX* (Galaxy Evolution Explorer), *HST*, DSS (Digital Sky Survey), SDSS (Sloan Digital Sky Survey), *Spitzer Space Telescope* and 2MASS (2 Microns All Sky Survey). High-spatial resolution images of the nuclear region acquired in the optical (*HST*), NIR (VLT/NaCo) and radio wavelengths (VLA/VLBI) are also shown. For each galaxy we study the main properties of the knots identified in the central parsecs including size, brightness, luminosity and an estimation of their ages and masses. Finally, we provide the results of the photometry for all the knots and the active nuclei in the Tables 3.1, 3.2, 3.3, 3.4, 3.5 and 3.6, at the end of this chapter. Besides the fluxes, we also include the equivalent width and luminosity of Hα or Brα, as the case may be, and an estimation of the visual extinction (A_V) based on the Balmer decrement of two of these three lines: Hα, Paα or Brα.

3.2 Notes on individual galaxies

The high-spatial resolution achieved in the IR to optical range permits us to isolate the AGN emission from the stellar light of the galaxy, avoiding the contamination of the nuclear SED in those wavelength ranges where the integrated stellar light competes with the active nucleus. This is the case, for example, in the optical range where the nuclear dust extinction is more pronounced, and also in the MIR, where the emission from dust heated in star-forming regions to temperatures up to $\sim 300\,\mathrm{K}$ becomes stronger.

Since most of the galaxies are nearby objects, there is much information in the literature about them, specially for some reference objects such as NGC 253, a starburst prototype, or NGC 7469, one of the first AGNs studied by Seyfert (1943). Thus, we selected those references dealing with high-spatial resolution data to give a general picture for each object. From now on, these are sorted by increasing distance, i.e. NGC 253 (3.94 Mpc), NGC 1097 (14.5 Mpc), NGC 1386 (15.3 Mpc), NGC 1052

(18.0 Mpc), NGC 7582 (19.9 Mpc) and NGC 7469 (65.2 Mpc). For each galaxy we also show either a high-spatial resolution image in the optical/NIR or a colour composition for the nuclear region, surrounding by circles all the point-like sources identified, together with the individual MIR-to-optical SEDs for a small sample of them. A global and more complete comparison of the knots among the different galaxies will be addressed in the next Chapter.

3.2.1 NGC 253

This is one of the nearest starburst galaxies, located at 3.94 ± 0.5 Mpc (Karachentsev et al. 2003) in the Sculptor group. The top panels in Fig. 3.1 reveal a nearly edge-on SAB(s)c galaxy hosting a number of young stellar clusters detected in the optical range in its nucleus, surrounded by large patches of dust (Forbes et al. 2000). The 2MASS image shows the real structure of the galaxy beneath the dusty face: two spiral arms are connected by a stellar bar (possibly also by a faint ring), and a strong infrared nucleus. At these scales, a strong bipolar outflow cone is traced, perpendicular to the galaxy plane, by ionized gas and X-ray emission (Strickland et al. 2002; Weaver et al. 2002). In the central region, the VLT/NaCo *L*-band image reveals strong starburst activity, mostly obscured in the optical, within the inner ~ 600 pc. At radio wavelengths (1.3–20 cm) Ulvestad & Antonucci (1997) identified more than 60 individual sources along the north-east to south-west direction associated with a 300 pc radius nuclear ring. Among them, a strong non-thermal compact (< 2 pc) source with brightness temperature of $T_{2\,\mathrm{cm}} > 40\,000$ K and spectral index of $\alpha_{1.3}^{3.6} = 0.3$ ($S_\nu \propto \nu^{-\alpha}$) lies in its centre (called TH2 in Turner & Ho 1985). Previous IR observations revealed the presence of bright hotspots in the nuclear starburst region (Sams et al. 1994), with a bright source called "IR peak" dominating the emission in this range (Galliano et al. 2005).

Fig. 3.1 clearly shows that the morphology of NGC 253 varies strongly with wavelength, which led to many different registrations in the literature (see Galliano et al. 2005, and references therein). As a result, several and different IR hotspots have been associated to the compact radio core. In Section 2.3.2 we found a very fine registration of the central region based on the adaptive optics IR data with FWHM $\leq$ 200 mas resolution (≤ 4 pc), comparable to those in existing radio maps (Fernández-Ontiveros et al. 2009), which resulted in the identification of IR counterparts for eight radio sources located in the inner 600 pc. As mentioned before, the location of the nucleus in this galaxy is a controversial subject. It seems clear that the dominant nuclear source is a different one at radio, IR, optical and X-ray wavelengths (Section 2.3.2). The nature of these "candidates" and the identification of the nucleus in this galaxy will be further analyzed in Section 4.9.

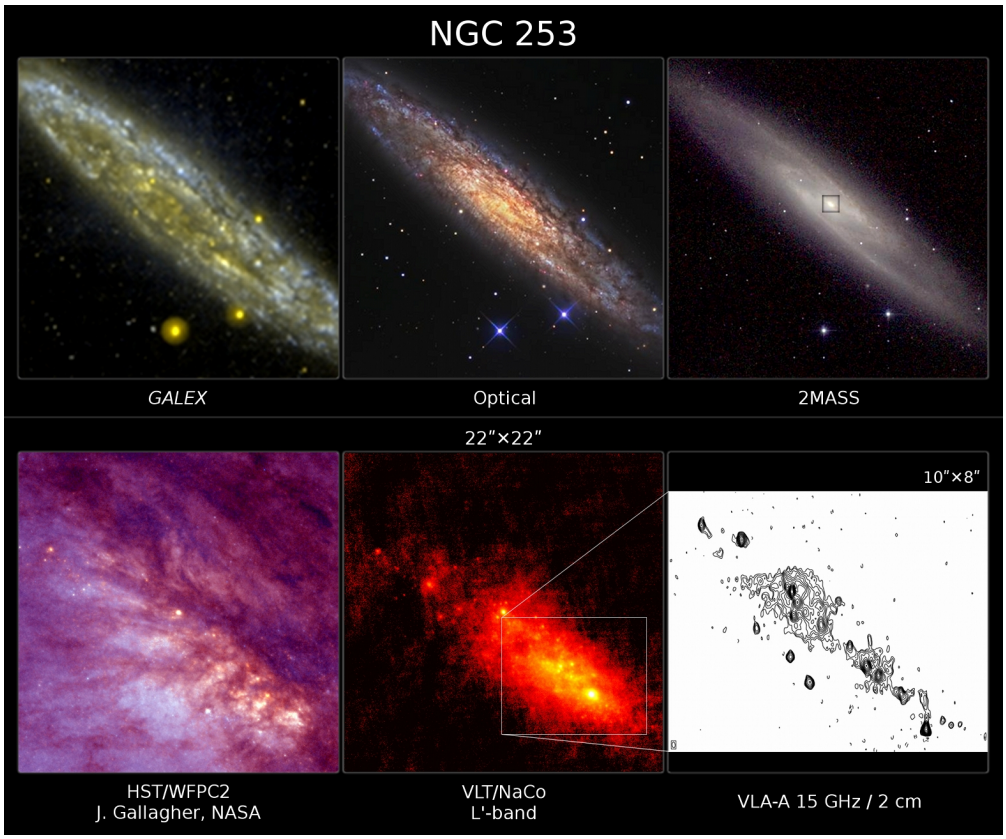

FIGURE 3.1— NGC 253 at optical, infrared and radio wavelengths (North is up and East is to the left). The upper panels correspond to different views (UV, optical, NIR) at large scale and cover the same field of view. Lower-left and centre panels correspond to the black box region ($22'' \times 22''$) in the 2MASS image. The radio map in the lower-right panel covers $10'' \times 8''$ and was taken from Ulvestad & Antonucci (1997).

Fig. 3.2 shows the VLT/NaCo *J* (blue), *Ks* (green) and *L*-band (red) colour composition with the knots encircled. The availability of the VLT/NaCo *L*-band image with $0\farcs13$ (2.5 pc) resolution permitted us to find a total of 37 point-like sources above a 3σ threshold in the central $22'' \times 22''$, a factor of ~ 3 over the number of sources resolved in the same region by Forbes et al. (2000). The *J* and *Ks*-band knots are all found to have an *L*-band counterpart, although the converse is not true for a number of, probably very extinct, sources. Of the 37 sources identified in the *L*-band, 31 were detected in the F814W filter and 23 in the F555W band. Most of the brightest or isolated knots in the *N* and *Q*-bands were also found to have a counterpart in the *L*-band (see Fig. 2.2). Within our sample, this object is the closest one and therefore

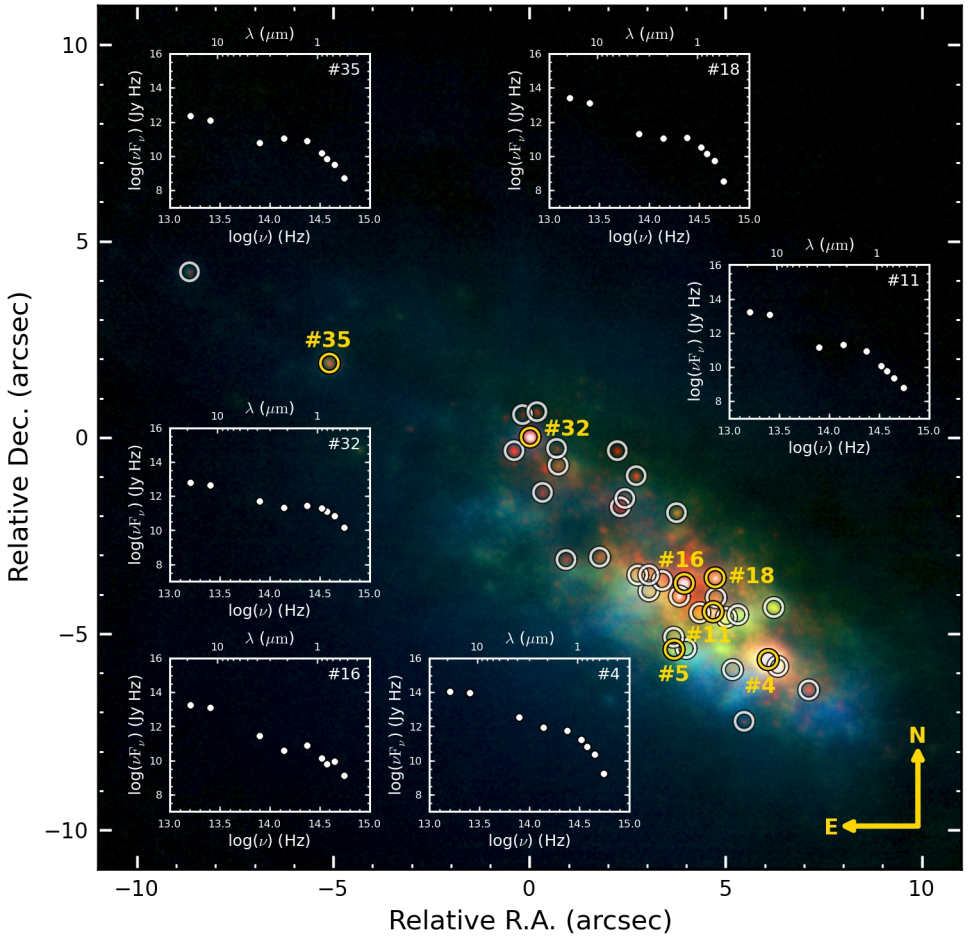

FIGURE 3.2— Adaptive optics *J* (blue), *Ks* (green) and *L* (red) colour composite image of the central $22'' \times 22''$ in NGC 253. The 37 knots identified in this galaxy are marked and we also show the SEDs in the optical-IR range for a representative sample of 5 of them.

represents a very special case due to the high-spatial resolution achieved in its central region. Thus, this resolved starburst will be used as a reference to compare with the knots found in the rest of galaxies. This comparison will be addressed in Section 5.4, although their photometry in the IR-optical range (Table 3.1) and average properties will be mentioned below.

The knots in NGC 253 are very compact, with a median half-light radius ($\mathrm{FWHM_{obs}}$) of 3.4 pc in the *L*-band. For comparison, the instrumental resolution is $\mathrm{FWHM_{inst}} = 0\farcs13 \approx 2.5$ pc. They also show a median brightness in the *Ks*-band of

$m_K = 15.3$ mag, which corresponds to an absolute magnitude of $M_K = -12.7$ mag with the outstanding knot #4, the IR peak, dominating the emission in this range ($M_{K_{\#4}} = -15.5$ mag). Their Hα equivalent width cluster about a median value of W(Hα) = 500 Å, with 221 Å and 770 Å as the first and third quartiles, respectively. Assuming instantaneous star-formation and solar metallicity, those correspond to an age interval between ~ 3.4 and 5.7 Myr, with its median value around 4.2 Myr (Leitherer et al. 1999). From the Hα/Brα ratio we estimated a median extinction value of $A_V = 6.1$ mag, using the method described in Section 2.3.4. The high obscuration exhibited, together with the young ages displayed by most of the knots, suggest that these are active star-forming clusters surrounded by a very dusty environment, which is the common picture for young embedded clusters, still buried in their birth material (Johnson 2005). Based on the age-dependent mass-luminosity ratio assumed STARBURST99 models (Leitherer et al. 1999), we estimate a mass value for the knots from their K-band luminosity and W(Hα) (see Section 5.4.5 for details). This results in a median value for the mass of about $7 \times 10^4\,M_\odot$, with 50% of the knots between $4 \times 10^4\,M_\odot$ and $2 \times 10^5\,M_\odot$.

TABLE 3.1— Main characteristics of the knots found in NGC 253. The absolute (Δ) or relative error (δ) for each magnitude is: $\delta(F555W) = 22\%$, $\delta(F675W) = 16\%$, $\delta(F814W) = 11\%$, $\delta(F850LP) = 10\%$, $\delta(J) = 4\%$, $\delta(Ks) = 5\%$, $\delta(L') = 4\%$, $\delta(N) = 6\%$, $\delta(Q) = 4\%$, $\delta(\mathrm{H}\alpha/\mathrm{Br}\alpha) = 19\%$, $\Delta A_V = 0.2$ mag, $\delta[W(\mathrm{H}\alpha)] = 23\%$ and $\delta(L_{\mathrm{H}\alpha}) = 10\%$. Relative R.A. and Dec. correspond to the shift in equatorial coordinates with respect to knot #32, which was used as reference for the alignment. The luminosity of the Hα line ($L_{\mathrm{H}\alpha}$) is corrected by the extinction given in A_V. The size column corresponds to the half-light radius ($\mathrm{FWHM_{obs}}$).

#	Relative R.A.	Relative Dec.	F555W	F675W	F814W	F850LP	*J*	*Ks*	*L'*	*N*	*Q*	Size [pc]	$\frac{\mathrm{H}\alpha}{\mathrm{Br}\alpha}$	A_V [mag]	$W(\mathrm{H}\alpha)$ [Å]	$\log(L_{\mathrm{H}\alpha})$ [erg s^{-1}]
							[μJy]									
0	5.″47	−7.″23	5.0	34	41	70	4.0×10^{2}	3.0×10^{2}	3.0×10^{2}	2.0×10^{5}	4.0×10^{5}	5.4		..	530	....
1	7.″12	−6.″43	0.6	7	14	31	$< 1.0\times10^{2}$	3.0×10^{2}	7.0×10^{2}	4.0×10^{5}	8.0×10^{5}	4.6	0.53	5.9	660	38.5
2	5.″17	−5.″91	1.4	4	27	51	3.0×10^{2}	3.0×10^{2}	5.0×10^{2}	1.1×10^{6}	2.4×10^{6}	< 2.5	1.12	4.9	710	38.5
3	6.″33	−5.″83	0.6	19	26	71	2.1×10^{3}	4.2×10^{3}	5.0×10^{3}	3.7×10^{6}	7.1×10^{6}	< 2.5	0.14	7.8	710	39.4
4	6.″08	−5.″66	3.2	50	171	534	2.3×10^{3}	6.4×10^{3}	4.4×10^{4}	3.7×10^{6}	6.9×10^{6}	3.1	0.07	8.7	330	40.2
5	3.″68	−5.″40	1.3	16	35	87	9.0×10^{2}	1.2×10^{3}	8.0×10^{2}	2.0×10^{5}	5.0×10^{5}	7.0	1.46	4.5	360	38.2
6	3.″99	−5.″38	1.1	14	30	67	1.2×10^{3}	1.2×10^{3}	$5.0\times10^{2}<$	1.0×10^{5}	2.0×10^{5}	5.1	1.43	4.5	260	38.0
7	3.″67	−5.″09	0.5	< 3	9	20	3.0×10^{2}	6.0×10^{2}	4.0×10^{2}	2.0×10^{5}	2.0×10^{5}	4.0		..	...	....
8	5.″02	−4.″58	3.5	31	37	77	7.0×10^{2}	1.4×10^{3}	1.2×10^{3}	6.0×10^{5}	1.3×10^{6}	4.9	1.21	4.8	840	38.7
9	4.″34	−4.″46	< 0.2	< 3	< 1	< 2	$< 1.0\times10^{2}$	2.0×10^{2}	9.0×10^{2}	1.0×10^{5}	2.0×10^{5}	4.3		..	...	....
10	5.″31	−4.″51	6.2	44	78	154	7.0×10^{2}	1.3×10^{3}	1.0×10^{3}	3.0×10^{5}	1.0×10^{6}	< 2.5	5.78	2.6	570	38.2
11	4.″68	−4.″44	1.1	5	16	37	4.0×10^{2}	1.4×10^{3}	1.9×10^{3}	5.0×10^{5}	1.1×10^{6}	5.1	0.14	7.8	470	39.1
12	6.″23	−4.″33	0.7	6	18	49	5.0×10^{2}	1.6×10^{3}	1.0×10^{3}	5.0×10^{5}	6.0×10^{5}	3.1	18.32	1.0	190	36.5
13	3.″82	−4.″04	2.3	25	19	21	1.0×10^{2}	2.0×10^{2}	2.2×10^{3}	4.0×10^{5}	1.1×10^{6}	< 2.5	0.23	7.1	530	39.0
14	4.″75	−4.″08	0.7	8	22	57	4.0×10^{2}	$7.0\times10^{2}<$	1.0×10^{2}	5.0×10^{5}	1.3×10^{6}	4.2	3.98	3.1	450	37.6
15	3.″05	−3.″91	1.9	28	27	61	9.0×10^{2}	9.0×10^{2}	9.0×10^{2}	5.0×10^{5}	1.4×10^{6}	3.5	6.80	2.4	1650	38.1
16	3.″94	−3.″71	2.4	20	17	43	3.0×10^{2}	3.0×10^{2}	3.7×10^{3}	5.0×10^{5}	1.1×10^{6}	3.5	0.11	8.1	820	39.5
17	3.″38	−3.″64	5.4	41	28	48	8.0×10^{2}	5.0×10^{2}	9.0×10^{2}	4.0×10^{5}	1.2×10^{6}	3.5	1.52	4.5	1380	38.8
18	4.″73	−3.″58	0.6	12	38	103	5.0×10^{2}	8.0×10^{2}	2.8×10^{3}	5.0×10^{5}	1.5×10^{6}	3.1	0.14	7.8	210	39.0
19	2.″76	−3.″50	2.5	31	18	35	6.0×10^{2}	7.0×10^{2}	1.2×10^{3}	3.0×10^{5}	1.0×10^{6}	3.5	1.19	4.8	1090	38.6
20	3.″04	−3.″50	1.6	21	7	17	5.0×10^{2}	8.0×10^{2}	1.4×10^{3}	4.0×10^{5}	1.1×10^{6}	3.5	0.81	5.3	2240	38.8
21	0.″93	−3.″11	< 0.2	< 3	< 1	< 2	2.0×10^{2}	3.0×10^{2}	$5.0\times10^{2}<$	$1.0\times10^{5}<$	1.0×10^{5}	13.3		..	...	....
22	1.″79	−3.″05	0.3	< 3	2	< 2	$< 1.0\times10^{2}<$	1.0×10^{2}	$5.0\times10^{2}<$	1.0×10^{5}	3.0×10^{5}	10.1		..	...	....
23	3.″75	−1.″92	< 0.2	8	7	20	2.0×10^{2}	5.0×10^{2}	$6.0\times10^{2}<$	1.0×10^{5}	3.0×10^{5}	4.3	0.12	8.1	100	38.4
24	2.″31	−1.″77	0.9	9	7	14	$1.0\times10^{2}<$	1.0×10^{2}	6.0×10^{2}	2.0×10^{5}	7.0×10^{5}	< 2.5	0.28	6.8	710	38.6
25	2.″43	−1.″55	3.1	19	47	92	3.0×10^{2}	3.0×10^{2}	4.0×10^{2}	2.0×10^{5}	7.0×10^{5}	3.4	1.16	4.8	200	38.2
26	0.″33	−1.″40	0.4	10	4	9	$< 1.0\times10^{2}<$	1.0×10^{2}	$4.0\times10^{2}<$	1.0×10^{5}	2.0×10^{5}	< 2.5		..	4130	....
27	2.″72	−0.″97	< 0.2	4	5	10	4.0×10^{2}	4.0×10^{2}	$6.0\times10^{2}<$	1.0×10^{5}	3.0×10^{5}	3.4		..	470	....
28	0.″73	−0.″71	0.6	< 3	4	4	$< 1.0\times10^{2}$	3.0×10^{2}	$3.0\times10^{2}<$	1.0×10^{5}	4.0×10^{5}	2.8	0.18	7.4	350	38.3

29	$-0\farcs39$	$-0\farcs34$	1.8	20	37	72	4.0×10^{2}	4.0×10^{2}	1.1×10^{3}	2.0×10^{5}	6.0×10^{5}	3.3	2.06	4.0	740	38.4
30	$2\farcs24$	$-0\farcs33$	0.6	<3	<1	<2	$<1.0\times10^{2}$	$<1.0\times10^{2}$	5.0×10^{2}	$<1.0\times10^{5}$	$<1.0\times10^{5}$	3.1	0.02	10.3	90	38.4
31	$0\farcs69$	$-0\farcs28$	<0.2	<3	2	4	$<1.0\times10^{2}$	$<1.0\times10^{2}$	$<1.0\times10^{2}$	$<1.0\times10^{5}$	$<1.0\times10^{5}$	2.8		..	770	....
32	$0\farcs00$	$0\farcs00$	26.6	150	334	613	1.2×10^{3}	1.5×10^{3}	6.4×10^{3}	2.0×10^{5}	4.0×10^{5}	2.8	0.39	6.4	90	39.2
33	$-0\farcs18$	$0\farcs58$	<0.2	<3	3	<2	3.0×10^{2}	1.0×10^{2}	3.0×10^{2}	$<1.0\times10^{5}$	1.0×10^{5}	<2.5	0.07	8.8	190	38.3
34	$0\farcs19$	$0\farcs66$	<0.2	<3	<1	<2	$<1.0\times10^{2}$	2.0×10^{2}	4.0×10^{2}	$<1.0\times10^{5}$	$<1.0\times10^{5}$	3.3		..	...	....
35	$-5\farcs10$	$1\farcs90$	0.9	7	18	47	3.0×10^{2}	8.0×10^{2}	8.0×10^{2}	$<1.0\times10^{5}$	1.0×10^{5}	5.0	0.36	6.5	240	38.4
36	$-8\farcs66$	$4\farcs22$	3.4	21	71	120	4.0×10^{2}	5.0×10^{2}	5.0×10^{2}	$<1.0\times10^{5}$	$<1.0\times10^{5}$	3.4	0.48	6.1	50	38.1

3.2.2 NGC 1097

NGC 1097 is a SB(r′l)b galaxy located at 14.5 Mpc (Tully 1988) owning one of the best-studied nuclear rings (due to its large angular size and high luminosity) and four faint optical kiloparsec-scale jets, which probably have a tidal origin due to gravitational interaction with the close elliptical companion NGC 1097A (Wehrle et al. 1997). The nuclear ring, rich in molecular gas (Gerin et al. 1988; Kohno et al. 2003; Hsieh et al. 2008), consists of two spiral arms of H II knots with the two arms delineated by dust lanes crossing into the ring (Rickard 1975; Barth et al. 1995). At high-spatial resolution (bottom panel in Fig. 3.3) it is resolved in a number of bluish Hα+[N II] patches and red (obscured in the optical) knots, some of them detected at radio wavelengths (bottom-right panel). The dust lanes appear at the leading edges of the main bar ($\sim$ 16 kpc long, $PA \sim 137^{\circ}$) and curve around the nucleus into the $\sim$ 1.3 kpc ring (bottom-left panel). A faint nuclear stellar bar is also seen in the *Ks*-band image (bottom-centre panel) and in the 1–0 S(1) H_2 emission-line map from Kotilainen et al. (2000). The H_2 emission is also extended along the direction of the jets (Reunanen et al. 2002; Hicks et al. 2009). In the *Spitzer* colour composite IR image (top-right panel in Fig. 3.3), the ring appears very bright with regard to the spiral arms, but in contrast it is quite faint in the FUV. This suggests that the clusters in the ring have ages older than 10 Myr, assuming that most of the FUV emission disappeared with the death of O and B type stars. In addition, a star-formation rate of $5\,M_{\odot}\,yr^{-1}$, a supernova rate of $0.2\,yr^{-1}$ and a mean visual extinction of $A_V = 1.1$ mag have been estimated for this structure by Hummel et al. (1987) and Barth et al. (1995).

Within the ring, the presence of an irregular three-arm spiral pattern of dust lanes has been proposed as evidence for the feeding of gas and dust into the central parsecs of the galaxy (Prieto et al. 2005; Fathi et al. 2006; Davies et al. 2009; van de Ven & Fathi 2009). In the centre, the active nucleus originally classified as a LINER (Heckman 1980) began to exhibit the typical spectrum of a Seyfert 1 type with a broad, double-peaked Hα profile in 1991 (Storchi-Bergmann et al. 1993), fading gradually the years after (Storchi-Bergmann et al. 1995, 2003). On the other hand, Iyomoto et al. (1996) reported a hard X-ray (2–10 keV) luminosity of about $3.7 \times 10^{40}\,erg\,s^{-1}$ (at 14.5 Mpc) absorbed by a column density of $N_H = 1.3 \times 10^{21}\,cm^{-2}$ together with a soft X-ray component associated with starburst activity, which accounts for 20% of the integrated X-ray luminosity (Perez-Olea & Colina 1996). At radio wavelengths, the nucleus is compact and weak (bottom-right panel; Wolstencroft et al. 1984) and shows an inverted non-thermal spectrum (Morganti et al. 1999). Using the Balmer decrement, Storchi-Bergmann et al. (1993) gives a nuclear reddening of $E(B-V) \geq 0.73$. Finally, van de Ven & Fathi (2009) derived a central black hole mass of $M_{BH} = 1.2 \times 10^8\,M_{\odot}$ based on the central stellar velocity dispersion.

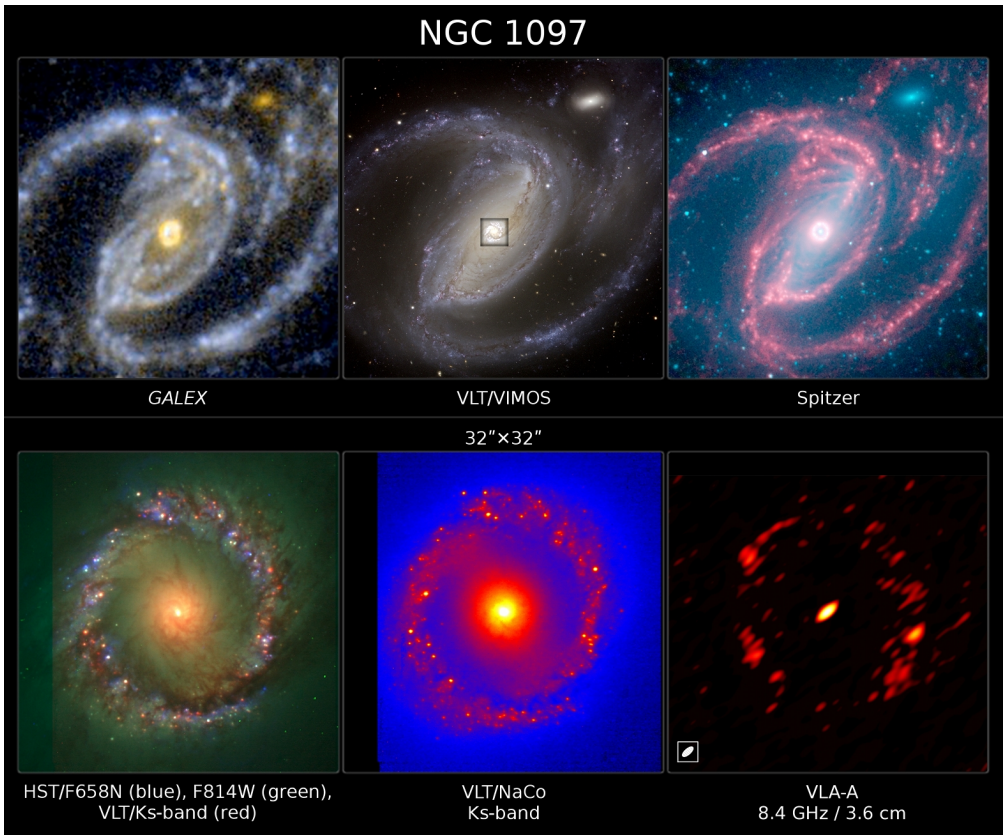

FIGURE 3.3— NGC 1097 at optical, infrared and radio wavelengths (North is up and East is to the left). The upper panels correspond to different views (UV, optical, MIR) at large scale and cover the same field of view. Lower panels correspond to the black box region ($32'' \times 32''$) in the VIMOS image.

Fig. 3.4 shows a colour composition of the Hα (F658N), *I*-band (F814W) and *Ks*-band filters. As well as the white bluish knots that appear on the *HST* images, one can see a number of reddish knots, which are probably very extinct sources unveiled in the NaCo image. Since the NIR range is less affected by extinction, we looked for point-like sources in the VLT/NaCo *Ks*-band, finding a total of 74 knots in the ~ 1.3 kpc diameter star-forming ring. The SEDs for a small sample of these knots are also shown in Fig. 3.4. As in the case of NGC 253, a first look at the individual energy distributions in NGC 1097 reveals a similar shape, i.e. a MIR maximum with a NIR excess.

The knots in NGC 1097 show a median half light radius of about 17.2 pc ($D = 14.5$ Mpc, $\mathrm{FWHM_{inst}} = 0\farcs13 \approx 9.1$ pc), suggesting that they present some extended

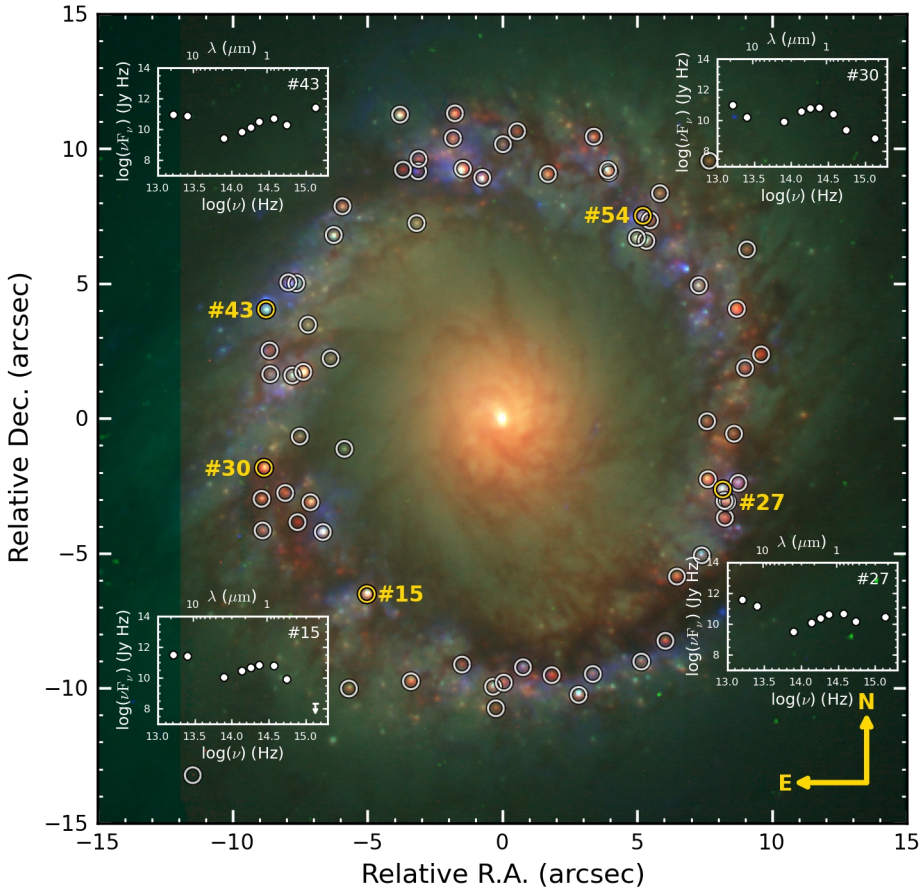

FIGURE 3.4— F658N (blue), F814W (green) and *Ks*-band (red) colour composite image of the central $32'' \times 32''$ in NGC 1097. The 74 knots identified in this galaxy are marked and we also show the SEDs in the optical-IR range for a representative sample of 4 of them.

emission. Their median K-band brightness is $m_K = 17.5$ mag, which corresponds to an absolute magnitude of $M_K = -13.3$ mag, i.e. slightly brighter than the knots in NGC 253. The visual extinction is derived from the Hα/Paα ratio and presents a median value of $A_V = 7.6$ mag, higher than the 6.1 mag measured in NGC 253. Surprisingly, the W(Hα) estimates cluster around ~ 13.6 Å, a very low value for a young starburst population. This corresponds to ages of about 10.9 Myr (assuming instantaneous star-formation and solar metallicity, Leitherer et al. 1999). This anomaly was also reported by Dors et al. (2008), and can be produced by other effects than the age: *i)* a deficiency of high-mass stars in the Initial Mass Function (IMF), *ii)* very high

dust extinction[1], *iii)* contamination of the continuum by contribution of other stellar population, and *iv)* continuous star-formation (Kennicutt et al. 1989). However, all these effects are discarded in the work by Dors et al. (2008) for the case of NGC 1097, since none of them explain how a very young population with O and B stars looks much older with such low W(Hα) values. Interestingly, the *GALEX* colour composite image in Fig. 3.3 clearly shows that the star-forming ring exhibit much less FUV emission than the spiral arms do, the contrary of what one would expect from a young star-forming region plenty of massive stars, which dominate this range. Since the latter almost disappear after $\sim 10\,$Myr from the initial star-formation burst, the *GALEX* image is consistent with a slightly evolved starburst ring, in agreement with our age estimation, rather than being an intrinsic anomalous value of W(Hα) on a very young population. Finally, the median mass of the knots, derived from the *K*-band luminosity as in the case of NGC 253, is about $5 \times 10^4\,M_\odot$, with 50% of the sources between $2 \times 10^4\,M_\odot$ and $10^5\,M_\odot$.

[1]Only if there is a shift between the line and the assumed continuum or the line and continuum emissions come from different physical regions.

TABLE 3.2— Main characteristics of the knots found in NGC 1097. The absolute (Δ) or relative error (δ) for each magnitude is: $\delta(F218W) = 6\%$, $\delta(F555W) = 6\%$, $\delta(F814W) = 3\%$, $\delta(J) = 2\%$, $\delta(H) = 2\%$, $\delta(Ks) = 2\%$, $\delta(L') = 14\%$, $\delta(N) = 21\%$, $\delta(Q) = 26\%$, $\delta(\mathrm{H}\alpha/\mathrm{Pa}\alpha) = 17\%$, $\Delta A_V = 0.2$ mag, $\delta[W(\mathrm{H}\alpha)] = 20\%$ and $\delta(L_{\mathrm{H}\alpha}) = 3\%$. Relative R.A. and Dec. correspond to the shift in equatorial coordinates with respect to active nucleus ($\star$), which was used as reference for the alignment. The luminosity of the Hα line ($L_{\mathrm{H}\alpha}$) is corrected by the extinction given in A_V. The size column corresponds to the half-light radius ($\mathrm{FWHM_{obs}}$).

#	Relative R.A.	Relative Dec.	F218W	F555W	F814W	J	H	Ks	L′	N	Q	Size	Hα/Paα	A_V	W(Hα)	log($L_{H\alpha}$)
			[μJy]									[pc]		[mag]	[Å]	[erg s^{-1}]
0	−11.″90	−16.″02	1.7	< 0.5	< 1	..	..	..	< 1	...	..	< 9.1	...	..	...	....
1	14.″83	−16.″02	< 0.2	...	< 1	..	..	..	..	...	..	< 9.1	...	..	...	....
2	−11.″48	−13.″22	1.2	< 0.5	< 1	3	3	5	21	...	..	< 9.1	...	..	...	....
3	−0.″25	−10.″74	< 0.2	< 0.5	< 1	19	40	32	6	...	..	22.7	...	..	...	....
4	2.″82	−10.″25	6.0	31.5	157	174	132	94	55	...	..	16.4	...	..	...	....
5	−5.″69	−10.″01	< 0.2	1.4	23	56	67	45	< 1	...	..	19.6	...	..	...	....
6	−0.″35	−9.″95	5.7	16.9	76	120	100	67	30	...	..	31.0	...	..	...	....
7	0.″05	−9.″79	1.2	2.7	12	72	87	64	25	...	..	31.0	0.01	11.7	3	39.0
8	−3.″40	−9.″74	< 0.2	2.0	29	106	125	102	29	...	..	16.8	...	..	...	....
9	1.″82	−9.″52	< 0.2	< 0.5	9	29	70	75	16	...	..	17.2	0.01	11.8	19	39.6
10	3.″35	−9.″47	1.2	3.5	25	66	63	44	< 1	...	..	29.5	...	..	...	....
11	0.″76	−9.″22	< 0.2	2.2	32	91	68	54	26	1.4×10^4	1.6×10^5	20.6	0.08	7.5	46	39.6
12	−1.″50	−9.″12	< 0.2	1.3	< 1	< 1	4	25	32	$< 2.0\times10^3$	7.0×10^3	19.5	...	..	...	....
13	5.″15	−9.″01	2.6	5.1	21	55	58	43	5	$< 2.0\times10^3$	9.0×10^3	30.8	...	..	...	....
14	6.″04	−8.″24	< 0.2	2.4	17	85	76	71	48	$< 2.0\times10^3$	1.6×10^4	13.9	0.04	8.8	44	39.3
15	−5.″03	−6.″51	< 0.2	16.3	168	293	262	215	143	1.0×10^4	1.9×10^4	12.0	0.34	5.2	12	39.0
16	6.″47	−5.″86	< 0.2	3.7	29	101	108	80	29	$< 2.0\times10^3$	6.0×10^3	19.2	0.02	10.1	4	39.1
17	7.″39	−5.″08	4.7	14.8	53	77	52	35	22	$< 2.0\times10^3$	$< 1.0\times10^3$	29.7	...	..	28	....
18	−6.″66	−4.″21	0.4	24.5	209	224	171	144	177	1.5×10^4	4.5×10^4	11.2	0.29	5.5	19	39.5
19	−8.″90	−4.″15	< 0.2	2.6	19	89	78	58	< 1	$< 2.0\times10^3$	$< 1.0\times10^3$	16.8	0.12	7.0	20	38.7
20	−7.″60	−3.″85	< 0.2	< 0.5	< 1	< 1	19	39	< 1	1.5×10^4	$< 1.0\times10^3$	20.8	...	..	...	....
21	8.″24	−3.″68	0.2	1.3	19	95	114	95	36	$< 2.0\times10^3$	5.0×10^3	20.2	0.03	9.1	15	39.3
22	−7.″12	−3.″10	0.3	5.3	60	155	174	136	48	$< 2.0\times10^3$	4.0×10^3	15.4	...	..	1	....
23	8.″33	−3.″09	10.1	10.4	53	149	132	92	24	$< 2.0\times10^3$	6.0×10^3	23.7	0.02	10.0	1	39.0
24	8.″23	−3.″06	9.3	12.1	54	152	130	93	41	$< 2.0\times10^3$	2.0×10^3	23.7	0.04	8.6	4	39.0
25	−8.″93	−2.″98	< 0.2	0.7	28	46	67	93	192	1.6×10^4	4.0×10^3	11.6	0.10	7.2	15	38.8
26	−8.″06	−2.″76	< 0.2	< 0.5	12	87	83	61	14	$< 2.0\times10^3$	6.0×10^3	28.8	0.03	9.3	25	39.1
27	8.″17	−2.″63	20.9	29.7	119	210	147	96	59	6.0×10^3	2.2×10^4	16.7	0.23	5.9	13	39.2
28	8.″74	−2.″39	1.6	8.7	48	210	126	91	75	...	5.3×10^4	23.7	0.09	7.4	86	40.0

29	7.″62	−2.″25	< 0.2	6.1	50	178	208	166	35	$< 2.0\times10^3$	2.0×10^3	15.4	...	..	...	....
30	−8.″84	−1.″83	0.5	6.0	71	300	345	292	106	$< 2.0\times10^3$	7.0×10^3	11.2	...	..	...	....
31	−5.″86	−1.″13	0.6	1.1	26	37	34	18	33	$< 2.0\times10^3$	$< 1.0\times10^3$	29.0	...	..	...	....
32	−7.″52	−0.″67	1.0	7.1	27	67	56	37	15	1.9×10^4	5.0×10^3	9.9	...	..	...	....
33	8.″58	−0.″57	< 0.2	< 0.5	13	65	60	39	9	3.1×10^4	8.0×10^3	21.8	...	..	14	....
34	7.″59	−0.″10	< 0.2	0.7	13	52	60	50	11	$< 2.0\times10^3$	5.0×10^3	21.9	...	..	...	....
35	−7.″79	1.″60	73.4	23.6	87	198	99	52	16	$< 2.0\times10^3$	3.0×10^3	< 9.1	...	..	...	....
36	−8.″61	1.″64	19.7	7.2	22	89	61	31	< 1	$< 2.0\times10^3$	$< 1.0\times10^3$	< 9.1	...	..	10	....
37	−7.″39	1.″73	87.3	30.5	175	467	479	352	85	$< 2.0\times10^3$	6.0×10^3	11.6	...	..	...	....
38	8.″99	1.″87	< 0.2	0.8	16	90	89	65	< 1	...	$< 1.0\times10^3$	20.3	0.13	6.8	16	38.4
39	−6.″37	2.″22	6.4	4.1	17	51	41	29	< 1	4.0×10^3	$< 1.0\times10^3$	9.6	0.01	10.5	1	38.7
40	9.″59	2.″38	< 0.2	< 0.5	6	78	94	77	28	...	..	18.1	...	..	...	....
41	−8.″64	2.″52	< 0.2	< 0.5	5	36	38	39	50	$< 2.0\times10^3$	1.0×10^4	32.2	0.04	8.8	220	39.3
42	−7.″21	3.″48	0.9	4.2	23	57	41	25	< 1	4.0×10^3	6.0×10^3	11.6	...	..	...	....
43	−8.″77	4.″04	188.0	41.3	139	135	82	55	36	3.0×10^3	1.1×10^4	14.6	0.05	8.4	2	39.3
44	8.″69	4.″07	0.3	1.6	36	240	308	280	105	...	$< 1.0\times10^3$	15.0	...	..	...	....
45	7.″28	4.″93	< 0.2	6.5	64	106	82	68	74	3.0×10^3	2.1×10^4	23.3	0.13	6.9	15	39.2
46	−7.″65	5.″01	204.9	29.9	96	140	82	51	42	1.3×10^4	4.6×10^4	28.8	0.07	8.0	11	39.8
47	−7.″94	5.″05	140.0	17.1	50	124	89	75	53	1.9×10^4	5.6×10^4	28.8	0.70	4.1	322	39.5
48	9.″07	6.″27	< 0.2	7.6	8	35	46	33	< 1	...	..	27.3	0.01	10.9	3	38.7
49	5.″34	6.″58	49.8	18.9	101	124	84	56	< 1	$< 2.0\times10^3$	7.0×10^3	15.9	...	..	...	....
50	4.″98	6.″70	95.4	24.8	85	155	116	83	< 1	$< 2.0\times10^3$	1.2×10^4	17.3	...	..	...	....
51	−6.″26	6.″80	38.9	20.2	102	118	97	80	19	$< 2.0\times10^3$	9.0×10^3	12.0	...	..	...	....
52	−3.″18	7.″24	4.5	4.9	30	73	56	33	22	3.0×10^3	8.0×10^3	13.3	...	..	...	....
53	5.″47	7.″34	6.4	4.7	33	124	93	57	18	5.0×10^3	1.9×10^4	17.3	0.01	11.4	1	39.3
54	5.″20	7.″51	17.2	12.6	68	154	106	71	54	9.0×10^3	3.1×10^4	12.0	0.06	8.2	14	39.6
55	−5.″94	7.″87	1.1	7.5	38	118	113	84	< 1	7.0×10^3	3.0×10^3	13.4	...	..	...	....
56	5.″84	8.″35	0.9	< 0.5	20	56	53	47	12	$< 2.0\times10^3$	7.0×10^3	23.4	...	..	...	....
57	−0.″75	8.″92	< 0.2	9.9	127	182	147	146	259	...	..	12.7	0.13	6.9	33	39.8
58	1.″69	9.″06	2.2	2.8	29	98	112	101	26	...	..	15.8	...	..	...	....
59	3.″94	9.″13	34.3	13.1	99	189	174	129	37	...	..	19.6	...	..	...	....
60	−3.″13	9.″16	< 0.2	< 0.5	3	< 1	< 1	17	82	...	..	25.6	0.13	6.8	1506	39.7
61	−3.″69	9.″22	< 0.2	< 0.5	< 1	< 1	17	38	45	...	..	14.3	...	..	...	....
62	−1.″47	9.″26	11.1	21.5	145	338	295	271	365	...	..	13.3	0.00	12.4	0	39.2
63	3.″92	9.″21	42.2	21.5	122	198	169	128	41	...	..	19.6	12.62	−0.6	2	36.3
64	7.″67	9.″56	< 0.2	...	6	28	38	32	< 1	...	..	19.7	...	..	...	....
65	−3.″11	9.″62	0.3	1.0	11	68	68	62	27	...	..	25.6	0.02	10.1	11	39.2
66	0.″02	10.″17	0.4	1.5	16	27	37	27	8	...	..	27.9	...	..	...	....

67	−1.″83	10.″39	1.1	2.5	25	71	78	64	< 1	...	..	22.9	...	..	...	....
68	3.″39	10.″45	< 0.2	< 0.5	25	51	77	78	18	...	..	15.9	0.01	11.0	3	39.3
69	0.″54	10.″65	< 0.2	< 0.5	5	31	54	43	20	...	..	28.6	...	..	...	....
70	−3.″80	11.″27	2.3	...	131	215	202	166	86	...	..	11.6	0.08	7.6	1	38.7
71	−1.″76	11.″31	< 0.2	...	40	172	192	155	34	...	..	13.1	0.05	8.5	5	38.9
72	−11.″90	15.″80	< 0.2	...	< 1	..	..	..	< 1	...	..	< 9.1	...	..	...	....
73	14.″83	15.″80	< 0.2	...	< 1	..	..	..	< 1	...	..	< 9.1	...	..	...	....
⋆	0.″00	0.″00	31.4	64.3	276	1380	1697	1837	1605	1.4×10^4	3.3×10^4	12.3	2.03	2.3	96	39.2

3.2.3 NGC 1386

NGC 1386 is an Sa galaxy located at 15.3 Mpc (Jensen et al. 2003), although its morphology and situation has been a matter of debate. Several authors favour the S0 classification (de Vaucouleurs 1963), while some others assume an Sa type due to the presence of star-forming knots in the central region (Corwin 1968; Weaver et al. 1991), or even an SB0+ classification (Tsvetanov & Petrosian 1995), although there are no clear indications for the existence of a bar (see Fig. 3.5). Moreover, there is some confusion whether this galaxy belongs to the Fornax cluster or not (see Rossa et al. 2000, and references therein). Fig. 3.5 reveals an apparent early type galaxy with some FUV and IR excess in a central disk-like structure. At high-spatial resolution, this results in a $\sim$ 1 kpc circumnuclear ring ($PA = 35^\circ$) with an ellipticity that rises from $\sim$ 0.25 at 8″–10″ to $\sim$ 0.4–0.5 at 15″ (Ferruit et al. 2000). *Ks*-band image in Fig. 3.5 reveals a boxy shaped ring with increasing ellipticity in the inner $5'' \times 5''$. The ring is covered by dust lines with typical $E(B-V) \sim 0.1$–0.3 mag, with a very reddened northwest side when compared to the southeast side [$E(B-V) \sim 0.6$ mag], suggesting that the former is the nearest part of the ring (Ferruit et al. 2000). Our alignment (see Sec. 2.3.2) shows that the active nucleus is only visible longwards of 2 μm and dominates the emission from *L* to *Q*-band at $\sim$ 20 μm, in agreement with the location of the kinematical centre found 0.″6 northeast of the Hα+[N II] and the [O III] maximum, within a dust lane (Schulz & Henkel 2003). A number of point-like knots are detected in the ring, probably associated with the FUV emission, thus suggesting recent star-formation activity. The radio emission consist basically on a compact core with extended emission at $PA = 170^\circ$ (Ulvestad & Wilson 1984; Nagar et al. 1999), as can be seen in the 8.4 GHz image (bottom-right panel in Fig. 3.5) where a tiny jet-like extension is located south of the nucleus. A strong H_2O megamaser ($\sim 210\,L_\odot$ at a distance of 15.3 Mpc) has also been detected in the nuclear region (Braatz et al. 1996). None of the regions in the ring are detected, but this may be due to a lack of sensitivity in the radio image.

In the centre of the ring, the galaxy hosts a Seyfert 2 nucleus which shows a very high optical-excitation narrow emission-line spectrum, although its luminosity in the optical emission-lines is considerably less than those of other Seyferts 2 (Phillips & Frogel 1980). Nevertheless, spatially unresolved IR coronal lines such as [Si VI], [Ca VIII] and [Si VII] and north–south extended coronal optical emission in [Fe VII], [Fe X] and [Fe XI] have been detected in NGC 1386 (Reunanen et al. 2002; Rodríguez-Ardila et al. 2006). Bennert et al. (2006) report a transition of emission-line ratios from the central AGN region to the surrounding H II ring at $\sim 6''$ ($\sim$ 450 pc) to the north and south of the active nucleus. This is probably caused by a string of emission regions in Hα+[N II] and [O III] that take up the central 6″ aligned in the north-south direction,

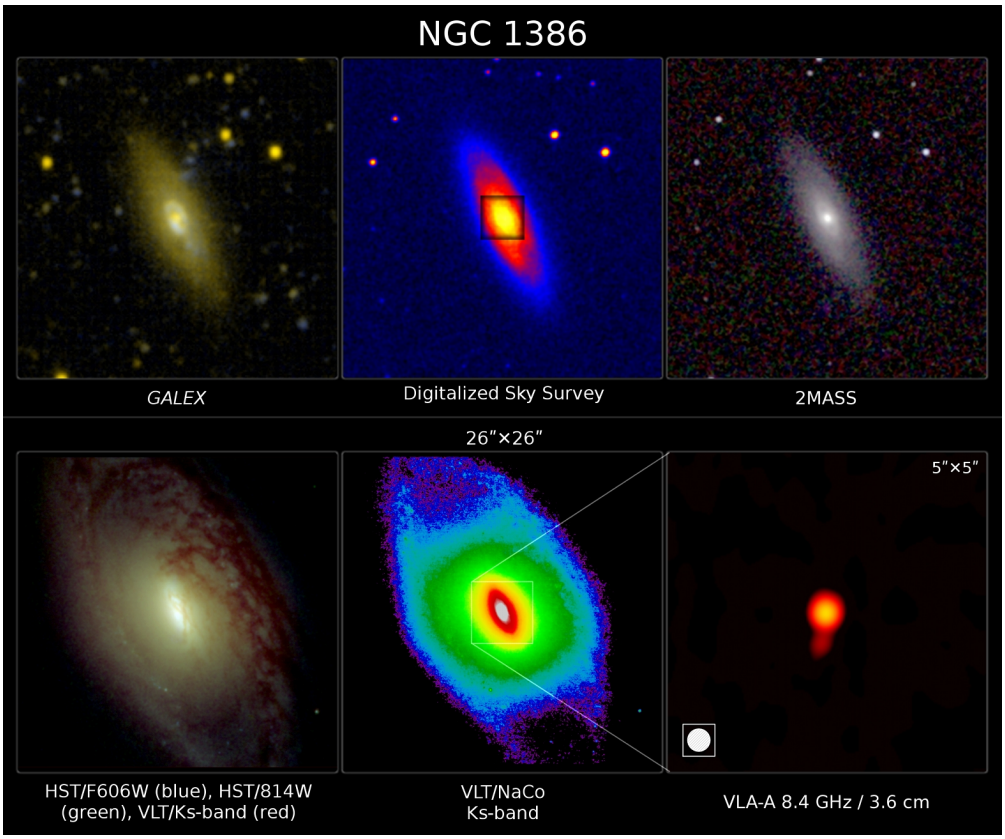

FIGURE 3.5— NGC 1386 at optical, infrared and radio wavelengths (North is up and East is to the left). The upper panels correspond to different views (UV, optical, NIR) at large scale and cover the same field of view. Lower-left and centre panels correspond to the black box region ($26'' \times 26''$) in the DSS image. The radio map on the lower-right panel corresponds to the central $5'' \times 5''$.

thus forming a double-sided NLR that Rossa et al. (2000) resolve in 9 individual components (5 redshifted and 4 blueshifted from the systemic velocity). The line emission is also extended in the east–west direction, but only $1''$ (75 pc), forming a kind of crossed-shaped ionized region with a brighter "plume" of emission on east side (Ferruit et al. 2000). Furthermore, extended 1–0 S(1) H_2 emission is detected parallel to the ionization cone, $4\farcs5$ (330 pc) toward the north and $3\farcs5$ (260 pc) towards the south (Reunanen et al. 2002). These authors also measured a high ratio of [Fe II]/Br$\gamma \sim 1.7$, pointing to the X-rays as the excitation mechanism for the nebular gas in the nucleus. The extended H_2 component has no Brγ emission, which suggest that it is shock-heated. This is further supported by the spectra presented by Phillips & Frogel (1980) and Schulz & Henkel (2003) for the NLR, where the $[\mathrm{N\,II}]_{\lambda 6583}$ line clearly dominates

the Hα+[N II] blend ([N II]/H$\alpha \approx 1.5$). In X-rays NGC 1386 appears as a Low-Luminosity AGN (LLAGN), with an absorption corrected 2–10 keV luminosity of 1.8×10^{40} erg s^{-1} and a column density of $N_H = 2.8 \times 10^{23}$ cm^{-2} (Iyomoto et al. 1997).

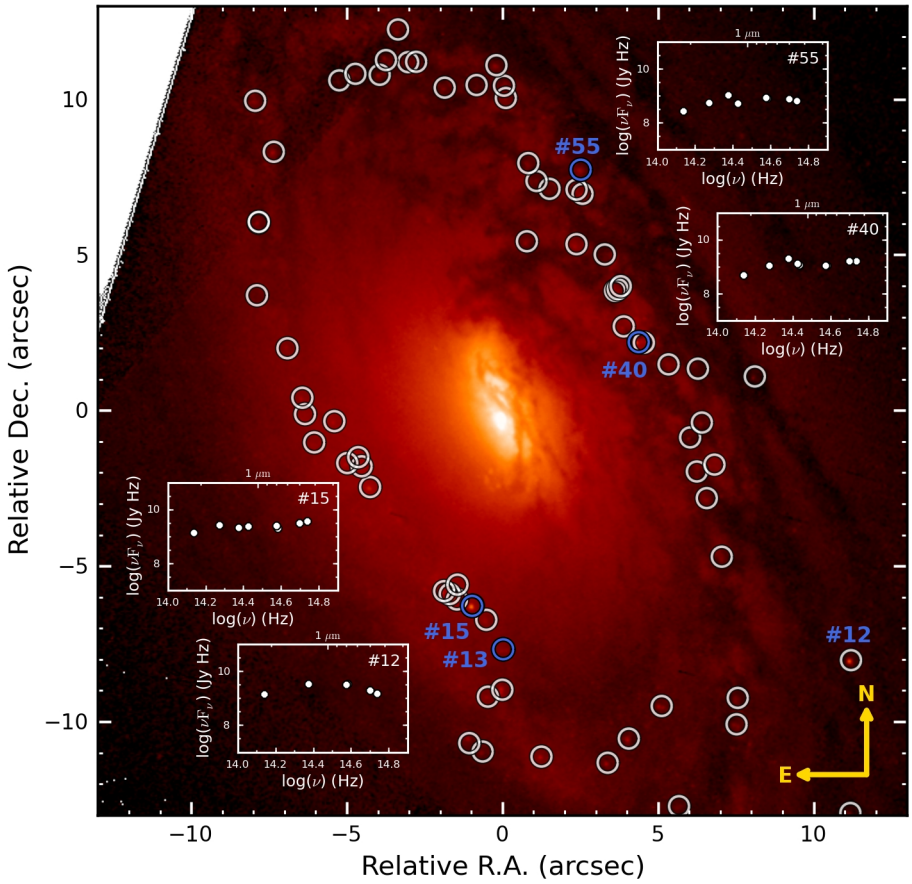

FIGURE 3.6— *HST*/F606W image of the central $26'' \times 26''$ in NGC 1386. The 71 knots identified in this galaxy are marked and we also show the SEDs in the optical-IR range for a representative sample of 4 of them.

As mentioned before, the central region of NGC 1386 consist basically on a ~ 1.9 kpc diameter nuclear ring with an inclination of about $\sim 55^\circ$ partially covered by dust lanes (Fig. 3.6). A total of 70 point-like sources were visually identified distributed along the star-forming ring in the F606W, F658N and *Ks*-bands. We opted for a visual identification instead an analytical method, e.g. DAOPHOT, due to the

faintness of the majority of the knots with respect to the diffuse galaxy background. The asymmetries in the ring, produced by the obscuring dust lanes, did not permit a reliable 2D modelling and subtraction as in the case of NGC 7582 (see Section 2.3.3). No point-like sources were detected inside the ring, i.e. the inner $r \sim 4''$ (~ 300 pc), where the nuclear activity is highlighted by the bright emission-line plumes detected in Hα+[N II] and [O III], the strong H_2O megamaser and the tiny jet-like radio structure (Fig. 3.5, Ferruit et al. 2000; Braatz et al. 1996; Nagar et al. 1999).

The knots present a median half-light radius of 18.4 pc in the K-band ($D = 15.3$ Mpc, $\mathrm{FWHM_{inst}} = 0\farcs09 \approx 6.7$ pc). Although the median size is nearly three times greater than the spatial resolution, the images in Figs 2.5 and 3.6 suggest that most of the knots are not resolved, but are very faint when compared with the diffuse stellar light of the galaxy and the circumnuclear ring. Moreover, their median brightness in the K-band is $m_K = 22.1$ mag, corresponding to $M_K = -8.9$ mag, i.e. the lowest luminosity knots among the galaxies of our sample. Their faintness suggests that the diffuse component alters the measurement of the FWHM and these should be adopted as upper limits for the faintest knots. From the K-band luminosity, we derive a median mass of $1.5 \times 10^3\,\mathrm{M}_\odot$. For stellar clusters with such a low mass value, the stochastic effects from single stars cannot be negligible, and thus the mass-luminosity relation that we adopted may not behave reliably (Cerviño & Valls-Gabaud 2009). Considering their median W(Hα) ~ 70.9 Å, we estimate ages of about 6.3 Myr, as expected for a young starburst ring with FUV emission (see Fig. 3.5, upper-left panel). However, the brightness and $L_{\mathrm{H}\alpha}$ of the knots can be also explained in terms of single massive stars and we cannot rule out this possibility. Nevertheless, this would imply a very low star-formation density with only one star for each ~ 6.7 pc.

TABLE 3.3— Main characteristics of the knots found in NGC 1386. The relative error (δ) for each magnitude is: $\delta(F547M) = 22\%$, $\delta(F606W) = 16\%$, $\delta(F791W) = 34\%$, $\delta(F814W) = 31\%$, $\delta(F110M) = 18\%$, $\delta(F110W) = 22\%$, $\delta(J) = 9\%$, $\delta(F160W) = 22\%$, $\delta(Ks) = 15\%$, $\delta[W(\mathrm{H}\alpha)] = 39\%$ and $\delta(L_{\mathrm{H}\alpha}) = 23\%$. *L'*, *N* and *Q*-bands are not included due to the absence of sources but the nucleus in these images, probably below the 3σ limit of ~ 0.3, 4 and 20 mJy, respectively. Relative R.A. and Dec. correspond to the shift in equatorial coordinates with respect to active nucleus ($\star$). The size column corresponds to the half-light radius ($\mathrm{FWHM_{obs}}$).

#	Relative		F547M	F606W	F791W	F814W	F110M	F110W	*J*	F160W	*Ks*	Size	W(Hα)	log($L_{\mathrm{H}\alpha}$)
	R.A.	Dec.	[μJy]									[pc]	[Å]	[erg s^{-1}]
0	11.″18	−12.″93	0.5	0.6	0.5	1.1	...	...	...	...	...	...	10	34.9
1	5.″67	−12.″71	0.5	0.7	0.5	0.7	...	...	...	...	...	...	410	36.7
2	3.″38	−11.″32	0.7	0.9	0.4	0.4	...	...	0.5	...	0.5	< 6.7	20	35.6
3	1.″25	−11.″12	1.3	1.4	0.8	0.5	...	...	1.7	...	0.3	7.2	40	36.0
4	−0.″64	−10.″96	0.3	0.5	< 0.3	< 0.3	...	...	< 0.2	...	< 0.2	< 6.7	...	....
5	−1.″07	−10.″69	0.5	0.5	1.0	0.9	...	...	1.9	...	0.5	< 6.7	130	36.2
6	4.″06	−10.″54	1.5	1.5	0.9	1.0	...	...	0.7	...	1.2	< 6.7	130	36.5
7	7.″52	−10.″08	0.4	0.7	< 0.3	0.4	...	4	0.7	1	0.5	< 6.7	150	36.4
8	5.″11	−9.″50	1.1	1.0	1.3	0.8	...	< 2	0.5	< 1	< 0.2	< 6.7	60	36.1
9	7.″56	−9.″23	0.6	0.5	0.8	0.4	...	2	0.6	2	2.2	10.1	620	36.9
10	−0.″47	−9.″20	0.5	0.8	1.1	0.5	...	...	2.7	...	0.7	16.7	70	36.1
11	−0.″01	−8.″97	2.5	2.6	1.2	1.6	...	...	1.4	...	0.3	7.2	40	36.2
12	11.″20	−8.″02	2.7	4.0	9.1	8.8	...	...	14.7	...	10.5	7.9	40	36.6
13	0.″02	−7.″67	0.7	1.0	0.5	1.0	...	3	3.9	5	2.0	14.3	80	36.1
14	−0.″52	−6.″73	0.6	0.7	1.0	0.8	...	< 2	4.7	1	1.4	< 6.7	40	35.8
15	−0.″97	−6.″28	6.7	6.3	5.4	6.7	...	9	8.9	16	9.8	8.2	10	36.1
16	−0.″96	−6.″27	5.9	5.4	4.6	5.8	...	9	8.7	16	9.0	8.2	20	36.3
17	−1.″46	−6.″07	3.2	3.5	2.0	1.2	...	2	2.2	2	1.4	17.3	...	....
18	−1.″70	−5.″90	1.1	1.1	0.8	1.2	...	3	2.5	2	0.8	13.4	0	34.7
19	−1.″88	−5.″80	1.7	1.5	1.4	1.3	...	3	1.7	1	< 0.2	6.8	20	35.7
20	−1.″45	−5.″60	< 0.2	< 0.2	< 0.3	< 0.3	...	2	3.3	3	0.8	8.2	...	....
21	7.″05	−4.″70	0.7	0.8	0.5	0.6	...	< 2	0.6	< 1	< 0.2	84.4	320	36.7
22	6.″56	−2.″82	0.8	0.8	0.7	1.4	...	5	3.4	3	1.0	181.9	270	36.6
23	−4.″25	−2.″46	1.9	2.1	2.5	2.1	3.6	6	2.7	6	2.0	67.8	30	36.2
24	6.″24	−1.″96	0.3	< 0.2	< 0.3	< 0.3	...	< 2	< 0.2	< 1	< 0.2	172.2	870	36.7
25	−4.″53	−1.″79	1.1	1.3	1.6	1.5	3.1	5	3.2	3	1.2	111.7	230	36.8
26	6.″81	−1.″74	1.1	1.1	1.5	1.5	...	4	5.7	3	0.9	185.7	150	36.5
27	−4.″99	−1.″69	0.5	1.0	0.7	1.1	2.2	2	3.2	3	0.4	139.8	140	36.4
28	−4.″63	−1.″50	0.8	1.0	1.3	0.9	3.3	< 2	1.2	< 1	< 0.2	104.0	170	36.6
29	−6.″05	−1.″03	< 0.2	< 0.2	< 0.3	0.9	...	2	< 0.2	< 1	< 0.2	182.8	960	36.7

30	6.″03	−0.″87	0.3	< 0.2	< 0.3	< 0.3	< 0.3	< 2	2.0	< 1	< 0.2	159.6	...	....
31	6.″41	−0.″39	0.4	0.4	< 0.3	< 0.3	...	20	1.7	2	1.0	168.8	...	....
32	−5.″40	−0.″34	0.7	0.8	0.6	0.5	...	< 2	5.4	3	0.9	164.7	10	35.3
33	−6.″34	−0.″12	0.6	0.4	1.3	0.6	...	4	1.9	3	0.8	158.6	20	35.3
34	−6.″43	0.″41	0.7	0.8	0.6	0.8	...	< 2	< 0.2	< 1	< 0.2	144.2	50	35.9
35	8.″11	1.″09	0.4	0.4	< 0.3	< 0.3	...	2	< 0.2	< 1	< 0.2	< 6.7	...	....
36	6.″28	1.″34	< 0.2	< 0.2	< 0.3	< 0.3	< 0.3	< 2	4.8	4	2.7	176.0	70	35.6
37	5.″34	1.″48	1.0	1.2	1.1	1.4	4.5	3	3.7	6	1.4	153.4	180	36.6
38	−6.″91	2.″00	0.5	0.5	0.5	0.6	...	< 2	1.0	2	0.5	192.5	20	35.3
39	4.″54	2.″18	1.8	2.7	1.9	2.5	7.0	8	11.7	8	3.3	103.6	270	37.1
40	4.″38	2.″20	3.2	3.6	3.0	3.1	5.0	5	8.5	6	3.5	89.0	140	37.0
41	3.″90	2.″70	0.3	< 0.2	< 0.3	0.4	4.0	2	2.9	4	1.0	65.0	...	....
42	−7.″89	3.″70	< 0.2	< 0.2	< 0.3	< 0.3	...	< 2	0.5	< 1	0.2	14.0	...	....
43	3.″62	3.″85	1.6	1.8	2.1	2.3	7.7	4	5.7	7	3.2	71.8	50	36.3
44	3.″71	3.″90	1.0	1.2	1.0	1.7	4.9	4	5.7	6	3.3	97.4	70	36.2
45	3.″80	3.″99	0.4	0.4	< 0.3	1.1	1.5	2	3.9	1	0.9	104.7	...	....
46	3.″29	5.″01	< 0.2	< 0.2	< 0.3	< 0.3	< 0.3	< 2	< 0.2	< 1	< 0.2	116.7	1160	36.8
47	2.″38	5.″34	1.4	1.7	1.6	1.9	7.2	5	6.7	5	1.6	114.7	20	35.8
48	0.″78	5.″44	0.8	1.1	0.9	1.6	15.1	< 2	1.6	4	0.7	117.4	80	36.2
49	−7.″84	6.″04	0.3	0.7	0.9	1.8	...	...	4.0	13	3.0	9.6	0	34.5
50	−7.″83	6.″06	0.2	0.6	0.5	1.7	...	...	3.9	...	2.3	9.6	20	35.4
51	2.″57	6.″96	1.8	1.6	2.0	1.6	...	3	2.9	3	1.0	107.9	30	36.0
52	2.″38	7.″10	1.0	1.3	1.0	1.1	...	< 2	3.4	1	1.0	134.2	20	35.6
53	1.″51	7.″12	0.4	< 0.2	< 0.3	< 0.3	...	< 2	0.5	2	0.2	155.8	...	....
54	1.″09	7.″37	0.2	0.5	< 0.3	< 0.3	...	< 2	< 0.2	< 1	< 0.2	167.9	1010	37.0
55	2.″51	7.″74	1.4	1.8	2.1	2.4	...	2	4.5	4	2.0	144.5	20	35.8
56	0.″83	7.″95	0.2	< 0.2	< 0.3	< 0.3	...	< 2	< 0.2	< 1	< 0.2	178.3	...	....
57	−7.″35	8.″31	1.4	1.6	1.6	2.5	...	4	4.6	...	2.3	12.0	10	35.4
58	−7.″95	9.″95	1.1	1.0	1.3	0.7	...	...	2.5	...	1.0	21.3	110	36.4
59	0.″11	10.″04	0.8	1.0	1.0	1.0	...	177	2.6	...	0.6	8.2	20	35.7
60	−1.″86	10.″37	0.5	0.7	1.1	0.9	...	199	1.6	330	1.1	15.9	70	36.0
61	0.″05	10.″44	0.8	0.8	0.5	0.6	...	...	2.7	...	0.8	9.9	80	36.1
62	−5.″24	10.″61	0.3	0.3	< 0.3	< 0.3	...	< 2	< 0.2	1	0.8	8.8	680	36.7
63	−3.″95	10.″79	1.1	1.1	0.9	1.3	...	...	1.2	...	0.5	< 6.7	10	35.4
64	−4.″73	10.″82	0.5	0.7	0.8	0.8	...	...	2.1	< 1	0.3	7.5	90	36.1
65	−0.″19	11.″09	1.2	1.3	1.3	1.7	...	...	3.3	...	1.0	19.5	...	....
66	−3.″03	11.″19	0.8	0.9	1.3	1.6	...	...	3.6	...	1.6	13.4	80	36.2
67	−2.″77	11.″20	0.6	0.8	1.3	0.9	...	...	2.0	...	1.0	10.6	110	36.3
68	−3.″74	11.″26	0.7	1.0	0.7	1.2	...	...	1.4	...	< 0.2	9.1	130	36.4

69	$-3\overset{''}{.}36$	$12\overset{''}{.}24$	0.5	0.5	0.9	1.1	...	...	5.9	...	0.5	< 6.7	80	36.0
$\star$	$0\overset{''}{.}00$	$0\overset{''}{.}00$	13.5	21.5	50.9	60.7	295.1	313	469.3	527	483.9	20.9	590	38.5

3.2.4 NGC 1052

This is an elliptical galaxy (E4) located at 18.0 Mpc (Jensen et al. 2003) with a stellar mass of $M_\star \sim 10^{11}\,M_\odot$ (derived from 2MASS[2] photometry, assuming $M_\star/L_K = 1.32\,M_\odot/L_\odot$, Cole et al. 2001). This objects is often considered to be the prototypical LINER (Low-Ionization Nuclear Emission-line Region), and was the primary motivator for the classification of similar galaxies as shock-heated (Koski & Osterbrock 1976; Fosbury et al. 1978; Heckman 1980; Ho et al. 1997). At large scale, the radio continuum emission consist of a compact, variable, flat-spectrum core together with two asymmetric lobes with $PA = 95°$ enclosed within the optical galaxy (Wrobel 1984). The diffuse extended X-ray emission at 0.1–1 keV is also well aligned with the large-scale radio lobes, suggesting that jet-triggered shocks might play an important role in this galaxy (Kadler et al. 2004). UV observations reveal a bright nucleus and a spectrum consisting of narrow lines on top of a featureless continuum (Fosbury et al. 1981; Allen et al. 1999; Gabel et al. 2000). At higher resolution, VLBI mapping reveals that the compact core exhibit an elongated structure with a ~ 0.9 pc extension along $PA \sim 65°$ (Jones et al. 1984). The jet axis seems nearly parallel to the sky plane, showing proper motion and structural evolution in both sides (Sawada-Satoh et al. 2008). Moreover, a new nuclear component appeared between the eastern and western jets (Kameno et al. 2001). In the innermost part, VLBI observations revealed the presence of a luminous H_2O megamaser ($L_{maser} \sim 200\,L_\odot$) redshifted by 50–350 km s^{-1} with a broad velocity width of ~ 100 km s^{-1}. The maser spots consist of two clusters distributed along the jet axis, rather than perpendicular to it, spanning ~ 0.1 pc (Braatz et al. 1994, 2003; Claussen et al. 1998; Sawada-Satoh et al. 2008).

Upper panels in Fig. 3.7 show a featureless spheroid with an IR point-source in the nucleus, in contrast with the images at high-spatial resolution (lower panels) which reveal a number of features: an emission-line biconical structure with $PA \sim 96°$ in the F658N image (including Hα+[N II]) aligned with the kpc-scale radio lobes (Pogge et al. 2000), some knots with stellar cluster appearance and a radio jet. The cones are indeed aligned with the radio structure at large scale. NGC 1052 belongs to a group (de Vaucouleurs et al. 1976; Fosbury et al. 1978) and shows many evidences for being involved in a recent merger: H I absorption redshifted on the nucleus (infalling H I gas), two tidal tails indicative of a gaseous merger about 1 Gyr ago (van Gorkom et al. 1986), a misalignment between the rotation axes of the H I and the ionized gas ($PA =$ 134° and 125°–131°, respectively) and the stellar rotation axis ($PA = 28°$), suggesting that the gas has an external origin (van Gorkom et al. 1986, 1989; Forbes et al. 2001), and a bimodal colour distribution for the Globular Cluster (GC) system (Forbes et al. 2001; Pierce et al. 2005). Furthermore, the presence of dust lanes perpendicular to

[2] 2 Micron All Sky Survey, see `http://www.ipac.caltech.edu/2mass/`

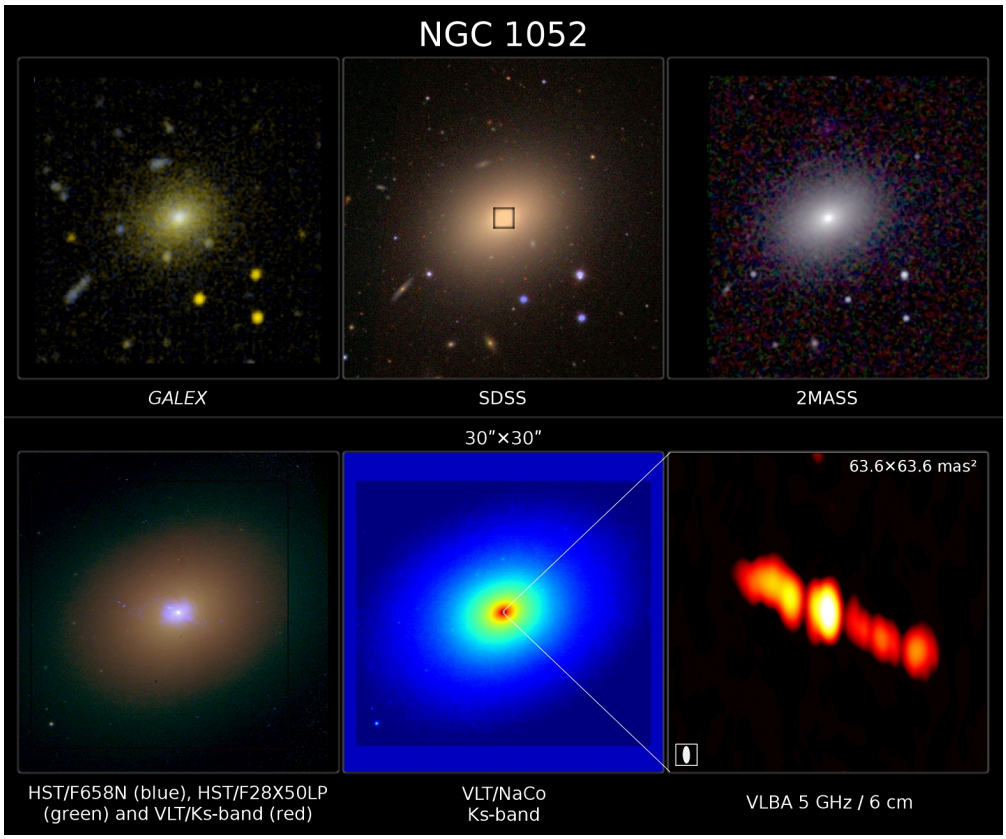

FIGURE 3.7— NGC 1052 at optical, infrared and radio wavelengths (North is up and East is to the left). The upper panels correspond to different views (UV, optical, NIR) at large scale and cover the same field of view. Lower-left and centre panels correspond to the black box region ($30'' \times 30''$) in the SDSS image. The VLBA radio map on the lower-right panel corresponds to the inner $63.6 \times 63.6\,\mathrm{mas}^2$.

the radio jet and near the galaxy centre have been detected in optical images (Carter et al. 1983; Wrobel 1984; Forbes et al. 1990). The detection of a broad polarized Hα emission line with FWHM $\approx 5000\,\mathrm{km\,s^{-1}}$ (Barth et al. 1999) and a broad component in the Hβ emission line which extends to $\pm$2000–3000 $\mathrm{km\,s^{-1}}$ (Sugai et al. 2005) hints for the existence of a broad–line region. The former suggest the presence of an obscuring structure close to the compact core of this galaxy, which is highly reddened in the inner $82 \times 82\,\mathrm{pc}^2$ ($E(B-V) = 0.42\,\mathrm{mag}$, Gabel et al. 2000) and shows OH molecular line absorption at 13.4 GHz (Impellizzeri et al. 2008). Moreover, the presence of masers on both jets states for a torus thickness along the jet axis of about $\gtrsim 0.2\,\mathrm{pc}$ (Sawada-Satoh et al. 2008). X-ray observations reveal a nuclear source with a 2–10 keV luminosity of about $\sim 4 \times 10^{41}\,\mathrm{erg\,s^{-1}}$ absorbed by a high column density of $N_H \gtrsim 3 \times 10^{23}\,\mathrm{cm^{-2}}$,

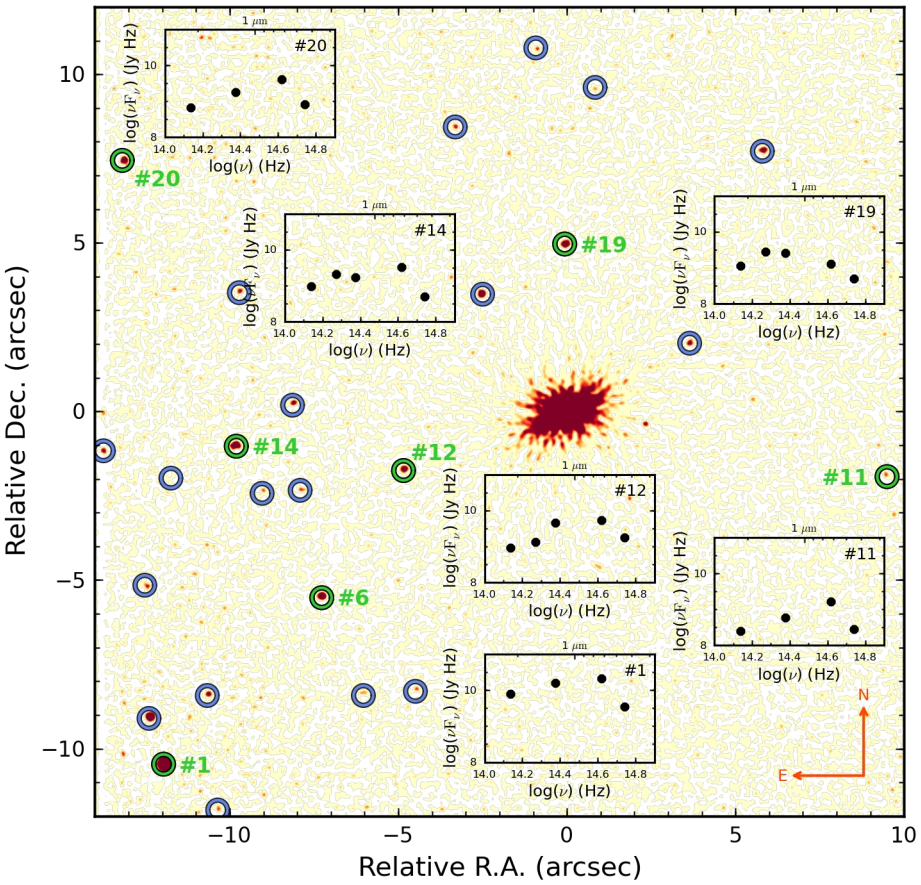

FIGURE 3.8— Unsharp-masked *Ks*-band image of the central $24'' \times 24''$ in NGC 1052. The 25 knots identified in this galaxy are marked and we also show the SEDs in the optical-IR range for a representative sample of 6 of them.

also supporting the existence of a dense gas torus (Weaver et al. 1999).

Unlike the majority of the galaxies in this study, which are spirals, the host of this active galactic nuclei is an elliptical galaxy and thus presents significant differences with the rest of the sample. First of all, this is the only object without any known star-forming structure close to the active nucleus, although Pierce et al. (2005) identified signs for the presence of an intermediate-age population (~ 2 Gyr) in the central $10''$. The VLT/NaCo *Ks*-band image revealed the presence of a randomly distributed number of point-like sources in the inner $30'' \times 30''$, over the profile of the elliptical galaxy. Two of them (knots #6 and #9) were found to be common to all filters

and were used for the alignment of the dataset, avoiding the AGN source which is apparently obscured as mentioned before. Then, an unsharp-masked *Ks*-band image was obtained (see Section 2.3.3) using a median circular filter with $r \sim 0\farcs12$, in order to enhance the rest of the knots in the field (Fig. 3.8). A total of 25 knots were found spread over the central $30'' \times 30''$, still without a clear association or defined structure. The only exception is the south-west quadrant in Fig. 3.8 where only one knot was detected. Surprisingly, 15 of the total 25 knots exhibit emission in Hα after continuum subtraction, indicative of a very young stellar population ($\lesssim 10$ Myr). Since a previous study by Pierce et al. (2005) only revealed old globular clusters in the outskirts of NGC 1052 (~ 13 Gyr), we will analyze in depth the case for this knots in Section 5.3. However, their individual SEDs in Fig. 3.8 apparently differ from those in NGC 253, some of them peaking in the STIS band at $\sim 0.72\,\mu$m (e.g. knots #1, #11 and #20) and some others showing a more irregular behaviour (knot #14).

The majority of the knots have half-light radius of about 13.9 pc ($D = 18.0$ Mpc, $\mathrm{FWHM_{inst}} = 0\farcs12 \approx 10.5$ pc), based on the VLT/NaCo *Ks*-band image. Their median brightness, $m_K = 20.9$ mag, turns out in an absolute magnitude of $M_K = -10.4$ mag, discarding the possibility of being foreground stars (Tabur et al. 2009). All are distributed in the $-12 \leq M_K \leq -9$ mag range except the knot #1, which is the brightest with $M_{K_{\#1}} = -13.6$ mag, leaving aside the nucleus. The knots show also a median $J-K$ colour of about 0.4 mag. Assuming a mass-luminosity ratio for young clusters as in the case of NGC 253, we estimate a median mass for the knots of about $\sim 4 \times 10^3\,\mathrm{M_\odot}$, based on the *K*-band luminosity.

TABLE 3.4— Main characteristics of the knots found in NGC 1052. The relative error (δ) for each magnitude is: $\delta(F555W) = 19\%$, $\delta(F28X50LP) = 12\%$, $\delta(J) = 8\%$, $\delta(F160W) = 25\%$, $\delta(Ks) = 11\%$, $\delta[W(\mathrm{H}\alpha)] = 39\%$ and $\delta(L_{\mathrm{H}\alpha}) = 31\%$. L'-band is not included due to the absence of knots above a 3σ limit of ~ 0.3 mJy. Relative R.A. and Dec. correspond to the shift in equatorial coordinates with respect to the active nucleus ($\star$). The size column corresponds to the half-light radius ($\mathrm{FWHM_{obs}}$).

#	Relative		F555W	F28X50LP	*J*	F160W	*Ks*	Size	W(Hα)	log($L_{\mathrm{H}\alpha}$)
	R.A.	Dec.			[μJy]			[pc]	[Å]	[erg s^{-1}]
0	$-10\farcs36$	$-11\farcs82$	0.4	3	4.5	...	2.5	< 10.5	80	36.2
1	$-11\farcs96$	$-10\farcs46$	6.3	52	66.5	...	56.9	11.3	120	37.5
2	$-12\farcs40$	$-9\farcs10$	0.6	6	8.7	...	8.4	< 10.5	180	36.7
3	$-10\farcs67$	$-8\farcs42$	0.3	3	3.3	< 2	3.5	< 10.5	...	....
4	$-6\farcs04$	$-8\farcs42$	< 0.2	1	2.3	< 2	2.0	18.9	...	....
5	$-4\farcs49$	$-8\farcs30$	< 0.2	2	3.2	3	1.9	19.8	130	36.1
6	$-7\farcs27$	$-5\farcs52$	1.1	6	8.6	11	6.6	13.3	120	36.7
7	$-12\farcs52$	$-5\farcs15$	1.4	11	7.6	...	2.9	< 10.5	110	36.8
8	$-9\farcs04$	$-2\farcs43$	0.5	2	3.8	6	1.9	14.9	...	....
9	$-7\farcs91$	$-2\farcs34$	0.7	4	5.8	6	2.2	245.5	10	35.5
10	$-11\farcs75$	$-1\farcs98$	< 0.2	< 1	1.3	...	0.9	< 10.5	10	35.0
11	$9\farcs49$	$-1\farcs93$	0.5	4	2.5	...	1.7	18.5	200	36.6
12	$-4\farcs85$	$-1\farcs75$	3.2	13	18.7	17	6.7	173.4	30	36.5
13	$-13\farcs75$	$-1\farcs17$	< 0.2	2	< 0.2	...	7.2	< 10.5	220	36.2
14	$-9\farcs81$	$-1\farcs03$	0.9	8	7.3	12	7.0	14.9	180	36.8
15	$-8\farcs14$	$0\farcs19$	< 0.2	4	4.0	5	2.3	243.7	...	....
16	$3\farcs64$	$2\farcs02$	3.9	18	21.8	23	9.7	114.9	10	35.8
17	$-2\farcs50$	$3\farcs48$	2.9	14	15.5	19	8.1	97.0	10	35.8
18	$-9\farcs72$	$3\farcs52$	0.7	6	4.7	7	2.9	11.3	80	36.4
19	$-0\farcs07$	$4\farcs97$	0.9	3	10.6	15	8.2	164.1	110	36.6
20	$-13\farcs19$	$7\farcs45$	1.5	10	7.7	...	4.8	< 10.5	110	36.8
21	$5\farcs80$	$7\farcs72$	0.9	5	5.4	< 2	4.2	18.7	40	36.2
22	$-3\farcs31$	$8\farcs44$	0.4	3	4.2	8	2.4	< 10.5	250	36.6
23	$0\farcs84$	$9\farcs61$	< 0.2	2	2.9	...	2.4	11.6	160	36.2
24	$-0\farcs92$	$10\farcs78$	0.4	4	3.7	...	2.0	< 10.5	110	36.3
$\star$	$0\farcs00$	$0\farcs00$	109.8	1146	1388.9	2692	1599.3	14.4	890	39.7

3.2.5 NGC 7582

Located at 19.9 Mpc (Terry et al. 2002), this object belongs to the Grus Quartet, an association of four interacting spiral galaxies (NGC 7552, NGC 7582, NGC 7590 and NGC 7599), as shown by the H I maps of Dahlem (2005). Three of them present X-ray emission, but NGC 7582 is the dominant source in the hard band (2–10 keV), with such a rapid variability that requires the presence of an AGN source (Schachter et al. 1998; Piconcelli et al. 2007). The high luminosity in this spectral region –typical of a Seyfert 1 nucleus (Ward et al. 1980; Morris et al. 1985)–, together with the lack of broad emission lines in the nuclear optical spectra, suggests that this is a Narrow Emission Line Galaxy (NELG). Top panels in Fig. 3.9 show a highly inclined ($i \sim 65^\circ$) spiral

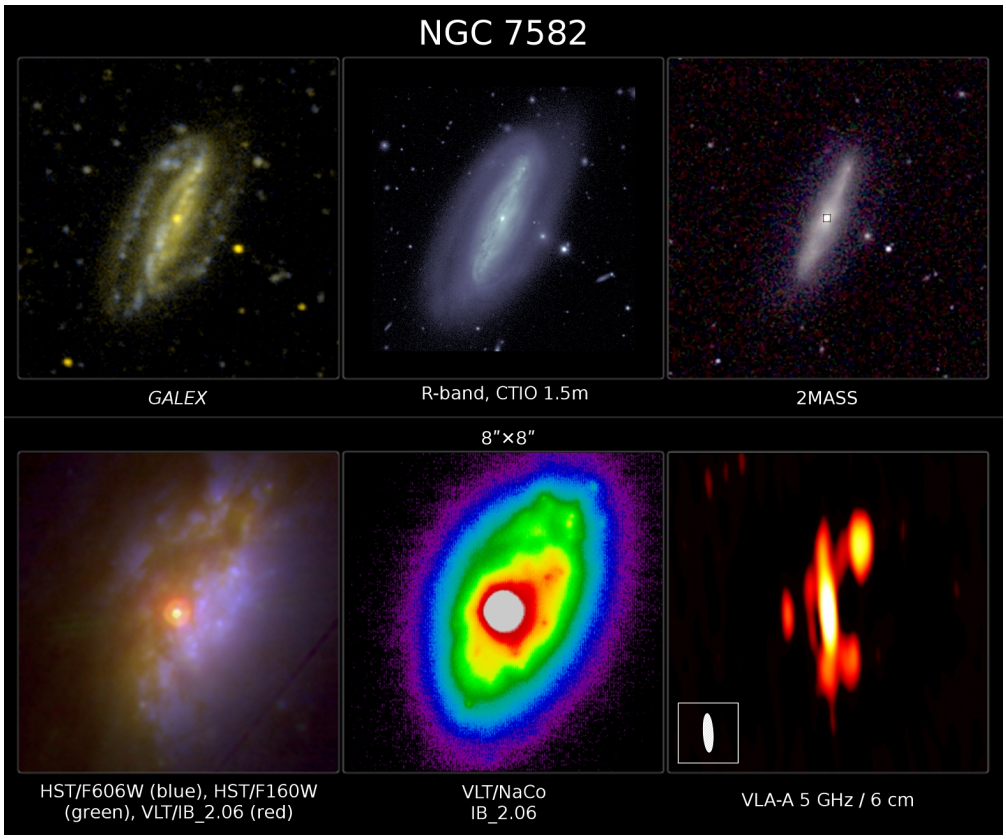

FIGURE 3.9— NGC 7582 at optical, infrared and radio wavelengths (North is up and East is to the left). The upper panels correspond to different views (UV, optical, NIR) at large scale and cover the same field of view. Lower panels correspond to the black box region ($8'' \times 8''$) in the 2MASS image.

galaxy with a stellar bar ($PA = 165^\circ$) that almost covers the full extension of the galaxy

major axis. The morphology in these ranges is dominated by dust lanes distributed in the disk and the bar. Morris et al. (1985), Cid Fernandes et al. (1998) and Sosa-Brito et al. (2001) reported a superposition of the Seyfert 2 nucleus and a starburst spectra, although the former is almost hidden in the optical range. A mixed nuclear emission is also suggested from the analysis of the MIR to far-infrared (FIR) emission (Radovich et al. 1999). Although this object is five times farther than NGC 253, the central region is pretty similar for both objects: a strong IR nucleus –almost hidden in the optical– surrounded by a compact starburst component (bottom panel in Fig. 3.9), i.e. a number of H II regions distributed around the nucleus in a ~ 0.5 kpc diameter disk (Morris et al. 1985; Wold & Galliano 2006). The latter also contributes to the soft X-ray extended emission (0.2–2.0 keV, Levenson et al. 2001; Dong et al. 2004). Moreover, Claussen & Sahai (1992) reported an intrinsic asymmetry of the molecular gas distribution in the nucleus that may correspond to the disk, since the presence of molecular material is usually associated with H II regions.

This galaxy shows evidences for being a type 2 nucleus, although Aretxaga et al. (1999) reported a transition towards a typical type 1 Seyfert when NGC 7582 developed temporarily broad permitted lines. In spite of this, there is no evidence of a hidden broad line region in polarized light (Heisler et al. 1997), but a persistent broad Brγ component ($\sim 4000\,\mathrm{km\,s^{-1}}$) appeared just after the Seyfert 1 transition (Sosa-Brito et al. 2001; Davies et al. 2005). Recently, Ricci et al. (2010) detected a broad Hα component in the position of the almost-obscured nucleus. Piconcelli et al. (2007) introduced a model, based on *XMM-Newton* observations, to explain the obscuration in terms of two absorbers: a thick one ($N_H \approx 5 - 10 \times 10^{23}\,\mathrm{cm^{-2}}$), obscuring only the nuclear source, and a thin one ($N_H \approx 4 \times 10^{22}\,\mathrm{cm^{-2}}$), obscuring both primary and reflected emissions. A progressive diminution of the absorber by a factor 6 was detected in the six years prior to the Seyfert 1 transition, becoming one of the larger variations in column density known in AGNs in this timescale (Schachter et al. 1998). A monitoring campaign with *Suzaku* by Bianchi et al. (2009) revealed changes of the column density on day timescales.

To complete the picture, Storchi-Bergmann & Bonatto (1991) detected a cone of radiation in the $[\mathrm{O\,III}]_{\lambda 5007}$ line centred in the hidden nucleus of NGC 7582 and directed towards the south-west, perpendicular to the mentioned disk. Evidences for the presence of this cone in Brα has been presented by (Riffel et al. 2009). Finally, Wold et al. (2006) determined the central black hole mass, $M_{BH} = 5.5 \times 10^7\,\mathrm{M_\odot}$, using VLT/VISIR spectroscopy in the MIR.

The colour composite V-band (F606W), H-band (F160W) and K-band (IB_2.06, narrow filter) image in Fig. 3.10 shows a strong and compact starburst (in blue) in the central $8'' \times 8''$ ($0.8 \times 0.8\,\mathrm{kpc^2}$) in NGC 7582, obscured by a conspicuous dust lane distributed along the south-east to north-west direction. The active nucleus,

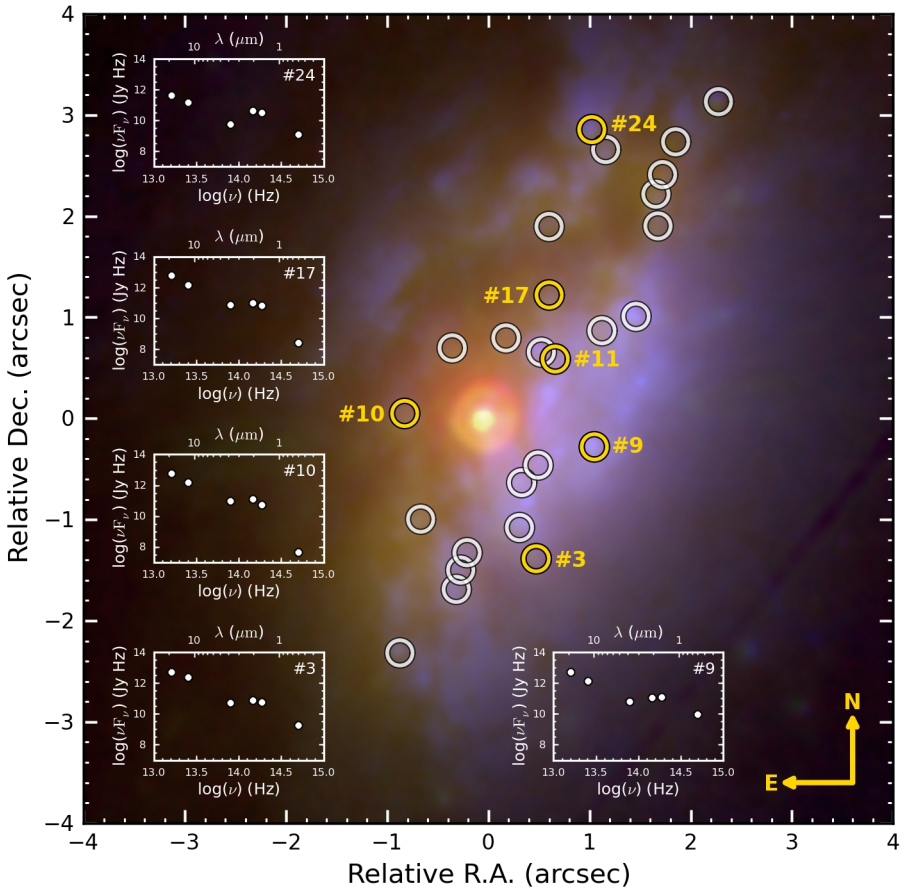

FIGURE 3.10— F606W (blue), F160W (green) and IB_2.06 (red) colour composite image of the central $8'' \times 8''$ in NGC 7582. The 26 knots identified in this galaxy are marked and the optical-IR SEDs are shown for representative sample of 5. The identification of the knots is shown more clearly in Fig. 2.7.

almost hidden in the optical range, becomes an outstanding source in the IR and dominates the nuclear emission longwards of 2 μm. The unsharp-mask filter applied on the IB_2.06 image (see Section 2.3.3) permitted us to identify a total of 26 knots, one of them (knot #10) located only 75 pc away far from the active nucleus. Their energy distributions (see Fig. 3.10) show a MIR maximum followed by a soft NIR bump and a fall in the optical range, as in the case of NGC 253 (Fig. 3.2). The median half-light radius of the knots in the IB_2.06 band is 20.9 pc ($D = 19.9$ Mpc, FWHM $= 0\farcs16 \approx 15.4$ pc), indicating that most of them or even all are spatially unresolved. Their median brightness is $m_K = 15.1$ mag, which corresponds to an

absolute magnitude of $M_K = -16.4$ mag. The compactness of the starburst and the high luminosity of the knots, 3.7 mag brighter that those in NGC 253, suggest that for each point-like source in NGC 7582 we have the equivalent luminosity of ≈ 30 knots in NGC 253. This means, for instance, that a single knot in NGC 7582 can account for the luminosity of almost all the nuclear starburst in NGC 253, or otherwise 2–3 knots like the brightest IR source in this galaxy. As expected, the median mass derived in this case from the K-band luminosity is very high, of about $1 \times 10^6\,\mathrm{M}_\odot$.

TABLE 3.5— Main characteristics of the knots found in NGC 7582. The relative error (δ) for each magnitude is: $\delta(F606W) = 5\%$, $\delta(F160W) = 1\%$, $\delta(IB\_2.06) = 2\%$, $\delta(L') = 3\%$, $\delta(N) = 8\%$, $\delta(Q) = 4\%$, $\delta[W(\mathrm{Br}\alpha)] = 11\%$ and $\delta(L_{\mathrm{Br}\alpha}) = 8\%$. Relative R.A. and Dec. correspond to the shift in equatorial coordinates with respect to the active nucleus ($\star$). The size column corresponds to the half-light radius ($\mathrm{FWHM_{obs}}$).

#	Relative		F606W	F160W	IB_2.06	L'	N	Q	Size	W(Brα)	log($L_{\mathrm{Br}\alpha}$)
	R.A.	Dec.	[μJy]						[pc]	[Å]	[erg s^{-1}]
0	$-0\farcs88$	$-2\farcs32$	1.6	200	270	180	3.0×10^{4}	4.0×10^{4}	98.9	...	....
1	$-0\farcs32$	$-1\farcs69$	4.4	390	560	500	9.0×10^{4}	2.8×10^{5}	70.3	94	37.7
2	$-0\farcs28$	$-1\farcs50$	4.6	410	640	660	1.0×10^{5}	3.2×10^{5}	24.1	111	37.9
3	$0\farcs47$	$-1\farcs39$	3.9	310	550	630	9.0×10^{4}	3.7×10^{5}	20.9	...	....
4	$-0\farcs21$	$-1\farcs33$	3.8	400	680	1020	1.0×10^{5}	3.7×10^{5}	<15.4	52	37.7
5	$0\farcs31$	$-1\farcs08$	12.5	720	930	1120	1.0×10^{5}	4.9×10^{5}	<15.4	...	....
6	$-0\farcs67$	$-1\farcs00$	1.0	500	760	860	5.0×10^{4}	2.8×10^{5}	17.5	...	....
7	$0\farcs33$	$-0\farcs64$	16.2	970	1540	1870	1.5×10^{5}	7.5×10^{5}	20.7	...	....
8	$0\farcs49$	$-0\farcs46$	14.7	820	1450	2080	1.6×10^{5}	7.2×10^{5}	<15.4	...	....
9	$1\farcs05$	$-0\farcs28$	19.0	680	800	1030	6.0×10^{4}	3.4×10^{5}	<15.4	...	....
10	$-0\farcs83$	$0\farcs05$	1.3	310	840	1390	6.0×10^{4}	4.3×10^{5}	28.6	...	....
11	$0\farcs66$	$0\farcs59$	9.0	740	1340	1820	8.0×10^{4}	5.4×10^{5}	19.1	...	....
12	$0\farcs52$	$0\farcs66$	7.6	700	1290	1910	8.0×10^{4}	5.5×10^{5}	<15.4	0	35.7
13	$-0\farcs36$	$0\farcs70$	0.7	340	810	1390	6.0×10^{4}	4.4×10^{5}	19.6	...	....
14	$0\farcs17$	$0\farcs80$	1.2	440	1000	1600	7.0×10^{4}	5.2×10^{5}	25.7	13	37.3
15	$1\farcs12$	$0\farcs87$	7.2	760	950	640	6.0×10^{4}	4.0×10^{5}	17.5	...	....
16	$1\farcs46$	$1\farcs01$	19.8	670	860	890	5.0×10^{4}	3.3×10^{5}	33.8	...	....
17	$0\farcs60$	$1\farcs22$	1.2	370	690	920	6.0×10^{4}	4.0×10^{5}	16.2	60	37.7
18	$0\farcs60$	$1\farcs90$	0.6	260	440	650	5.0×10^{4}	3.2×10^{5}	82.2	169	38.0
19	$1\farcs68$	$1\farcs90$	1.0	280	430	720	4.0×10^{4}	1.9×10^{5}	18.9	...	....
20	$1\farcs66$	$2\farcs22$	0.6	350	520	760	3.0×10^{4}	1.3×10^{5}	55.7	...	....
21	$1\farcs72$	$2\farcs41$	0.3	270	480	750	2.0×10^{4}	1.2×10^{5}	36.3	...	....
22	$1\farcs16$	$2\farcs66$	1.3	250	380	340	1.0×10^{4}	1.3×10^{5}	34.2	189	37.8
23	$1\farcs85$	$2\farcs74$	0.2	130	250	730	2.0×10^{4}	5.0×10^{4}	116.1	...	....
24	$1\farcs02$	$2\farcs86$	2.9	200	310	370	1.0×10^{4}	9.0×10^{4}	105.1	206	37.9
25	$2\farcs28$	$3\farcs13$	0.5	80	120	<20	0.0×10^{0}	$<0.0\times10^{0}$	37.9	...	....
$\star$	$0\farcs00$	$0\farcs00$	4.7	10680	25080	109270	3.9×10^{5}	7.8×10^{5}	17.5	6	38.8

3.2.6 NGC 7469

This galaxy is known as Mrk 1514, Arp 298 or also as UGC 12332. It was included in the original list of galaxies with active galactic nuclei by Seyfert (1943), is located at ~ 65 Mpc (Keel 1996, $H_0 = 75\,\mathrm{km\,s^{-1}\,Mpc^{-1}}$) and hosts a well-studied type 1.2 Seyfert nucleus. Upper panel in Fig. 3.11 shows some wide-field images in the UV (*GALEX*), optical (*HST*) and IR (2MASS). At this resolution, the main features detected are the strong nucleus, an inner disk (major axis $\sim 15''$), a bright nuclear ring and two or maybe three spiral arms which exhibit stronger star-forming activity in the northern side, close to the interacting companion IC 5283 which is located at $\sim 1\farcm3$ (Burbidge et al. 1963; Dahari 1985; Marquez & Moles 1994). At higher-spatial resolution (bottom panels in Fig. 3.11), the active nucleus is well resolved from the starburst ring, which seems to be connected with the spiral structure at larger scales. The ring has a size of $\sim 4''$ (≈ 1.3 kpc) and consist of a powerful starburst deeply embedded in a large concentration of molecular gas and dust, with a luminosity of $\approx 3\times10^{11}\,\mathrm{L_\odot}$, i.e. two thirds of the bolometric luminosity of the whole galaxy, turning this object into a Luminous InfraRed Galaxy (LIRG, Wilson et al. 1991; Genzel et al. 1995; Miles et al. 1996; Sanders et al. 2003; Davies et al. 2004). The most likely triggering mechanism for both the star-formation and nuclear activity is the interaction with IC 5283, which apparently happened about 1.5×10^8 yr ago (Genzel et al. 1995).

In the X-rays, NGC 7469 shows a very complex spectrum with rapid variability, a soft excess and a non-resolved iron line (Barr 1986; Turner et al. 1991; De Rosa et al. 2002). The nucleus is a luminous hard X-ray source ($L_{2-10\,\mathrm{keV}} \sim 2.6\times10^{43}\,\mathrm{erg\,s^{-1}}$) with almost no intrinsic absorption at all (Shinozaki et al. 2006). Moreover, Papadakis et al. (2001) report the discovery of time lags in the spectra of the X-ray light curves for this galaxy of about 3.5 h between the 2–4 and 4–10 keV bands, very similar to those observed in Galactic black hole and neutron star binaries –i.e. Cyg X-1 in its hard state, see Miyamoto et al. (1992)– but scaled by a factor of $\sim 10^6$. Similar delays with increasing wavelength in continuum UV bands (Kriss et al. 2000) and in the optical (Collier et al. 1998) were detected. At larger time-scales, from days to years, this galaxy is also know for being highly variable in the optical (Doroshenko et al. 1990; Dultzin-Hacyan et al. 1992) and NIR (Glass 1998) with a high-activity period from 1996 to the early 2000s (Merkulova 2000). Moreover, this galaxy has been monitored to perform a comprehensive study of the size of the BLR, which resulted in the discovery of wavelength-dependent time lags in the continuum, pointing to the presence of a reprocessing region located several light days from the central source (Collier et al. 1998). Furthermore, a correlation between the 2–10 keV flux and the 6.4 keV iron Kα line suggest that part of the line flux originates within $\sim 1\,\mathrm{light-day}$

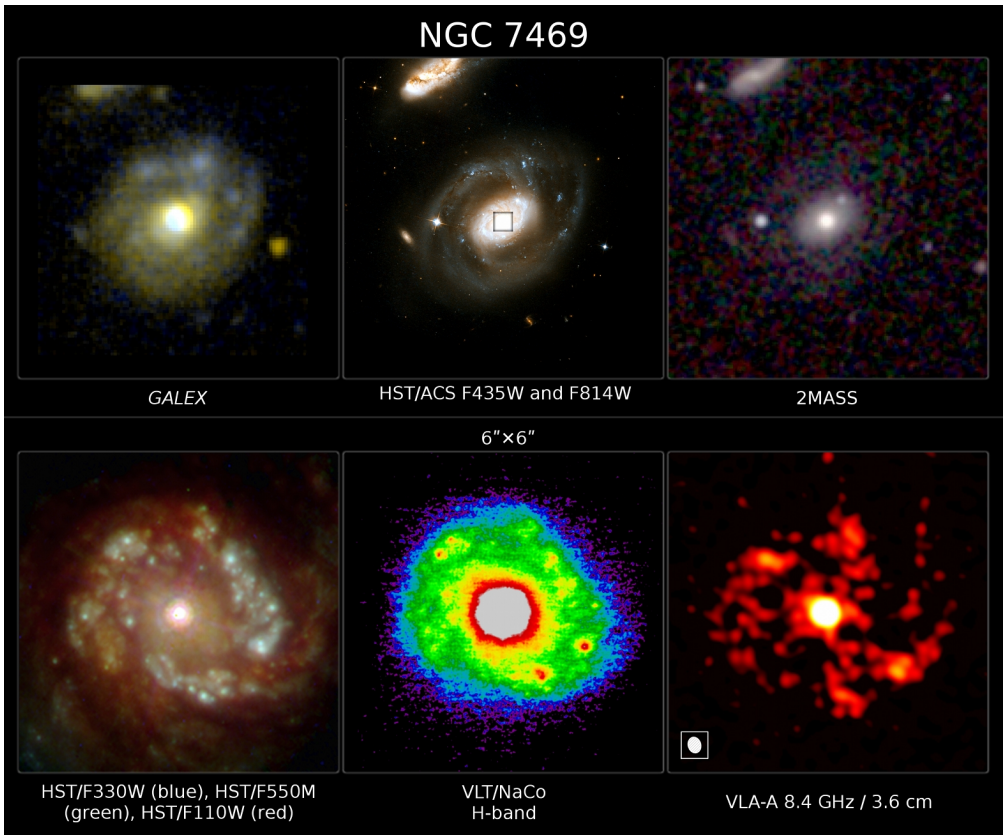

FIGURE 3.11— NGC 7469 at optical, infrared and radio wavelengths (North is up and East is to the left). The upper panels correspond to different views (UV, optical, NIR) at large scale and cover the same field of view. Lower panels correspond to the black box region ($6'' \times 6''$) in the *HST* image.

of the X-ray continuum source (Nandra et al. 2000).

At radio wavelengths, the nuclear emission is dominated by the bright unresolved nucleus which shows a spectral index of $\alpha \approx 0.73$, consistent with non-thermal radio emission, surrounded by an halo of diffuse radio emission from $\sim 1''$ to $2\farcs5$ away from the nucleus with a deep absorption feature in H I (Beswick et al. 2002). Colina et al. (2001, 2007) and Perez-Torres et al. (2009) discovered one of the brightest radio supernova yet observed, situated $1\farcs65$ north-west of the nucleus, confirming that the diffuse radio structure around the Seyfert nucleus is produced by the circumnuclear starburst. The $J = 3$–2 ^{12}CO maps also show emission from the centre superposed on a more extended disk, with a relative CO minimum in the nucleus (Israel 2009). Finally, VLBI observations at 1.67 GHz (18 cm) resolve the nuclear source in three emitting

regions aligned in the east-west direction (Lonsdale et al. 2003).

Outside, Díaz-Santos et al. (2007) identify ~ 30 massive star-forming knots (1–10 $M_{\odot}$) in the starburst ring, divided in two different populations: a young and mildly extinct one ($\sim$ 1–3 Myr, $A_V = 3$ mag) including 25% of the knots, and an a second population with 75% of them having intermediate ages ($\sim$ 8–20 Myr, $A_V \sim 1.25$ mag). The molecular gas morphology suggests that the ring also harbours a nuclear bar, which coincides at both ends with two bright MIR and radio peaks (Laine et al. 2002; Davies et al. 2004; Díaz-Santos et al. 2007). A dynamical model based in spectro-imaging by Davies et al. (2004) points to the presence of a second internal ring with a diameter of 0.″5 (160 pc) and a nuclear stellar cluster with ages in the 10–

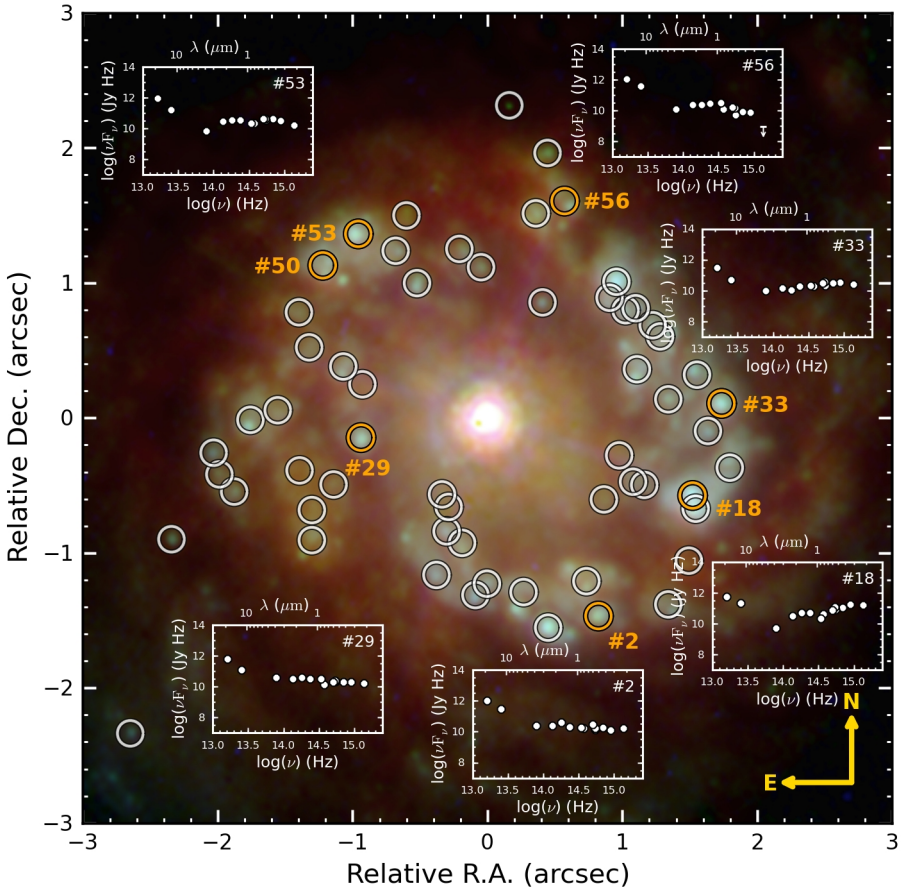

FIGURE 3.12— F330W (blue), F550M (green) and F110W (red) colour composite image of the central $6'' \times 6''$ in NGC 7469. The 59 knots identified in this galaxy are marked, showing the optical-IR SEDs for a representative sample of 6. Half of the regions were identified in the NIR by Díaz-Santos et al. (2007).

60 Myr range extended over the central $\sim 0\farcs19$ (60 pc) at $PA = 33°$, and contributing with 20%–30% of the nuclear K-band continuum ($\sim$ 10% of the nuclear bolometric luminosity). Moreover, Hicks et al. (2009) found a molecular gas distribution in H_2 1–0 S(1) forming a geometrically thick rotating disk with a size of about 30 pc and an enclosed dynamical mass of $10.1 \times 10^7\,M_\odot$. The CO-to-$H_2$ conversion is found to be 0.4–0.8 times that of the Milky Way, following the trend to small factors that has been reported for intense star-forming environments (Genzel et al. 1995; Davies et al. 2004).

Fig. 3.12 shows a u-band (F330W), y-band (F550M) and J-band (F110W) colour composition for the central $6'' \times 6''$ ($\sim 2 \times 2\,\mathrm{kpc}^2$). For this galaxy we found a total of 59 knots, 30 of them taken from Díaz-Santos et al. (2007), and distributed in a 0.9–1.3 kpc diameter elongated ring which also seem to be connected somehow with the inner end of the spiral arms (see Fig. 3.12). Dust lanes cut the starburst ring in three pieces, although the ring is complete in Paα emission (Fig. 3.13). Most of the knots' individual SEDs are very similar, being almost flat in the NUV, optical and NIR ranges with an increasing slope towards the MIR. When compared the knots found in NGC 1097 or NGC 1386, which also host starburst rings with comparable sizes, the energy distributions in the case of NGC 7469 seem to be quite different.

The median half-light radius of the knots in the F550M band is 28.2 pc ($D =$ 65.2 Mpc, FWHM $= 0\farcs07 \approx 22.1$ pc). They show a typical brightness of $m_K =$ 15.7 mag, which corresponds to $M_K = -18.4$ mag, i.e. the equivalent of ~ 6 knots in NGC 7582 or 15 knots like the brightest IR source in NGC 253. The high K-band luminosity exhibited by the clusters in this galaxy is expected since it is a LIRG and also the farthest object of the sample (the physical scale for a given area is multiplied by a factor of 10 when compared with NGC 7582). The mass estimation from the K-band luminosity give us a median value of $1.5 \times 10^7\,M_\odot$, with 50% of the sources between $9 \times 10^6\,M_\odot$ and $3.6 \times 10^7\,M_\odot$. Most of the knots have an W(Hα) of about 193 Å, corresponding to ages around 5.8 Myr. From the Hα/Paα ratio we derive a median extinction of $A_V = 4.4$ mag. In the case of this galaxy, it seems that the origin of the starburst activity, and thus of the knots also, is clearly linked with the ongoing interaction with its companion IC 5283. As evidence, the Paα continuum-subtracted image in Fig. 3.13 shows a spiral tail of Paα blops extended in the direction of IC 5283.

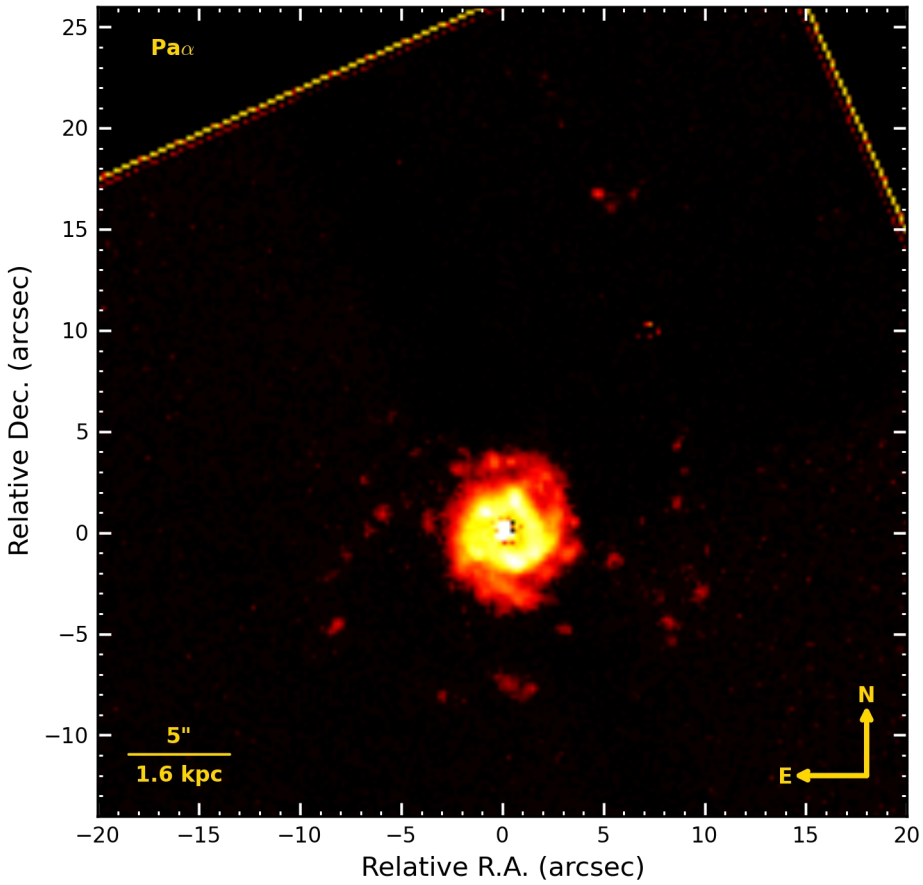

FIGURE 3.13— Continuum-subtracted Paα image for NGC 7469. The IR luminous ring surrounds the active nucleus. The stream of Paα blops follows a spiral pattern centred in the ring and disappears towards the north, in the direction of the interacting companion IC 5283.

TABLE 3.6— Main characteristics of the knots found in NGC 7469. The absolute (Δ) or relative error (δ) for each magnitude is: $\delta(F218) = 20\%$, $\delta(F330W) = 4\%$, $\delta(F435W) = 6\%$, $\delta(F547M) = 31\%$, $\delta(F550M) = 4\%$, $\delta(F606W) = 9\%$, $\delta(F814W) = 12\%$, $\delta(F785LP) = 18\%$, $\delta(J) = 10\%$, $\delta(H) = 10\%$, $\delta(F222M) = 18\%$, $\delta(L') = 15\%$, $\delta(N) = 23\%$, $\delta(Q) = 18\%$, $\delta(\mathrm{H}\alpha/\mathrm{Pa}\alpha) = 63\%$, $\Delta A_V = 0.5$ mag, $\delta[W(\mathrm{H}\alpha)] = 30\%$ and $\delta(L_{\mathrm{H}\alpha}) = 20\%$. The luminosity of the Hα line ($L_{\mathrm{H}\alpha}$) is corrected by the extinction given in A_V. Relative R.A. and Dec. correspond to the shift in equatorial coordinates with respect to the active nucleus ($\star$). The size column corresponds to the half-light radius ($\mathrm{FWHM_{obs}}$).

#	Relative		F218W	F330W	F435W	F547M	F550M	F606W	F814W	F785LP	*J*	*H*	F222M	*L'*	*N*	*Q*
	R.A.	Dec.	[μJy]													
0	$-2\farcs65$	$-2\farcs34$	< 1	2	2	< 1	3	< 2	< 3	< 4	20	< 10	< 20	< 10	...	...
1	$0\farcs45$	$-1\farcs55$	21	65	78	72	118	108	66	75	190	290	170	95	1.5×10^4	8.6×10^4
2	$0\farcs82$	$-1\farcs47$	12	24	31	28	60	58	46	57	90	230	210	486	1.2×10^4	6.9×10^4
3	$1\farcs34$	$-1\farcs38$	2	10	11	8	22	19	15	63	20	20	180	29	3.0×10^3	6.1×10^4
4	$-0\farcs09$	$-1\farcs31$	18	29	27	21	48	39	19	16	10	< 10	190	322	6.0×10^3	3.0×10^4
5	$0\farcs27$	$-1\farcs29$	5	23	22	23	53	39	26	38	40	70	210	85	1.4×10^4	6.1×10^4
6	$-0\farcs00$	$-1\farcs23$	15	25	17	7	38	27	17	16	30	40	200	402	6.0×10^3	2.5×10^4
7	$0\farcs73$	$-1\farcs21$	3	19	24	29	55	44	43	59	190	290	260	386	9.0×10^3	6.3×10^4
8	$-0\farcs38$	$-1\farcs16$	15	23	11	3	26	27	8	75	60	120	230	555	$< 1.0\times10^3$	$< 5.0\times10^3$
9	$1\farcs49$	$-1\farcs06$	4	< 1	< 1	< 1	6	5	9	31	100	130	230	348	1.2×10^4	6.5×10^4
10	$-0\farcs19$	$-0\farcs93$	14	14	13	20	17	14	15	95	220	210	180	813	$< 1.0\times10^3$	2.6×10^4
11	$-1\farcs30$	$-0\farcs91$	2	5	9	9	29	28	28	6	130	160	190	53	1.0×10^3	2.2×10^4
12	$-2\farcs34$	$-0\farcs90$	< 1	< 1	< 1	6	3	3	4	25	< 10	30	30	< 10	$< 1.0\times10^3$	3.2×10^4
13	$-0\farcs30$	$-0\farcs84$	15	15	17	17	19	20	11	119	360	470	140	1076	$< 1.0\times10^3$	4.5×10^4
14	$-1\farcs30$	$-0\farcs68$	< 1	< 1	3	< 1	14	15	12	44	90	130	220	< 10	2.0×10^3	3.5×10^4
15	$1\farcs54$	$-0\farcs67$	135	190	170	192	233	190	142	58	220	280	360	90	1.1×10^4	4.3×10^4
16	$-0\farcs29$	$-0\farcs66$	11	3	< 1	< 1	< 1	4	5	110	450	590	140	1911	2.0×10^3	1.7×10^5
17	$0\farcs86$	$-0\farcs60$	< 1	< 1	4	8	6	< 2	12	58	60	120	210	493	$< 1.0\times10^3$	$< 5.0\times10^3$
18	$1\farcs52$	$-0\farcs57$	126	193	158	158	235	149	117	61	210	280	320	64	9.0×10^3	3.8×10^4
19	$-0\farcs34$	$-0\farcs57$	8	4	< 1	< 1	5	8	7	104	510	770	290	2782	1.0×10^4	2.6×10^5
20	$-1\farcs88$	$-0\farcs55$	< 1	4	5	9	11	12	8	83	50	100	110	75	4.0×10^3	1.5×10^4
21	$1\farcs16$	$-0\farcs50$	2	11	8	9	10	12	34	21	40	30	50	< 10	3.0×10^3	$< 5.0\times10^3$
22	$-1\farcs14$	$-0\farcs49$	< 1	< 1	< 1	12	6	5	6	44	50	10	190	322	3.0×10^3	3.9×10^4
23	$1\farcs08$	$-0\farcs47$	< 1	10	8	< 1	10	12	48	41	20	20	40	101	2.0×10^3	$< 5.0\times10^3$
24	$-1\farcs99$	$-0\farcs42$	< 1	4	3	4	11	15	8	66	90	70	100	45	$< 1.0\times10^3$	1.9×10^4
25	$-1\farcs39$	$-0\farcs39$	2	< 1	< 1	< 1	11	9	11	32	50	80	210	31	3.0×10^3	3.2×10^4
26	$1\farcs80$	$-0\farcs37$	32	32	28	48	53	53	30	59	140	120	180	< 10	4.0×10^3	3.5×10^4
27	$0\farcs98$	$-0\farcs28$	< 1	4	119	< 1	< 1	< 2	206	48	100	180	70	515	$< 1.0\times10^3$	$< 5.0\times10^3$

28	−2.″03	−0.″26	2	5	7	< 1	16	18	12	63	20	70	80	36	$< 1.0\times10^3$	$< 5.0\times10^3$
29	−0.″94	−0.″15	12	23	32	39	45	41	36	96	180	280	260	989	5.0×10^3	4.1×10^4
30	1.″63	−0.″10	17	12	10	< 1	14	14	< 3	30	30	20	140	38	1.0×10^3	2.7×10^4
31	−1.″76	−0.″01	4	16	22	41	41	32	28	70	70	90	190	174	2.0×10^3	$< 5.0\times10^3$
32	−1.″56	0.″06	2	6	9	15	21	17	16	43	40	20	140	49	3.0×10^3	$< 5.0\times10^3$
33	1.″74	0.″11	21	40	47	38	71	61	52	61	80	60	200	317	2.0×10^3	2.9×10^4
34	1.″34	0.″14	7	5	5	9	12	16	8	34	< 10	30	130	228	$< 1.0\times10^3$	8.0×10^3
35	−0.″93	0.″25	9	4	39	< 1	8	13	65	66	160	180	90	743	4.0×10^3	3.4×10^4
36	1.″55	0.″32	10	12	13	54	18	17	10	33	40	40	160	401	1.0×10^3	3.7×10^4
37	1.″11	0.″36	17	41	37	31	68	50	34	11	90	120	200	304	$< 1.0\times10^3$	1.2×10^4
38	−1.″07	0.″38	4	15	29	5	27	25	71	55	70	110	100	504	3.0×10^3	3.3×10^4
39	−1.″32	0.″52	< 1	4	7	< 1	16	13	13	< 4	60	60	100	27	$< 1.0\times10^3$	2.6×10^4
40	1.″28	0.″60	13	28	24	26	48	43	25	19	80	90	160	34	$< 1.0\times10^3$	1.5×10^4
41	1.″22	0.″69	16	24	23	22	47	35	22	16	50	90	130	< 10	2.0×10^3	1.1×10^4
42	−1.″40	0.″78	< 1	3	6	8	14	12	9	12	20	60	150	478	8.0×10^3	4.4×10^4
43	1.″02	0.″80	33	32	30	32	48	51	35	28	100	100	120	146	1.0×10^4	3.6×10^4
44	1.″10	0.″81	33	28	28	22	44	44	28	27	70	60	80	113	8.0×10^3	2.3×10^4
45	0.″41	0.″86	6	3	4	4	5	3	< 3	61	< 10	20	190	319	$< 1.0\times10^3$	1.5×10^4
46	0.″91	0.″89	33	63	47	79	80	81	48	44	130	160	130	286	1.0×10^4	3.3×10^4
47	−0.″52	1.″00	5	9	13	2	19	16	14	25	< 10	< 10	80	171	3.0×10^3	3.1×10^4
48	0.″96	1.″01	39	117	125	124	157	141	109	63	160	200	110	334	6.0×10^3	5.3×10^4
49	−0.″05	1.″12	3	4	5	< 1	13	12	12	< 4	< 10	< 10	90	231	$< 1.0\times10^3$	$< 5.0\times10^3$
50	−1.″22	1.″13	10	27	30	48	57	54	44	63	160	190	260	443	1.5×10^4	7.8×10^4
51	−0.″68	1.″24	4	11	15	3	30	25	22	23	30	50	110	41	1.1×10^4	3.1×10^4
52	−0.″21	1.″25	< 1	6	7	12	17	17	17	13	< 10	30	50	193	1.0×10^3	$< 5.0\times10^3$
53	−0.″96	1.″36	14	46	63	68	98	89	60	68	150	210	240	356	7.0×10^3	5.8×10^4
54	−0.″60	1.″50	2	< 1	3	5	11	10	14	21	30	100	100	75	4.0×10^3	$< 5.0\times10^3$
55	0.″36	1.″52	< 1	8	16	25	43	37	37	54	130	190	260	221	1.3×10^4	7.5×10^4
56	0.″57	1.″61	< 1	10	14	10	33	32	32	97	130	130	230	151	1.5×10^4	6.9×10^4
57	0.″45	1.″96	< 1	2	5	6	16	16	21	79	70	80	120	258	1.0×10^4	5.4×10^4
58	0.″16	2.″32	< 1	< 1	< 1	< 1	< 1	< 2	< 3	33	< 10	< 10	30	24	$< 1.0\times10^3$	$< 5.0\times10^3$
⋆	0.″00	0.″00	2338	2599	444	2335	1709	251	349	1778	6750	13040	35460	84412	3.7×10^5	1.0×10^6

#	Relative R.A.	Relative Dec.	Size [pc]	$\frac{H\alpha}{Pa\alpha}$	A_V [mag]	W(Hα) [Å]	log($L_{H\alpha}$) [erg s^{-1}]
0	−2.″65	−2.″34	30.9	...	...	...	....
1	0.″45	−1.″55	25.2	...	...	212	....
2	0.″82	−1.″47	29.6	...	...	316	....
3	1.″34	−1.″38	59.2	...	...	249	....
4	−0.″09	−1.″31	52.0	2.36	2.1	258	40.2
5	0.″27	−1.″29	$<$ 22.1	1.03	3.5	312	40.7
6	−0.″00	−1.″23	$<$ 22.1	2.51	2.0	349	40.1
7	0.″73	−1.″21	$<$ 22.1	0.57	4.5	161	40.8
8	−0.″38	−1.″16	58.5	3.24	1.6	296	39.9
9	1.″49	−1.″06	28.2	0.27	5.7	432	40.8
10	−0.″19	−0.″93	75.7	3.93	1.3	492	39.8
11	−1.″30	−0.″91	87.0	...	...	163	....
12	−2.″34	−0.″90	26.8	...	...	...	....
13	−0.″30	−0.″84	75.7	...	...	314	....
14	−1.″30	−0.″68	87.0	6.91	0.4	113	38.9
15	1.″54	−0.″67	40.9	7.01	0.3	61	39.7
16	−0.″29	−0.″66	70.2	0.69	4.2	942	40.5
17	0.″86	−0.″60	23.6	...	...	...	....
18	1.″52	−0.″57	40.9	...	...	76	....
19	−0.″34	−0.″57	39.9	0.26	5.8	335	40.8
20	−1.″88	−0.″55	60.5	0.13	7.0	183	40.8
21	1.″16	−0.″50	29.6	...	...	76	....
22	−1.″14	−0.″49	25.2	...	...	90	....
23	1.″08	−0.″47	52.8	...	...	...	....
24	−1.″99	−0.″42	34.6	0.19	6.3	94	40.7
25	−1.″39	−0.″39	$<$ 22.1	...	...	8	....
26	1.″80	−0.″37	37.8	2.65	1.9	156	40.1
27	0.″98	−0.″28	34.6	...	...	...	....
28	−2.″03	−0.″26	$<$ 22.1	0.48	4.8	195	40.6
29	−0.″94	−0.″15	25.2	...	...	67	....
30	1.″63	−0.″10	25.2	...	...	2963	....
31	−1.″76	−0.″01	25.2	0.35	5.3	81	40.6
32	−1.″56	0.″06	25.2	...	...	76	....
33	1.″74	0.″11	25.2	...	...	150	....
34	1.″34	0.″14	$<$ 22.1	1.11	3.4	314	40.3
35	−0.″93	0.″25	$<$ 22.1	1.71	2.7	113	39.8

36	1.″55	0.″32	28.2	...	...	650	....
37	1.″11	0.″36	32.2	5.35	0.8	85	39.4
38	−1.″07	0.″38	42.8	...	...	...	....
39	−1.″32	0.″52	42.8	...	...	...	....
40	1.″28	0.″60	32.2	1.73	2.6	219	40.3
41	1.″22	0.″69	23.6	2.23	2.2	326	40.3
42	−1.″40	0.″78	$<$ 22.1	0.75	4.0	266	40.3
43	1.″02	0.″80	23.6	...	...	352	....
44	1.″10	0.″81	23.6	4.40	1.1	446	40.2
45	0.″41	0.″86	28.2	...	...	...	....
46	0.″91	0.″89	$<$ 22.1	...	...	213	....
47	−0.″52	1.″00	32.2	0.54	4.6	273	40.6
48	0.″96	1.″01	28.2	2.69	1.9	124	40.4
49	−0.″05	1.″12	38.9	...	...	...	....
50	−1.″22	1.″13	25.2	0.72	4.1	240	41.0
51	−0.″68	1.″24	$<$ 22.1	0.55	4.5	193	40.7
52	−0.″21	1.″25	38.9	...	...	...	....
53	−0.″96	1.″36	25.2	0.67	4.2	119	40.9
54	−0.″60	1.″50	$<$ 22.1	...	...	314	....
55	0.″36	1.″52	48.0	0.64	4.3	199	40.8
56	0.″57	1.″61	26.8	0.65	4.3	415	41.1
57	0.″45	1.″96	36.8	...	...	378	....
58	0.″16	2.″32	$<$ 22.1	...	...	413	....
$\star$	0.″00	0.″00	28.2	6.83	0.4	3476	41.7

3.3 Summary

Overall, some of these objects show peculiarities that must be pointed out. For instance, NGC 1386 hosts a star-forming ring similar in size to those of NGC 1097 or NGC 7469, but the knots are ~ 5 mag fainter in the former. NGC 1097 show knots as bright as those present in the nucleus of the starburst NGC 253, but their ages seem to be a factor of 2 higher. Finally, in the case of NGC 1052 we find a 15 knots that exhibit emission in Hα, suggesting young ages ($\lesssim 10$ Myr). In this case, the nature of the knots will be further analyzed in Section 5.3. Nevertheless, their origin could be associated with one of the star-formation bursts after the merger event that suffered this galaxy.

Finally, considering the median $\mathrm{FWHM_{obs}}$, IR magnitudes, colours, extinctions and ages provided in Section 3.2, we conclude that the majority of the knots found in NGC 253, NGC 1097, NGC 1386, NGC 7582 and NGC 7469, and probably an important fraction in NGC 1052, are star-forming regions very similar to those found in starburst and interacting galaxies like NGC 5253 or the Antennae (Vanzi & Sauvage 2004; Gilbert et al. 2000; Zhang et al. 2001). These are young, compact and massive star-forming clusters still embedded in their birth material. As a consequence, they exhibit a strong IR emission and high extinction values. In Chapter 5 we will study in detail the properties of these clusters, comparing them among the sample of galaxies. However, the next Chapter will focus on the high-spatial resolution SEDs obtained for the active nuclei.

4

The spectral energy distribution of AGNs at high-spatial resolution

In this Chapter we build Spectral Energy Distributions for the active galactic nuclei in the sample using the highest spatial resolution data available from radio to IR, optical and X-rays. The main properties of the brightest and faintest nuclei are reviewed separately. A median template for low-luminosity AGNs is presented. Finally, we discuss the particular case of NGC 253, which nuclear region displays different sources with hints of possible nuclear activity. Part of the results on the nature NGC 253's nucleus have been published in Fernández-Ontiveros et al. (2009) and Müller-Sánchez et al. (2010).

4.1 Introduction

In the SED of a classical AGN we can identify several components, as explained in Chapter 1. From lower to higher frequencies, one can identify: *i)* radio synchrotron emission from a compact core and/or a jet, which may be strong (radio-loud) or weak (radio-quiet), *ii)* a steep increase towards the IR bump, interpreted in terms of thermal re-radiation by dust, *iii)* the big blue bump rises in the optical/UV range, which consists on pseudo-blackbody emission from an optically thick, geometrically thin accretion disk (Shields & Wheeler 1978; Malkan & Sargent 1982), *iv)* a soft X-ray excess which does not have a clear origin (Done et al. 2007), and *v)* an underlying power-law increasing at hard X-rays and attributed to Comptonization of softer photons (Ho 2008), which is though to extend down to IR wavelengths. The range between the UV and the X-rays is invisible to us due to Galactic absorption, except for those objects at high redshift.

Nevertheless, this is the classical picture observed for bright and unobscured

nuclei, i.e. type 1 QSOs with $L_{bol} \sim 10^{46}\,\mathrm{erg\,s^{-1}}$, but the nearby universe gives us the opportunity to observe a wide variety of AGNs which span from $L_{bol} \sim 10^{44}\,\mathrm{erg\,s^{-1}}$ down to luminosities as faint as $\sim 10^{38}\,\mathrm{erg\,s^{-1}}$ (Cappellari et al. 1999). Furthermore, Low-Ionization Nuclear Emission Line Regions (LINERs) are present in half of the galaxies in the local universe and also trace the population of AGNs at the lowest luminosities. However, LLAGNs are not simply scaled-down versions of Seyferts and QSOs. Moreover, Kuraszkiewicz et al. (2009) propose that the Eddington ratio (L/L_{Edd}) is the most important factor in determining the properties of AGN SEDs. Below $\lesssim 10^{42}\,\mathrm{erg\,s^{-1}}$ and at low Eddington ratios ($L_{bol}/L_{Edd} \lesssim 10^{-3}$), the BLR and the torus itself are expected to vanish (Nicastro 2000; Elitzur & Shlosman 2006; Hönig & Beckert 2007; Ho 2008), and it is not completely clear which mechanism is the power source of the emission lines for these objects. Some suggestions are *i)* weak AGNs (Halpern & Steiner 1983; Ferland & Netzer 1983), *ii)* hot stars (either young or old, Terlevich & Melnick 1985; Barth & Shields 2000; Binette et al. 1994) and/or *iii)* shocks (Heckman 1980; Dopita et al. 1996). However, it seems that LLAGNs show a very little contribution from young stars (Ho 2008), and recent radio, UV and X-ray surveys with high-spatial resolution have uncovered weak AGNs in the majority of LINERs (Nagar et al. 2005; González-Martín et al. 2009b).

As mentioned before, the number of objects in this study is quite limited, but we sample well this range in luminosity (see Table 4.1). We assembled the central core SED for six nearby galaxies: the prototypical starburst NGC 253, two type 1 objects (NGC 1097 and NGC 7469) at the extremes of the luminosity range and three type 2 objects including a LINER in an elliptical galaxy (NGC 1052), a faint Seyfert 2 in an early-type spiral (NGC 1386) and a bright Seyfert 2 in a dusty spiral with a nuclear starburst (NGC 7582). Nevertheless this is, together with the nearby active galaxies which have already been studied at parsec scales, e.g. NGC 1068, Circinus, Centaurus A or NGC 4151 (Jaffe et al. 2004; Prieto et al. 2004; Tristram et al. 2007; Häring-Neumayer et al. 2006; Meisenheimer et al. 2007; Hönig et al. 2008; Ramos Almeida et al. 2009; Prieto et al. 2010; Pott et al. 2010), the further we can go nowadays at a spatial resolution of parsec scales. Using the aperture photometry fluxes in the UV, optical and IR for the nuclear core presented in Chapter 3 and the data collected from the literature with the best spatial resolution available at radio and X-ray wavelengths, we estimated the bolometric luminosity for the galaxies in the sample. Except for the case of NGC 253, in which the source that we consider as the core is only detected in the hard X-rays (see Sections 2.3.2 and 4.5 for details), the energy output for each galaxy was derived by integrating the SED in the same way as in Prieto et al. (2010). The SED is divided in two ranges: from radio to optical covering the IR bump, and the absorption-corrected data in the X-ray range. A linear interpolation for each 0.1 dex frequency increment was performed in the $\log L_\nu$–$\log \nu$ space in order to sample the SED in the $\sim 10^{10}$–10^{13} Hz range, where there is a lack

of measurements with a comparable spatial resolution.

TABLE 4.1— High-spatial resolution nuclear luminosities of the galaxies in the sample.

Name	L_{bol} $[\mathrm{erg\,s^{-1}}]$	Type	Class
NGC 253	1.1×10^{40}	SAB(s)c	Starburst
NGC 1097	6.8×10^{41}	SB(r′l)b	LINER 1
NGC 1386	3.1×10^{42}	SB(s)a	Sy 2
NGC 1052	3.2×10^{42}	E4	LINER 1.9
NGC 7582	1.6×10^{43}	SB(s)ab	Sy 2
NGC 7469	2.7×10^{44}	(R′)SAB(rs)a	Sy 1.2

Sorting the objects by its nuclear bolometric luminosity, as in Table 4.1, we find that the hard X-ray source in NGC 253 is the faintest one in the sample. NGC 1097, NGC 1386 and NGC 1052 present a similar energy output despite of their differences in classification (LINER 1, Sy2 and LINER 1.9, respectively). Nonetheless, the latter are based on the properties of the ionized gas clouds around the nucleus rather than the nuclear source itself. Finally, at the top of the luminosity distribution we find NGC 7582 and NGC 7469 with $L_{bol} \gtrsim 10^{43}\,\mathrm{erg\,s^{-1}}$. In further Sections 4.2 and 4.3 we will analyze, respectively, the cases of high-luminosity (NGC 7582 and NGC 7469) and low-luminosity nuclei (NGC 1097, NGC 1386 and NGC 1052), focusing on the changes in the SED at both extremes. In Section 4.4 we remark the main differences when using high and low-spatial resolution data. The particular nature of the nuclear region of NGC 253 makes of this galaxy a very interesting case, and thus will be discussed separately in Section 4.5.

4.2 High-luminosity nuclei

As mentioned before, the SEDs of the brightest objects in the sample correspond to NGC 7469 (LIRG/Sy1.2) and NGC 7582 (Sy2/starburst). These were compared with high-spatial resolution (HSR) average Sy1 and Sy2 templates derived from a dataset similar in wavelength coverage to those described in this thesis, published in Prieto et al. (2010). In this work, the dataset correspond to a small sample of type 1 (NGC 3783, NGC 1566 and NGC 7469) and type 2 objects (Circinus, NGC 1068, NGC 5506 and NGC 7582), including two of the nuclei in our sample. Fluxes in the X-rays are corrected from absorption and have been published in the literature (see Prieto et al. 2010, and references therein). In the IR, optical and UV the fluxes are not corrected for reddening. In order to obtain a representative SED for each Seyfert class, we first normalized every SED to its mean power, i.e. $\langle \nu L_\nu \rangle_j$. Being $\nu L^n_\nu|_j$

the normalized SED for each nuclei j, we obtained the representative SED as the mean value, evaluated for each filter centred in ν_i, of all the normalized distributions, $\left\langle \nu_i L^n_{\nu_i}\big|_j \right\rangle$. Due to the wide dynamical range in the power distribution of the individual nuclei (the difference in power between IR and radio is nearly six orders of magnitude), we used the mean normalization to take account for extreme values measured at radio wavelengths, which are rejected by the median. By using the mean power to normalize the SEDs, we avoid the assumption for all of them to coincide at a specific wavelength, e.g. at the dust sublimation temperature (1 μm) or the continuum for the old stellar population ($\sim$ 7000 Å). The latter introduces a higher dispersion at the edges of the distribution of normalized SEDs, with a nil dispersion at the reference wavelength. In contrast, the mean power is a representative value for the overall energy output, since the SEDs are well sampled over almost the whole spectral range, specially in the X-rays and the IR where the main contributions to the SED are found.

In Fig. 4.1 we show the complete rest-frame HSR SED from radio to X-rays for NGC 7469 (blue dots) and NGC 7582 (turquoise dots) together with the HSR average templates for Sy1 (open squares) and Sy2 (open circles) from Prieto et al. (2010). Both are scaled to the mean power distribution of the corresponding object, i.e. the average Sy1 to the SED of NGC 7469 and the average Sy2 to that of NGC 7582. For comparison, we plot fluxes based on low-spatial resolution data (spikes in Fig. 4.1, see Tables 4.5 and 4.6 at the end of this Chapter). We also show the SED of the bright quasar 3C 273 (Prieto et al. 2010) as a reference for a bright unabsorbed AGN (orange dots). The energy gap in the $\sim 10^{15}$–10^{17} Hz range corresponds to the Galactic absorption window. However, we expect, due to the brightness of this quasar, a more massive SMBH than in the case of Seyferts. This would cause the big blue bump to be displaced longwards in the UV, while the same feature in Seyferts would be located shortwards in the extreme UV or the soft X-rays.

The type 1 AGNs usually show the characteristic blue bump in the optical-to-UV range. As in the case of quasars, the inflection point observed around $\sim 1\,\mu$m is associated with the signature of dust emission and its limiting sublimation temperature (Sanders et al. 1989). However, when compared with the blue bump in 3C 273, the same feature looks weaker in Sy1s. This can be interpreted in terms of a more dusty environment in the latter (Prieto et al. 2010), may be by direct obscuration of the central source or by strong hot dust emission in the MIR (200–400 K) that conceals the blue bump. However, 3C 273 (and, in general, the majority of QSOs) is located in the range of the radiation-limited tori, i.e. $L \gtrsim 10^{45}\,\mathrm{erg\,s^{-1}}$ (Hönig & Beckert 2007). At high Eddington ratios ($L_{bol}/L_{Edd} \gtrsim 0.1$) this luminosity marks, for a clumpy torus formed by optically thick, self-gravitating dust clouds, the transition from a maximum cloud size limited by the tidal disruption in the gravitational potential (shear-limited

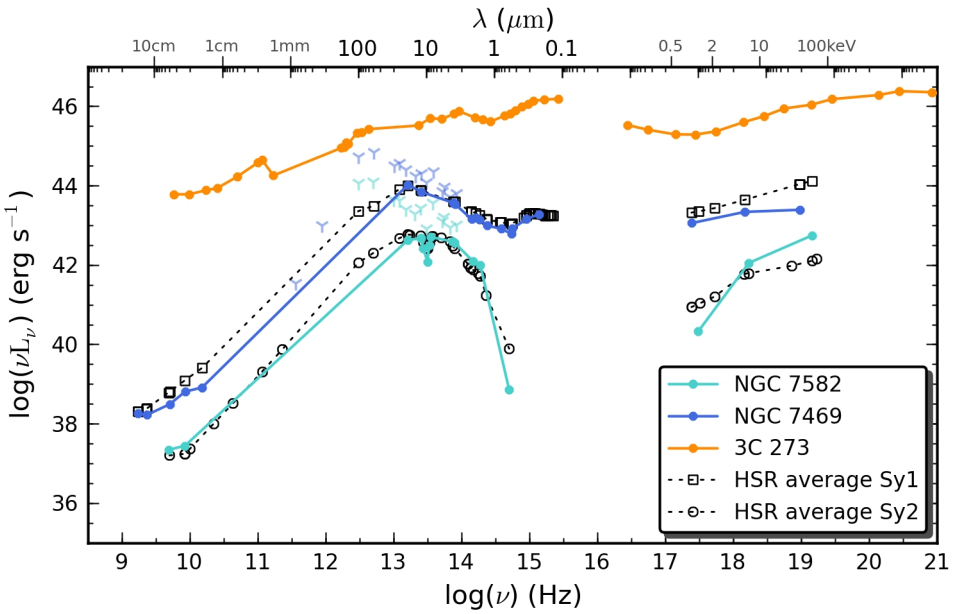

FIGURE 4.1— Spectral energy distribution for the brightest AGNs in the sample: the Sy1.2 NGC 7469 (blue dots), the Sy2 NGC 7582 (turquoise dots) and their corresponding low-spatial resolution data (three-spikes symbols). For comparison, we also show the SED of a HSR average Sy1 (open squares), a HSR average Sy2 (open circles) and the bright quasar 3C 273 (orange dots), taken from (Prieto et al. 2010).

tori) to a maximum size limited by the radiation pressure. As a consequence, the structure of the torus is expected to change, decreasing its covering fraction with increasing luminosity. In line with this "receding torus" scenario (Lawrence 1991), the majority of quasars do not exhibit a strong IR-bump (Elvis et al. 1994), while it is by far the most relevant feature in both types of Seyfert nuclei. Therefore, quasars are not exactly scaled up versions of Sy1s.

Shortwards of $\sim 1\,\mu$m, the SEDs of Sy2s are completely or almost obscured and thus do not show any feature corresponding to the blue bump, in agreement with the unified model scheme (Antonucci 1993). In contrast, they show a very steep decrease towards optical/UV wavelengths (Fig. 4.1, Ramos Almeida et al. 2009). The absence of a high-spatial resolution data in the 1 cm to 20 μm range do not permit us to follow the turnover from the MIR to radio wavelengths, although large aperture data in the case of NGC 7469 suggest that the energy distribution presents a smooth decrease in power with $\alpha \sim 0.6$–0.7 ($L_\nu \propto \nu^{-\alpha}$), rather than an important contribution from cold dust in the IR-millimetre range. This absence might result from the small physical region sampled on parsec scales, avoiding the main contribution at these wavelengths from the cold dust component in the rest of the galaxy (Prieto et al. 2010). In the X-

ray range, both types of Seyferts show a rise in power with increasing frequency very similar to the high-energy emission bump presented by 3C 273, but the former SEDs cannot be sampled at higher frequencies due to the Galactic absorption window.

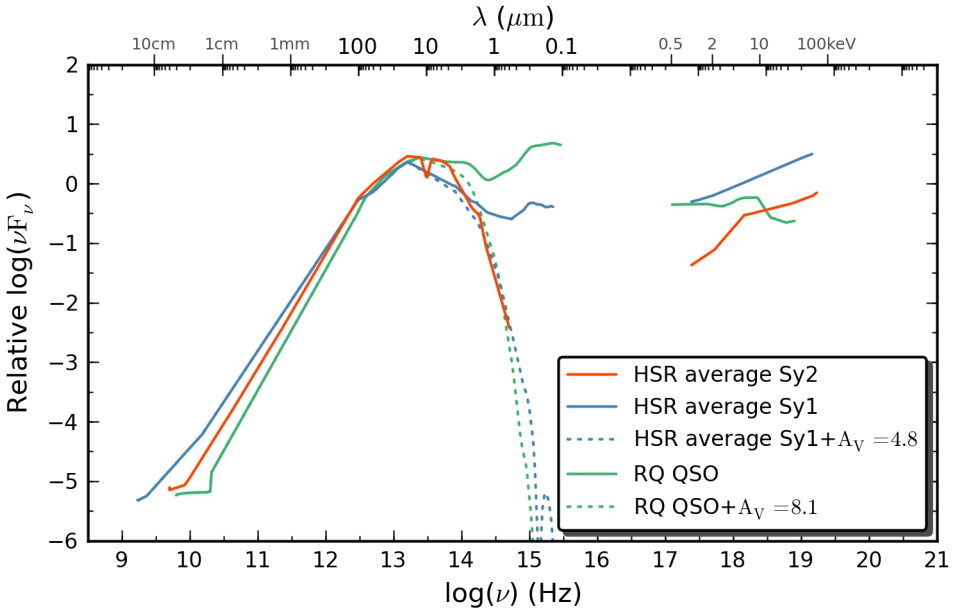

FIGURE 4.2— SEDs for the HSR Sy1 (blue colour) and HSR Sy2 templates (orange) from Prieto et al. (2010) and the RQ QSO template from Elvis et al. (1994) (green). The HSR Sy2 template can be well reproduced by either a HSR Sy1 obscured by $A_V = 4.8$ mag or a RQ QSO with $A_V = 8.1$ mag (dotted lines).

In Fig. 4.2 we compared the relative SEDs of the HSR templates for Sy1 (blue-solid line) and Sy2 (orange-solid line) from Prieto et al. (2010) with the RQ QSO template (green-solid line) from Elvis et al. (1994). Although the data associated to the RQ QSO template has been acquired with lower spatial resolution, the nuclear source is very bright and thus the integrated spectra is representative of the quasar core. However, as mentioned before, quasars are in the luminosity range of radiation-limited tori (Hönig & Beckert 2007), and thus cannot be strictly considered as representative of the Sy1 class. A χ^2–algorithm was used to fit both the Sy1 and RQ QSO templates to that of the average Sy2, deriving a scaling factor an a extinction value for each fit. As shown by Fig. 4.2, the shape of the average Sy2 can be very well reproduced in terms of an obscured type 1 AGN (blue-dotted line). The extinction values (A_V), derived by assuming a foreground dust screen (extinction law by Cardelli et al. 1989), correspond to 4.8 and 8.1 mag for the Sy1 and the RQ QSO templates, respectively. These are in

good agreement with the range of nuclear extinctions derived by Prieto et al. (2010) from the nuclear $J-K$ colours of the above-mentioned sample of Sy2s. The higher A_V required for the RQ QSO with regard to the Sy1s is caused by the strength of the big blue bump in the former. However, the extinction values inferred from the optical depth of the silicate feature at 9.7 µm or the X-ray column density (N_H) are much higher (see Prieto et al. 2010, and references therein). The former correspond to interferometric measurements in the MIR at very high-spatial resolution, and are found to be systematically higher by factors of 2–3, suggesting that the obscuring material is concentrated in the location of the nucleus rather than being smoothly distributed. On the other hand, the extinctions derived from the X-ray column density are orders of magnitude higher than those derived from the silicate feature. This difference rely probably on the standard Galactic dust-to-gas ratio assumed to translate the column density into extinction values, which seems to be not valid for AGN environments (Gaskell et al. 2004).

Fitting the type 1 SEDs to that of a type 2 shows us that the energy output of a genuine Sy2 nucleus can be very well described in terms of an obscured Sy1 or even an obscured RQ QSO, since the shape of the broad-band SED for the average Sy2 shortwards of $\sim 10\,\mu$m basically follows the fall of an extinction curve with $A_V \sim 5$ mag (Cardelli et al. 1989). However, some aspects suggest that the geometry very close to the AGN is not so simple. The higher extinction values derived from the silicate feature using interferometric data and the rapid variations of the X-ray absorber detected for some Seyfert 2s (e.g. NGC 7582, see Bianchi et al. 2009) suggest that the absorber is more concentrated and adopts a clumpy distribution (e.g. clouds) when we look very close around the central engine. For comparison, the fitting of clumpy torus models to high-spatial resolution data in the MIR by Ramos Almeida et al. (2009) yields extinction values higher than $A_V \gtrsim 50$ mag for type 2 AGNs. Finally, the X-ray data shown in Fig. 4.2 is corrected for absorption and thus do not reflect strong differences among the AGN classes. The spectral slope at radio and probably hard X-ray wavelengths is not very sensitive to changes in luminosity of the central source, as these ranges appear to be very similar for the scaled SED of both Seyferts and the RQ QSO. In contrast, the NIR to UV range differs strongly.

4.3 Low-luminosity nuclei

The SED of LLAGNs with low Eddington ratios ($L_{bol}/L_{Edd} < 10^{-3}$) is usually characterized by the absence of the big blue bump, at the expense of a MIR peak or "big red bump" (Ho 1999). As a consequence, the optical-UV slope is very steep and the X-ray-to-optical ratio is large, with no evidence for a soft X-ray excess. Finally, based on its radio-to-optical luminosity and radio-loudness, the shape of the SED for LLAGNs reminds distantly to that of radio-loud quasars (Ho 2008; Eracleous et al.

2010). In line with this, parsec-scale radio jets have been found to be more frequent in LLAGNs than in Seyferts (Nagar et al. 2005).

Fig. 4.3 shows the rest-frame HSR SEDs of the three LLAGNs in our sample: NGC 1097 (red dots), NGC 1052 (green dots) and NGC 1386 (yellow dots). These are compared with an average LINER template also built from HSR data (open triangles, Eracleous et al. 2010). As in the previous case, the HSR SEDs differ from those acquired with a lower spatial resolution (spikes in Fig. 4.3, see Tables 4.2, 4.3 and 4.4), specially in the optical/UV and in the MIR for the case of NGC 1097, due to the contribution of the starburst ring. The nucleus of NGC 1386 is obscured by a dust lane and it is only visible longwards of $\gtrsim 1.6\,\mu$m. At first glance, the low-luminosity SEDs have a different shape when compared with the brighter ones, with the big blue bump absent even for NGC 1097, which is an unobscured type 1 object. In contrast, the HSR SED for this nucleus presents a maximum in the NIR at $\sim 2\,\mu$m, while the rest of the objects peak at $\sim 10\,\mu$m. Shortwards of these maxima, the SEDs present a steep decrease with a tiny excess in the NIR range and a subsequent rise in the X-rays. Longwards of $\sim 20\,\mu$m all the SEDs decrease towards radio wavelengths, with a more pronounced slope in the cases of NGC 1097 and NGC 1386 but flatter in the case of NGC 1052, probably due to the contribution of the radio jet. Although NGC 1386 also shows signs or a recently formed elongated radio structure in its core (see Fig. 3.5, Mundell et al. 2009), this "tiny jet" only takes account for $\sim 15\%$ of the nuclear flux at 8.4 GHz. Overall, individual SEDs are very similar to the average LINER template in the optical and radio ranges, but the X-ray-to-optical ratio of the average LINER is much flatter, reaching its maximum for the Sy2 NGC 1386. However, our SEDs sample the MIR range, absent in the average template by Eracleous et al. (2010), where the contribution of the big red bump reaches its maximum. Note the overall similarity among the individual SEDs, even although they are still not scaled by their mean power.

The shape of the energy distribution for NGC 1097 changes slightly when compared with the type 2 objects NGC 1052 or NGC 1386 which, based on their respective radio jet and NLR, have a nearly edge-on orientation. In the case of NGC 1097, the big red bump peaks at bluer wavelengths and the X-ray and radio emission are lower when compared with the optical/IR part. Since this is a type 1 object, a lower dust content along the line of sight could explain the former. Nevertheless, changes in the shape of the SED are expected for lower Eddington ratios: decreasing L_{bol}/L_{Edd} recedes the big blue bump to longer wavelengths, while the X-ray and radio emission increase (Ho 2008). For values lower than $L_{bol}/L_{Edd} < 10^{-3}$ this feature is no longer detected and the distribution shows a peak in the MIR range. Following this, NGC 1097, which also suffered a transition to a Sy1 type, seems to have a higher Eddington ratio than NGC 1052 or NGC 1386. Overall, the three SEDs

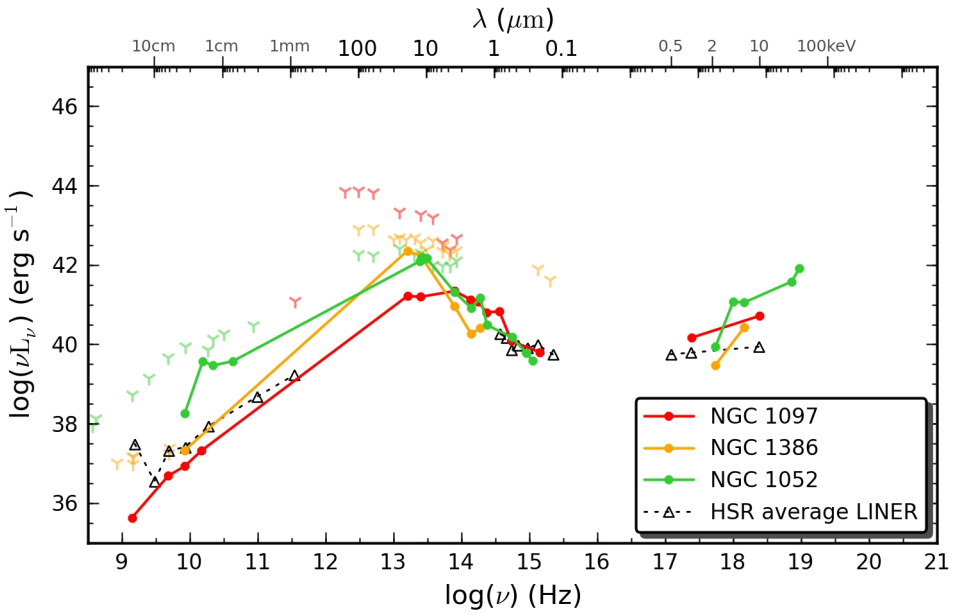

FIGURE 4.3— Spectral energy distribution for the LINER 1 NGC 1097 (red dots), the Sy2 NGC 1386 (yellow dots) and the LINER 1.9 NGC 1052 (green dots). The three-spike symbols correspond to data with lower-spatial resolution. An average template derived from a sample of LINERs by Eracleous et al. (2010) is also shown for comparison (black open triangles).

present very similar X-ray-to-optical ratios and a power-law like decreasing slope from their IR maximum to the optical range.

In a similar way as described in Section 4.2, we built the HSR average energy distribution of the LLAGNs in the sample, normalizing the individual SEDs by their mean power before the average. Fig. 4.4 shows the average distribution for LLAGNs (black dots) compared with that of Sy1s (blue dots) and Sy2s (orange dots) presented in Section 4.2. As mentioned before, both types of Seyferts are very similar over the radio, MIR and X-ray range, and their differences in the NIR to UV range can be well explained in terms of obscuration of the central source. However, LLAGNs only exhibit a similar behaviour in the MIR and the increasing flux with wavelength in the X-rays. In the radio range, the SEDs of NGC 1097 and NGC 1386 are more similar to the Seyfert templates, while that of NGC 1052 resembles to RL QSOs (see Fig. 4.7), probably due to the contribution of the twin parsec-scale radio jet. Shortwards of 10 μm, LLAGNs shows some features around $\sim$ 1 μm which might be associated with contamination by stellar light from the host galaxy. However, the general trend seems to follow the above-mentioned power-law decreasing slope from the MIR to the optical

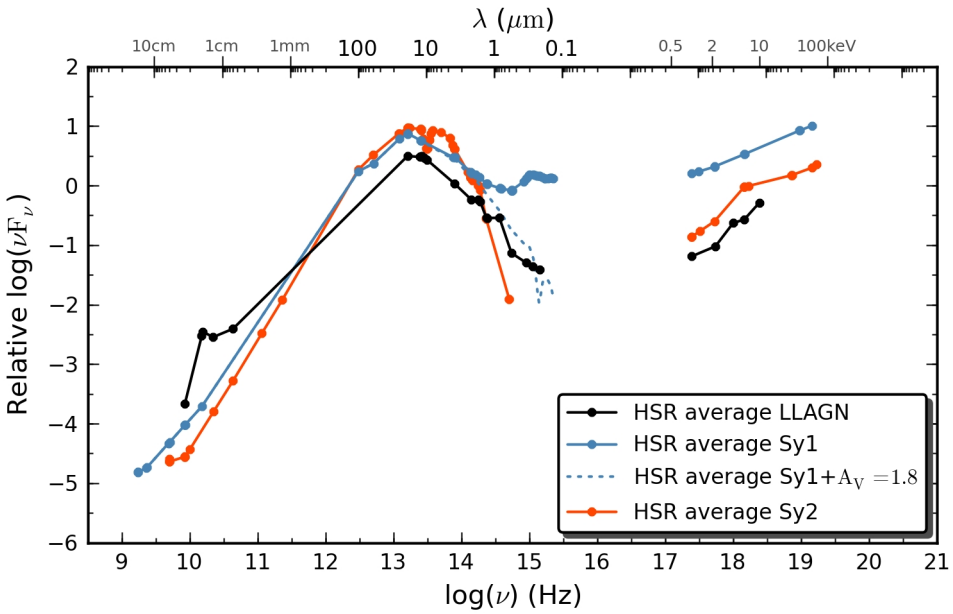

FIGURE 4.4— SEDs for the HSR Sy1 (blue colour) and HSR Sy2 templates (orange) from Prieto et al. (2010) and the average LLAGNs (black). The latter cannot be explained in terms of an obscured HSR Sy1 (dotted lines).

range. This behaviour is in contrast with the Sy2 template, which basically follows the fall of a extinction curve in this range, or the Sy1 template, rising in the optical/UV due to the contribution from the accretion disk. In order to explain the LLAGN average SED in terms of obscuration, we performed a fit of the Sy1 template in the MIR-to-optical range to obtain both a scaling factor and an extinction value (see Fig. 4.4). The latter resulted in $A_V = 1.8$ mag, but the shape of the average SED for LLAGNs (black dots in Fig. 4.4) is not well reproduced by the obscured Sy1 template –as in the case of Sy2s–, specially in the optical range where the Sy1 SED rises and the effect of the extinction is more noticeable (blue-dotted line in Fig 4.4).

In Fig. 4.5 we compare the average SED for LLAGNs derived in this work (black dots) with similar templates in the literature. One of them corresponds to the average of the data provided by Ho (1999) for 7 LINERs (blue dots, see individual SEDs in Fig. 1.6), following the same method explained in Section 4.2 for the average and rejecting the IR data due to their lower spatial resolution. The other LINER template corresponds to the average presented by Eracleous et al. (2010) for a sample of 21 objects (open triangles). The radio-loud quasar provided by Elvis et al. (1994) is also shown for comparison (green-solid line). The templates are scaled

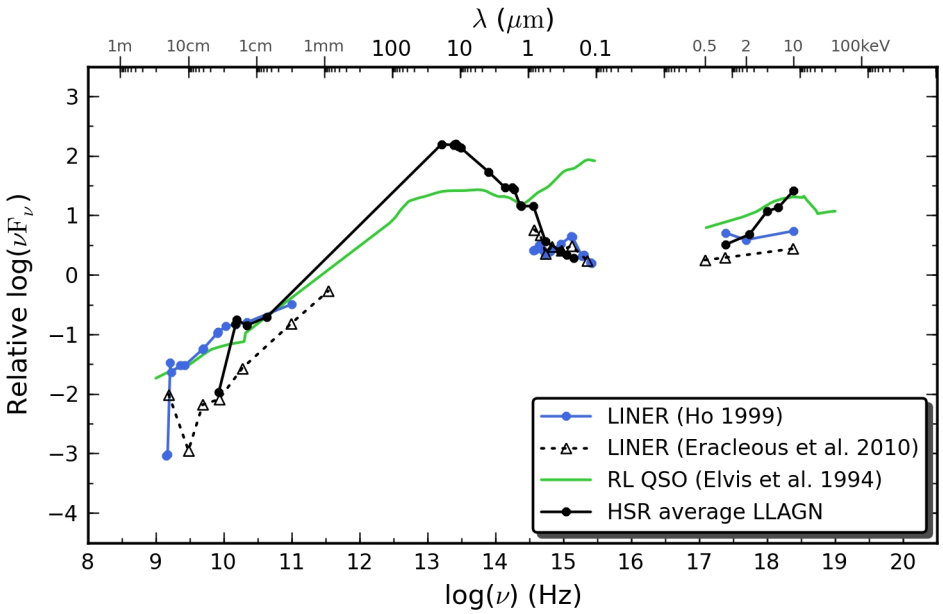

FIGURE 4.5— Two SED templates for LINERs are compared with our LLAGN average SED (black dots) and the radio-loud quasar template (green-solid line, Elvis et al. 1994). One of the LINER templates is obtained, as in Section 4.2, by averaging the data provided by Ho (1999) for 7 objects (blue dots). The second LINER template (black open triangles) corresponds to that of Eracleous et al. (2010).

arbitrarily to coincide in the radio and optical ranges. As shown by this Fig. 4.5, the LINER templates and the average for LLAGNs present a similar trend at the common wavelengths, i.e. radio, optical and X-rays. The average for LLAGNs is very steep at the lowest frequency value, but this is probably caused by the lack of data for NGC 1052 in this range, which is very bright and contributes to the average only at higher frequencies. A similar effect occurs on the average for the data by Ho (1999). On the other hand, our template has a similar shape in the optical/UV range when compared with that of Eracleous et al. (2010), while the one by Ho (1999) display a soft maximum shortwards of $\sim 1\,\mu$m. The latter reminds by far the rise of the big blue bump feature in quasars, although it could be caused also by contamination from stellar light. In the X-ray range our template shows a steeper rise towards higher frequencies, while those for LINERs increase softly and more similar to the quasar template. However, our template provides information in the NIR and MIR ranges at high-spatial resolution ($\lesssim 0\farcs2$ in the NIR and $\lesssim 1''$ in the MIR). When compared with the radio-loud quasar, LLAGNs show a strong bump in the 2–10 μm range with a decrease towards the optical/UV range. The latter seems to follow a power law rather than being absorbed by dust, suggesting that the absence of big blue bump in the SED

of LLAGNs in not simply a matter of obscuration of the central engine.

Within the unification scheme for Seyfert galaxies, it is believed that the Broad Line Region (BLR) and the nuclear continuum source are hidden, for type 2 objects, by an absorbing, edge-on torus. In contrast, for Sy1s our line of sight is directed within the absorption-free visibility cones (Antonucci & Miller 1985). Similarly, a combination of obscuration and beaming is essential for the unification of powerful radio sources (Barthel 1989). However, Fig. 4.5 suggests that this is not the case for LLAGNs. Furthermore, Chiaberge et al. (1999) found optical compact central cores dominated by a non-thermal synchrotron component in 85% of the objects of their low-luminosity radio galaxy sample. The latter points to a direct view of the innermost nuclear regions, suggesting that a "standard" parsec scale, geometrically thick torus is not present in low-luminosity radio galaxies. A different view is given by the models for Radiatively Inefficient Accretion Flows (RIAFs). In the schema explained by Ho (2008), the thin disk considered in classical AGN models recedes to larger radii as the accretion rate drops. At $r \sim 100$–$1000\,R_S$ the disk switches to a RIAF, in which the accreted material is tenuous, optically thin and cannot cool efficiently. As a consequence, the accretion flow blows up into a hot and vertically thick structure that could explain the formation of radio jets, common at the lower luminosity end of AGNs. In this context, the big red bump in LLAGNs can be produced by thermal emission from the disk, which is cooler due to both the lower accretion rate and the truncation at lower radii where the big blue bump originates.

4.4 The importance of the high-spatial resolution

In this thesis, we presented a set of high-spatial resolution SEDs for the central parsecs of a sample of nearby AGNs including 2 LINERs, 3 Seyferts and a Starburst. Since most of these systems show the presence of large quantities of dust in their nuclei, the spatial resolution in the NIR becomes essential in both the alignment process and the isolation of the AGN emission from the contribution of the host galaxy, specially for low-luminosity active nuclei. As an example, Prieto et al. (2010) show that AGN fluxes from large aperture data can be overestimated by an order of magnitude, distorting the bolometric luminosities based on high-spatial resolution data. Furthermore, a composite nuclear SED based on a vague alignment might include contributions from different sources at different wavelength ranges, as in the case of NGC 253 (Fernández-Ontiveros et al. 2009). Therefore, low-spatial resolution fluxes are not representative of the AGN emission, except for very bright QSO-like nuclei with $L \gtrsim 10^{44}\,\mathrm{erg\,s^{-1}}$ (Prieto et al. 2010), but even in this case one can find exceptions like NGC 7469, in which most of the infrared luminosity ($L_{IR} \approx 2 \times 10^{44}\,\mathrm{erg\,s^{-1}}$) is dominated by the starburst ring. At the far end, low-luminosity and/or very obscured nuclei with different structures close to the AGN (i.e. circumnuclear rings, starburst disks, etc.)

can be completely masked at certain wavelength ranges of their SEDs. For example, a strong starburst is able to dominate the optical/UV range and, in the presence of dust, contribute also to the IR due to reprocessed radiation released in this range.

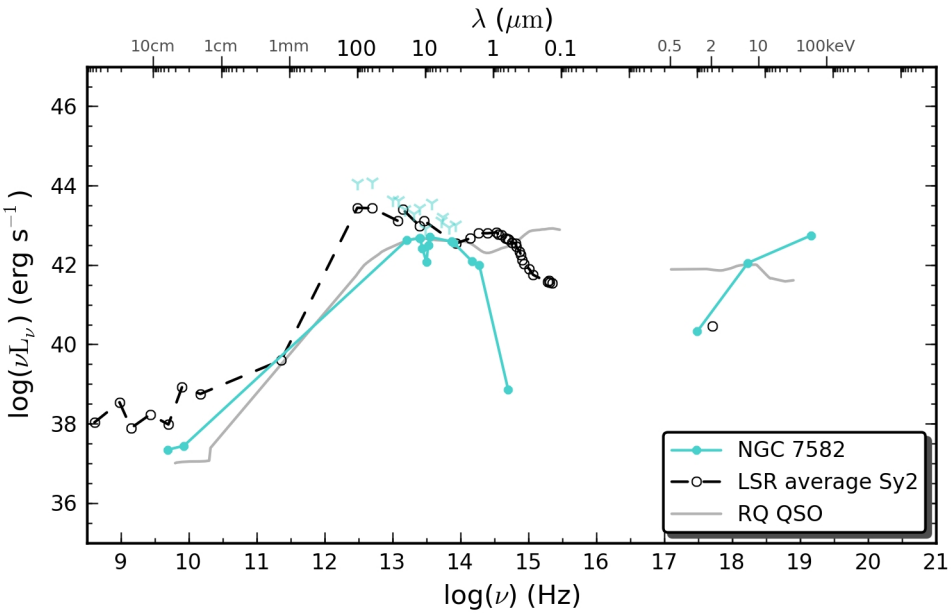

FIGURE 4.6— High-spatial resolution SED for the Sy2 plus starburst NGC 7582 (turquoise dots) and its correspondent low-spatial resolution data (turquoise spikes), compared with a low-spatial resolution average Sy2 template (open circles, Schmitt et al. 1997) and a RQ QSO (grey-solid line, Elvis et al. 1994).

Fig. 4.6 shows an illustrative case for the impact of the spatial resolution in the case of bright obscured nuclei. The HSR SED of NGC 7582 (a bright Sy2, turquoise dots) is plotted together with its low-spatial resolution (LSR) SED (turquoise spikes), a representative Sy2 derived from LSR data (open circles, Schmitt et al. 1997) and a template for a bright radio-quiet QSO (RQ QSO, grey-solid line) derived by Elvis et al. (1994). Both the RQ QSO and the LSR Sy2 templates are scaled to the luminosity at $\sim$ 2 μm since the nucleus is by far the dominant source in the VLT/NaCo *K*-band images. Surprisingly, the two main features in the LSR Sy2, a bump around $\sim$ 1 μm and a strong maximum in the 10–100 μm range, are not related with the direct contribution of the AGN itself. The former is probably associated with the old stellar population from the host galaxy, while the latter is probably due to hot dust at $\sim$ 30–300 K, mostly heated by star-formation, since the contribution of the AGN is much lower. Moreover, the LSR fluxes measured for NGC 7582, which also presents a nuclear starburst, match

closely the LSR Sy2 template. In the X-rays, the single value of the LSR template is consistent with HSR data, suggesting that high energies ($\gtrsim 2\,$keV) might be governed by the AGN component. The comparison of NGC 7582 with the RQ QSO is also interesting, since both show a similar trend from the IR towards radio wavelengths. As mentioned before, the spatial resolution is not critical in the case of quasar nuclei, as they are considerably much brighter than their hosts. In the optical, the SED of NGC 7582 is completely obscured, while that of the RQ QSO exhibits its characteristic big blue bump. However, in the X-rays both SEDs are consistent at energies higher than $\sim 2\,$keV.

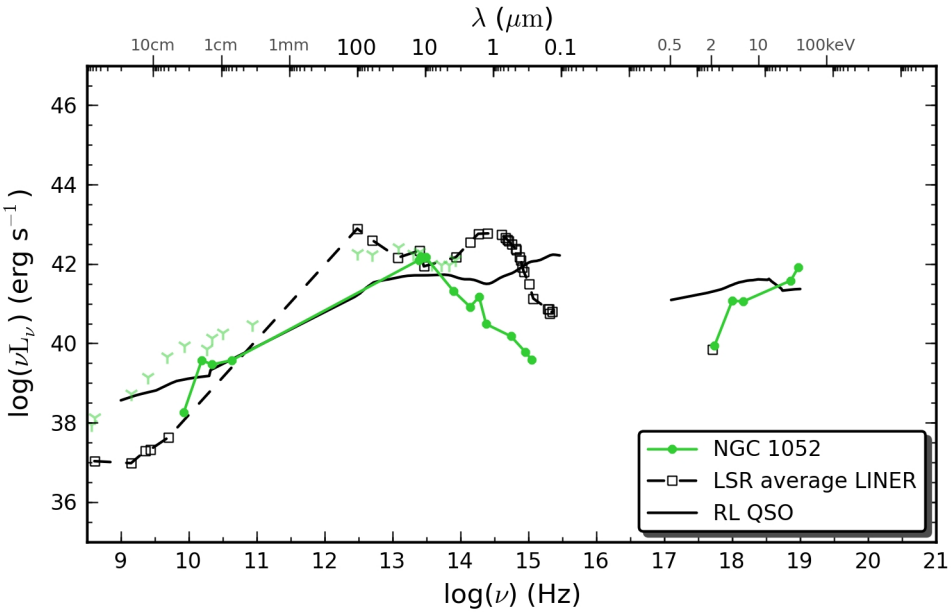

FIGURE 4.7— Spectral energy distribution for the prototypical LINER NGC 1052 (green dots) compared with an average LINER SED derived from low-spatial resolution (LSR) data (open squares, Schmitt et al. 1997) and a RL QSO (black-solid line, Elvis et al. 1994).

A more dramatic example for the effect of the spatial resolution in the shape of the SEDs of AGNs is found for LLAGNs. Fig. 4.7 shows the HSR SED of NGC 1052 (green dots) and its correspondent LSR data (green spikes), which are compared with a LSR average SED for LINERs (open squares, Schmitt et al. 1997) and a radio-loud QSO (RL QSO, black-solid line, Elvis et al. 1994). In this case, the LSR LINER template was scaled to the MIR peak in the SED of NGC 1052. The emission in this range is dominated by the AGN, as shown by the VLT/VISIR images and the LSR data longwards of 10 μm, with is in agreement with the HSR SED. However, the RL QSO

was scaled to the radio slope of NGC 1052, since the origin of the MIR emission in the former probably has a different origin (see Section 4.3), and the main contribution in this range seems to comes from radio jets in bot NGC 1052 and RL QSOs.

As in the previous case, an outstanding difference between the HSR SED of NGC 1052 and the LSR LINER is the contribution of the stellar population from the host galaxy at $\sim 1\,\mu$m, which completely dominates the SED in the NIR, optical and UV ranges. This trend is also suggested by the rise of the flux measured by *Spitzer* shortwards of $\sim 3\,\mu$m (green spikes). Therefore, the stellar light masks the real energy distribution of the LINER nuclei in this range. This, in contrast, peaks at MIR wavelengths and falls shortwards of $10\,\mu$m following a power-law slope with $\alpha \approx 2.6$ in the case of NGC 1052. When compared with the RL QSO, the SED of NGC 1052 displays a quasi-identical radio-to-MIR ratio, except at the lowest frequencies, with a flat distribution ($\alpha \approx 0.1$) and a very similar MIR-to-X-ray ratio. However, the big blue bump is absent in NGC 1052. The similarities are particularly surprising since QSOs are more than four orders of magnitude brighter than LINERs and do not habit the local universe, as LINERs do. Nevertheless, it seems that, for radio-loud objects, the inner source that originates the jets and the X-ray emission scales with luminosity without strong variations in the main body of the SED. However QSOs do not show a big red bump as in the case of LINERs, but only a soft maximum detected in the MIR. For NGC 1097 and NGC 1386, which do not show strong radio emission, the turnover from the MIR to radio wavelengths is more similar to the LSR LINER, with a steeper slope of about $\alpha \sim -0.3$.

Overall, one of the main differences between the LSR and the HSR SEDs is the lower radio-to-MIR ratio in the former, which may be produced by an observational bias or may be due to the higher contribution from hot dust ($\sim 300\,$K) heated by star-formation in starburst rings or disks and included in LSR data. NGC 1097 is a particularly clear example, dominated in the MIR by the starburst ring component. Finally, HSR SEDs exhibit a steeper decrease shortwards of $\sim 10\,\mu$m due to the isolation of the non-stellar nuclear light from the stellar contribution of the host galaxy.

4.5 The missing nucleus of NGC 253

As mentioned in Section 3.2.1, in the nucleus of this galaxy the radio emission is dominated by the source TH2 (Turner & Ho 1985), which is not only the strongest (21 mJy at 1.3 cm) but also the most compact ($< 2\,$pc) and the one with the highest brightness-temperature ($T_{2\,\mathrm{cm}} > 40\,000\,$K) in the central region. For these reasons, it has been historically assumed to be the radio counterpart of an AGN. The detection of a broad H_2O maser ($\Delta v \sim 100\,\mathrm{km\,s^{-1}}$) and the large velocity gradient in the H92α radio-recombination line ($\sim 110\,\mathrm{km\,s^{-1}\,arcsec^{-1}}$) suggested the presence of a dynamical mass of about $\sim 7 \times 10^6\,M_\odot$ (Nakai et al. 1995; Rodríguez-Rico et al. 2006), and

moreover, the H92α and H75α lines are consistent with ionization produced by an AGN (Mohan et al. 2002).

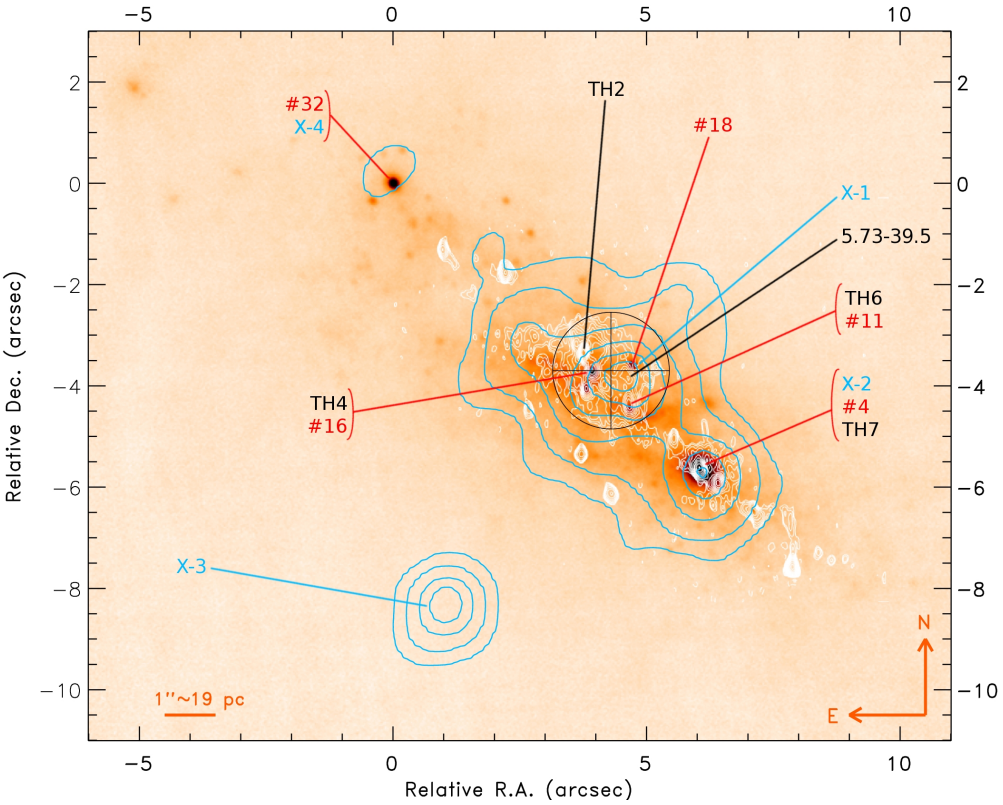

FIGURE 4.8— VLT/NaCo *L*-band map for the central $17'' \times 14''$ of NGC 253 plus VLA map at 2 cm (in white, from Ulvestad & Antonucci 1997) and the contours for the 4–10 keV X-ray band (in blue). Relevant sources at radio, IR and X-ray wavelengths are indicated in black, red and blue colours, respectively. The region where the stellar kinematic centre can be located is indicated by a crossed-circle with a radius of $\sim 1\farcs2$. Adapted from Müller-Sánchez et al. (2010).

Surprisingly, our new alignment (see Section 2.3.2, Fig. 2.2) revealed that this strongest radio source is not associated with any other source at optical or IR wavelengths. Although some diffuse IR emission is found at this position, yet, no point-like source commensurable with its radio strength is detected. This is a remarkable feature, since AGNs are usually strong sources in the NIR and MIR, mostly due to the presence of hot dust being accreted in the surroundings of the central black hole. Furthermore, a recent study by Brunthaler et al. (2009) demonstrated that the maser is instead associated with a close star-forming region, TH4, instead of TH2.

Additionally, a stellar cluster younger than 0.1 Myr cannot be completely ruled out as the origin of the H92α and H75α lines (Mohan et al. 2002). Fig. 4.8 shows the *L*-band image for the central region of NGC 253 together with the radio map at 2 cm (in white) and the overlaid contours for the 4–10 keV X-ray band (in blue). The relevant radio, IR and X-ray sources are labelled in the Figure in black, red and blue colours, respectively. As shown previously in Fig. 2.4, two of the brightest IR knots (#4 and #32) have individual counterparts in the X-rays (X-2 and X-4, respectively).

In the majority of AGNs, the source of the nuclear activity is expected to be located at the bottom of the potential well, which is traced by the kinematical centre of the galaxy. For NGC 253, this centre cannot be located more precisely than within a circle of radius $\sim 1\farcs2$ (22.8 pc, crossed-circle in Fig. 4.8), as derived from seeing-limited 3D spectroscopy data in the NIR acquired with VLT/SINFONI (Müller-Sánchez et al. 2010). This area encircles a total of 15 sources detected at different wavelengths: 6 sources in radio (including TH2), 8 IR knots and the X-1 source in the hard X-rays. In this scenario, the most likely candidates for being the counterpart of a central massive compact object are: *i)* the strongest and compact radio source TH2, and *ii)* the hard X-ray source X-1. However, as explained in Section 2.3.2, their positions are not compatible. The rest of sources in this area resemble either young massive clusters (YMCs) or supernova remnants (Ulvestad & Antonucci 1997; Lenc & Tingay 2006; Fernández-Ontiveros et al. 2009). Other X-ray sources like X-2 and X-3 are located $\sim 2\farcs6$ (49 pc) and $\sim 6''$ (114 pc) away from the kinematical centre (see Fig. 4.8), and thus are not considered as alternatives for being identified with the nucleus of this galaxy.

4.5.1 TH2

In the first place, we are going to focus on TH2. This is a very peculiar source detected only in the 2.3–23 GHz range (Sadler et al. 1995; Lenc & Tingay 2006), but undetected at lower frequencies probably due to strong free-free absorption (Tingay 2004). VLBI observations at higher spatial resolution ($\sim 15 \times 11$ mas^2 at 2.3 GHz and 2.5×1.1 mas^2 at 23 GHz) show that TH2 is completely resolved with an upper sensitivity limit of $\sim$ 1.1 mJy (Lenc & Tingay 2006; Brunthaler et al. 2009). Since this source is unresolved in the VLA maps (< 100 mas), we can derive an approximate size of ~ 0.5–1.9 pc.

To investigate the nature of this source, we compared it with Sgr A* in the Galactic Centre, another compact radio source with no optical counterpart, although the latter is much fainter than TH2. Fig. 4.9 shows the radio spectrum of Sgr A* (red stars, Falcke et al. 1998; An et al. 2005) scaled to that of TH2 at 2 cm (black dots, Sadler et al. 1995; Ulvestad & Antonucci 1997). As several IR flares have been detected in Sgr A*, we also included measurements for two of them in the *L*-band reported by Ghez et al. (2004). Both flares, without reddening correction and scaled by the same

factor as the radio data, fall just 3σ above the diffuse background level in NGC 253[1] (blue dots). A priori, based on its radio luminosity, one would expect an IR bump peaking at $\nu L_\nu \gtrsim 10^{41}\,\mathrm{erg\,s^{-1}}$, as for other AGNs in the sample (see Figs 4.1 and 4.3), but this is not the case. In contrast, most of the IR luminosity in NGC 253 comes from the contribution of the starburst component. For comparison, Fig. 4.9 shows the sum of all the knots found in Section 3.2.1 (purple dots), *IRAS* data in the IR (purple spikes, Sanders et al. 2003) and a model that reproduces the integrated emission from NGC 253 (green-solid line, Siebenmorgen & Krügel 2007).

Overall, AGNs present IR-to-radio ratios considerably higher than Sgr A*, since the latter lacks of a dusty torus or a similar dusty structure able to reprocess the emission at higher energies (Güsten et al. 1987). Therefore, our results for TH2 suggest that this source resembles closely Sgr A* rather than a classical AGN. Moreover, this source could be the counterpart for a SMBH located at the dynamical centre of this galaxy, although we cannot confirm or rule out this possibility (Müller-Sánchez et al. 2010).

4.5.2 X-1

Back to X-1, previous *Chandra* observations already revealed that this is a heavily obscured hard X-ray source embedded in the nuclear starburst, but it was assumed to be coincident with the radio core TH2 (Weaver et al. 2002). The reprocessed *Chandra* dataset (see Section 2.2.4) reveal that the position of X-1 is located $\sim 1\farcs1$ south-west of TH2 and its best fit X-ray spectrum consists on two absorbed power-laws with $N_{H1} = 4\times10^{22}\,\mathrm{cm^{-2}}$ and $N_{H2} = 7.5\times10^{23}\,\mathrm{cm^{-2}}$, respectively (Müller-Sánchez et al. 2010). Following the relation between the visual extinction and the hydrogen column density given by Predehl & Schmitt (1995) for the Milky Way $\left[N_H/A_V = 1.85\times10^{21}\,\mathrm{cm^{-1}\,mag^{-1}},\ \mathrm{R_V} = \mathrm{A_V/E(B-V)} = 3.1\right]$, the extinction associated with N_{H1} corresponds to $A_{V1} = 21.6\,\mathrm{mag}$, a factor of ~ 3 that of the knot #18 which is the closest one (see Table 3.1). The second component N_{H2} is much higher ($A_{V2} > 400\,\mathrm{mag}$) and indicates that X-1 is a "buried" source, a fact supported by the lack of emission in the soft X-ray band (0.5–2.0 keV). Furthermore, the low $F_{0.5-2\,\mathrm{keV}}/F_{2-10\,\mathrm{keV}}$ ratio of about 3×10^{-3}, together with the high value for the absorber N_{H2}, points to X-1 as a hidden AGN (Ueda et al. 2007; Winter et al. 2009; Müller-Sánchez et al. 2010). Furthermore, the intrinsic X-ray luminosity of X-1 , $L_{2-10\,\mathrm{keV}} \sim 10^{40}\,\mathrm{erg\,s^{-1}}$, is typical of LLAGNs (Terashima et al. 2002; González-Martín et al. 2009a). An alternative scenario contemplates X-1 as a background AGN, but the precise location in the kinematic centre of NGC 253 seems very unlikely, as discussed in Müller-Sánchez et al. (2010). Moreover, X-1 may have radio and/or IR

[1] See Section 5.4.7 for details on the background estimation.

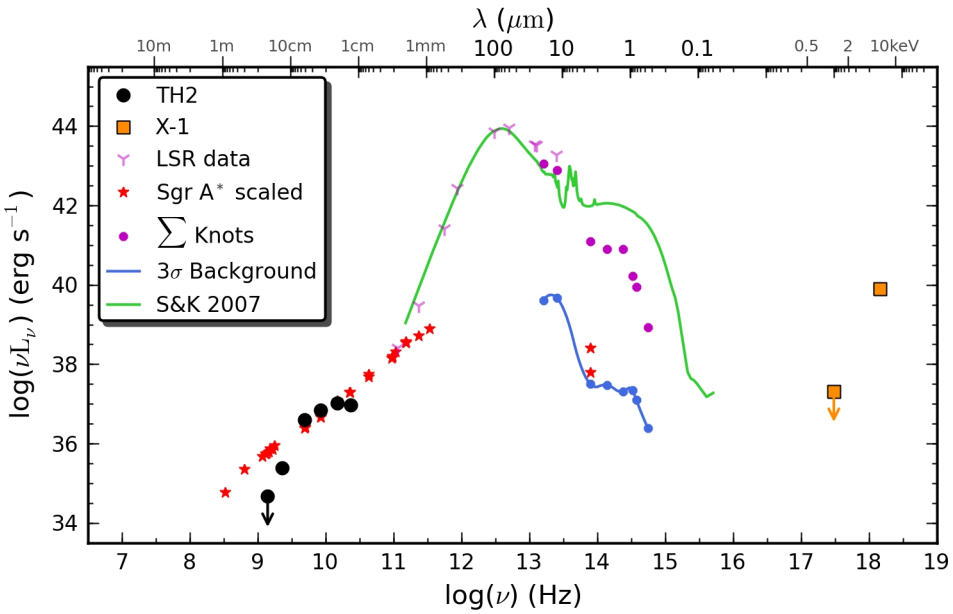

FIGURE 4.9— SEDs for TH2, the strongest radio source in NGC 253 (black dots, Sadler et al. 1995; Ulvestad & Antonucci 1997), X-1, the hardest X-ray source (orange squares), a scaled distribution of Sgr A* (red stars, Falcke et al. 1998; An et al. 2005). We also show the sum of all the star-forming knots found in Section 3.2.1 (purple dots), the 3σ median background distribution (blue dots, see Section 5.4.7), aperture photometry for the nuclear region based on LSR data (purple spikes) and a model template for NGC 253 based on LSR data (green-solid line, Siebenmorgen & Krügel 2007).

counterparts which are located in the galaxy.

However, if X-1 is indeed a very obscured source, one would expect a re-emission in the IR of the absorbed ionizing radiation. The nearest sources are the knots #11 and #18, the former associated with the radio source TH6 (see Fig. 4.8). Another radio source without an IR counterpart, 5.73–39.5, is compatible with the position of X-1, although it has been detected only at 8.4 and 23 GHz. The IR sources present similar sizes (3–5 pc), fluxes ($\sim$ 2–3 mJy) and SED shapes when compared with the rest of the knots found in the centre of NGC 253, and thus do not show any peculiarity to distinguish any of them as a possible counterpart for X-1.

In this context, it is very interesting the case of NGC 4945, one of the brightest extragalactic sources at 100 keV and also one of the closest galaxies where an AGN and a starburst coexist (Done et al. 1996). This is a nearly edge-on ($i \sim 80°$) SB(s)cd or SAB(s)cd nearby galaxy ($D = 3.8$ Mpc; Karachentsev et al. 2007) which shows strong starburst activity in the inner $\sim$ 100 pc and a central conical cavity evacuated by a supernova-driven wind (see Marconi et al. 2000, and references therein). However, the

only evidence for the presence of an AGN in this object comes from the detection of a bright, Compton-thick and variable hard X-ray core ($L_{2-10\,\mathrm{keV}} = 3 \times 10^{42}\,\mathrm{erg\,s^{-1}}$, $N_H \sim 5 \times 10^{24}\,\mathrm{cm^{-2}}$; Iwasawa et al. 1993; Guainazzi et al. 2000). No other manifestation of the AGN is found, neither a strong point source in the UV, optical or IR nor dilution of the CO stellar features (Marconi et al. 2000), although a jet-like structure detected at 2.3 GHz (VLBI map) in the central parsecs could be related with the X-ray core (Lenc & Tingay 2009). Moreover, high excitation gas emission lines are not observed in this object, and the conical cavity shows lower excitation that the surroundings. It seems that basically all the UV photons are absorbed within the inner $r \lesssim 1\farcs5$ ($\lesssim 30$ pc) along all lines of sight. This is indeed in contrast with the standard unified model for AGNs, in which the ionizing radiation escapes along the torus axis direction (Marconi et al. 2000), and also with theoretical predictions for LLAGNs, since the obscuring structure is supposedly no longer supported due to the faintness of the active nucleus (Elitzur & Shlosman 2006; Hönig & Beckert 2007). Nevertheless, the case of NGC 4945 proves that it is possible to hide an AGN contributing significantly to the bolometric emission, whereas optical to MIR spectroscopy and imaging reveal only a starburst component (Marconi et al. 2000).

4.6 Summary

Along this Chapter we have shown the impact of using high-spatial resolution data in the study of AGNs. Previous works using low-spatial resolution are only significant for luminous objects, i.e. quasars and bright Seyferts ($\gtrsim 10^{44}\,\mathrm{erg\,s^{-1}}$), in which the contamination of the host galaxy is negligible. Still, there are exceptions, as is the case of NGC 7469. High-spatial resolution SEDs for both Seyferts types are characterized basically by a strong IR bump and an increase of their power with frequency at high energies, while at radio wavelengths they appear to have a shape similar to radio-quiet quasars. In contrast, the differences between types 1 and 2 become evident in the optical/UV range, where the footprint of the big blue bump is noticed (see Fig. 4.2).

However, the need of high-spatial resolution becomes critical at the lowest luminosities. Our average template for LLAGNs samples all the wavelength ranges accessible at parsec scales nowadays, i.e. radio, IR, optical and UV, plus the X-rays. Despite of the assorted nature of the nuclei, our sample is very consistent in terms of luminosities (see Fig. 4.3) and distances (~ 16 Mpc). The recent work by Eracleous et al. (2010) includes a wider sample with 21 LINERs, but their spectral coverage is limited to radio, optical/UV and X-rays. Without the IR part, the average LINER SED resembles that of a radio-loud quasar, i.e. based on the radio-to-optical and optical-to-X-ray slopes. However, Figs 4.4 and 4.7 shows that the IR contribution is much higher than that suggested by the similarity with the RL QSO template. Furthermore, the individual SEDs follow closely a power-law behaviour from the IR to the optical/UV

range, which do not seem to be produced by extinction (Fig. 4.4). Although we still need more statistics to confirm this behaviour, the three LLAGNs in our sample are very consistent, showing strong maxima in the IR. Interesting aspects for a further study using a larger sample are the variations in the "big red bump" (peak wavelength and width) and the variations of the power-law like slope from the IR to the optical range.

A special case is the nucleus of NGC 253. The hard X-ray source X-1 is the brighter one but is only detected shortwards of $\gtrsim 2\,\mathrm{keV}$, meeting the requirements for being a hidden AGN. In the rest of the spectral range this source remains invisible. On the other hand, the powerful radio source TH2 was historically considered as a radio counterpart of X-1, but our new alignment proved that the locations of both sources are not compatible (Fig. 4.8). However, TH2 is still a candidate for being a radio-loud analogous of Sgr A* in the centre of our galaxy. When compared with the case of NGC 4945, this galaxy share many similarities with NGC 253. First of all, both have nearly edge-on orientations, are closer than 4 Mpc and present similar global IR luminosities (Rice et al. 1988). Moreover, both share a bar associated with the disk of the galaxy, a fast-rotating disk of cold gas, a nuclear starburst ring and a conical nuclear outflow (see Lenc & Tingay 2009, and references therein). Whereas all their IR properties are completely consistent with starburst activity, its strong hard X-ray emission cannot be easily explained without the presence of a hidden AGN, obscured even at MIR wavelengths. In this context, these objects can be considered as "local ULIRGs", in which the strong starburst and the AGN components compete against each other to drive the total energy output (Marconi et al. 2000).

TABLE 4.2— SED for the core of NGC 1097 at high and low-spatial resolution.

Origin	$\log(\nu/\mathrm{Hz})$	$\log(\nu \mathbf{F}_\nu/\mathrm{Jy\,Hz})$	**Error (%)**
ASCA 2–10 keV[a]	18.38	11.31	3
ASCA 0.5–4 keV[a]	17.38	10.76	1
HST/WFPC2 F218W	15.15	10.40	7
HST/WFPC F555W	14.73	10.68	1
HST/ACS-WFC F814W	14.56	11.43	1
VLT/NaCo *J*	14.36	11.40	1
VLT/NaCo *H*	14.25	11.68	1
VLT/NaCo *Ks*	14.13	11.73	1
VLT/NaCo L'	13.90	11.94	1
VLT/VISIR 11.88 μm[b]	13.40	11.80	11
VLT/VISIR 18.72 μm[b]	13.20	11.82	5
VLA[c]	10.17	7.92	10
VLA[c]	9.92	7.53	2
VLA[d]	9.68	7.28	7
VLA[d]	9.15	6.23	17
Spitzer/IRAC 3.6 μm[e]	13.92	13.28	1
Spitzer/IRAC 4.5 μm[e]	13.82	12.98	1
Spitzer/IRAC 5.8 μm[e]	13.71	13.16	2
Spitzer/IRAC 8.0 μm[e]	13.57	13.79	3
IRAS 12 μm[f]	13.40	13.88	15
IRAS 25 μm[f]	13.08	13.94	15
IRAS 60 μm[f]	12.70	14.42	15
IRAS 100 μm[f]	12.48	14.48	15
Spitzer/MIPS 160 μm[g]	12.28	14.46	12
JCMT/SCUBA 850 μm[h]	11.55	11.7	54

[a] Terashima et al. (2002)
[b] Reunanen et al. (2010)
[c] Orienti & Prieto (2010)
[d] Hummel et al. (1987)
[e] Gallimore et al. (2010)
[f] Rice et al. (1988)
[g] Dale et al. (2007)
[h] Dale et al. (2005)

TABLE 4.3— SED for the core of NGC 1386 at high and low-spatial resolution.

Origin	$\log(\nu/\mathrm{Hz})$	$\log(\nu \mathbf{F}_\nu/\mathrm{Jy\,Hz})$	**Error (%)**
ASCA 2–10 keV[a]	18.16	10.98	4
ASCA 0.5–4 keV[a]	17.74	10.03	3
HST/NIC2 F160W	14.27	10.96	6
VLT/NaCo *Ks*	14.14	10.81	2
VLT/NaCo L'	13.90	11.51	1
VLT/VISIR 11.88 μm[b]	13.40	12.77	1
VLT/VISIR 18.72 μm[b]	13.20	12.91	1
MERLIN[c]	9.92	7.88	5
GALEX FUV[d]	15.30	12.17	1
GALEX NUV[d]	15.12	12.46	1
Spitzer/IRAC 3.6 μm[e]	13.92	12.91	1
Spitzer/IRAC 4.5 μm[e]	13.82	12.82	1
Spitzer/IRS 5.5 μm[f]	13.74	13.04	7
Spitzer/IRAC 5.8 μm[e]	13.71	12.91	1
Spitzer/IRAC 8.0 μm[e]	13.57	13.16	1
Spitzer/IRS 10.0 μm[f]	13.48	12.94	12
IRAS 12 μm[g]	13.40	13.11	5
Spitzer/IRS 14.7 μm[f]	13.31	13.24	5
Spitzer/IRS 20.0 μm[f]	13.18	13.19	2
IRAS 25 μm[g]	13.08	13.24	1
Spitzer/IRS 30.0 μm[f]	13.00	13.20	2
IRAS 60 μm[g]	12.70	13.47	1
IRAS 100 μm[g]	12.48	13.46	1
Parkes[h]	9.70	7.93	10
VLA[i]	9.69	7.80	12
VLA[j]	9.17	7.72	2
VLA[i]	9.16	7.53	9
VLA[k]	9.15	7.72	4
MOST[l]	8.93	7.56	5

[a] Terashima et al. (2002)
[b] Reunanen et al. (2010)
[c] Mundell et al. (2009)
[d] Gil de Paz et al. (2007)
[e] Gallimore et al. (2010)
[f] Deo et al. (2009)
[g] Sanders et al. (2003)
[h] Disney & Wall (1977)
[i] Ulvestad & Wilson (1984)
[j] Condon et al. (1996)
[k] Condon et al. (1998)
[l] Mauch et al. (2003)

TABLE 4.4— SED for the core of NGC 1052 at high and low-spatial resolution.

Origin	$\log(\nu/\mathrm{Hz})$	$\log(\nu \mathbf{F}_\nu/\mathrm{Jy\,Hz})$	**Error (%)**
Integral 17–60 keV[a]	18.97	12.33	20
Integral 20–40 keV[b]	18.86	11.99	15
Chandra 2–10 keV[c]	18.16	11.5	26
Chandra 0.2–8 keV[d]	18.00	11.48	17
ASCA 0.5–4 keV[e]	17.74	10.35	1
HST/ACS-HRC F250W	15.04	10.00	3
HST/ACS-HRC F330W	14.95	10.19	2
HST/WFPC1 F555W	14.74	10.59	2
VLT/NaCo *J*	14.38	10.89	2
HST/NIC2 F160W	14.27	11.58	2
VLT/NaCo *Ks*	14.14	11.33	3
VLT/NaCo L'	13.90	11.72	1
VLT/VISIR 9.7 μm[f]	13.49	12.58	10
VLT/VISIR 10.7 μm[f]	13.45	12.57	9
VLT/VISIR 11.7 μm[f]	13.42	12.60	3
VLT/VISIR 11.88 μm[g]	13.40	12.55	3
VLT/VISIR 12.4 μm[f]	13.38	12.50	7
VLBI[d]	10.63	9.99	2
VLBI[d]	10.34	9.88	2
VLBA[h]	10.19	9.98	1
VLBI[d]	9.92	8.67	1
Spitzer/IRAC 3.6 μm[i]	13.92	12.52	13
Spitzer/IRAC 4.5 μm[i]	13.82	12.39	14
Spitzer/IRAC 5.8 μm[i]	13.71	12.39	11
Spitzer/IRAC 8.0 μm[i]	13.57	12.41	7
IRAS 12 μm[j]	13.40	12.71	11
ISO 15 μm[k]	13.30	12.7	28
IRAS 25 μm[j]	13.08	12.82	9
IRAS 60 μm[j]	12.70	12.64	6
IRAS 100 μm[j]	12.48	12.68	9
NRAO 3.5 mm[l]	10.93	10.9	26
NRAO 9.5 mm[l]	10.50	10.7	33
ATCA[m]	10.34	10.55	10
ATCA[m]	10.27	10.27	5
ATCA[n]	9.93	10.35	2
ATCA[n]	9.68	10.07	2

ATCA[n]	9.40	9.56	3
ATCA[n]	9.15	9.14	5
Molonglo Radio Telescope[o]	8.61	8.54	5
Texas Interferometer[p]	8.56	8.37	5
Culgoora Circular Array[q]	7.90	8.51	13
VLA[r]	7.87	7.80	15

[a] Sazonov et al. (2007)
[b] Bird et al. (2007)
[c] González-Martín et al. (2009b)
[d] Kadler et al. (2004)
[e] Terashima et al. (2002)
[f] E. Treister, private communication
[g] J. Reunanen, private communication
[h] Lister & Homan (2005)
[i] M. Montes, private communication
[j] NASA Extragalactic Database: `http://nedwww.ipac.caltech.edu/`
[k] Xilouris et al. (2004)
[l] Heeschen & Conklin (1975)
[m] Ricci et al. (2006)
[n] Tingay et al. (2003)
[o] Large et al. (1981)
[p] Douglas et al. (1996)
[q] Slee (1995)
[r] Cohen et al. (2007)

TABLE 4.5— SED for the core of NGC 7582 at high and low-spatial resolution.

Origin	$\log(\nu/\mathrm{Hz})$	$\log(\nu\mathbf{F}_\nu/\mathrm{Jy\,Hz})$	**Error (%)**
BeppoSAX 20–100 keV[a]	19.16	13.07	15
XMM-Newton 2–12 keV[b]	18.23	12.37	15
ASCA 0.5–2 keV[c]	17.48	10.65	3
HST/WFPC2 F606W	14.70	9.18	5
HST/NIC3 F160W	14.27	12.32	1
VLT/NaCo 2.06 μm	14.16	12.42	2
VLT/NaCo L'	13.90	12.88	3
VLT/NaCo 4.05 μm	13.87	12.91	3
ESO/3.6m/TIMMI2 8.5 μm[d]	13.55	13.0	30
ESO/3.6m/TIMMI2 9.0 μm[d]	13.52	12.8	30
ESO/3.6m/TIMMI2 9.6 μm[d]	13.50	12.4	30
ESO/3.6m/TIMMI2 11.0 μm[d]	13.44	12.7	30
ESO/3.6m/TIMMI2 12.0 μm[d]	13.40	13.0	30
VLT/VISIR 11.88 μm[e]	13.40	13.00	8
VLT/VISIR 18.72 μm[e]	13.20	12.94	4
VLA[f]	9.92	7.76	1
VLA[f]	9.69	7.67	1
Spitzer/IRAC 3.6 μm[g]	13.92	13.34	1
Spitzer/IRAC 4.5 μm[g]	13.82	13.28	1
Spitzer/IRS 5.5 μm[h]	13.74	13.54	8
Spitzer/IRAC 5.8 μm[g]	13.71	13.43	1
Spitzer/IRAC 8.0 μm[g]	13.57	13.89	1
Spitzer/IRS 10.0 μm[h]	13.48	13.24	13
IRAS 12 μm[i]	13.40	13.76	1
Spitzer/IRS 14.7 μm[h]	13.31	13.60	5
Spitzer/IRS 20.0 μm[h]	13.18	13.72	3
IRAS 25 μm[i]	13.08	13.95	1
Spitzer/IRS 30.0 μm[h]	13.00	13.97	3
IRAS 60 μm[i]	12.70	14.41	1
IRAS 100 μm[i]	12.48	14.40	1

[a] Turner et al. (2000)
[b] Dewangan & Griffiths (2005)
[c] Cardamone et al. (2007)
[d] Siebenmorgen et al. (2004)
[e] Reunanen et al. (2010)
[f] Orienti & Prieto (2010)
[g] Gallimore et al. (2010)
[h] Deo et al. (2009)
[i] Sanders et al. (2003)

TABLE 4.6— SED for the core of NGC 7469 at high and low-spatial resolution.

Origin	$\log(\nu/\mathrm{Hz})$	$\log(\nu \mathbf{F}_\nu/\mathrm{Jy\,Hz})$	**Error (%)**
Integral 17–60 keV[a]	18.97	12.68	16
XMM-Newton 2–10 keV[b]	18.16	12.62	3
ROSAT 0.1–2.4 keV[c]	17.38	12.34	9
HST/WFPC2 F218W	15.13	12.57	1
HST/ACS-HRC F330W	14.95	12.44	1
HST/WFPC2 F547M	14.74	12.20	2
HST/ACS-HRC F550M	14.73	12.07	1
HST/WFPC2 F814W	14.57	12.20	2
VLT/NaCo *J*	14.37	12.28	1
VLT/NaCo *H*	14.26	12.43	1
HST/NIC3 F187N	14.20	12.48	1
VLT/NaCo *Ks*	14.14	12.44	1
VLT/NaCo L'	13.90	12.82	1
VLT/NaCo 4.05 μm	13.87	12.85	1
VLT/VISIR 11.88 μm[d]	13.40	13.13	1
VLT/VISIR 18.72 μm[d]	13.20	13.31	1
VLA[e]	10.17	8.20	5
VLA[e]	9.92	8.10	2
MERLIN[f]	9.70	7.78	1
VLBI[g]	9.36	7.51	7
VLBI[g]	9.23	7.55	5
Spitzer/IRAC 3.6 μm[h]	13.92	13.10	1
Spitzer/IRAC 4.5 μm[h]	13.82	13.00	1
Spitzer/IRS 5.5 μm[i]	13.74	13.26	14
Spitzer/IRAC 5.8 μm[h]	13.71	13.15	1
Spitzer/IRAC 8.0 μm[h]	13.57	13.65	1
Spitzer/IRS 10.0 μm[i]	13.48	13.36	6
IRAS 12 μm[j]	13.40	13.60	2
Spitzer/IRS 14.7 μm[i]	13.31	13.53	3
Spitzer/IRS 20.0 μm[i]	13.18	13.69	3
IRAS 25 μm[j]	13.08	13.86	1
Spitzer/IRS 30.0 μm[i]	13.00	13.79	3
IRAS 60 μm[j]	12.70	14.14	1
IRAS 100 μm[j]	12.48	14.02	2
CSO[k]	11.93	12.28	9
JCMT/SCUBA[l]	11.55	10.83	14

[a] Sazonov et al. (2007)
[b] Shinozaki et al. (2006)
[c] Perez-Olea & Colina (1996)
[d] Reunanen et al. (2010)
[e] Orienti & Prieto (2010)
[f] Alberdi et al. (2006)
[g] Sadler et al. (1995)
[h] Gallimore et al. (2010)
[i] Deo et al. (2009)
[j] Sanders et al. (2003)
[k] Yang & Phillips (2007)
[l] Dunne et al. (2000)

TABLE 4.7— Average template for Sy1s, derived from HSR data.

$\log(\nu/\mathrm{Hz})$	**Relative** $\log(\widetilde{\nu \mathbf{F}_\nu})$
19.16	0.72
18.98	0.64
18.97	0.64
18.17	0.24
17.72	0.03
17.49	−0.05
17.38	−0.08
15.35	−0.15
15.32	−0.14
15.31	−0.14
15.27	−0.16
15.23	−0.16
15.22	−0.16
15.19	−0.13
15.15	−0.12
15.14	−0.11
15.12	−0.12
15.08	−0.10
15.06	−0.09
15.00	−0.10
14.99	−0.10
14.96	−0.15
14.95	−0.15
14.92	−0.21
14.75	−0.35
14.74	−0.37
14.73	−0.37
14.58	−0.33
14.57	−0.32
14.38	−0.25
14.37	−0.24
14.26	−0.14
14.21	−0.09
14.15	−0.06
14.14	−0.05
13.90	0.20

13.88	0.20
13.41	0.48
13.40	0.48
13.21	0.60
13.08	0.51
12.70	0.09
12.48	−0.04
10.18	−4.00
9.93	−4.31
9.71	−4.59
9.69	−4.61
9.37	−5.02
9.36	−5.02
9.24	−5.09
9.23	−5.08

TABLE 4.8— Average template for Sy2s, derived from HSR data.

$\log(\nu/\mathrm{Hz})$	**Relative** $\log(\widetilde{\nu \mathbf{F}_\nu})$
19.16	−0.19
18.86	−0.32
18.23	−0.51
18.16	−0.52
17.72	−1.10
17.51	−1.26
17.39	−1.36
17.38	−1.36
14.70	−2.41
14.36	−1.06
14.28	−0.58
14.25	−0.51
14.17	−0.42
14.14	−0.37
14.13	−0.37
14.10	−0.28
14.09	−0.27
13.90	0.12
13.87	0.18
13.83	0.30
13.70	0.39
13.58	0.42
13.57	0.42
13.55	0.38
13.53	0.26
13.50	0.12
13.49	0.11
13.48	0.12
13.44	0.28
13.40	0.45
13.23	0.46
13.21	0.47
13.20	0.47
13.08	0.37
12.70	0.00
12.48	−0.24

11.36	−2.43
11.06	−2.99
10.64	−3.79
10.35	−4.30
10.00	−4.93
9.93	−5.06
9.92	−5.06
9.70	−5.10

TABLE 4.9— Average template for LLAGNs, derived from HSR data.

$\log(\nu/\mathrm{Hz})$	**Relative** $\log(\widetilde{\nu \mathbf{F}_\nu})$
18.39	−0.29
18.16	−0.57
18.00	−0.63
17.74	−1.02
17.39	−1.19
15.15	−1.41
15.05	−1.36
14.95	−1.30
14.74	−1.13
14.56	−0.54
14.38	−0.54
14.36	−0.54
14.27	−0.27
14.25	−0.23
14.14	−0.23
13.90	0.03
13.49	0.44
13.45	0.46
13.42	0.50
13.40	0.49
13.38	0.48
13.21	0.50
10.64	−2.41
10.34	−2.54
10.19	−2.46
10.18	−2.53
9.93	−3.67

5

Star formation in the central parsecs of galaxies

In this Chapter we review the main properties of the star-forming clusters found in the central parsecs of the sample of galaxies. A representative SED is obtained for the stellar clusters of each galaxy. The properties of the knots and their average SEDs are compared with local star-forming regions in our Galaxy and the nearest galaxies, and also with the globular cluster system in the Milky Way. Finally, we provide a template for young stellar clusters based on the results obtained for the resolved starburst in the nucleus of NGC 253, published in Fernández-Ontiveros et al. (2009).

5.1 Introduction

THE arrival of the *HST* and its high-spatial resolution capabilities opened a new window in the study of stellar clusters with the discovery of a new type of objects: Young Massive Clusters, also known as Super Stellar Clusters (SSCs). These are young ($< 100\,$Myr), massive ($\sim 10^4$–$10^6\,M_\odot$) and compact ($\sim$ 1–6 pc) star-forming regions (Meurer 1995), which are usually found in violent environments as mergers (Whitmore et al. 1999) and starburst galaxies (O'Connell et al. 1995) but also in circumnuclear rings (Maoz et al. 1996) and, more discreetly, in the centre of the majority of galaxies (Böker 2010) including our Milky Way (Schödel et al. 2010). Like individual massive stars, YSCs appear to spend $\sim$ 10–20% of their lifetimes in a stage similar to ultracompact H II regions, within dense and dusty cocoons, being strong-thermal IR emitters but invisible at optical wavelengths (Fig. 1.10 Vacca et al. 2002). Observations reveal that about 70 to 90% of stars form in clustered environments (Lada & Lada 2003), hence the importance of these objects, which may be responsible for a

significant fraction of all current star-formation in the local universe.

However, young stellar clusters (YSCs) usually present a very high rate of "infant mortality" (possibly as high as 99%, see Fall & Zhang 2001) and, after their birth, they begin to dissolve as a result of different physical processes (see Section 1.2.2). The most massive ones have expected lifetimes comparable to the age of the universe and, thus, YSCs in the early universe are candidates for being "young globular clusters" (Portegies Zwart et al. 2010), i.e. precursors to the old globular clusters (GCs) that we observe in the local universe. Given their sizes and the crowded environments where they usually live, a high-spatial resolution ($\lesssim 10\,$pc) is required in order to isolate them individually. In this context, our adaptive optics images with VLT/NaCo in the NIR permits us to study these systems from the early phases of their lifes in the central parsecs of nearby objects. By combining our NIR photometry with the extinction and age estimates in Section 3.2, we can derive photometric masses for the individual clusters corrected by dust obscuration and evolutionary effects. This correction, not only in absolute terms but specially in relative, permit us to investigate the cluster initial mass function (CIMF). The latter is directly related with the star-formation process and the natal cloud where the individual clusters were born.

Nonetheless, this Chapter begins with the case of NGC 253 in Section 5.2, the closest galaxy in the sample and also one of the closest starbursts, which has been resolved in a total of 37 very young and compact stellar clusters. We present a SED template for extragalactic star-forming regions based on the isolated emission of these clusters, with special attention on the origin of the NIR emission. Then, we present the special case of NGC 1052 in Section 5.3, an elliptical galaxy in which we have reported the detection of YSCs in its central $\sim 2 \times 2\,$kpc^2 region (Fernández-Ontiveros et al., submitted to MNRAS). In Section 5.4 we introduce the main characteristics derived for all the YSCs found for the objects in the sample (see Section 3.2), organized by their host galaxies. Size, brightness, colour, age, mass, star-formation rate and their average SEDs are compared across the whole sample. For comparison, we also show a representative SED, for each galaxy, of the diffuse light or background contribution that was measured locally around the clusters. In Section 5.5 we derive the luminosity and mass functions for the populations of YSCs, comparing them with star-forming clusters in similar environments and also GCs in the Milky Way.

5.2 NGC 253: a resolved starburst

This galaxy represents a special case within the sample due to its proximity ($\sim 4\,$Mpc) which permits us to resolve the nuclear starburst into its building blocks. These are 37 knots detected in the *L*-band, which was the image with the highest spatial resolution. First of all, we collected the SEDs obtained in Section 3.2.1 for these knots. For the eight sources with radio counterparts, these were extended from radio VLA to MIR

subarcsec and NIR adaptive optics VLT to optical *HST*. For the remaining sources, the SEDs are limited to the IR/VLT range, completed with optical/*HST* data when detected.

5.2.1 An average SED template for extragalactic star-forming regions

At fist glance, most of the knots show very similar SEDs, characterized by a maximum in the MIR and a gentle 'bump' at $\sim 1\,\mu$m (see Fig. 3.2). To provide a genuine radio to optical SED template of a circumnuclear star-forming region, an average SED of all the knots was constructed, following a similar method as in Section 4.2. Each knot's SED was normalized to that of knot #5 (green circles in Fig. 5.1), using their respective median power (νF_ν) in the 0.5–20 µm range (see Section 5.4.7 for details). The purple-shaded region in Fig. 5.1 represents values between the first and third quartiles for each band scaled to knot #5. The narrowness of the strip proves the

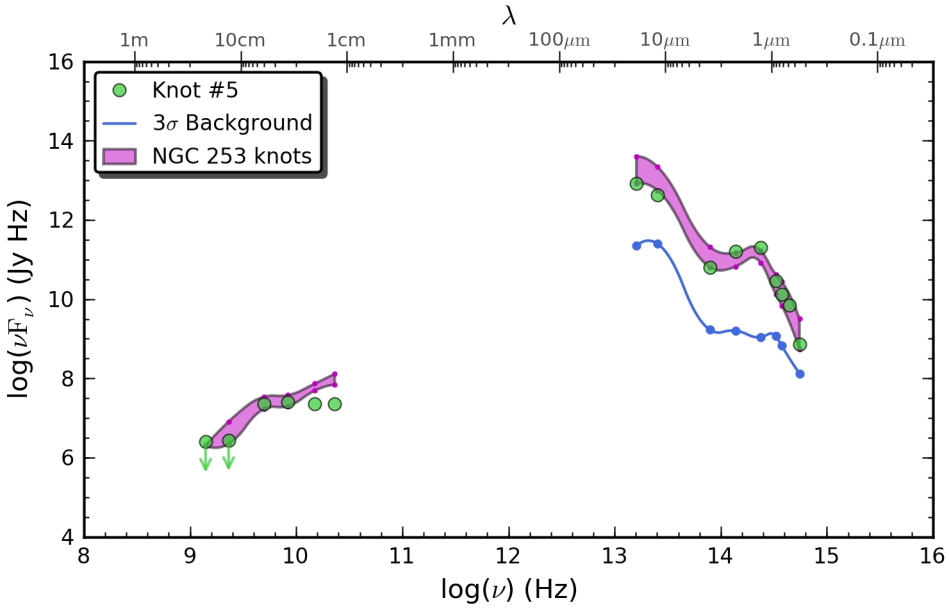

FIGURE 5.1— Energy distribution of the representative knot #5 (green circles) compared with the representative SED, between the first and third quartiles, of the 37 knots found in NGC 253 (purple-shaded area). The small purple dots placed along the quartile distributions mark the central wavelengths of the filters used to derive the representative distribution. The smooth curves that connect these dots and delimit the purple-shaded area correspond to spline interpolations. Blue dots represent the 3σ background distribution, also connected by splines. At radio wavelengths the average includes 8 sources with IR counterparts.

similarity of individual SEDs. Background values measured around each knot were also averaged without normalizing. The SED for the 3σ averaged background is shown in Fig. 5.1 (blue dots). Comparing both –median knot and background SEDs– shows that the characteristic NIR bump in the 1–2 μm range is not a feature of the background emission but is intrinsic to the SED of the knots, whereas the background SED is rather flat at these wavelengths (Fig. 5.1). The median template obtained is given in Table 5.1, together with the equivalent distribution derived from the extinction-corrected data and the 3σ background level. The templates are normalized to the median power of knot #5, which was selected as a representative knot.

TABLE 5.1— Median SED template derived from the sample of 37 YSCs found in the nucleus of NGC 253. $\widetilde{\nu F_\nu}$ correspond to the median power, while νF_ν^{25} and νF_ν^{75} are the first and third quartiles of the power distribution, respectively. The 3σ background level is represented by $\nu F_\nu^{3\sigma}$. Magnitudes labelled with $'$ correspond to the power distribution derived from extinction-corrected clusters, using the values given in Table 3.1. Average distributions and their respective quartiles are normalized to the median power of knot #5, selected as reference.

$\log(\nu)$ [Hz]	$\log(\nu\mathbf{F}_\nu^{\mathbf{25}})$	$\log(\widetilde{\nu\mathbf{F}_\nu})$	$\log(\nu\mathbf{F}_\nu^{\mathbf{75}})$	$\log(\nu\mathbf{F}_\nu^{\mathbf{3\sigma}})$ [Jy Hz]	$\log(\nu\mathbf{F}'^{\mathbf{25}}_\nu)$	$\log(\widetilde{\nu\mathbf{F}'_\nu})$	$\log(\nu\mathbf{F}'^{\mathbf{75}}_\nu)$
14.74	8.71	9.08	9.48	8.12	10.26	10.59	11.12
14.57	9.84	10.15	10.40	8.82	10.77	10.96	11.12
14.52	10.13	10.29	10.61	9.06	10.73	11.00	11.12
14.38	10.85	11.00	11.23	9.05	11.12	11.33	11.55
14.14	10.78	10.99	11.16	9.20	10.59	11.12	11.35
13.90	10.78	10.79	11.38	9.21	10.68	10.95	11.12
13.40	12.75	12.96	13.34	11.25	12.28	12.81	13.16
13.20	12.87	13.14	13.60	10.95	12.60	12.98	13.30
10.36	7.83	8.02	8.10	....	7.33	7.52	7.60
10.18	7.68	7.75	7.86	....	7.18	7.25	7.35
9.92	7.29	7.38	7.57	....	6.79	6.88	7.06
9.70	7.22	7.25	7.53	....	6.71	6.75	7.03
9.36	6.34	6.34	6.90	....	5.83	5.83	6.40
9.15	6.29	6.29	6.29	....	5.79	5.79	5.79

5.2.2 The origin of the NIR excess

Similar NIR excesses have been detected in young stellar clusters like Henize 2–10 (Cabanac et al. 2005) and NGC 1365 (Galliano et al. 2008) and has been associated to hot dust. To investigate the nature of the NIR excess, the SEDs of the knots were compared with theoretical models and observational templates of various types: an average H II region template, two types of supernova remnants, a stellar cluster model, a grid of Young Stellar Object (YSO) models and median SEDs obtained from YSOs

with circumstellar disks. For the sake of simplicity each of these templates was fitted to knot #5 SED, using a χ^2-minimization algorithm from which a scaling factor and a foreground extinction estimate A_V are obtained (galactic extinction law adopted from Cardelli et al. 1989). In Figs 5.2 and 5.3 we compare the best fits of these templates to the SED of knot #5.

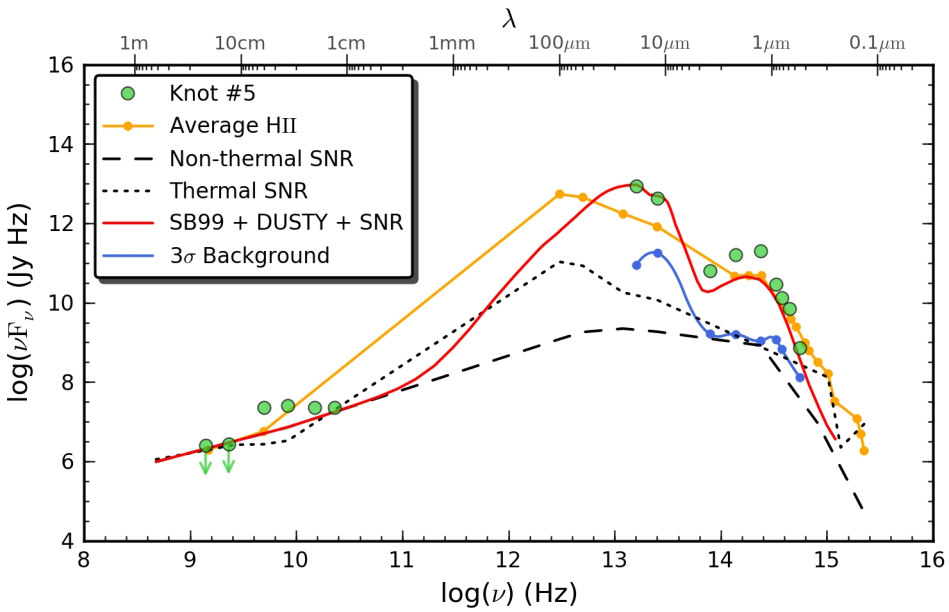

FIGURE 5.2— SED templates for a stellar cluster model plus dust and non-thermal SNRs (red-solid line), H II region (yellow-solid line), thermal SNR (dotted line) and non-thermal SNR (dashed line), compared with the SED of the representative knot #5 (green circles). Blue dots correspond to the 3σ median background.

H II region average template

Schmitt et al. (1997) provide an average template from four well-known observed H II regions. The fitted template (yellow-solid line in Fig. 5.2) shows a soft excess in the NIR ($\sim 1\,\mu$m), and peaks at $\sim 100\,\mu$m, providing a general account of the knot #5 SED from radio to optical within one order of magnitude. In detail, its featureless shape in the 1 to 20 μm range largely departs from that of the knots. Given the particular SED shape of the knots, the difference cannot be driven by extinction unless the applicable extinction law is very different from that in our neighbourhood.

Supernova remnant templates

The analysis of high-spatial resolution radio SED in NGC 253 suggests the presence of many supernova remnants (SNRs) in the nuclear region (Lenc & Tingay 2006). Thus, the optical to radio SED of a non-thermal (Crab, dashed line) and a thermal (N49, dotted line) SNR, both from Schmitt et al. (1997), were fitted to knot #5 SED. Fig. 5.2 shows the large difference between these SEDs and that of the knots, in particular the inferred SNR IR fluxes are lower by several orders of magnitude with respect to those of the knots. The intrinsic shape of the original template is flatter than the distribution for the knot #5, which has a much higher IR-to-radio ratio. Additional extinction would only decrease this ratio, worsen the fit.

Stellar cluster model plus dust and SNRs

The characteristics of the knots (Section 3.2.1) point more in the direction of these being young star-forming regions. Accordingly, a stellar cluster template from Leitherer et al. (1999), aged 5 Myr (in agreement with W(Hα) age estimation) with instantaneous star formation and solar metallicity, was input to DUSTY (Ivezic et al. 1999) to account for the dust emission. The best fit to knot #5 SED assumes a spherical dust distribution with a temperature of 200 K on the shell inner boundary. $A_V \sim 15$ mag is needed to reproduce the SED optical range, a factor ~ 4 larger than that estimated from the Hα/Brα ratio. This may be related to the different assumptions on the extinction: DUSTY consider internal extinction, whereas we assume a simple foreground dust screen. However, the major discrepancy arises again in the NIR: the model underestimates the emission even if considering different metallicities, cluster ages, inner shell temperatures, grain sizes or dust density distributions. A possible contributing mechanism in this range is stochastic heating of small grains, an effect not included in DUSTY. This model was completed with the contribution of SNRs at radio wavelengths. For comparison, a total of 20 non-thermal SNRs as bright as the Crab, or 5 thermal SNRs as bright as N49, are needed to reproduce the radio emission of knot #5.

Young Stellar Objects

Young stellar clusters appear to show SEDs very similar to those of YSO, suggesting that the early stages of their evolution may be parallel to those of massive stars (Johnson 2005). Motivated by this similarity, a comparison with YSO models was attempted. These are luminous IR sources formed by a protostar plus an accretion disk, all enshrouded in a dense dust cloud (Nakai et al. 1995). They show NIR excesses attributed to hot dust from the disk, a surplus that can be present in 30% of the members of a young cluster (Roman-Lopes & Abraham 2006). Comparing with these models, a simplified scenario is adopted: YSOs are assumed as the main

contributors to the knots' IR spectrum. Models were selected from the YSO grid provided by Robitaille et al. (2007). Best fits to the knots' SED correspond to very young (0.1–3 Myr) luminous ($L_{bol} > 10^2 L_\odot$) and massive stars ($M > 5 M_\odot$) seen at high inclination angles ($\sim 80°$). Extinction derived from the fits ranges from $A_V \sim 5.0$ (knot #5) to 11.6 mag (knot #4), in agreement with those obtained from Hα/Brα ratios. If scaled the models to NGC 253 distance, a total of about 10^5 YSOs per knot are required. Overall, the optical to IR SED of individual knots are surprisingly well reproduced by these models (see Fig. 5.3), which naturally incorporates the hot dust contribution. The extinctions inferred from the fits being also in fair agreement with those measured from Hα/Brα ratios. The ages of the protostars are, however, smaller than those inferred from W(Hα).

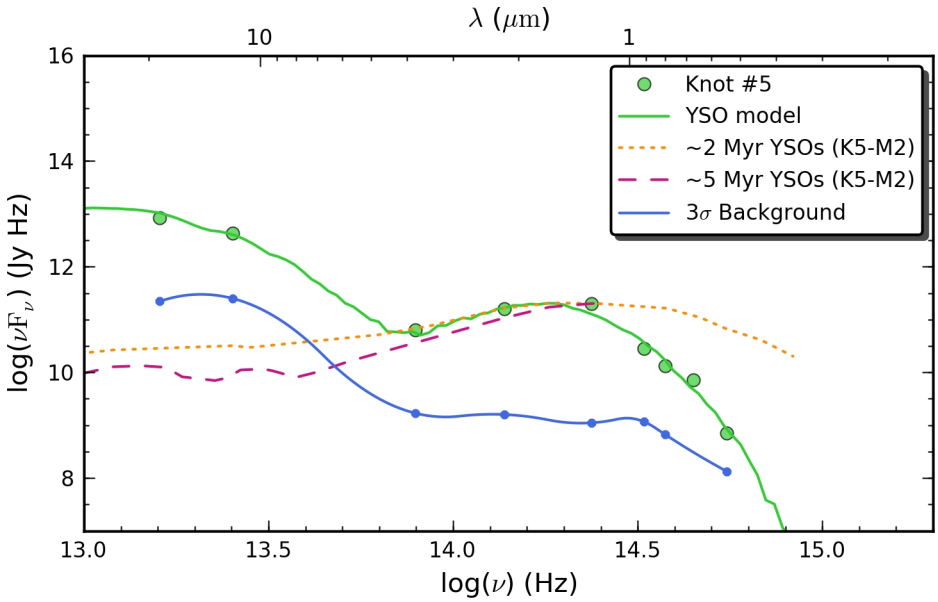

FIGURE 5.3— SED templates for YSO model (green-solid line) and median distributions obtained from YSOs with disks in Taurus Auriga ($\sim$ 2 Myr, orange-dotted line) and Upper Scorpius ($\sim$ 5 Myr, purple-dashed line), compared with the SED of the representative knot #5 (green circles). Blue dots correspond to the 3σ median background.

Furthermore, we compared the IR SED of knot #5 with median distributions obtained from YSOs in Taurus Auriga and Upper Scorpius star-forming regions. Taurus Auriga is a nearby ($\sim$ 140 pc) well-studied molecular cloud complex characterized by low extinction values and ages in the 1–3 Gyr range, which results in many of its pre-main sequence stars being still surrounded by circumstellar disks made of gas

and dust from their formation processes (Furlan et al. 2006). On the other hand, Upper Scorpius is among the nearest OB associations to the Sun (~ 145 pc) and its members present ages of ~ 5 Myr with no evidence for a significant dispersion around this value (Dahm & Carpenter 2009). In first case, a total of 39 K5–M2 stars with infrared excesses were selected from Kenyon & Hartmann (1995) in order to isolate a restricted range of stellar effective temperature for objects that are likely to have protostellar disks. Those objects with IR excesses dominated by envelope rather than disk emission were not included in this sample. Finally, individual extinction-corrected SEDs were normalized at 1.6 μm in D'Alessio et al. (1999) to derive a median YSO SED in the 0.36–1300 μm range (orange-dotted line in Fig. 5.3). This distribution is thus considered as a representative SED of late-type (K5–M2) YSOs with NIR excesses (probably associated with disks) in Taurus Auriga. If considering all spectral types for NIR excess YSOs, the median SED shape is not significantly altered (Furlan et al. 2006). A similar criteria was applied in the case of Upper Scorpius by Dahm & Carpenter (2009) to derive a median SED from 10 sources with spectral type in the K5–M2 range (purple-dashed line in Fig. 5.3).

The median NIR colours of YSOs in Taurus Auriga and Upper Scorpius are very similar to those of knots in NGC 253, which also display an excess of emission in this range. As mentioned at the beginning of this Section, this colour excess is intrinsic to the knots and absent in the background distribution. Shortwards of ~ 1 μm, the extinction-corrected Taurus Auriga distribution do not fall as steeply as the knot #5 SED, still obscured by a foreground extinction screen of $A_V \sim 3.5$ mag (Table 3.1). Longwards of 3.8 μm, the former decrease smoothly since objects with strong MIR emission are not considered in this average. Results for Upper Scorpius are qualitatively similar with a steeper slope in the NIR, although the sources in this star-forming complex are older (~ 5 Myr) than those in Taurus Auriga (~ 2 Myr) and the wavelength range covered is restricted to the 1.25–34 μm range. What Fig. 5.3 suggests is that the NIR bump detected in the nuclear clusters of NGC 253 represents the contribution of many YSOs bursting in their dust cocoons. The MIR is probably dominated by dust emission associated to the envelopes around these protostars, with a maximum around $T \sim 200$ K. Nonetheless, this contribution is probably produced by re-emission of the strongly absorbed optical light ($A_V \gtrsim 4$ mag).

5.3 The case of NGC 1052: young clusters in the centre of an elliptical

As mentioned in Section 3.2.4, NGC 1052 is a nearby elliptical galaxy located at ~ 18 Mpc with a low-level activity LINER nucleus (Heckman 1980). The inner 24×24 arcsec^2 ($\sim 2 \times 2$ kpc^2) are characterized by two radio lobes (Cooper et al. 2007, Fig. 5.4) and a collimated ionized gas structure in Hα+[N II] (Pogge et al. 2000), both extended in the east–west direction, plus a parsec-scale twin jet (PA $\sim 60°$) with an

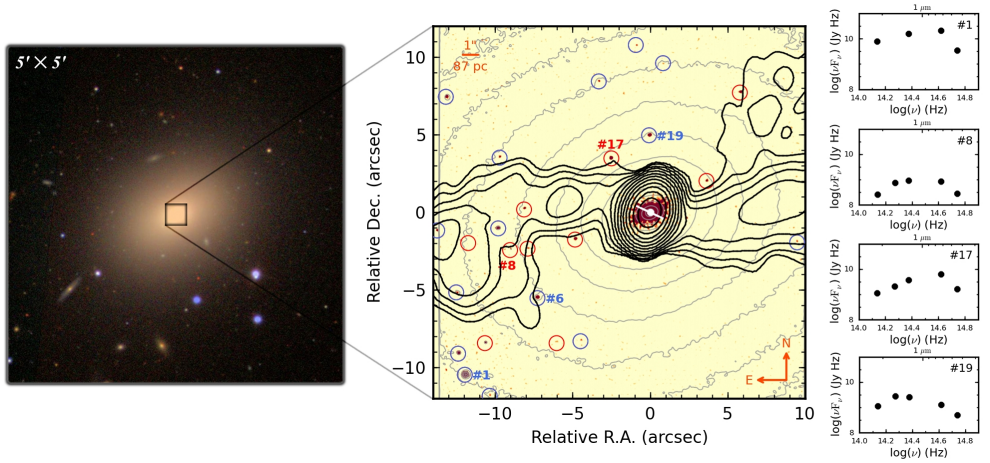

FIGURE 5.4— *Left:* SDSS *g* (blue), *r* (green) and *i*-band (red) colour composite image for NGC 1052. VLT/NaCo $24'' \times 24''$ FOV is marked by a black square. *Centre:* Unsharp-masked VLT/NaCo *Ks*-band image, logarithmic contours for the natural *Ks*-band image (grey colour) and VLA contours at 1.4 GHz (black, Cooper et al. 2007). In blue, knots with W(Hα) $\geq$ 50 Å, in red those with $<$ 50 Å. The central white barred-dot marks the position of the nucleus and the direction of the parsec-scale twin jet. *Right:* SEDs for two "blue" (#1 and #19) and two "red" knots (#8 and #17).

emission gap between the brighter part in the north-east (NE) and the counter jet in the south-west (SW) direction (Kadler et al. 2004). The radio lobes are also spatially coincident with the distribution of the X-ray emission reported by Kadler et al. (2004). The presence of two tidal tails, extended from NE to SW, and infalling gas in the H I distribution are interpreted as evidence of a minor merger event about 1 Gyr ago (van Gorkom et al. 1986, 1989). This scenario is supported by the different rotation axes found for the gas and the stars (Plana & Boulesteix 1996) and the presence of dust lanes along the N–S direction near the galaxy centre (Forbes et al. 1990).

On the other hand, unsharp-masking on the *J* and *Ks*-band images reveal a total of 25 point-like sources over a 3σ threshold, aside of the nucleus, in the central $24'' \times 24''$ (circles in Figs 3.8 and 5.4). None of these knots are detected in the *HST*/ACS images acquired in the UV range with the F250W and F330W filters, nor in the *L'*-band, in which the only source detected is the LINER nucleus. The wider FOV of the STIS/F28X50LP image ($\sim 28'' \times 51''$) shows nearly 70 knots, which seem to be more dispersed with increasing radius. Unfortunately, counterparts in other bands (F555W, *J*, F160W, *Ks*) exist only for the 25 knots in the common FOV. The photometry of these sources was extracted from the natural images, i.e. not filtered by unsharp-masking (see Section 2.3.4). The median size of the 25 knots, measured in the VLT/NaCo *Ks*-band image, is less than our spatial resolution, FWHM $\lesssim 0\farcs12 \approx 10.5$ pc, and thus

they are separated but not spatially resolved. The knots show a median brightness of $m_K = 20.9$ mag, which corresponds to an absolute magnitude of $M_K = -10.4$ mag, too bright for being individual stars (Tabur et al. 2009). They are distributed in the $-12 \leq M_K \leq -9$ mag range, except knot #1, which is by far the brightest with $M_{K_{\#1}} = -13.6$ mag. In the optical, they are characterized by a median $m_V = 24.3$ mag and $m_I = 22.1$ mag, which corresponds to $M_V = -7.0$ mag, $M_I = -9.2$ mag and a median $V - I = 2.4$ mag[1].

Surprisingly, some of the knots stand out in the narrow-band F658N, centred on the Hα+[N II] blend, suggesting that these might be identified with YSCs (see Fig 5.5). These emission-line knots are not apparently related with the strong emission around the LINER nucleus. To estimate the emission-line fluxes for these knots we subtracted the continuum, as a first approximation, by using the flux-calibrated image in the V-band (F555W). Thus, we assumed a constant continuum level from the V-band to the F658N filter. Although we detected counterpart line emission for ~ 10 knots found in the K-band image, this continuum estimation was improved using a linear interpolation between the V and J-bands (see Fig. 5.6). Finally, the Hα flux was corrected by the [N II] contribution, as explained in Section 2.3.4, assuming that to be 40% of the total (Baldwin et al. 1981). The Hα equivalent width (W(Hα)) distribution for the 25 knots shows a differentiated group with $\gtrsim 50$ Å, thus we adopted this value as a lower cut to separate these knots from the rest. Therefore, we found 15 knots having W(Hα) ≥ 50 Å (blue circles in Fig. 5.4 and white circles in Fig. 5.5), a number that only increases to 16 by assuming the [N II] contribution to be 20% instead of 40% in the Hα+[N II] blend. Moreover, the Hα luminosity ($L_{\mathrm{H}\alpha}$) of the 15 knots spans the range $[1\text{–}33] \times 10^{36}$ erg s^{-1}. Assuming they are stellar clusters, their ages were derived from their W(Hα) (Leitherer et al. 1999), by assuming an instantaneous burst model with the highest available metallicity, $Z = 0.04$. This follows the results by Pierce et al. (2005), who found higher than solar metallicity abundances ($Z > 0.08$) in the central $\sim 10''$ (~ 1 kpc) region of NGC 1052 from the analysis of spectral indices measured at various radii in an optical long-slit spectrum. This estimation for the 15 knots yields ages of $\lesssim 6.8$ Myr, with a median W(Hα) value corresponding to 6.2 Myr (116 Å). About half of them are in the 5.4–6.5 Myr range (105–175 Å), i.e. the first and third quartiles, respectively. Lower W(Hα) values for the remaining knots may be produced by older clusters or by higher extinction that might affect the interpolation estimate for the continuum level. Considering lower metallicities, e.g. $Z = 0.001$, result in older ages for the same W(Hα), but W(Hα) ≥ 50 Å still limits the age to ≤ 12.2 Myr.

Notwithstanding, ionizing photons may be produced by an old stellar population due to the "UV-upturn" (see O'Connell 1999, and references therein). This additional

[1] Strictly speaking, the F555W−F28X50LP colour.

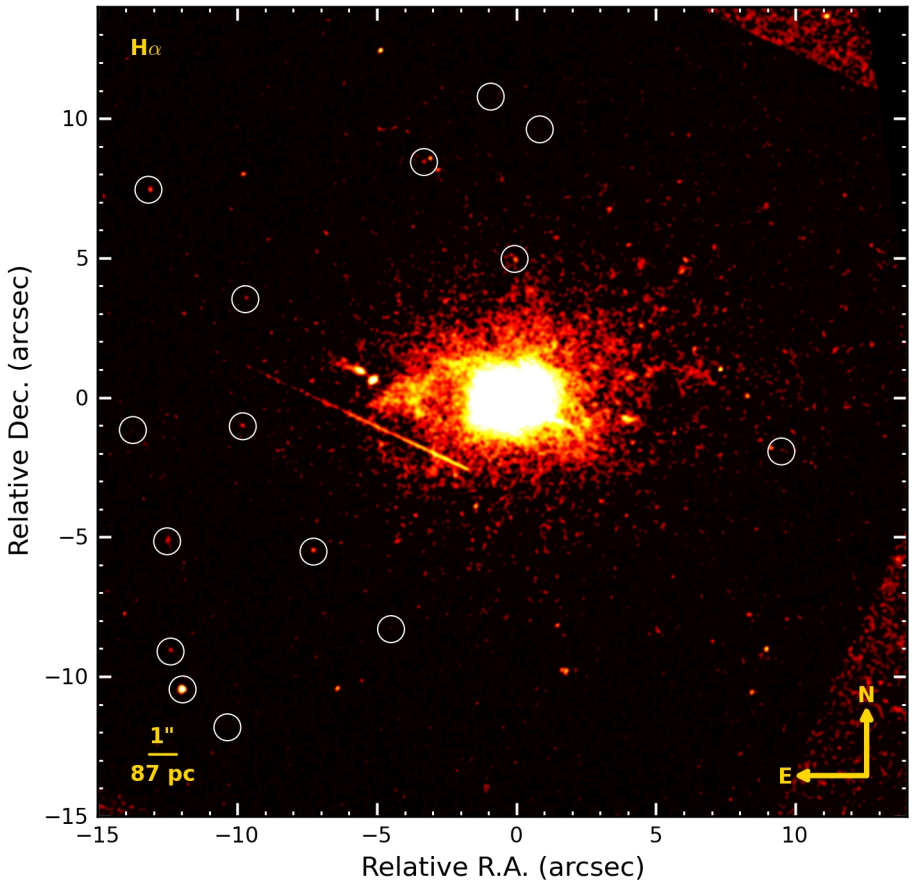

FIGURE 5.5— Continuum-subtracted Hα+[N II] emission blend for the central $29'' \times 29''$ in NGC 1052. The continuum image used to build this emission-line map corresponds to the *V-band* (F555W). Note that this is different from the continuum values assumed to estimate the Hα+[N II] fluxes, which were derived by interpolation between the *V* and *J*-bands. White circles mark the position of the 15 knots, found in the *K*-band image, with W(Hα) $\geq$ 50 Å. The position of the LINER nucleus is found at the origin.

contribution in the UV range originates in some low-mass, helium-burning stars in the extreme horizontal branch (EHB) and subsequent phases of evolution. In this scenario, the compact knots in NGC 1052 could be either GCs with an EHB component or YSCs probably linked with the merger event occurred in the recent history of this galaxy. A detailed analysis was then performed for knot #6 (Fig. 5.4), which is representative of the 15 knots' sample in terms of brightness and SED's shape. From its Hα luminosity ($L_{\mathrm{H}\alpha} = 5.2 \times 10^{36}\,\mathrm{erg\,s^{-1}}$) we derived an ionizing photon rate of $\sim 3.8 \times 10^{48}\,\mathrm{ph\,s^{-1}}$

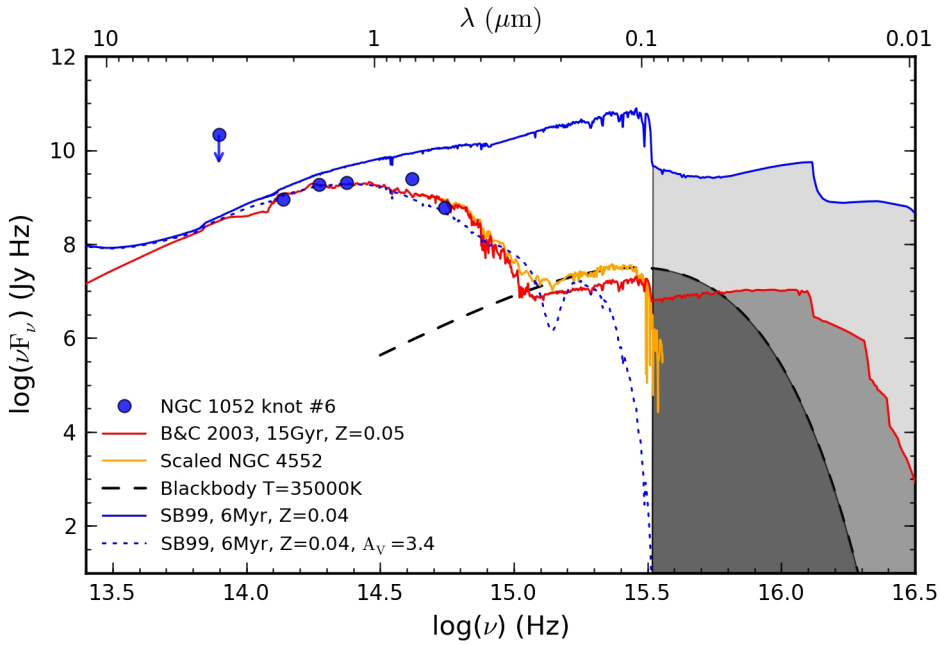

FIGURE 5.6— Knot #6 SED (blue circles) compared with a 15 Gyr, $Z = 0.05$ template (Bruzual & Charlot 2003, red-solid line), a composite spectrum of NGC 4552 (Yi et al. 1998, yellow-solid line) plus a blackbody spectrum ($T = 35000$ K, black-dashed line) and a 6 Myr, $Z = 0.04$ template from STARBURST99 (Leitherer et al. 1999, blue-solid line), also shown with an obscuration of $A_V = 3.4$ mag (blue-dotted line). Shaded areas correspond to photons with $\lambda \leq 910$ Å.

($Q(H^0) = 7.33 \times 10^{11} L_{H\alpha}$, Osterbrock 1989), that was compared with estimates for old and young stellar population templates.

5.3.1 Old globular clusters?

Fig. 5.6 shows the spectral energy distribution (SED) of the knot #6, which is derived from broad-band photometry (blue dots) including the upper limit in the *L*-band. First, we show the SED of a 15 Gyr old, $Z = 0.05$ population (red-solid line, Bruzual & Charlot 2003) fitted to the NIR SED of the knot #6 (*HST*/F160W, NaCo *J* and *Ks*-bands) in order to minimize the effect of possible dust extinction. This gives us a scaling factor for the template. The rate of ionizing photons is then estimated by integrating the shaded area under the red-solid line in Fig. 5.6, resulting in 1.2×10^{47} ph s^{-1}, i.e. more than an order of magnitude lower than the value measured for the knot #6; thus, the Hα emission cannot be explained by such an old stellar

population.

However, the EHB component is not included in the 15 Gyr old template. EHB stars present small envelopes around the helium core, showing a hot thermal spectrum with $T \gtrsim 20000$ K. The integrated energy distribution of such an old population ($\gtrsim 10$ Gyr) increases shortwards of ~ 2000 Å and is thus capable of emitting FUV photons (Greggio & Renzini 1990). To estimate the possible contribution of these stars to the SED we adopted, as a template for a EHB dominated population, a composite spectrum formed by the UV-strong elliptical galaxy NGC 4552 (yellow-solid line in Fig. 5.6, Yi et al. 1998) and, shortwards of 900 Å, a $T = 35000$ K blackbody spectrum scaled to NGC 4552 in the UV (black-dashed line in Fig. 5.6). For consistency, the former was scaled to the 15 Gyr old template in the optical range. In this case, the predicted rate of 1.8×10^{47} ph s^{-1} is still an order of magnitude below the measured value. Moreover, if we consider the presence of an absorption component in the Hα line, which is expected for an old population, the rate of ionizing photons needed in this case is even higher than the $\sim 3.8 \times 10^{48}$ ph s^{-1} derived by assuming only a emission component for this line.

5.3.2 Young stellar clusters?

We also consider a young 6 Myr, $Z = 0.04$ stellar cluster template from STARBURST99 (blue-solid line in Fig. 5.6, Leitherer et al. 1999), based on the W(Hα) of knot #6. When scaled to the NIR SED of knot #6, this template predicts 2.5×10^{49} ph s^{-1}, corresponding to $L_{\mathrm{H}\alpha} \sim 3.5 \times 10^{37}$ erg s^{-1}, i.e. higher than the Hα luminosity measured for knot #6. Moreover, the shape of the young template SED overestimates the emission in the optical range. Since extinction by dust is frequent in the environment of young clusters, we estimated an initial guess value of $A_V \sim 2.5$ mag, which is based on the $L_{\mathrm{H}\alpha}$ ratio from knot #6 and the young template, assuming the extinction law by Cardelli et al. (1989). This extinction was applied to the 6 Myr template, scaling it again to the NIR SED of knot #6. Then, a new intrinsic $L_{\mathrm{H}\alpha}$ luminosity was derived from the re-scaled template, which results in a new A_V for the next iteration. After three steps, this converged to a young template with $A_V \sim 3.4$ mag, an intrinsic rate of 4.9×10^{49} ph s^{-1}, $L_{\mathrm{H}\alpha} \sim 6.6 \times 10^{37}$ erg s^{-1} and 1.3×10^4 M$_\odot$ (blue-dotted line in Fig. 5.6). However, since we are assuming a simple foreground dust screen to derive A_V, this value should be considered as a lower limit.

5.3.3 Colours

The 25 knots appear very different in brightness and colours with respect to those of the GCs studied in the outer 2–20 kpc of the galaxy by Pierce et al. (2005), which present a median $m_V \sim 22.0$ mag. The $V - I$ colour for the young regions is, on average,

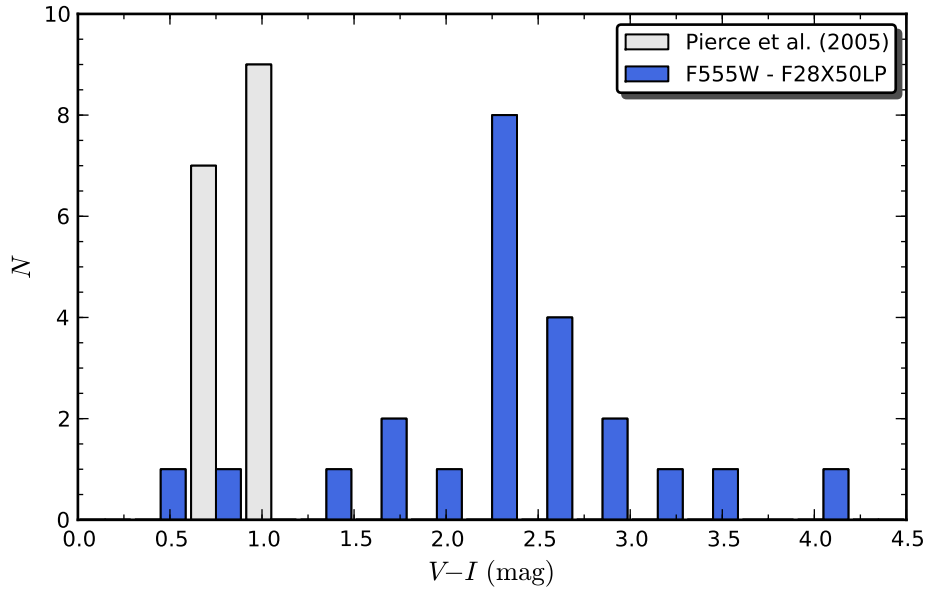

FIGURE 5.7— In grey, the $V-I$ colour distribution for the GCs found by Pierce et al. (2005) in NGC 1052. In blue, the F555W−F28X50LP colour distribution for the 25 clusters found in this work.

~ 1.5 mag redder than that of the GCs (Fig. 5.7). Note that the F28X50LP filter is even bluer than the I-band, suggesting that both populations are intrinsically different. This filter also includes the Hα+[N II] blend ($\sim 0.660\,\mu$m at $z = 0.005$) very close to the transmission peak[2], but this contribution to the broad-band magnitude (~ 0.3 dex for knot #6) is not enough to explain the large difference in colour observed between the knots and the GCs. Only knot #1 has a V magnitude of 21.9 mag, compatible with the GCs, but its $V-I$ colour is much redder (2.6 mag). This discrepancy cannot be ascribed to the colour bimodality reported by Forbes et al. (2001), since all the GCs in this study lie in the range $1.2 < V-I < 1.7$ mag. However, an obscuration of $A_V = 3.4$ mag may explain why the knots in the central part look much redder than the GCs. Similar extinction values and colours to those shown by the knots have been reported for young stellar clusters (YSCs) in the starbursts galaxies NGC 5253 (Vanzi & Sauvage 2004) and NGC 253 (Fernández-Ontiveros et al. 2009).

5.3.4 Discussion

More than half of local early-type galaxies exhibit tidal tails and clouds in their H I distributions (Morganti et al. 2006), $\gtrsim 16\%$ display shells (Malin & Carter 1983)

[2] http://www.stsci.edu/hst/stis/design/filters/

and $\sim$ 30% present signs of residual star formation (RSF $\sim$ 1–3% of their stellar mass) having started in the last Gyr, as inferred from their blue UV–optical colours ($NUV-r < 5.5$ mag Kaviraj et al. 2007; Shapiro & et al. 2010). In contrast, their optical colours correspond to the red sequence ($u-r > 2.2$ mag; Strateva et al. 2001). A widely discussed scenario to explain these peculiarities is the inclusion of minor mergers (1:4 to 1:10 in mass ratio) as a part of the evolutionary process of massive early-type galaxies (Bezanson et al. 2009; Kaviraj et al. 2009; Cenarro & Trujillo 2009).

As mentioned in the beginning of this Section, NGC 1052 exhibit many of these characteristics and also displays integrated colours typical of a "rejuvenated" early-type galaxy (Kaviraj et al. 2007), with $NUV-r = 4.9$ mag, while the $u-r = 2.8$ mag colour still places this galaxy in the red sequence (*NUV* from Rampazzo et al. 2007; *u* and *r*-band from SDSS). In this context, the origin of the knots seems to be related with the last burst of star formation induced by a minor merger event. Hydrodynamical *N*-body minor merger simulations with mass ratios of 1:6 to 1:10 by Peirani et al. (2009) suggest that star formation occurs in several bursts after the merger event rather than being a continuous process (see also Kaviraj et al. 2009). This is in agreement with our observations: we find two very young clusters (W(Hα) $\sim$ 230 Å $\approx$ 5.1 Myr), 4 young ones (140 $\leq$ W(Hα) $<$ 200 Å; 5.2–5.6 Myr), 7 slightly older ones (90 $\leq$ W(Hα) $<$ 140 Å; 5.6–6.6 Myr) and 12 with W(Hα) $<$ 90 Å ($>$ 6.6 Myr). This means that we are probably looking at either the final stage or one minimum of the RSF induced by the merger event. In their simulations, Kaviraj et al. (2009) explore the E$(B-V) = 0-0.5$ mag range, showing that observations favour those models with higher extinction values (E$(B-V) \gtrsim 0.3$ mag). For comparison, the colour excess of knot #6 suggest even higher values, i.e. E$(B-V) \sim 1.1$ mag ($A_V \sim 3.4$ mag).

Regarding at their spatial distribution, the knots with W(Hα) $\geq$ 50 Å are located randomly and do not seem to follow any special pattern except for a weak preference for the NW–SE direction (see Fig. 5.5). Moreover, we do not find any clear connection with either the kpc-scale radio lobes at 1.4 GHz (Fig. 5.4) or with the extended emission in X-rays detected by *Chandra* (Kadler et al. 2004). This indicates that the RSF episode in the centre was not, at least directly, driven by nuclear activity. The absence of a high spatial resolution map in CO does not allow us to connect the knots with density enhancements in the cold material, but the dust lanes in the N–S direction seen in the STIS/F28X50LP image are not apparently related with the knots. However, this scattered star formation is in line with the "widespread" star-formation mode found by Shapiro & et al. (2010) for early-type galaxies with multiple and mismatched kinematic components. This is also the case of NGC 1052, which shows 2 counter-rotating gaseous components decoupled from the stellar kinematics (Plana & Boulesteix 1996). Furthermore, Shapiro & et al. (2010) find that those objects with very low SFRs ($\lesssim 0.06\,M_\odot\,yr^{-1}$) exhibit a more centralized star-formation activity,

which is also favoured by recent simulations (Peirani et al. 2009). This might explain why Forbes et al. (2001) and Pierce et al. (2005) did not find these young clusters in their study, as they covered the outskirts of NGC 1052 (2–20 kpc). Nevertheless, an Hα image with a wider FOV is needed to check the young cluster distribution at larges scales.

Since we determine the age of the knots on the basis of Hα emission, we are only sensitive to very recent star-formation episodes ($\lesssim 10$ Myr) and cannot provide a reliable age for the 10 out of 25 knots with W(Hα) < 50 Å. However, these show very similar properties (i.e. sizes, magnitudes, colours) to those with W(Hα) > 50 Å, are also randomly distributed and their SEDs are qualitatively similar (see Fig. 5.4). Results from stellar population models on the integrated spectrum of the central ~ 1 kpc indicate luminosity-weighted ages of ~ 2 Gyr (Pierce et al. 2005). The contribution of the 15 knots reported in this work is not sufficient to account for the excess emission due to this 2 Gyr population. A "middle age" population (10 Myr $<$ t $<$ 2 Gyr) is still needed, that would be probably related with a more intense star-formation episode in the past, in line with the scenario proposed by Shapiro & et al. (2010). A comprehensive spectroscopic study of the central part with two populations (old plus mid-age) is required to complete the suggested picture.

5.4 Comparison between cluster properties

Summarizing, in Chapter 3 we found a number of compact sources (knots) for all the objects. These knots resulted in young clusters associated with very recent episodes of star formation ($\lesssim 10$ Myr) in the central parsecs of the galaxies in the sample. In this Section we review the main properties of these clusters, i.e. size, brightness, colour, age, mass, star-formation rate (SFR) and SED. Since they inhabit different environments due to the assorted nature of the objects in the sample, the knots span a very wide range in properties like brightness, colours and masses, although their sizes and ages are rather consistent among the different galaxies. In Table 5.2 we collect we median, first and third quartile values for the mentioned properties.

5.4.1 Size

In Section 3.2 we measured the projected half-light diameter of the clusters, i.e. FWHM. This region also includes $\sim 58\%$ of the total mass if we assume a constant mass-to-light ratio within each cluster. However, as the observed $\mathrm{FWHM_{obs}}$ is quite close to the intrumental resolution ($\mathrm{FWHM_{inst}}$), the sizes given previously might be masked by the latter. Thus we corrected the former as $\mathrm{FWHM} = \sqrt{\mathrm{FWHM_{obs}} - \mathrm{FWHM_{inst}}}$. The VLT/NaCo *K*-band was selected as the reference image to measure the sizes, except in the cases of NGC 253 and NGC 7469, in which the VLT/NaCo *L*-band and *HST*/F550M images were selected, respectively, due to

their higher spatial resolution in the former and higher sensitivity in the latter. Fig. 5.8 shows the size distribution of the clusters found in this reference image, grouped by their host galaxy. In the vertical axis, p represents a probability density, i.e. the counts normalized by the total number of clusters (N, different for each galaxy) and the width of the bin (fixed at the same value for all the objects). This probability density is normalized, i.e. the sum of p for each galaxy is 1. The choice of this parameter instead of the counts facilitates the comparison between different objects which have a different number of clusters.

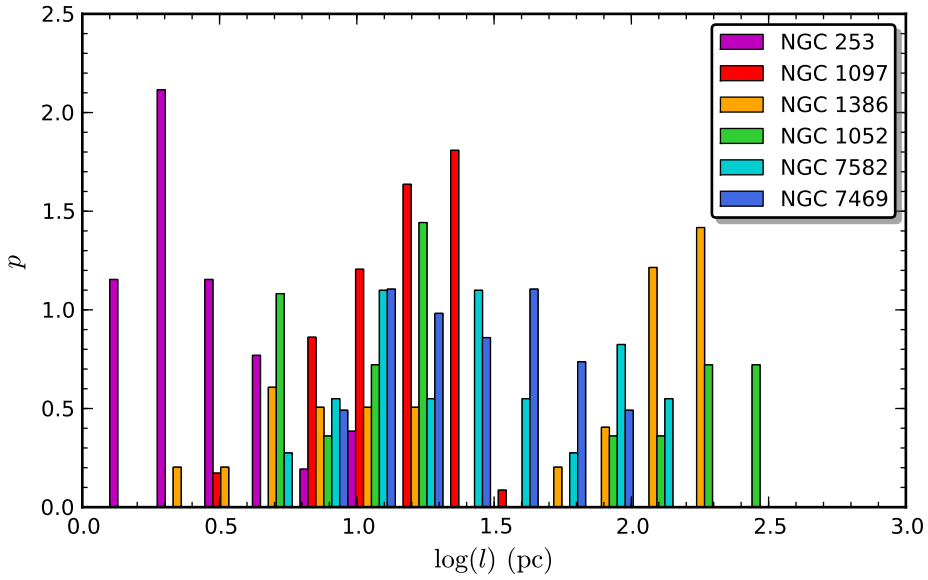

FIGURE 5.8— Logarithmic cluster size distribution, grouped by object. The vertical axis represents the number of clusters normalized to a probability density. The width of the bars is smaller than the real width of the bin, in order to plot all the objects at the same time.

NGC 253 hosts the most compact clusters with a median size of 2.4 pc, a very similar value to the sizes measured for compact YSCs in M31 by Kodaira et al. (2004). The high-spatial resolution achieved in this object can be ascribed to its proximity ($\sim$ 4 Mpc) and also to the filter where we measure the sizes, the L-band in this case, which might be more sensitive to younger and embedded star-forming regions. The median cluster size for the rest of galaxies in the sample is, in crescent order, 7.1 pc for NGC 1386 ($D = 15.3$ Mpc, $\mathrm{FWHM_{inst}} \sim 6.7$ pc in K-band), 10.5 pc NGC 1052 (18.0 Mpc, 10.5 pc in K-band), 16.9 pc for NGC 1097 (14.5 Mpc, 9.1 pc in K-band), 23.4 pc for NGC 7469 (65.2 Mpc, 22.1 pc in F550M) and 24.1 pc for

NGC 7582 (19.9 Mpc, 15.4 pc in IB_2.06, K-band). Sizes of about $\gtrsim 100$ pc probably correspond to faint knots which are mostly diluted in the diffuse light of the galaxy, ant thus these values should be considered as upper limits to their sizes. Thus, to compute the median value of the knots in NGC 1386 we do not considered those knots with $\log(l/pc) \gtrsim 1.5$.

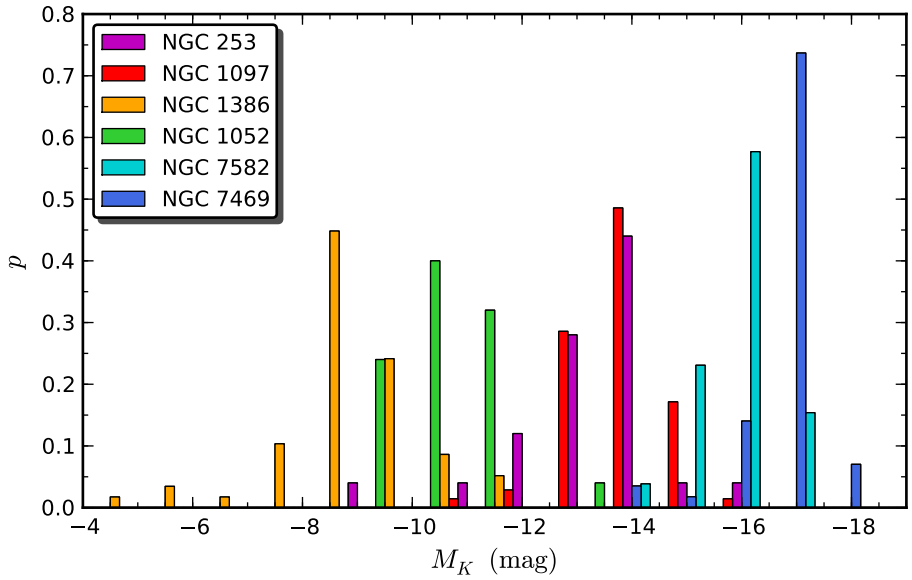

FIGURE 5.9— K-band absolute magnitude distribution for all the clusters, grouped by their host galaxy.

5.4.2 Brightness

Since we lack of extinction estimates for half of the galaxies in the sample, the magnitudes given in this Section are not unreddened, in order to simplify their comparison. Fig. 5.9 shows the distribution of the K-band absolute magnitudes for all the clusters grouped by their host galaxy. At first sight, the clusters in NGC 1386 look much fainter when compared with those found in other objects, showing a median K-band absolute magnitude of $M_K = -8.9$ mag, far from the -10.4 mag in NGC 1052, -13.0 mag in NGC 253 and -13.3 mag in NGC 1097. This difference of $\gtrsim 1.5$ mag with the clusters in NGC 1052, an elliptical galaxy, or $\gtrsim 4$ mag with the clusters in NGC 253 and NGC 1097, two nearby spirals, cannot be simply ascribed to dust extinction, since these differences would imply values in the $A_V \sim 20$–40 mag range,

very high when compared with the average $A_V \approx 1.6$ mag given by Ferruit et al. (2000) for the kiloparsec-scale starburst ring, where most of the clusters are located. However, the clusters found in NGC 1386, and even those in NGC 1052, are comparable in brightness to YSCs in the Large Magellan Cloud (LMC, Persson et al. 1983) and M31 (Perina et al. 2010), while the cases of NGC 253 and NGC 1097 resemble more to the case of the strong starburst NGC 5253 (Vanzi & Sauvage 2004). Nevertheless, the clusters found in NGC 7582 and NGC 7469 are much brighter with -16.4 mag and -17.4 mag in the K-band, respectively. This can be ascribed to the compactness of the starburst in the former and the larger distance to the latter, which drops the spatial resolution in this galaxy.

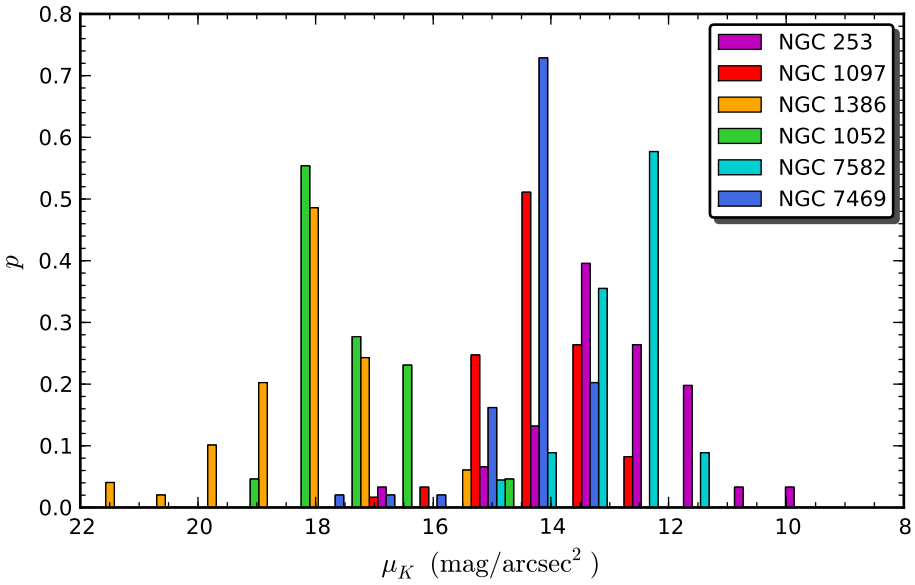

FIGURE 5.10— K-band surface brightness distribution for all the clusters, grouped by their galaxy.

Nevertheless, as the physical scale associated with the spatial resolution varies from one object to another, we should consider that the area where the photometry is extracted (diameter $\equiv 2\times$ FWHM$_{\rm inst}$) corresponds also to regions with different physical sizes for each galaxy, and thus the previous brightness comparison in Fig. 5.9 is not straightforward. To balance for this effect we derived the K-band surface brightness (μ_K) using π (FWHM)^2 [arcsec^2] as the effective area corresponding to the photometry aperture in the K-band (Section 2.3.4). Fig. 5.10 shows the resulting distribution for μ_K, joining up the clusters by their host galaxies. Now,

the width of the range in brightness is reduced for the μ_K distribution. Nonetheless, NGC 1386 and NGC 1052 still host the faintest clusters with $\mu_K \sim 18.3\,\mathrm{mag/arcsec^2}$ and $17.8\,\mathrm{mag/arcsec^2}$, respectively, while the rest of the galaxies span the ~ 17.5–$10\,\mathrm{mag/arcsec^2}$ range. NGC 7582 leads the brightness/compactness ranking with a median value of $\mu_K \sim 12.4\,\mathrm{mag/arcsec^2}$ followed by NGC 253 ($13.1\,\mathrm{mag/arcsec^2}$), NGC 7469 ($13.8\,\mathrm{mag/arcsec^2}$) and NGC 1097 ($14.6\,\mathrm{mag/arcsec^2}$). Note that the surface brightness do not correlates with the spatial resolution. In contrast, the most bright and compact clusters within the sample occur for those galaxies in which the starburst is located closer to the nucleus, while those showing star-forming rings or dispersed star-formation present lower brightness/compactness ratios. Moreover, the earliest type galaxies (NGC 1386 and NGC 1052) are clearly at the tail of this distribution with $\sim 4\,\mathrm{mag/arcsec^2}$ over the rest. Note that Figs 5.9 and 5.10 represent a first approach to the K-band luminosity function for the YSCs in the sample, although they are still not corrected by extinction or evolutionary effects.

5.4.3 Colour

Fig. 5.11 shows the $V-J$, $I-J$ and $J-K$ colour distribution for all the clusters grouped by their host galaxy. Extinction-corrected colours are shown for NGC 253, NGC 1097 and NGC 7469, while unreddened colours correspond to NGC 1386, and NGC 1052. The absence of NGC 7582 in this Figure is due to the lack of data in the J-band for this galaxy. Note that NGC 253 exhibit the reddest optical colours with a median value of $V-J \sim 3.1\,\mathrm{mag}$, even after being extinction-corrected. $I-J$ colours are very similar for most of the objects except in the case of NGC 1386, which is not unreddened. $J-K$ colours are even more similar and span a shorter range, probably due to the lower effect of the extinction at NIR wavelengths. Overall, the range of colours are very similar to those of young and massive stellar clusters found in extragalactic starbursts and/or merging galaxies like NGC 5253 (Vanzi & Sauvage 2004) or the Antennae (Zhang et al. 2001), respectively.

5.4.4 Age

Assuming that all the knots are young stellar clusters, ages were derived from their W(Hα), based on the STARBURST99 models by Leitherer et al. (1999). We assumed an instantaneous burst model with solar metallicity except in the case of NGC 1052, in which we adopted a model with $Z = 0.04$ (see Section 5.3). As mentioned before, we found a total of 15 clusters with W(Hα) ≥ 50 Å within the central parsecs, corresponding to ages of $\lesssim 6.8\,\mathrm{Myr}$. Therefore, ages and star-formation rates (SFRs) derived for this galaxy are restricted to these 15 clusters. In the case of NGC 7582 we do not provide an estimate for the age of the clusters due to the lack of data for

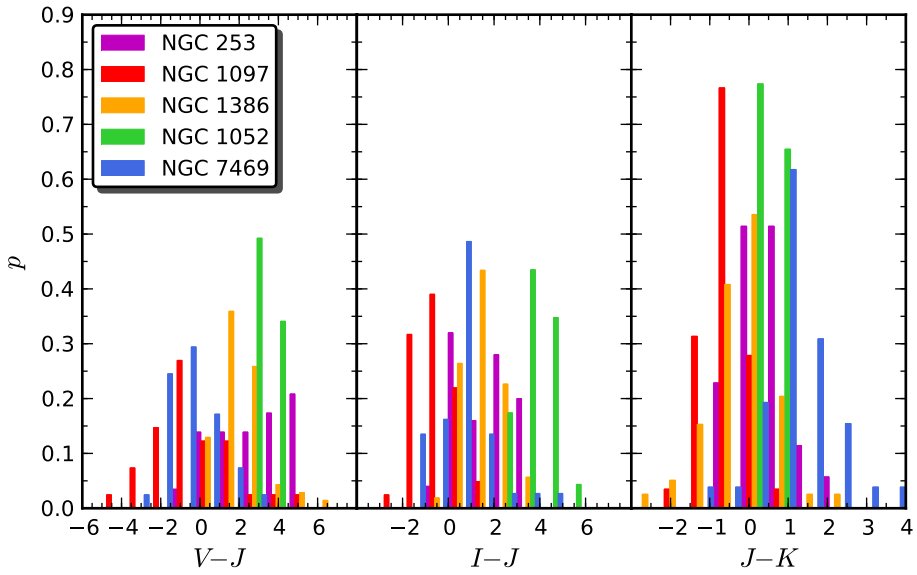

FIGURE 5.11— $V-J$, $I-J$ and $J-K$ colours for all the clusters, grouped by their host galaxy.

the Hα emission at high spatial resolution. However, we still have a narrow-band centred on Brα, but only a few bright clusters are detected in this image. Thus, based on the W(Brα) of these clusters, a constant age estimate of about 6 Myr was assumed for the whole starburst. Based on the uncertainty of W(Hα), we estimate age errors in the $\sim$ 0.1–0.4 Myr range (see Tables and the end of this Chapter), although these values could increase considerably if the metallicities assumed here are far from the real values.

Fig. 5.12 shows the W(Hα) distribution for all the clusters, grouped by their host galaxy. NGC 1097 shows the lowest values around a median W(Hα) $\sim$ 14 Å, corresponding to ages of $\sim$ 10 Myr. However, some of the knots in this galaxy reach more than 100 Å ($\lesssim$ 6 Myr), specially those located close to one of the two interfaces between the starburst ring and the dust lanes (NE and SW in the ring). The median W(Hα) for the clusters in the rest of the galaxies are, at least, an order of magnitude higher: 71 Å for NGC 1386, 116 Å for NGC 1052, 193 Å for NGC 7469 and 471 Å for NGC 253, which hosts the youngest knots. These correspond to 6.3, 6.2, 5.8 and 4.3 Myr, respectively. As mentioned in Section 3.2.2, very low W(Hα) values based on two-dimensional spectroscopic data were also reported by Dors et al. (2008) for NGC 1097. The ages provided here are consistent with the fading of the most massive

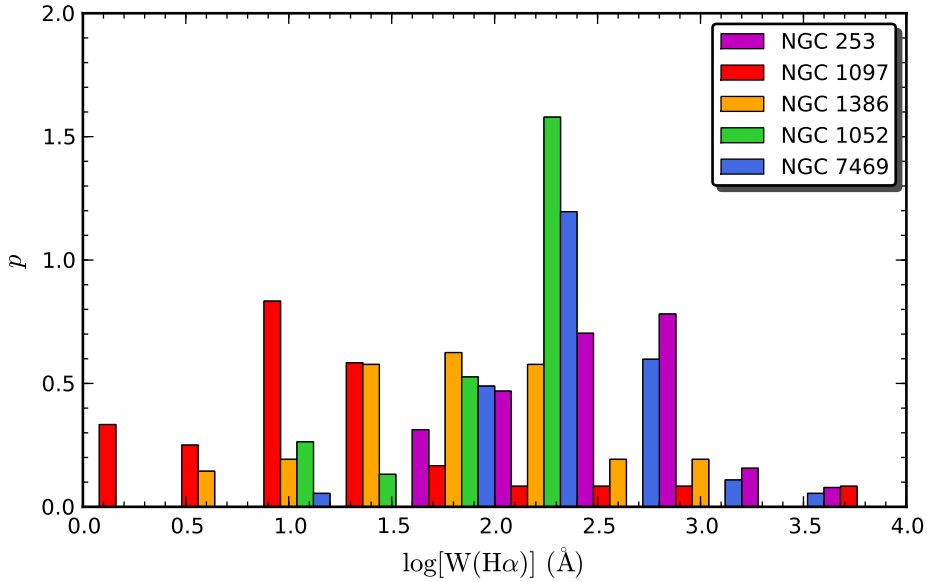

FIGURE 5.12— Hα equivalent width distribution for all the clusters, grouped by their host galaxy.

stars and the lack of FUV emission in the starburst ring with regard to the spiral arms (see Fig. 3.3). This difference cannot be explained by extinction, since the values measured in the ring are no larger than ~ 1.1 mag (Hummel et al. 1987; Barth et al. 1995).

5.4.5 Mass of the clusters

Photometric masses were estimated from the K-band luminosity by assuming an age-dependent mass–luminosity ratio (M/L), given by STARBURST99 models for the case of an instantaneous burst with solar metallicity ($Z = 0.04$ in the case of NGC 1052). Thus, this estimate correspond to the initial mass of the cluster. The adopted mass-loss rates predicted by Leitherer et al. (1999), used to derive the evolution of the cluster mass with age, are not those predicted by the stellar evolutionary models, but rather the approach favoured in Leitherer et al. (1992) and Leitherer & Heckman (1995). This dependence of the mass–luminosity relation with the cluster age is strictly valid only in those cases with $\gtrsim 10^5\,M_\odot$, i.e. massive clusters (Cervino & Valls-Gabaud 2008). Estimates for less massive clusters can be affected by stochastic fluctuations of the number of thermally pulsing stars in the asymptotic giant branch (AGB), which can dominate the luminosity for faint clusters (Santos & Frogel 1997). The error for the derived mass is mainly dominated by uncertainties in metallicity, stellar initial mass

function, stellar evolutionary tracks and mass loss rates of the clusters. Overall, it is reasonable to assume a relative error of $\sim 30\%$ for the mass estimates (see Leitherer et al. 1999, and references therein).

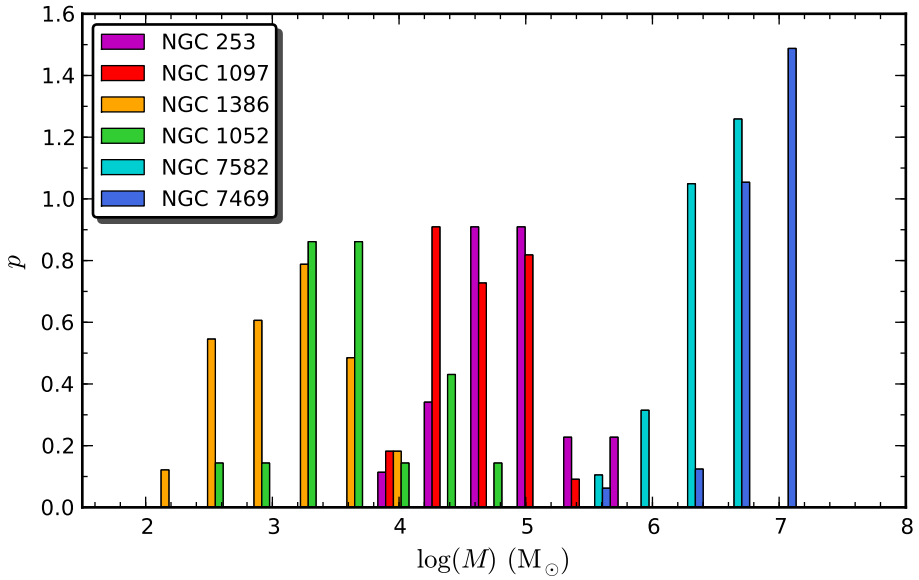

FIGURE 5.13— Mass distribution for all the clusters, grouped by their host galaxy.

For those objects with extinction estimates, i.e. NGC 253, NGC 1097 and NGC 7469, the masses were derived from the unreddened K-band magnitudes. Due to the lack of an age estimation in the case of NGC 7582 (see Section 5.4.4), the mass–luminosity ratio assumed was $(M/M_\odot)/(L_K/L_\odot) \approx 1.2$, corresponding to a star-formation burst of ~ 6 Myr. During the first ~ 10 Myr, the M/L ratio remains constrained between 0.6 and 1.3, and thus greater variations are only expected for clusters with $\gtrsim 10$ Myr, when the red supergiants appear (Leitherer et al. 1999). Fig. 5.13 shows the mass distribution for all the clusters, grouped by their host galaxy. Those corresponding to NGC 253, NGC 1097 and NGC 7469 are corrected by extinction and evolutionary effects, while those of NGC 1386 and NGC 1052 are initial masses derived from luminosities not corrected by reddening effects. In the case of NGC 7582 we have translated the brightness distribution into a mass distribution (not corrected for reddening) by assuming a constant age for all the clusters. Overall, the distribution of masses is very similar to that of the K-band brightness (see Fig. 5.9), as the age differences are not bigger than a few Myr among the clusters. NGC 7582

and NGC 7469 host the most massive ones, which are probably unresolved clumps with $\sim$ 30–200 YSCs in each one like those in NGC 253 or NGC 1097.

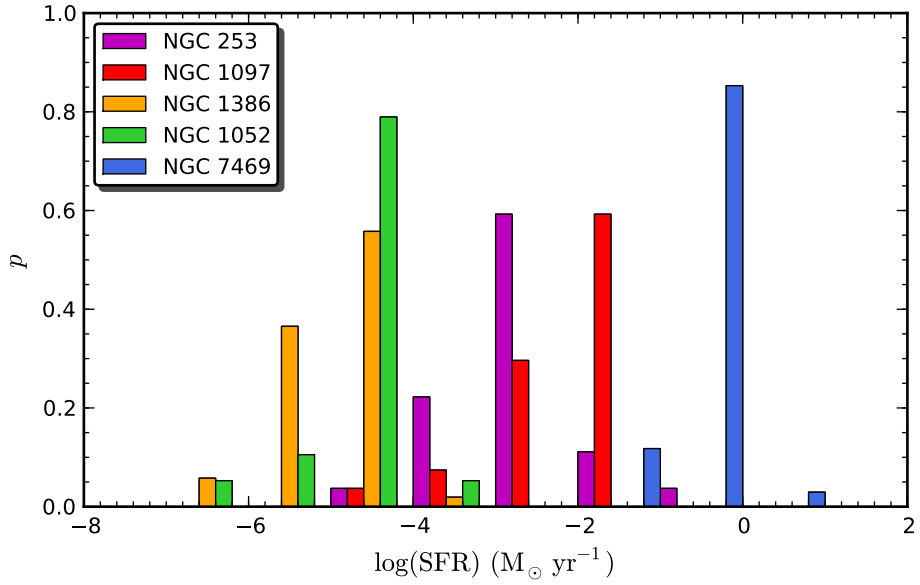

FIGURE 5.14— Star-formation rate (SFR) distribution for all the clusters, grouped by their host galaxy.

5.4.6 Star-Formation Rate

The star-formation rate (SFR) for each cluster was derived from its Hα luminosity ($L_{\mathrm{H}\alpha}$) as in Kennicutt (1998):

$$\frac{\mathrm{SFR}}{\mathrm{M}_\odot\,\mathrm{yr}^{-1}} = 7.9\times10^{-42}\frac{L_{\mathrm{H}\alpha}}{\mathrm{erg\,s}^{-1}} \tag{5.1}$$

The SFR distribution is shown in Fig. 5.14, grouping the clusters by their host galaxy. The most active star-forming clusters correspond to those in the LIRG galaxy NGC 7469, at a median rate of $0.24\,\mathrm{M}_\odot\,\mathrm{yr}^{-1}$. NGC 1097 is an order of magnitude below with $0.01\,\mathrm{M}_\odot\,\mathrm{yr}^{-1}$, followed by NGC 253 with $10^{-3}\,\mathrm{M}_\odot\,\mathrm{yr}^{-1}$. The less active objects are NGC 1052 and NGC 1386 with median values of $2\times10^{-5}\,\mathrm{M}_\odot\,\mathrm{yr}^{-1}$ and $10^{-5}\,\mathrm{M}_\odot\,\mathrm{yr}^{-1}$, respectively. Based on the variations among the different calibrations of Eq. 5.1, we estimate an error of about $\sim 30\%$ for the values derived using this relation (Kennicutt 1998). For comparison, the total SFR of a typical S0 is $\lesssim 0.01\,\mathrm{M}_\odot\,\mathrm{yr}^{-1}$, a gas-rich spiral presents $\sim 20\,\mathrm{M}_\odot\,\mathrm{yr}^{-1}$ and a starburst can even reach $\sim 100\,\mathrm{M}_\odot\mathrm{yr}^{-1}$

(Kennicutt 1998). Moreover, the SFR within 4 kpc of the Sun is $\sim 0.02\,M_\odot\,yr^{-1}$ (Portegies Zwart et al. 2010). It is also interesting to note that the total SFR for the whole starburst in NGC 253 ($\sim 0.23\,M_\odot\,yr^{-1}$) is very similar to the median SFR value for a single average cluster in NGC 7469. This suggests that each of the ~ 50 knots that form the starburst ring in this galaxy could be, in turn, a whole starburst like that in the nucleus of NGC 253. However, at the distance of NGC 7469 we are not able to resolve these structures and discern if they are clumps of stellar clusters like those in NGC 253 or single and extremely massive clusters.

TABLE 5.2— *Upper table:* in this order, first quartile, median and third quartiles for the size, absolute magnitude, $V-J$ and $J-K$ colours for the of YSCs in the sample, grouped by their host galaxy. *lower table:* the same as above for the visual extinction (A_V), W(Hα), photometric mass and star-formation rate (SFR).

Galaxy	**FWHM [pc]**			**M_K** [mag]			**$V-J$** [mag]			**$J-K$** [mag]		
NGC 253	2.1	2.4	4.1	−12.0	−12.7	−13.5	4.6	3.1	1.7	0.2	0.5	0.8
NGC 1097	10.8	16.9	21.9	−12.8	−13.3	−13.7	0.7	−0.6	−1.8	−0.9	−0.6	−0.3
NGC 1386	7.8	77.6	144.3	−8.1	−8.9	−9.5	2.6	2.0	1.4	−0.6	−0.1	0.3
NGC 1052	9.9	15.6	125.2	−10.1	−10.4	−11.3	3.6	3.2	2.8	0.2	0.4	0.7
NGC 7582	12.1	24.1	53.5	−16.0	−16.4	−16.7		–			–	
NGC 7469	12.2	23.4	36.6	−17.1	−17.4	−17.8	−0.0	−0.7	−1.5	0.5	0.8	1.7

Galaxy	**A_V** [mag]			**W(Hα)** [Å]			log(M) [$M_\odot$]			log(SFR) [$M_\odot\,yr^{-1}$]		
NGC 253	3.8	6.1	7.4	218.0	498	751	4.9	5.1	5.4	−3.0	−2.7	−2.4
NGC 1097	5.6	6.9	8.4	7.0	14	29	4.7	5.0	5.3	−2.3	−1.9	−1.7
NGC 1386		–		28.0	71	140	2.6	3.1	3.4	−5.2	−4.9	−4.6
NGC 1052		–		80.0	112	162	3.3	3.6	3.9	−4.9	−4.7	−4.4
NGC 7582		–			–		6.2	6.4	6.5		–	
NGC 7469	2.9	4.6	5.2	119	193	297	6.9	6.9	7.1	−0.8	−0.6	−0.4

5.4.7 Spectral energy distributions

Since the total number of clusters is quite large, we averaged the SEDs of the YSCs in each galaxy to evaluate their shape and investigate the main features, as was done for NGC 253 in Section 5.2. The representative cluster SED was obtained following a similar method as the one performed in Section 4.2 for active nuclei. First of all, we normalized every distribution to $\langle \widetilde{\nu F_\nu} \rangle_{\#n}$, i.e. the median power of a representative cluster called *knot #n*. This means that knot #n has properties very similar to the median values for each galaxy (see Table 5.2). The knots selected as representative are #5 in NGC 253, #54 in NGC 1097, #12 in NGC 1386, #6 in NGC 1052, #11

in NGC 7582 and #50 in NGC 7469. Being $\nu F_\nu^n|_{\#k}$ the normalized SED for each knot *#k*, we obtained the representative SED as the median value, evaluated for each filter centred in ν_i, of all the normalized distributions $\langle \widetilde{\nu_i F_{\nu_i}^n|_{\#k}} \rangle$. Notice that the median algorithm was selected, instead of the mean value as in Section 4.2, for the normalization and subsequent average. In this case, the dynamical range for individual clusters is not as large as for active nuclei, and thus the median was favoured in order to reject extreme values. However, using the mean to build the average SED do not alters significantly further results.

Note that the median SED includes less knots in the optical and the MIR, as a consequence of dust extinction in the first case and lower sensitivity and spatial resolution in the second. In order to estimate the dispersion around the average SED, we also derived the first and third quartiles of the normalized SEDs (Q_1 and Q_3 in $\nu_i F_{\nu_i}^n\big|_{\#k}$). For those objects with individual extinction measurements, i.e. NGC 253, NGC 1097 and NGC 7469, we also obtained the representative distributions for the extinction-corrected clusters.

NGC 253

As mention in the beginning of this Chapter (see Section 5.2), most of the 37 clusters in the nucleus of this galaxy display very similar SEDs, characterized by a maximum in the MIR and a gentle "bump" around $\sim$ 1–2 μm, which results in NIR colours of about $J - K \sim 1.4$ mag. To prove this likeness, a representative SED was constructed (Fig. 5.1), as explained above, using knot #5 as reference. This cluster was selected since it is representative in terms of brightness, colour and SED shape, of the 37 knots found in the nuclear region of NGC 253. However, choosing another representative knot for the normalization do not modify further results. Fig. 5.15 display the representative SED previously shown in Fig. 5.1 centred in the MIR-to-UV range, in order to facilitate the comparison with the rest of the galaxies in the sample, for which we could not extend the representative SED down to radio wavelengths due to the lack of data. The purple-shaded region represents the area delimited, for each filter, by the first and third quartiles of the normalized SED, thus including 50% of the knots. The smooth curves that connect the quartile values (small purple dots) and delimit the purple-shaded area correspond to spline interpolations. Again, the above mentioned NIR bump between 1 and 2 μm is clearly seen.

Nevertheless, it is also interesting to evaluate the median SED of the local background measured around each knot during the subtraction of the local background (see Section 2.3.4). The representative background distribution was derived as the median background value subtracted in the photometry, for all the clusters, plus three times the median value of the background scatter estimate. Thus, we account

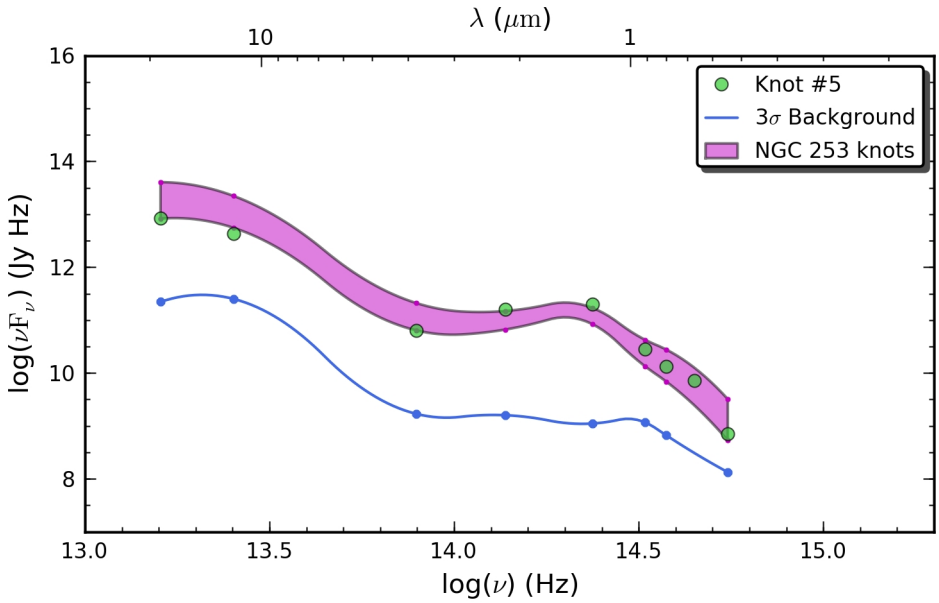

FIGURE 5.15— Energy distribution of the representative knot #5 (green circles) compared with the representative SED, between the first and third quartiles, of the 37 knots found in NGC 253 (purple-shaded area). Blue dots represent the 3σ background distribution.

for both the overall background value and its dispersion (blue dots in Figs 5.1 and 5.15). The comparison between the representative distributions for the clusters and the 3σ background proves that the characteristic NIR bump in the 1–2 μm range is not a feature of the background emission, but is intrinsic to the clusters, whereas the background distribution is rather flat at these wavelengths. As discussed in Section 5.2.2, the nature of this NIR excess seems to be associated with the presence of hot dust very close to the protostars that form these young clusters. Photometric error bars are not plotted in Fig. 5.15 as they are smaller than the size of the symbols.

NGC 1097

The representative SED for the clusters in this galaxy is shown in Fig. 5.16, traced by the first and third quartiles of the normalized SEDs collection (purple-shaded area). The reference in this case is the knot #54, which was selected as representative of the rest. Most of the clusters in NGC 1097 show a similar NIR excess in their SEDs when compared with the case of NGC 253 (Fig. 5.15), with a bump peaking in the 1–2 μm range and increasing its flux towards the MIR. However, their median NIR colour ($J-K \sim 0.6$ mag) and the MIR-to-optical ratio are lower than in the case of NGC 253,

suggesting less emission from warm dust in this case. Moreover, the representative SED for NGC 1097 rises again towards the optical/UV range, probably due to the lower extinction in this galaxy. The median SED of the 3σ background (blue dots) is also flat from the optical to the NIR, increasing slightly only in the MIR range, which points again to the clusters as the origin of the NIR excess. To derive the background distribution we rejected those filters with relatively short exposures, which introduce a feature in the average distribution as a consequence of the higher noise level.

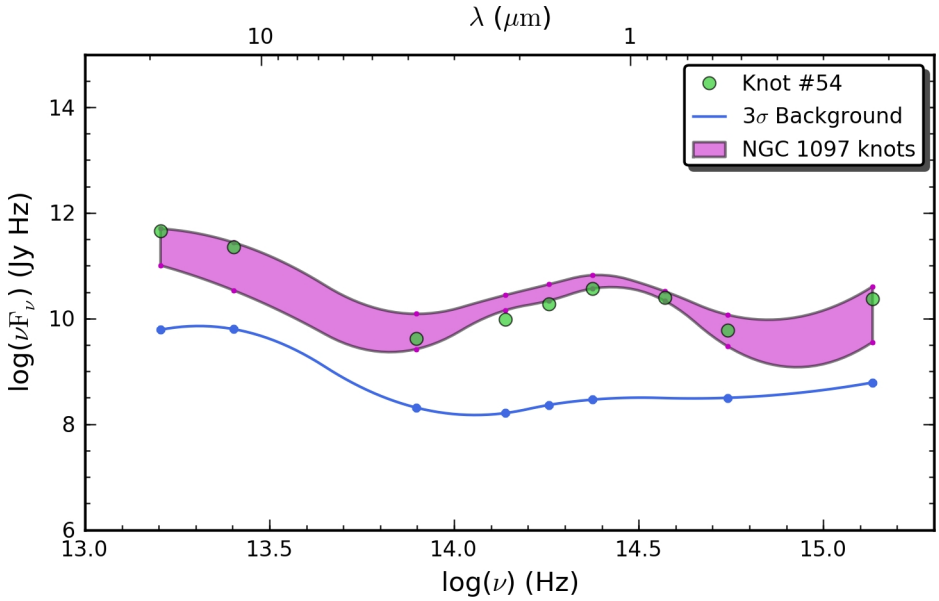

FIGURE 5.16— Energy distribution of the representative knot #54 (green circles) compared with the representative SED, between the first and third quartiles, of the 74 knots found in NGC 1097 (purple-shaded area). Blue dots represent the 3σ background distribution.

NGC 1386

In this galaxy, some of the clusters exhibit a soft decrease from the J to the H-band (e.g. knots #40 and #55 in Fig. 3.6), although this is marginally detected for the majority of them, which usually show a flat distribution in this range (Fig. 5.17). In contrast, the median NIR colour is about $J-K \sim -0.1$ mag, suggesting that the NIR bump is more pronounced in this object, but the background distribution (blue dots) is very close to the K-band flux. This relatively high background could affect the fainter knots in the K-band, underestimated in its value in this case. In the L-band none of the clusters were detected. The background distribution shows a feature in the

NICMOS *H*-band with regard to the NaCo *J* and *Ks*-bands. This discrepancy is also observed for datasets in other galaxies between the *HST*/NICMOS and VLT/NaCo data (e.g. NGC 1052, NGC 7469). A possible explanation is that part of the background emission is already removed in the ground-based data during the reduction process, and thus the median background in the *J* and *Ks*-bands could be underestimated in those cases where the brightness surface of the stellar component is weak. This effect is particularly enhanced when the background is very flat within the FOV.

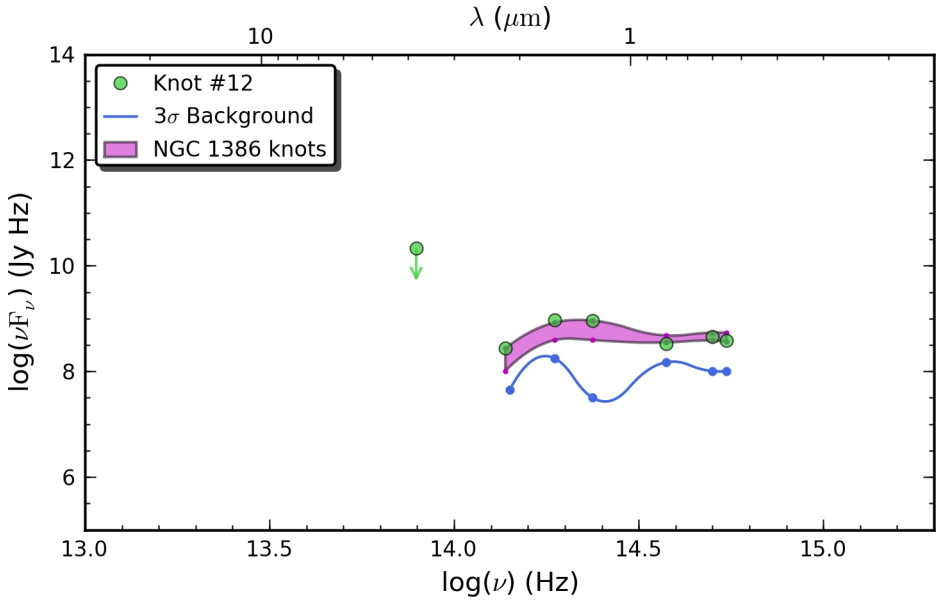

FIGURE 5.17— Energy distribution of the representative knot #12 (green circles) compared with the representative SED, between the first and third quartiles, of the 71 knots found in NGC 1386 (purple-shaded area). Blue dots represent the 3σ background distribution.

NGC 1052

The representative SED for the clusters in this galaxy is shown in Fig. 5.18. Upper limits for VLT/VISIR in the $\sim$ 8–13 μm range (Treister et al. and Reunanen et al., private communication) and VLT/NaCo in the *L*-band, where no knots were detected, are also included. The median $J-K$ colour for the clusters is around 0.4 mag, similar to the case of NGC 1097. Although the purple-shaded area in Fig. 5.18 suggests the presence of a bump around $\sim$ 0.8 μm, this is an effect of the interpolation, as the quartiles are not sampled in the peak of this feature. Moreover, fluxes for the F28X50LP filter are probably overestimated, since the Hα line emission is located

very close to the transmission peak of this wide filter (see Section 5.3.3). Finally, the background SED is almost flat except for the *HST*/NICMOS F160W filter (*H*-band), which has a higher background value than the NaCo *J* and *Ks*-bands as in the case of NGC 1386.

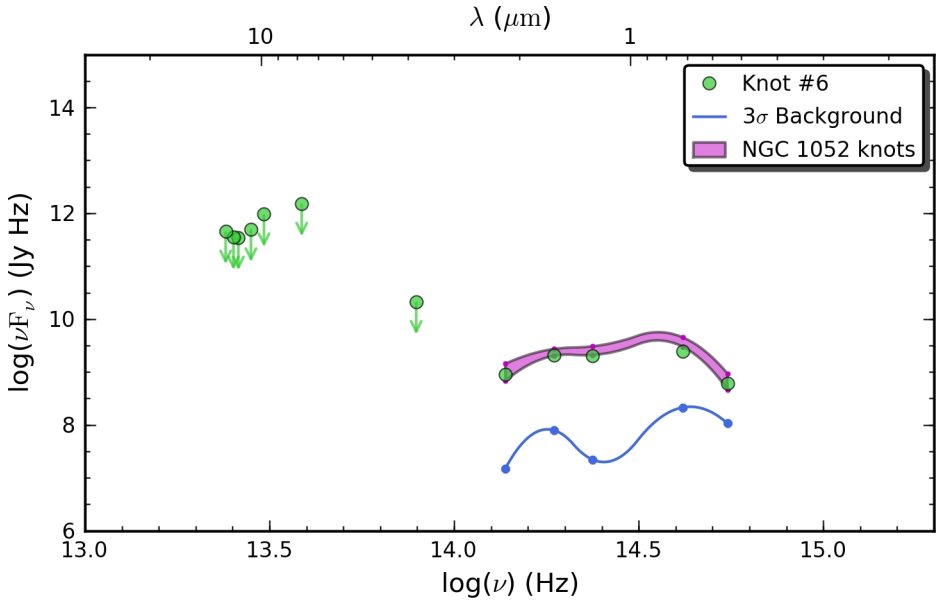

FIGURE 5.18— Energy distribution of the representative knot #6 (green circles) compared with the representative SED, between the first and third quartiles, of the 25 knots found in NGC 1052 (purple-shaded area). Blue dots represent the 3σ background distribution.

NGC 7582

The median energy distribution in Fig. 5.19 also reminds one to that of NGC 253 (Fig. 5.1), although the NIR bump is less pronounced in this case and the overall SED is not as well sampled and for the latter. In contrast, the background SED for NGC 7582 also shows a NIR bump, suggesting that this excess is present also in the diffuse light around the clusters. However, the contribution in the background softens with increasing sky aperture, i.e. the NIR feature in the background decreases with the distance to the centre of the clusters. This can be explained either by a contribution of light in the wings of the PSFs associated with the clusters or the presence of unresolved clusters in the background component. The *V*-band suggests a strong extinction, although additional data in the optical/UV range is required to confirm this behaviour.

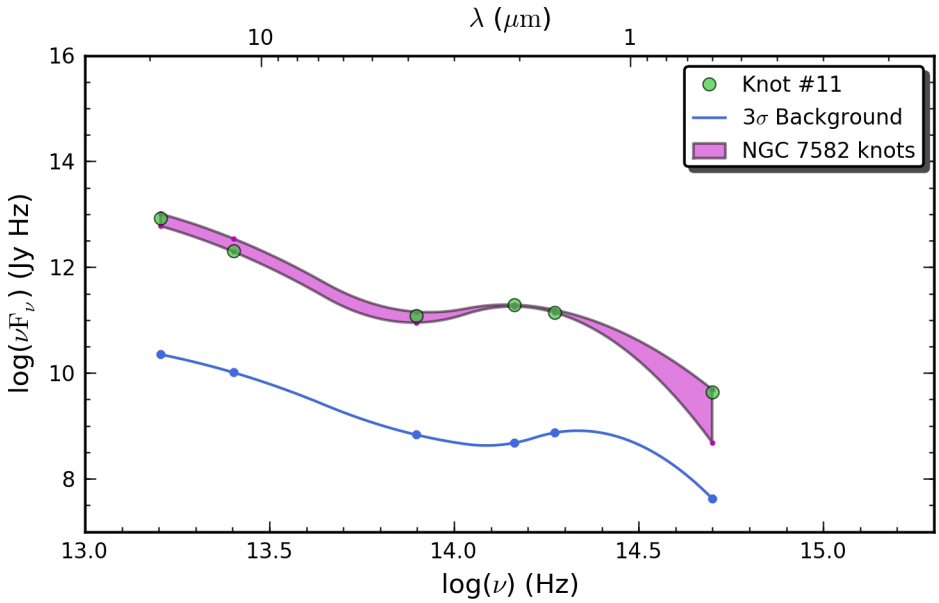

FIGURE 5.19— Energy distribution of the representative knot #11 (green circles) compared with the representative SED, between the first and third quartiles, of the 26 knots found in NGC 7582 (purple-shaded area). Blue dots represent the 3σ background distribution.

NGC 7469

The median SED of NGC 7469 apparently differs from those of other galaxies (Fig. 5.20). There is an increase longwards of 2 μm as in NGC 253, NGC 1097 and NGC 7582, but the average behaviour of the clusters in NGC 7469 suggests a flat distribution towards the optical/UV range. Furthermore, there is no evidence of a NIR excess in the representative SED, as in the previous cases. The background SED is flat over the NIR to NUV range with systematic falls in the VLT/NaCo bands *J*, *H* and *L*. In this case, the NaCo *Ks*-band was not considered due to the low integration time of the image.

Extinction-corrected SEDs

In Fig. 5.21 we compare the representative distributions obtained from the extinction-corrected collection of SEDs. Thus, those galaxies with extinction estimates are represented, i.e. NGC 253 (purple circles), NGC 1097 (red squares) and NGC 7469

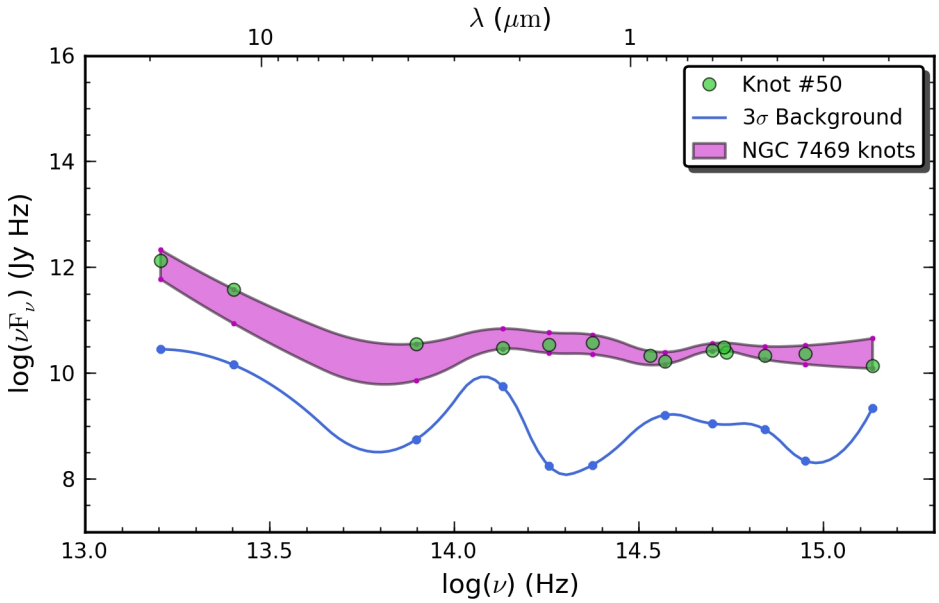

FIGURE 5.20— Energy distribution of the representative knot #50 (green circles) compared with the representative SED, between the first and third quartiles, of the 59 knots found in NGC 7469 (purple-shaded area). Blue dots represent the 3σ background distribution.

(blue triangles). The representative SEDs are arbitrarily scaled for the sake of clarity. For the error bars we considered the photometric errors, which dominate in the MIR and the *L*-band, plus those derived from the extinction correction, which are larger than the former shortwards of $\sim 2\,\mu$m. The unreddened SEDs of NGC 253 and NGC 7469 present quite flat distributions, within the error, in the NIR to optical range. The former still shows a soft decrease from *J* to *L*-band remaining to the NIR bump mentioned before. The latter increase towards the UV, but the errors derived from the extinction correction are very large and the median SED is also consistent with a flat distribution. However, this in not the case for NGC 1097, which increases shortwards of $\sim 4\,\mu$m, although values in the UV present also very large errors. This suggests that the stellar emission for these clusters is, in average, stronger than the dust emission in the νF_ν distribution. This is in agreement with the ages derived in Section 5.4.4, which favour the picture of a more evolved starburst component in this galaxy. Overall, the representative SEDs increase longwards of $\sim 4\,\mu$m, probably due to the contribution of warm dust ($\lesssim 300\,$K).

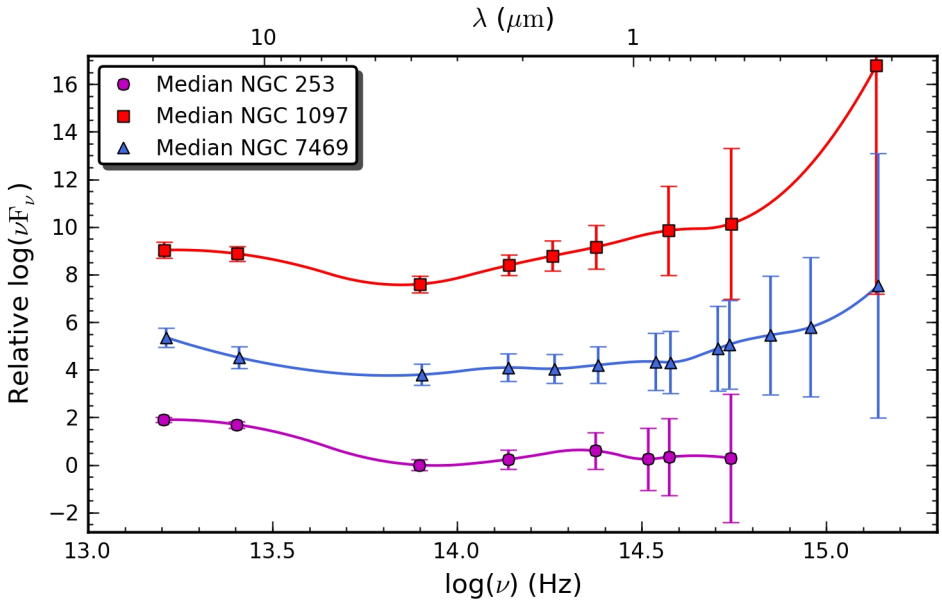

FIGURE 5.21— Representative distributions for the unreddened SEDs of NGC 253 (purple circles), NGC 1097 (red squares) and NGC 7469 (blue triangles). We considered the photometric errors plus those derived from the extinction correction.

5.4.8 The age–NIR excess correlation

In Section 5.2.2 we showed that the contribution from YSOs or protostars to the SED of a representative cluster in NGC 253 is able to explain the NIR excess measured for these regions, which are considered to be YSCs. Moreover, this excess is interpreted as the total thermal contribution from individual optically thick circumstellar disks associated to the protostars. However, clusters in NGC 1097 or NGC 7582 present also a similar excess, suggesting that this component could have a similar origin for these objects.

Nevertheless, IR observations by Haisch et al. (2001) and Mamajek et al. (2004) revealed that the majority of thick disks surrounding protostars are dispersed in the first ~ 10 Myr. Considering these, one would expect the NIR excess to decrease with increasing age, as the protostellar disks are blown away by the central stars. On the other hand, the knots with an age estimation in the whole sample span the 3–20 Myr range, and thus we can address this question. At this point, we considered only those knots with both an extinction and an age estimate, i.e. those found in NGC 253, NGC 1097 or NGC 7469, although the clusters in the latter do not show a NIR excess in their average SED. However, the range of ages mentioned previously is still valid

since the youngest and oldest knots are found in NGC 253 and NGC 1097, respectively.

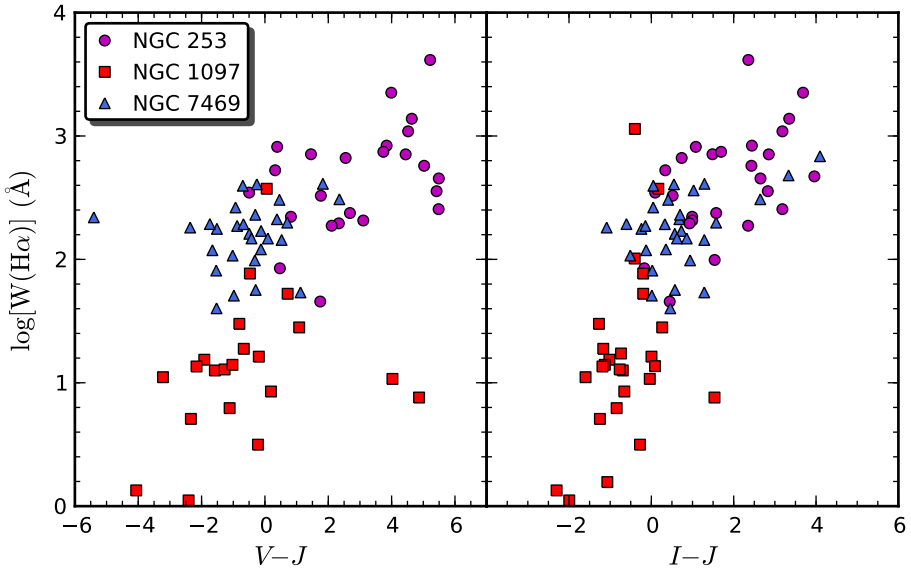

FIGURE 5.22— Age–NIR colour relation for the knots in NGC 253 (purple circles), NGC 1097 (red squares) and NGC 7469 (blue triangles). $V-J$ and $I-J$ colours are corrected for dust extinction estimated from the Hα/Brα ratio in the case of NGC 253 and the Hα/Paα ratio in the cases of NGC 1097 and NGC 7469.

Fig. 5.22 shows the relation between the NIR excess, measured as the extinction-corrected $V-J$ and $I-J$ colours, and the age of the knots represented by $log(\mathrm{W(H}\alpha)\,)$. The dispersion is higher for the $V-J$ colour, in the left panel, but the right one shows a clear tendency for the intrinsic $I-J$ colour to increase at lower ages (higher W(Hα)). This behaviour is observed for a wide variety of knots in different objects, and cannot be explained by the possible contribution from red giants to the NIR integrated light (Lançon et al. 2009), since the latter would result in an increasing excess with age. In contrast, the redder colours ($I-J\sim 4$ mag) are found for the youngest clusters in NGC 253 (~ 3 Myr), while bluer colours ($I-J\sim -2$ mag) correspond to the oldest clusters in NGC 1097 (~ 20 Myr). This relation seems to flatten at ages younger than $\lesssim 5$ Myr (W(Hα) $\gtrsim 420$ Å), although data for younger regions are needed in order to check this result. However, the knots in NGC 7469 do not show any correlation by themselves, although they fit in the age–NIR excess gap between those in NGC 253 and NGC 1097 (Fig. 5.22). This might be a side effect of the lower spatial resolution,

that do not permit us to isolate individual YSCs in this galaxy, but due to the absence of a NIR excess in the representative SED of these clusters we do not expect any dependence with age for this galaxy. Finally, a similar trend for the age–NIR excess correlation is reported by Reines et al. (2008) for the stellar clusters in low-metallicity galaxy SBS 0335–052. Moreover, Calzetti et al. (1997) detected an anti-correlation between the presence of dust and the age of the young stellar clusters found in NGC 5253.

5.5 Cluster luminosity and initial mass functions

As mentioned in Section 5.1, YSCs have been observed in very different places from interacting and starburst galaxies to quiescent spirals. The properties of these YSCs seem to be related with the environment in which they formed, but there are also many similarities among all of them. One of the best examples is the luminosity function (LF), defined as the number of clusters per unit luminosity (dN/dL), which is usually well described by a power-law:

$$\phi(L) \equiv \frac{dN}{dL} \propto L^{-\alpha} \tag{5.2}$$

with $\alpha \approx 2$ (Miller et al. 1997; Larsen 2002; de Grijs et al. 2003). An interesting property of a power law with an index of $\alpha = 2$ is that the most luminous object increases its luminosity (L_{max}) linearly with the total number of clusters (N). Based on the study of the brightest clusters in different galaxies, Whitmore (2003) reported that the value of L_{max} scales as $L_{max} \approx N^{\eta}$. This index suggest that the LF is slightly steeper at its bright end, as $\eta = 1/(\alpha - 1)$ for a pure power law (Hunter et al. 2003), and a value of $\eta = 0.75$ corresponds to $\alpha = 2.4$. This method is in agreement with estimations of the slope for the LF at its bright end in individual galaxies (Whitmore et al. 1999; Larsen 2002; Gieles et al. 2006a; Hwang & Lee 2008), since the L_{max} method traces the brightest clusters. Nevertheless, due to statistical fluctuations and photometric uncertainties, values in the $1.8 \lesssim \alpha \lesssim 2.8$ range are more reliable for the slope of the LF (Dolphin & Kennicutt 2002; Elmegreen et al. 2002).

Usually, the LF is interpreted directly as the underlying cluster initial mass function (CIMF), i.e. the distribution of masses in the initial stage of an starburst or a group of open clusters formed at the same time. However, this relation is not one-to-one as the former consists of clusters with different ages. The new clusters fade rapidly during their first ~ 1 Gyr and, as a consequence of their evolution, clusters of the same mass with different ages contribute at different luminosities (Portegies Zwart et al. 2010). Thus, one of the the main sources of error to derive the CIMF from the LF is the estimation of cluster ages, specially when their spread is high with regard to the average age of the clusters (Fall 2006).

In this context, the higher slope of the LF at the bright end is interpreted as a truncation of the CIMF at some upper mass (Gieles 2009a). As mentioned in Section 1.2.2, the functional form of the initial mass function for young star clusters, $\psi(M)$, is well represented by a Schechter (1976) distribution:

$$\psi(M) \equiv \frac{dN}{dM} \propto \left(\frac{M}{M_*}\right)^{-\gamma} \exp\left(-\frac{M}{M_*}\right) \tag{5.3}$$

where M_* is the characteristic mass and γ is the index of the power law distribution. For Milky Way type spiral galaxies we have $M_* \approx 2\times10^5\,\mathrm{M}_\odot$ (Gieles et al. 2006b; Larsen 2009), while interacting and luminous infrared galaxies show $M_* \gtrsim 10^6\,\mathrm{M}_\odot$ (Bastian 2008). Overall, it seems that the value of M_* depends on the local environment, i.e. it is possible to form more massive clusters in the Antennae galaxies than in more quiescent environments (Portegies Zwart et al. 2010). The empirically determined power-law index is found to be $\gamma \approx 2$ (Elmegreen & Efremov 1997; Zhang & Fall 1999; McCrady & Graham 2007), with the spread between different studies much smaller than that found for the luminosity function (Gieles 2009a).

5.5.1 The Cluster Luminosity Function

Fig. 5.23 shows the K-band absolute magnitude distribution for the clusters in NGC 253, NGC 1097 and NGC 7469. These galaxies are selected because they have extinction estimates, which were used to correct the cluster magnitudes from absorption. As a consequence, the number of knots is limited to 26, 42 and 42, i.e. those with extinction estimates in Tables 3.1, 3.2 and 3.6, respectively. The slope of the LF is thus inferred from the fit of a power law to the slope of the brighter side of the distribution.

The slopes obtained for NGC 253 and NGC 1097 are much lower than the expected value of $\alpha \sim 2$, although the errors induced by the low statistics can be quite high. In the best case, these are of about 30%, but can increase up to $\sim 50\%$ in the case of NGC 253, with the lower number of clusters. Moreover, the power-law index is strongly dependent of the bin size and spacing for such small data samples, an effect that increases the errors estimated above. Following Rosolowsky (2005), we estimated the K-band cumulative LF for the knots in each galaxy, i.e. $N(L'_K > L_K) \propto L_K^{\alpha+1}$, where $N(L'_K > L_K)$ (or $N(M'_K < M_K)$ in magnitudes) is the number of knots brighter than a certain L_K. The slope of this distribution in a logarithmic representation is $\alpha + 1$, with α being that of the standard LF. Fig. 5.24 shows that the slopes derived with this method are more consistent with the range of values observed in similar star-forming regions. Grey-solid lines represent the fraction above which we lose completeness for the faintest knots. The cumulative distribution of NGC 253, the object which hosts

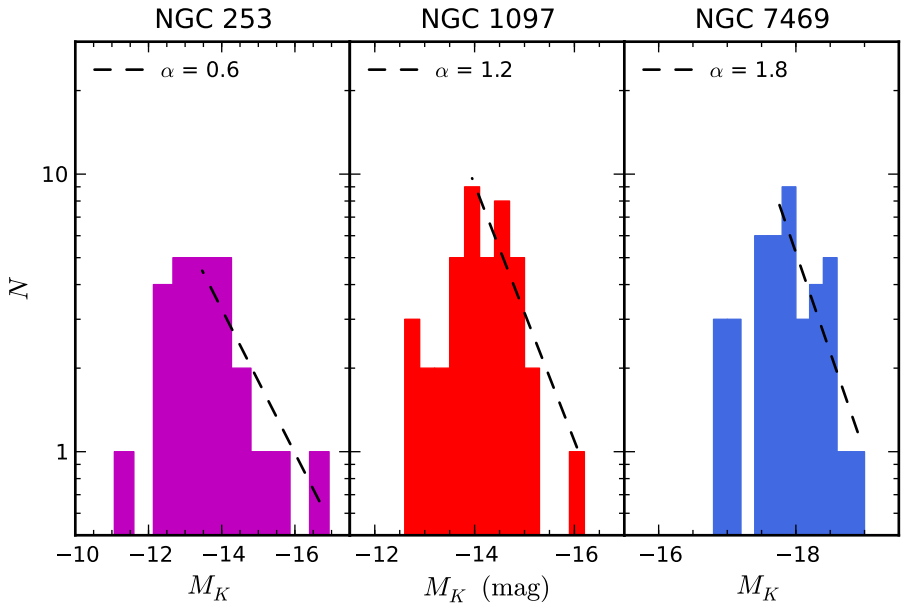

FIGURE 5.23— K-band luminosity function for the knots in NGC 253 (purple), NGC 1097 (red) and NGC 7469 (blue). A power-law is fitted to the brighter side of each distribution (dashed line).

the youngest clusters (~ 4.3 Myr) follows a power law with $\alpha = 1.9$. NGC 1097, which present older clusters (~ 10 Myr) shows also a steeper distribution with $\alpha = 2.8$. However, NGC 7469 (~ 5.8 Myr) presents the highest value with $\alpha = 3.7$. In this case, there is no dependence on the sampling of the distribution function, and the errors derived by statistical uncertainty are $\sim 20\%$ in the worst case, decreasing to $\sim 15\%$ in the most favourable situation. As discussed in Section 3.2.6, it is very likely that each knot in NGC 7469 is an unresolved clump formed by $\gtrsim 100$ stellar clusters like those in NGC 253, and therefore we do not expect, a priori, the knots in this galaxy to follow a power law similar to those systems with individually resolved clusters. However, if the knots identified in this galaxy are oversized stellar clusters, steeper luminosity and mass functions are not rare, as mentioned in Section 1.2.2.

Finally, Fig. 5.25 shows the normalized K-band cumulative LF for all the knots without extinction correction, grouped by their host galaxy. In this case, $p(M'_K < M_K)$ represents the fraction of knots brighter than a certain value M_K. Resulting indices from the fits of power-laws to the cumulative LF, excluding those values above the completeness limit, are $\alpha = 2.1$ (NGC 253), 2.8 (NGC 1097), 2.2 (NGC 1386), 2.0 (NGC 1052), 3.7 (NGC 7582) and 4.2 (NGC 7469). Variations in the slopes using magnitudes affected by extinction are not very strong. Those galaxies for

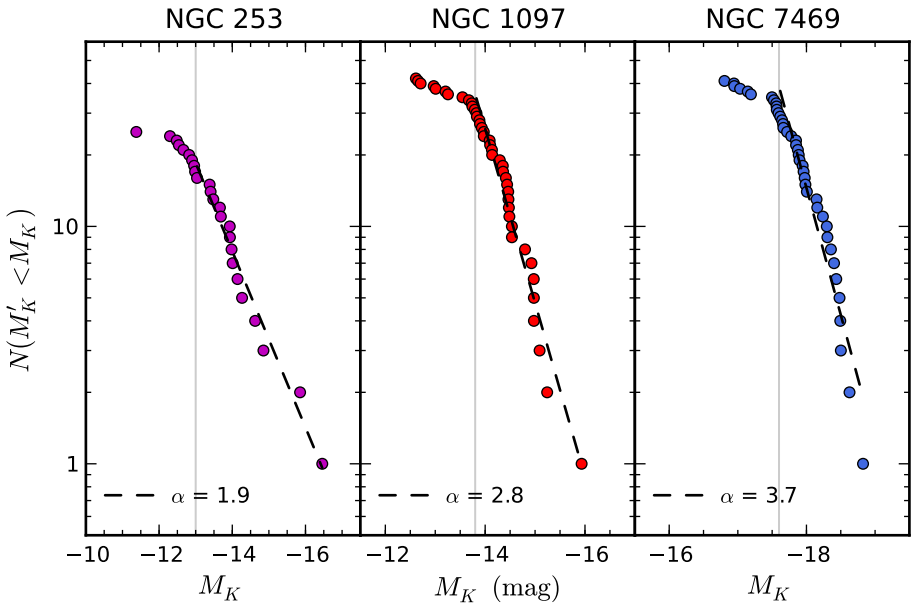

FIGURE 5.24— *K*-band cumulative luminosity function for the knots in NGC 253 (purple), NGC 1097 (red) and NGC 7469 (blue). A power-law is fitted in each case (dashed line). The grey vertical line represents the completeness limit in each case.

which we expect to resolve individual star-forming clusters (NGC 253, NGC 1097, NGC 1386 and NGC 1052), show slopes in agreement with the range of expected values mentioned earlier. In contrast, NGC 7582 and NGC 7469, for which we are not resolving individual clusters, exhibit the highest values for α. However, it is not clear how the lower-spatial resolution in these cases (FWHM $\sim$ 15 for NGC 7582 and 22 pc for NGC 7469) modifies the luminosity function.

For comparison, similar power-law index as those found in NGC 253 and NGC 1097 have been reported for young star-forming regions in M81 (Santiago-Cortés et al. 2010) and the circumnuclear rings of NGC 1512 and NGC 5248 (Maoz et al. 2001). In the cases of Antennae and M51, Whitmore et al. (1999) and Gieles et al. (2006b) find, respectively, a power law with $\alpha \sim 2.5$ at the bright end and $\alpha \sim 2$ at the faint end of the LF.

5.5.2 The Cluster Initial Mass Function

To derive the CIMF we used the mass values obtained in Section 5.4.5, which are corrected by extinction and also consider the age of each knot in their individual mass-to-light ratio and mass estimations. When compared with dynamical mass

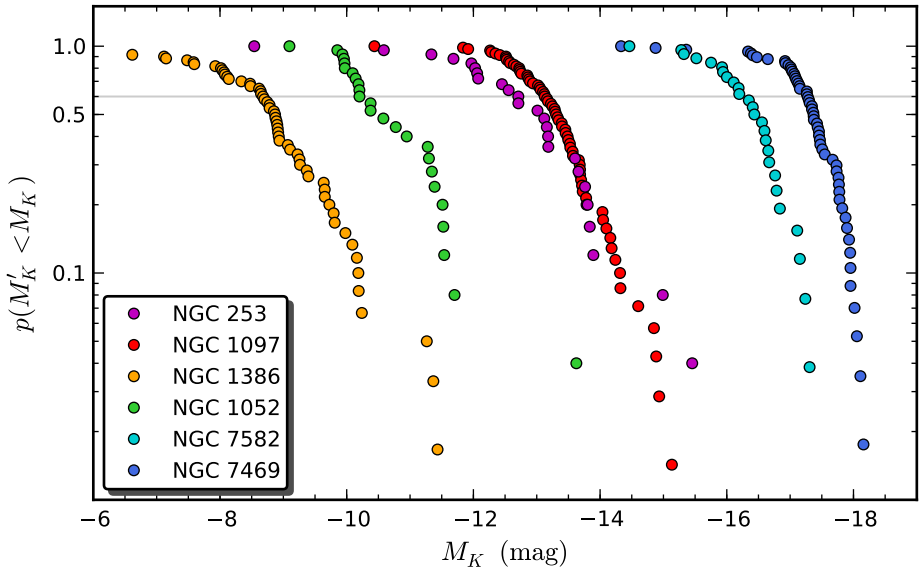

FIGURE 5.25— Normalized *K*-band cumulative luminosity function for all the knots grouped by galaxy.

determinations using spectroscopic techniques, photometric masses present larger uncertainties since they are conditioned to different assumptions, such as the stellar population model which also relies on a stellar IMF and theoretical isochrones (McCrady & Graham 2007). However, dynamical determinations for clusters are less sensitive and cannot sample with enough completeness the low-mass tail of the IMF, specially in the centre of galaxies.

Fig. 5.26 shows the distribution of masses for NGC 253 (purple), NGC 1097 (red) and NGC 7469 (blue), together with a power-law fit for the higher masses (dashed line). For comparison, we also show the mass function for old GCs in the Milky Way (dotted line), which follows a lognormal distribution with a peak at $M_* \sim 2 \times 10^5\,\mathrm{M}_\odot$ and a dispersion of $\sigma(\log M) = 0.5$ (Harris 1991; Fall & Zhang 2001).

As in the case of the LF (Fig. 5.23), the low number of knots do not permit a reliable power-law fit. The case of NGC 1097 is specially dramatic with a nearly flat index, which would imply a larger number of massive clusters than the low mass ones. However, the peak of the Milky Way GCs at $2 \times 10^5\,\mathrm{M}_\odot$ appears to be very close to the centre of NGC 253 and NGC 1097 distributions. In the case of NGC 7469, the mass distribution reaches its maximum at $\sim 6.3 \times 10^6\,\mathrm{M}_\odot$.

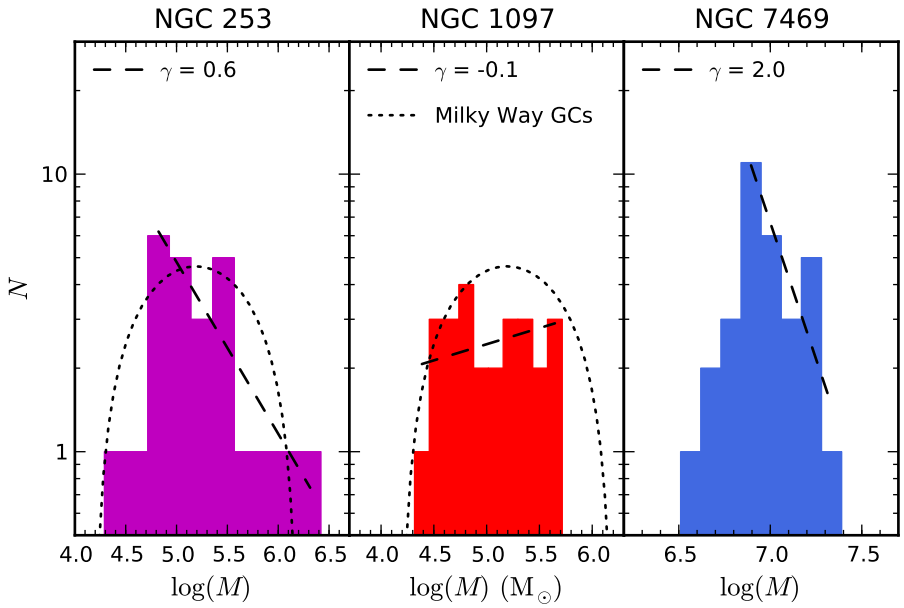

FIGURE 5.26— *K*-band cluster initial mass function for YSCs in NGC 253 (purple circles), NGC 1097 (red circles) and NGC 7469 (blue circles). A power-law is fitted to the higher masses in each distribution (dashed line). The dotted line represents the lognormal distribution of GCs in the Milky Way, peaking at $M_* \sim 2 \times 10^5\,\mathrm{M}_\odot$.

Again, the cumulative CIMF (Fig. 5.27) suggest a different behaviour when compared with the standard distribution. The power-law fit over the completeness limit gives $\gamma = 1.8$ and 1.9 for NGC 253 and NGC 1097, respectively, and a steeper slope of 3.5 in the case of NGC 7469. These values are consistent with those derived from the cumulative LF (1.9, 2.8 and 3.7). Note that the larger variation occurs for NGC 1097, with shows a slope change in the profile of its cumulative mass distribution, absent in the corresponding LF in Fig. 5.24. The cumulative distribution for GCs in the Milky way is also plotted for comparison (dotted line in Fig. 5.27). The latter differs completely from the young cluster distribution at the lowest masses, but resembles slightly the turn-over in NGC 1097 at the high mass end (middle panel in Fig. 5.27). Since the turn-over in the mass distribution for NGC 1097 could be related with the characteristic mass in Eq. 5.3, we fitted the numeric integral of the Schechter distribution to the cumulative CIMF for NGC 1097 (Fig. 5.28). The resulting fit describes very well the behaviour of the cumulative CIMF, with a flatten profile at low masses ($\gamma \approx 0.9$) that bends down at values close to the characteristic mass ($M_* \approx 2.1 \times 10^5\,\mathrm{M}_\odot$). We estimate a relative error of $\delta\gamma \sim 20\%$ in the power-law index

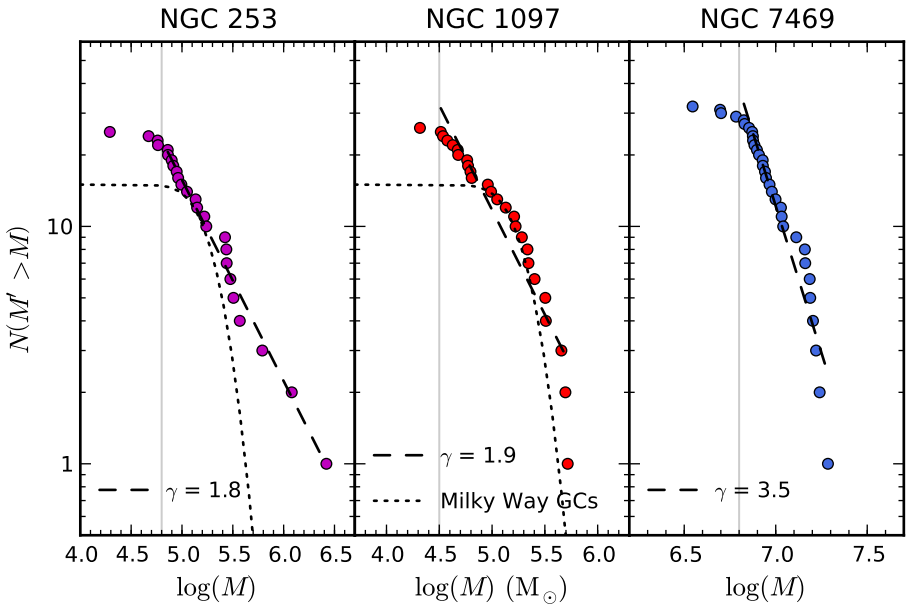

FIGURE 5.27— *K*-band cumulative initial mass function for YSCs in NGC 253 (purple circles), NGC 1097 (red circles) and NGC 7469 (blue circles). A power-law is fitted in each case (dashed line). For comparison, we show the cumulative distribution for the GCs in the Milky Way (dotted line). The grey vertical line represents the completeness limit in each case.

and an absolute error of $\Delta M_* \sim 0.4 \times 10^5\,\mathrm{M}_\odot$ in the estimation of the characteristic mass. Moreover, the knots in NGC 1097 appear to be the oldest ones among the whole sample with a median age of $\sim 10\,$Myr, very close to the disruption timescale observed in diverse YSC systems (Mengel et al. 2005). This suggests that the low mass tail of the CIMF in NGC 1097 has suffered from disruption effects (e.g. two-body relaxation or gravitational shocks) and thus shows a flatten power-law behaviour. Furthermore, the characteristic mass is very close to the peak of the mass distribution for GCs in the Milky Way, $2 \times 10^5\,\mathrm{M}_\odot$ (Harris 1991). Nevertheless, we remain cautious about this result since the photometric mass estimations are particularly sensitive around 10 Myr, when the cluster luminosity changes rapidly with age. However, we checked the mass-to-light ratio distributions used in each galaxy and none of them introduced any feature when deriving the CIMF. Finally, the highest end of the cumulative CIMF in Fig. 5.28 appears to be truncated when compared with the Schechter profile, although this can also be an effect caused by the low statistics in the high-mass range.

Simple analytical models for young stellar clusters by Fall & Zhang (2001) yield very interesting results about the dynamical evolution of the CIMF. The latter seems to be dominated for the less massive clusters ($M \lesssim M_*$) by disruption via two-body

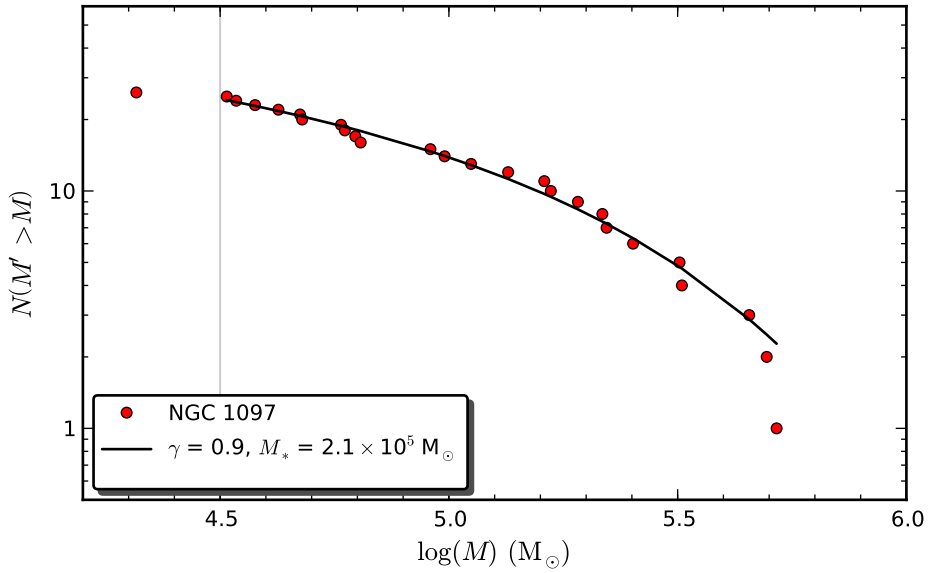

FIGURE 5.28— *K*-band cumulative initial mass function for YSCs in NGC 1097 (red circles) and best fit to a Schechter profile (black-solid line). The grey vertical line represents the completeness limit.

relaxation (i.e. internal scatter which causes some stars to gain enough energy to escape from the clusters), flattening the low mass tail of the distribution. The high mass end of the distribution ($M \gtrsim M_*$) is mostly affected by stellar evolution and gravitational shocks, which are roughly independent of the masses of the clusters and hence tend to preserve the shape of the CIMF at this end. Moreover, the mass function in these models develops a turnover or peak which, after ~ 12 Gyr, is remarkably close to $\sim 2 \times 10^5\,\mathrm{M}_\odot$, the peak of the GCs distribution.

Several CIMF determinations have also found a power-law behaviour with indices close to $\gamma \sim 2$, as in the Large Magellanic Cloud (LMC, Larsen 2009), M51 (Gieles 2009b), M82 (McCrady & Graham 2007), M31 (Vansevičius et al. 2009) and the Antennae galaxies Zhang & Fall (1999). In the latter case, Mengel et al. (2005) report evidences for a turnover in the slope of the mass distribution of this system. Interestingly, molecular clouds in the inner part of the Milky Way follow a truncated power-law distribution with index $\gamma \approx 1.5$ and a cutoff at $\sim 3.2 \times 10^6\,\mathrm{M}_\odot$. Those clouds in the outer part show $\gamma \sim 2.1$, with no evidence of a cutoff. In M33, the situation is similar to the outer Milky Way with a steeper distribution, $\gamma \approx 2.9$. Finally, molecular clouds in the LMC present a marginally steeper distribution with $\gamma \approx 1.7$ and also a cutoff at $\sim 3.2 \times 10^6\,\mathrm{M}_\odot$, very similar to the inner part of the Milky Way

(see Rosolowsky 2005).

5.6 Summary

High-spatial resolution techniques are not only useful for the study of AGNs (see Chapter 4), but also permit us to resolve crowded star-forming regions in the centre of galaxies. By observing in the NIR we can avoid most of the harmful effect of the extinction and unveil very young populations of stellar clusters which are still embedded in their birth material. Two exemplary cases are NGC 253 and NGC 1052. The former is one of the closest starbursts which has been resolved in a total of 37 very young and compact stellar clusters. An average template for these clusters, from radio wavelengths to optical, is provided as a representative extragalactic star forming region (Fig. 5.1, Table 5.1). Due to the high-spatial resolution achieved, the genuine cluster emission is isolated from the diffuse light of the galaxy, allowing us to distinguish the contribution of protostellar objects to the SED in the NIR. Moreover, the fading of the NIR excess with increasing age agrees very well with the evolution of circumstellar disks in YSOs, which are dispersed as the young stars approach the Main Sequence. On the other hand, NGC 1052 is an early-type galaxy with signs of having experienced a recent interaction and subsequent rejuvenation of its stellar population due to induced star-formation activity, specially in its centre. Although this is also the case for a number of early-type galaxies in the local universe (e.g. Centaurus A, NGC 1316 or NGC 3597), we resolve for the first time a very young population of 15 stellar clusters with $\lesssim 10$ Myr in the centre of NGC 1052. Previous studies on the subject report either older cluster with intermediate ages (a few Gyr, e.g. Goudfrooij et al. 2001), average bluer colours (Kaviraj et al. 2007) or resolved individual young stars (Rejkuba et al. 2001). Our age estimate is robust since it relies on the detection of Hα in emission, and thus is nearly independent of the cluster mass and slightly dependent on the metallicity. However, in the less favourable case, i.e. the lowest metallicity considered, the W(Hα) measured predict ages below $\lesssim 12$ Myr.

Nevertheless, the presence of clusters in the centre of galaxies is not rare, and thus we have studied all the YSCs found in the objects of the sample. Overall, they show very similar sizes and span similar age ranges (3–15 Myr). However, their brightness, mass and SFR seem to be strongly dependent on the local environment, i.e. the galaxy and the region within were they were born. Individual knots in the starburst ring of NGC 7469 are as bright as the whole starburst component in NGC 253. This could be caused by special conditions in the former, which permit the formation of clusters much brighter and massive than those seen in the local universe, or may be by a side effect of the lower spatial resolution at larger distances, which do not permit us to resolve structures formed by a number of individual clusters like those in NGC 253.

TABLE 5.3— Main properties derived for the knots found in NGC 253. The radial distance corresponds to the angle with respect to the knot #32, used as reference for the alignment. The absolute (Δ) or relative errors (δ) corresponding to the different magnitudes are: $\Delta M_K = 0.1$ mag, $\Delta(V-I) = 0.3$ mag, $\Delta(V-J) = 0.3$ mag, $\Delta(J-K) = 0.1$ mag, $\delta(\mathrm{H}\alpha/\mathrm{Br}\alpha) = 19\%$, $\Delta A_V = 0.3$ mag, $\delta[W(\mathrm{H}\alpha)] = 23\%$, $\delta(\mathrm{M}) \sim 30\%$, $\Delta(\mathrm{t}) \sim 0.1$ Myr, $\delta(L_{\mathrm{H}\alpha}) = 10\%$, $\delta(\mathrm{SFR}) \sim 30\%$. Colours and derived magnitudes are corrected for extinction.

#	Radial distance	M_K	V − I	V − J	J − K	$\frac{\mathrm{H}\alpha}{\mathrm{Br}\alpha}$	A_V	W(Hα)	log($L_{\mathrm{H}\alpha}$)	log(M)	log(t)	log(SFR)
		[mag]					[mag]	[Å]	[erg s^{-1}]	[$M_\odot$]	[yr]	[$M_\odot$ yr^{-1}]
0	9.″06	−12.2	...	...	...	...	...	530	....	...	6.6	....
1	9.″59	−12.1	1.5	1.9	1.4	0.53	5.9	660	38.5	4.8	6.5	−2.6
2	7.″86	−12.3	1.7	3.1	0.5	1.12	4.9	710	38.5	4.9	6.5	−2.6
3	8.″60	−15.0	1.4	4.2	0.4	0.14	7.8	710	39.4	6.1	6.5	−1.7
4	8.″31	−15.5	1.2	1.8	0.6	0.07	8.7	330	40.2	6.4	6.7	−0.9
5	6.″54	−13.6	2.2	4.7	0.5	1.46	4.5	360	38.2	5.5	6.7	−2.9
6	6.″69	−13.7	2.2	5.2	0.2	1.43	4.5	260	38.0	5.5	6.8	−3.1
7	6.″27	−13.0	...	...	...	...	...	...	....	...	...	....
8	6.″80	−13.8	1.1	3.3	0.8	1.21	4.8	840	38.7	5.5	6.5	−2.4
9	6.″23	−11.9	...	...	...	...	...	...	....	...	...	....
10	6.″97	−13.8	2.2	4.2	1.2	5.78	2.6	570	38.2	5.3	6.6	−2.9
11	6.″45	−13.8	0.3	1.6	1.2	0.14	7.8	470	39.1	5.7	6.7	−2.0
12	7.″58	−14.0	3.5	7.3	2.1	18.32	1.0	190	36.5	5.5	6.8	−4.6
13	5.″56	−11.7	−0.1	0.1	0.3	0.23	7.1	530	39.0	4.7	6.6	−2.1
14	6.″26	−13.0	2.9	5.6	1.0	3.98	3.1	450	37.6	5.1	6.7	−3.5
15	4.″95	−13.4	2.4	5.9	0.6	6.80	2.4	1650	38.1	5.1	6.4	−3.0
16	5.″42	−12.0	−0.7	0.4	−0.6	0.11	8.1	820	39.5	4.9	6.5	−1.6
17	4.″97	−12.7	0.5	3.1	−0.3	1.52	4.5	1380	38.8	5.0	6.5	−2.3
18	5.″93	−13.2	1.9	2.7	0.1	0.14	7.8	210	39.0	5.5	6.8	−2.1
19	4.″46	−13.1	0.7	3.3	0.5	1.19	4.8	1090	38.6	5.2	6.5	−2.5
20	4.″64	−13.2	−0.1	3.3	0.5	0.81	5.3	2240	38.8	5.1	6.3	−2.3
21	3.″25	−12.2	...	...	...	...	...	...	....	...	...	....
22	3.″53	−10.3	...	...	...	...	...	...	....	...	...	....
23	4.″21	−12.7	...	...	0.7	0.12	8.1	100	38.4	5.2	6.8	−2.7
24	2.″91	−10.6	0.0	1.5	−0.9	0.28	6.8	710	38.6	4.3	6.5	−2.5
25	2.″88	−12.0	1.5	2.4	0.0	1.16	4.8	200	38.2	4.9	6.8	−2.9
26	1.″44	−8.5	...	...	...	...	...	4130	....	...	...	....
27	2.″89	−12.5	...	...	...	...	...	470	....	...	6.7	....
28	1.″02	−12.1	−0.6	−0.6	2.5	0.18	7.4	350	38.3	5.0	6.7	−2.8
29	0.″52	−12.6	2.1	3.8	0.4	2.06	4.0	740	38.4	5.0	6.5	−2.7
30	2.″26	...	−3.2	...	...	0.02	10.3	90	38.4	...	6.8	−2.7

31	0.″75	...	...	...	...	...	...	770	....	...	6.5	....
32	0.″02	−13.9	0.6	0.4	0.2	0.39	6.4	90	39.2	5.6	6.8	−1.9
33	0.″61	−11.3	−0.4	2.3	−1.2	0.07	8.8	190	38.3	4.8	6.8	−2.9
34	0.″69	−11.6	...	...	...	...	...	...	....	...	...	....
35	5.″44	−13.2	1.1	2.7	0.8	0.36	6.5	240	38.4	5.4	6.8	−2.7
36	9.″64	−12.7	1.3	1.7	0.2	0.48	6.1	50	38.1	4.9	6.8	−3.0

TABLE 5.4— Main properties derived for the knots found in NGC 1097. The radial distance corresponds to the angle with respect to the active nucleus. The absolute (Δ) or relative errors (δ) corresponding to the different magnitudes are: $\Delta M_K = 0.1$ mag, $\Delta(V-I) = 0.1$ mag, $\Delta(V-J) = 0.1$ mag, $\Delta(J-K) = 0.1$ mag, $\delta(\mathrm{H}\alpha/\mathrm{Pa}\alpha) = 17\%$, $\Delta A_V = 0.2$ mag, $\delta[W(\mathrm{H}\alpha)] = 20\%$, $\delta(\mathrm{M}) \sim 30\%$, $\Delta(\mathrm{t}) \sim 0.4$ Myr, $\delta(L_{\mathrm{H}\alpha}) = 3\%$, $\delta(\mathrm{SFR}) \sim 30\%$. Colours and derived magnitudes are corrected for extinction.

#	Radial distance	M_K	V − I	V − J	J − K	$\frac{\mathrm{H}\alpha}{\mathrm{Pa}\alpha}$	A_V	$W(\mathrm{H}\alpha)$	$\log(L_{\mathrm{H}\alpha})$	log(M)	log(t)	log(SFR)
		[mag]					[mag]	[Å]	[erg s^{-1}]	[$M_\odot$]	[yr]	[$M_\odot$ yr^{-1}]
0	19.″95	...	...	...	...	...	...	...	....	...	...	....
1	21.″83	...	...	...	...	...	...	...	....	...	...	....
2	17.″51	−10.4	...	...	...	...	...	...	....	...	...	....
3	10.″75	−12.5	...	...	...	...	...	...	....	...	...	....
4	10.″63	−13.7	...	...	...	...	...	...	....	...	...	....
5	11.″52	−12.9	...	...	...	...	...	...	....	...	...	....
6	9.″95	−13.3	...	...	...	...	...	...	....	...	...	....
7	9.″79	−13.3	−2.7	−3.9	−1.1	0.01	11.7	3	39.0	5.2	7.1	−2.1
8	10.″32	−13.8	2.7	4.1	0.6	...	...	...	....	...	...	....
9	9.″69	−13.5	...	...	0.1	0.01	11.8	19	39.6	5.1	6.9	−1.5
10	10.″05	−12.9	...	...	...	...	...	...	....	...	...	....
11	9.″25	−13.1	0.3	−0.5	−0.8	0.08	7.5	46	39.6	5.1	6.8	−1.5
12	9.″25	−12.3	...	...	...	...	...	...	....	...	...	....
13	10.″38	−12.9	1.6	2.8	0.5	...	...	...	....	...	...	....
14	10.″22	−13.4	−1.0	−1.5	−0.7	0.04	8.8	44	39.3	5.3	6.8	−1.8
15	8.″23	−14.6	0.8	0.3	−0.3	0.34	5.2	12	39.0	5.1	7.0	−2.1
16	8.″73	−13.5	−1.5	−2.7	−0.9	0.02	10.1	4	39.1	5.1	7.1	−2.0
17	8.″96	−12.6	...	...	...	...	...	28	....	...	6.8	....
18	7.″88	−14.2	0.5	−0.7	−0.4	0.29	5.5	19	39.5	5.1	6.9	−1.6
19	9.″82	−13.2	−0.3	−0.3	−0.7	0.12	7.0	20	38.7	4.7	6.9	−2.4
20	8.″52	−12.7	...	...	...	...	...	...	....	...	...	....
21	9.″03	−13.7	−0.4	−1.0	−0.5	0.03	9.1	15	39.3	4.9	7.0	−1.8
22	7.″77	−14.1	...	...	...	...	...	1	....	...	7.3	....
23	8.″88	−13.7	−1.9	−3.4	−1.2	0.02	10.0	1	39.0	5.6	7.3	−2.1
24	8.″78	−13.7	−1.4	−2.5	−1.0	0.04	8.6	4	39.0	5.1	7.1	−2.1
25	9.″42	−13.7	1.6	0.3	0.5	0.10	7.2	15	38.8	4.8	7.0	−2.3
26	8.″52	−13.2	...	...	−1.0	0.03	9.3	25	39.1	5.0	6.8	−2.0
27	8.″58	−13.7	−0.5	−1.2	−0.9	0.23	5.9	13	39.2	4.8	7.0	−1.9
28	9.″06	−13.7	−0.8	−1.0	−1.2	0.09	7.4	86	40.0	5.5	6.8	−1.1
29	7.″94	−14.3	...	...	...	...	...	...	....	...	...	....
30	9.″03	−14.9	...	...	...	...	...	...	....	...	...	....

31	5.″97	−11.9	1.2	0.1	−0.8	...	...	...	....	...	...	....
32	7.″55	−12.7	−1.3	−2.2	−1.0	...	...	...	....	...	...	....
33	8.″60	−12.7	...	...	...	...	...	14	....	...	7.0	....
34	7.″59	−13.0	...	...	...	...	...	...	....	...	...	....
35	7.″95	−13.1	...	...	...	...	...	...	....	...	...	....
36	8.″77	−12.5	...	...	...	...	...	10	....	...	7.1	....
37	7.″58	−15.1	...	...	...	...	...	...	....	...	...	....
38	9.″18	−13.3	0.9	1.1	−0.5	0.13	6.8	16	38.4	4.6	7.0	−2.8
39	6.″75	−12.4	−2.4	−3.9	−1.4	0.01	10.5	1	38.7	5.1	7.3	−2.4
40	9.″88	−13.5	...	...	...	...	...	...	....	...	...	....
41	9.″00	−12.8	...	...	−0.4	0.04	8.8	220	39.3	5.4	6.8	−1.8
42	8.″00	−12.3	−0.1	−0.4	−0.9	...	...	...	....	...	...	....
43	9.″65	−13.1	−1.7	−3.8	−1.4	0.05	8.4	2	39.3	5.3	7.2	−1.8
44	9.″59	−14.9	...	...	...	...	...	...	....	...	...	....
45	8.″79	−13.4	0.1	−1.0	−0.6	0.13	6.9	15	39.2	4.7	7.0	−1.9
46	9.″14	−13.0	−1.6	−3.2	−1.4	0.07	8.0	11	39.8	4.6	7.1	−1.3
47	9.″41	−13.5	−0.1	0.1	−0.3	0.70	4.1	322	39.5	5.4	6.7	−1.6
48	11.″02	−12.6	−3.9	−5.3	−0.9	0.01	10.9	3	38.7	4.9	7.1	−2.4
49	8.″48	−13.1	...	...	...	...	...	...	....	...	...	....
50	8.″35	−13.6	...	...	...	...	...	...	....	...	...	....
51	9.″24	−13.5	...	...	...	...	...	...	....	...	...	....
52	7.″91	−12.6	2.0	3.2	−0.1	...	...	...	....	...	...	....
53	9.″16	−13.2	−2.1	−3.7	−1.7	0.01	11.4	1	39.3	5.5	7.3	−1.8
54	9.″14	−13.4	−1.1	−2.3	−1.2	0.06	8.2	14	39.6	4.8	7.0	−1.5
55	9.″86	−13.6	...	...	...	...	...	...	....	...	...	....
56	10.″19	−12.9	...	...	...	...	...	...	....	...	...	....
57	8.″96	−14.2	0.4	−0.9	−0.4	0.13	6.9	33	39.8	5.4	6.8	−1.3
58	9.″22	−13.8	2.5	3.9	0.8	...	...	...	....	...	...	....
59	9.″95	−14.0	0.9	0.8	−0.2	...	...	...	....	...	...	....
60	9.″68	−11.8	...	...	...	0.13	6.8	1506	39.7	4.7	6.5	−1.4
61	9.″93	−12.7	...	...	...	...	...	...	....	...	...	....
62	9.″37	−14.9	−2.6	−5.0	−1.3	0.00	12.4	0	39.2	6.2	7.5	−1.9
63	10.″01	−14.0	2.6	3.8	0.6	12.62	−0.6	2	36.3	5.1	7.2	−4.8
64	12.″25	−12.5	...	...	0.0	...	...	...	....	...	...	....
65	10.″11	−13.3	−1.1	−1.8	−0.8	0.02	10.1	11	39.2	4.8	7.1	−1.9
66	10.″17	−12.3	...	...	...	...	...	...	....	...	...	....
67	10.″55	−13.3	...	...	...	...	...	...	....	...	...	....
68	10.″98	−13.5	...	...	−0.4	0.01	11.0	3	39.3	5.3	7.2	−1.8
69	10.″66	−12.9	...	...	...	...	...	...	....	...	...	....

70	11.″89	−14.3	...	...	−0.6	0.08	7.6	1	38.7	5.8	7.3	−2.4
71	11.″45	−14.2	...	...	−0.6	0.05	8.5	5	38.9	5.3	7.1	−2.2
72	19.″78	...	...	...	...	...	...	...	....	...	...	....
73	21.″67	...	...	...	...	...	...	...	....	...	...	....

TABLE 5.5— Main properties derived for the knots found in NGC 1386. The radial distance corresponds to the angle with respect to the active nucleus. The absolute (Δ) or relative errors (δ) corresponding to the different magnitudes are: $\Delta M_K = 0.2$ mag, $\Delta(V-I) = 0.4$ mag, $\Delta(V-J) = 0.2$ mag, $\Delta(J-K) = 0.2$ mag, $\delta[W(\mathrm{H}\alpha)] = 39\%$, $\delta(\mathrm{M}) \sim 30\%$, $\Delta(\mathrm{t}) \sim 0.2$ Myr, $\delta(L_{\mathrm{H}\alpha}) = 23\%$, $\delta(\mathrm{SFR}) \sim 30\%$.

#	Radial distance	M_K	V − I	V − J	J − K	W(Hα)	log($L_{\mathrm{H}\alpha}$)	log(M)	log(t)	log(SFR)
		[mag]				[Å]	[erg s^{-1}]	[$M_\odot$]	[yr]	[$M_\odot$ yr^{-1}]
0	17.″09	0.3	0.1	...	...	10	34.9	−0.9	7.1	−6.2
1	13.″92	...	0.1	9.0	...	410	36.7	...	6.7	−4.4
2	11.″81	−8.1	−0.6	0.0	1.0	20	35.6	2.4	6.9	−5.5
3	11.″19	−7.5	−0.4	1.0	−1.0	40	36.0	2.4	6.8	−5.1
4	10.″98	...	−2.1	...	...	...	....	...	...	....
5	10.″74	−8.1	1.0	2.2	−0.5	130	36.2	3.1	6.8	−4.9
6	11.″30	−9.1	−0.2	0.1	1.5	130	36.5	3.5	6.8	−4.6
7	12.″58	−8.1	−2.1	0.7	0.5	150	36.4	3.1	6.8	−4.7
8	10.″79	−5.7	0.5	0.0	−1.5	60	36.1	1.9	6.8	−5.0
9	11.″93	−9.7	0.9	1.0	2.3	620	36.9	3.5	6.5	−4.2
10	9.″21	−8.5	0.6	2.1	−0.6	70	36.1	3.1	6.8	−5.0
11	8.″97	−7.5	−0.5	0.2	−0.8	40	36.2	2.4	6.8	−4.9
12	13.″78	−11.4	1.2	2.2	0.6	40	36.6	4.0	6.8	−4.5
13	7.″67	−9.6	−0.3	2.3	0.2	80	36.1	3.6	6.8	−5.0
14	6.″75	−9.2	0.7	2.9	−0.4	40	35.8	3.2	6.8	−5.3
15	6.″35	−11.4	0.2	1.2	1.0	10	36.1	3.6	7.1	−5.0
16	6.″35	−11.3	0.1	1.3	1.0	20	36.3	3.6	6.9	−4.8
17	6.″25	−9.3	−0.3	0.3	0.5	...	....	...	...	....
18	6.″14	−8.6	0.0	1.7	−0.3	0	34.7	2.9	7.2	−6.4
19	6.″10	−5.0	0.3	1.0	−3.6	20	35.7	1.1	6.9	−5.4
20	5.″78	−8.6	1.8	5.3	−0.6	...	....	...	...	....
21	8.″47	...	−0.3	0.5	...	320	36.7	...	6.7	−4.4
22	7.″14	−8.9	0.1	2.4	−0.4	270	36.6	3.4	6.8	−4.5
23	4.″91	−9.7	0.5	1.1	0.6	30	36.2	3.2	6.8	−4.9
24	6.″54	...	...	...	...	870	36.7	...	6.5	−4.4
25	4.″87	−9.1	0.5	1.8	−0.1	230	36.8	3.5	6.8	−4.3
26	7.″03	−8.8	0.7	2.7	−1.1	150	36.5	3.3	6.8	−4.6
27	5.″27	−7.9	0.0	2.1	−1.3	140	36.4	3.0	6.8	−4.7
28	4.″87	−5.7	0.6	1.1	−2.5	170	36.6	2.1	6.8	−4.6
29	6.″14	...	0.4	...	...	960	36.7	...	6.5	−4.4
30	6.″09	...	...	3.5	...	...	....	...	...	....
31	6.″42	−8.9	−1.3	2.4	0.4	...	....	...	...	....

32	5.″41	−8.7	0.1	2.9	−1.0	10	35.3	2.5	7.0	−5.8
33	6.″35	−8.7	1.6	2.5	0.1	20	35.3	2.6	6.9	−5.8
34	6.″44	...	0.0	...	...	50	35.9	...	6.8	−5.2
35	8.″18	...	...	...	...	...	....	...	...	....
36	6.″42	−10.0	...	4.1	0.3	70	35.6	3.6	6.8	−5.5
37	5.″54	−9.3	0.2	2.0	−0.1	180	36.6	3.5	6.8	−4.5
38	7.″19	−8.1	0.3	1.6	0.1	20	35.3	2.4	6.9	−5.8
39	5.″04	−10.2	−0.1	2.4	−0.4	270	37.1	3.9	6.7	−4.0
40	4.″90	−10.2	0.1	1.8	0.0	140	37.0	3.9	6.8	−4.1
41	4.″74	−8.9	−0.6	4.8	−0.2	...	....	...	...	....
42	8.″71	−7.1	...	...	−0.1	...	....	...	...	....
43	5.″28	−10.2	0.5	2.1	0.3	50	36.3	3.7	6.8	−4.8
44	5.″38	−10.2	0.1	2.5	0.3	70	36.2	3.8	6.8	−4.9
45	5.″51	−8.8	−1.2	3.3	−0.7	...	....	...	...	....
46	5.″99	...	...	...	...	1160	36.8	...	6.5	−4.3
47	5.″85	−9.4	0.3	2.3	−0.6	20	35.8	2.9	6.9	−5.3
48	5.″49	−8.5	0.2	1.3	0.0	80	36.2	3.1	6.8	−4.9
49	9.″89	−10.1	0.6	2.7	0.6	0	34.5	3.7	7.2	−6.6
50	9.″90	−9.8	0.1	2.8	0.4	20	35.4	3.1	6.9	−5.7
51	7.″42	−8.9	0.6	1.5	−0.2	30	36.0	2.9	6.8	−5.1
52	7.″49	−8.9	0.1	1.9	−0.4	20	35.6	2.7	6.9	−5.5
53	7.″28	−7.1	...	1.9	0.0	...	....	...	...	....
54	7.″45	...	...	...	...	1010	37.0	...	6.5	−4.1
55	8.″14	−9.7	0.5	1.8	0.1	20	35.8	3.0	6.9	−5.3
56	7.″99	...	−2.3	...	...	...	....	...	...	....
57	11.″09	−9.8	0.3	2.0	0.2	10	35.4	3.0	7.1	−5.7
58	12.″73	−8.9	0.6	1.8	0.0	110	36.4	3.3	6.8	−4.7
59	10.″04	−8.3	0.4	1.9	−0.7	20	35.7	2.5	6.9	−5.4
60	10.″54	−8.9	0.8	1.8	0.4	70	36.0	3.2	6.8	−5.1
61	10.″44	−8.6	−0.1	2.2	−0.4	80	36.1	3.2	6.8	−5.0
62	11.″83	−8.7	0.0	...	...	680	36.7	3.2	6.5	−4.4
63	11.″48	−8.0	0.0	0.9	−0.1	10	35.4	2.3	7.1	−5.7
64	11.″81	−7.6	0.6	2.1	−1.1	90	36.1	2.8	6.8	−5.0
65	11.″09	−8.9	0.4	1.8	−0.3	...	....	...	...	....
66	11.″60	−9.4	0.7	2.4	0.0	80	36.2	3.5	6.8	−4.9
67	11.″54	−8.9	0.9	1.8	0.2	110	36.3	3.3	6.8	−4.8
68	11.″87	−6.4	0.0	1.2	−1.9	130	36.4	2.4	6.8	−4.7
69	12.″69	−8.0	1.0	3.5	−1.8	80	36.0	2.9	6.8	−5.1

TABLE 5.6— Main properties derived for the knots found in NGC 1052. The radial distance corresponds to the angle with respect to the active nucleus. The absolute (Δ) or relative errors (δ) corresponding to the different magnitudes are: $\Delta M_K = 0.1$ mag, $\Delta(V-I) = 0.3$ mag, $\Delta(V-J) = 0.3$ mag, $\Delta(J-K) = 0.2$ mag, $\delta[W(\mathrm{H}\alpha)] = 39\%$, $\delta(\mathrm{M}) \sim 30\%$, $\Delta(\mathrm{t}) \sim 0.4$ Myr, $\delta(L_{\mathrm{H}\alpha}) = 31\%$, $\delta(\mathrm{SFR}) \sim 30\%$.

#	Radial distance	M_K	V − I	V − J	J − K	W(Hα)	log($L_{\mathrm{H}\alpha}$)	log(M)	log(t)	log(SFR)
		[mag]				[Å]	[erg s^{-1}]	[$M_\odot$]	[yr]	[$M_\odot$ yr^{-1}]
0	15.″72	−10.2	2.3	3.5	0.3	80	36.2	3.3	6.8	−4.9
1	15.″89	−13.6	2.6	3.5	0.8	120	37.5	4.8	6.8	−3.6
2	15.″38	−11.5	2.9	3.9	0.9	180	36.7	4.4	6.7	−4.4
3	13.″59	−10.6	2.9	3.6	1.0	...	....	...	...	....
4	10.″36	−10.0	2.0	3.9	0.8	...	....	...	...	....
5	9.″44	−9.9	3.0	4.1	0.3	130	36.1	3.4	6.8	−5.0
6	9.″13	−11.3	2.3	3.2	0.6	120	36.7	3.8	6.8	−4.4
7	13.″54	−10.4	2.5	2.7	−0.1	110	36.8	3.4	6.8	−4.3
8	9.″36	−10.0	1.9	3.1	0.2	...	....	...	...	....
9	8.″25	−10.1	2.2	3.2	−0.1	10	35.5	2.9	7.0	−5.6
10	11.″91	−9.1	...	...	0.5	10	35.0	2.6	7.0	−6.1
11	9.″69	−9.8	2.7	2.8	0.5	200	36.6	3.8	6.7	−4.5
12	5.″15	−11.3	1.8	2.8	−0.2	30	36.5	3.6	6.8	−4.6
13	13.″80	−11.4	2.9	...	...	220	36.2	4.5	6.7	−4.9
14	9.″86	−11.3	2.7	3.2	0.9	180	36.8	4.3	6.7	−4.3
15	8.″14	−10.1	...	...	0.3	...	....	...	...	....
16	4.″16	−11.7	2.0	2.8	0.1	10	35.8	3.8	7.0	−5.3
17	4.″28	−11.5	2.1	2.8	0.2	10	35.8	3.6	7.0	−5.3
18	10.″34	−10.4	2.6	3.0	0.4	80	36.4	3.3	6.8	−4.8
19	4.″97	−11.5	1.7	3.6	0.7	110	36.6	3.8	6.8	−4.5
20	15.″15	−10.9	2.4	2.7	0.4	110	36.8	3.6	6.8	−4.3
21	9.″65	−10.8	2.3	2.9	0.6	40	36.2	3.5	6.8	−4.9
22	9.″07	−10.2	2.4	3.6	0.3	250	36.6	4.0	6.7	−4.5
23	9.″65	−10.2	2.9	3.9	0.7	160	36.2	3.8	6.7	−4.9
24	10.″82	−10.0	2.7	3.4	0.2	110	36.3	3.3	6.8	−4.8

TABLE 5.7— Main properties derived for the knots found in NGC 7582. The radial distance corresponds to the angle with respect to the active nucleus. The absolute (Δ) or relative errors (δ) corresponding to the different magnitudes are: $\Delta M_K = 0.1$ mag, $\Delta(V-H) = 0.1$ mag, $\Delta(V-K) = 0.1$ mag, $\Delta(H-K) = 0.1$ mag, $\delta[W(\mathrm{Br}\alpha)] = 11\%$, $\delta(\mathrm{M}) \sim 30\%$, $\delta(L_{\mathrm{Br}\alpha}) = 8\%$, $\delta(\mathrm{SFR}) \sim 30\%$.

#	Radial distance	M_K	V − H	V − K	H − K	W(Brα)	log($L_{\mathrm{Br}\alpha}$)	log(M)	log(SFR)
		[mag]				[Å]	[erg s^{-1}]	[$M_\odot$]	[$M_\odot$ yr^{-1}]
0	2.″48	−15.4	6.4	7.2	0.7	....	....	6.0	....
1	1.″72	−16.2	6.1	6.9	0.9	94	37.7	6.3	−1.9
2	1.″53	−16.4	6.1	7.0	0.9	111	37.9	6.4	−1.7
3	1.″47	−16.2	6.0	7.0	1.1	....	....	6.3	....
4	1.″34	−16.4	6.2	7.3	1.0	52	37.7	6.4	−1.8
5	1.″12	−16.8	5.6	6.3	0.7	....	....	6.5	....
6	1.″20	−16.5	8.0	8.9	0.9	....	....	6.4	....
7	0.″71	−17.3	5.6	6.6	0.9	....	....	6.7	....
8	0.″67	−17.2	5.6	6.6	1.1	....	....	6.7	....
9	1.″08	−16.6	5.1	5.7	0.6	....	....	6.5	....
10	0.″83	−16.7	7.1	8.7	1.5	....	....	6.5	....
11	0.″88	−17.2	6.0	7.1	1.1	....	....	6.7	....
12	0.″84	−17.1	6.1	7.2	1.1	0	35.7	6.7	−3.9
13	0.″78	−16.6	7.9	9.3	1.4	....	....	6.5	....
14	0.″82	−16.8	7.6	8.9	1.3	13	37.3	6.6	−2.2
15	1.″42	−16.8	6.3	6.9	0.7	....	....	6.5	....
16	1.″78	−16.7	5.0	5.7	0.7	....	....	6.5	....
17	1.″36	−16.4	7.5	8.6	1.1	60	37.7	6.4	−1.8
18	1.″99	−15.9	7.8	8.8	1.0	169	38.0	6.2	−1.5
19	2.″54	−15.9	7.3	8.2	0.9	....	....	6.2	....
20	2.″77	−16.1	8.1	9.0	0.9	....	....	6.3	....
21	2.″96	−16.0	8.5	9.6	1.1	....	....	6.2	....
22	2.″90	−15.8	6.9	7.8	0.9	189	37.8	6.1	−1.7
23	3.″30	−15.3	8.4	9.6	1.1	....	....	6.0	....
24	3.″04	−15.6	5.8	6.7	0.9	206	37.9	6.0	−1.7
25	3.″87	−14.5	6.7	7.6	0.9	....	....	5.6	....

TABLE 5.8— Main properties derived for the knots found in NGC 7469. The radial distance corresponds to the angle with respect to the active nucleus. The absolute (Δ) or relative errors (δ) corresponding to the different magnitudes are: $\Delta M_K = 0.2$ mag, $\Delta(V-I) = 0.2$ mag, $\Delta(V-J) = 0.2$ mag, $\Delta(J-K) = 0.3$ mag, $\delta(\mathrm{H}\alpha/\mathrm{Pa}\alpha) = 63\%$, $\Delta A_V = 0.5$ mag, $\delta[W(\mathrm{H}\alpha)] = 30\%$, $\delta(\mathrm{M}) \sim 30\%$, $\Delta(\mathrm{t}) \sim 0.2$ Myr, $\delta(L_{\mathrm{H}\alpha}) = 20\%$, $\delta(\mathrm{SFR}) \sim 30\%$. Colours and derived magnitudes are corrected for extinction.

#	Radial distance	M_K	V − I	V − J	J − K	$\frac{\mathrm{H}\alpha}{\mathrm{Pa}\alpha}$	A_V	$W(\mathrm{H}\alpha)$	$\log(L_{\mathrm{H}\alpha})$	log(M)	log(t)	log(SFR)
		[mag]					[mag]	[Å]	[erg s^{-1}]	[$M_\odot$]	[yr]	[$M_\odot$ yr^{-1}]
0	3.″53	...	...	...	...	...	...	...	....	...	...	....
1	1.″62	−17.7	...	...	...	...	...	210	....	...	6.8	....
2	1.″68	−17.9	...	...	...	...	...	320	....	...	6.7	....
3	1.″92	−17.7	...	...	...	...	...	250	....	...	6.8	....
4	1.″31	−17.8	−1.4	−2.2	3.7	2.36	2.1	260	40.2	7.1	6.8	−0.9
5	1.″32	−17.8	−1.7	−1.8	2.1	1.03	3.5	310	40.7	7.1	6.7	−0.4
6	1.″23	−17.8	−1.3	−0.8	2.7	2.51	2.0	350	40.1	7.0	6.7	−1.0
7	1.″41	−18.1	−1.6	−0.9	0.6	0.57	4.5	160	40.8	7.3	6.8	−0.3
8	1.″22	−18.0	−1.5	0.6	2.2	3.24	1.6	300	39.9	7.1	6.7	−1.2
9	1.″83	−18.0	−1.3	0.0	1.0	0.27	5.7	430	40.8	7.3	6.7	−0.3
10	0.″94	−17.7	−0.2	2.7	0.6	3.93	1.3	490	39.8	6.8	6.6	−1.3
11	1.″59	−17.8	...	...	...	...	...	160	....	...	6.8	....
12	2.″51	−15.7	...	...	...	...	...	...	....	...	...	....
13	0.″89	−17.4	...	...	...	...	...	310	....	...	6.7	....
14	1.″47	−17.9	0.1	2.6	1.9	6.91	0.4	110	38.9	7.0	6.8	−2.2
15	1.″68	−18.5	−0.2	0.6	1.4	7.01	0.3	60	39.7	7.0	6.8	−1.4
16	0.″72	−17.4	0.1	4.2	−1.0	0.69	4.2	940	40.5	6.9	6.5	−0.6
17	1.″05	−17.9	−0.6	0.3	1.5	...	...	...	....	...	...	....
18	1.″63	−18.3	...	...	...	...	...	80	....	...	6.8	....
19	0.″66	−18.2	−1.6	1.8	−0.6	0.26	5.8	340	40.8	7.4	6.7	−0.3
20	1.″96	−17.1	−2.6	−2.3	0.6	0.13	7.0	180	40.8	7.0	6.8	−0.3
21	1.″26	−16.4	...	...	...	...	...	80	....	...	6.8	....
22	1.″24	−17.8	...	...	...	...	...	90	....	...	6.8	....
23	1.″18	−16.2	−1.3	−4.4	0.4	...	...	...	....	...	...	....
24	2.″03	−17.1	−2.4	−1.2	0.0	0.19	6.3	90	40.7	6.9	6.8	−0.4
25	1.″45	−17.8	...	...	...	...	...	10	....	...	7.1	....
26	1.″83	−17.7	−0.9	0.6	0.9	2.65	1.9	160	40.1	7.0	6.8	−1.0
27	1.″01	−16.7	...	...	0.0	...	...	...	....	...	...	....
28	2.″05	−16.9	−1.8	−2.0	1.5	0.48	4.8	200	40.6	6.8	6.8	−0.5
29	0.″95	−18.1	...	...	...	...	...	70	....	...	6.8	....
30	1.″64	−17.4	...	...	...	...	...	2960	....	...	...	....

31	1.″76	−17.8	−2.1	−2.2	1.1	0.35	5.3	80	40.6	7.1	6.8	−0.5
32	1.″56	−17.4	...	...	...	...	...	80	....	...	6.8	....
33	1.″74	−17.8	...	...	...	...	...	150	....	...	6.8	....
34	1.″35	−17.3	−1.4	...	...	1.11	3.4	310	40.3	6.9	6.7	−0.8
35	0.″96	−16.9	1.6	2.2	−0.1	1.71	2.7	110	39.8	6.7	6.8	−1.3
36	1.″59	−17.5	...	...	...	...	...	650	....	...	6.5	....
37	1.″17	−17.8	−0.6	0.7	1.7	5.35	0.8	90	39.4	6.9	6.8	−1.7
38	1.″14	−17.0	−0.5	−1.6	0.5	...	...	...	....	...	...	....
39	1.″42	−17.0	−2.1	−1.7	0.5	...	...	...	....	...	...	....
40	1.″42	−17.6	−1.3	−0.5	1.4	1.73	2.6	220	40.3	7.0	6.8	−0.8
41	1.″40	−17.4	−1.3	−0.5	1.6	2.23	2.2	330	40.3	6.9	6.7	−0.8
42	1.″60	−17.5	−1.6	−1.7	2.6	0.75	4.0	270	40.3	7.0	6.8	−0.8
43	1.″30	−17.2	...	...	...	...	...	350	....	...	6.7	....
44	1.″37	−16.9	−0.5	0.7	0.9	4.40	1.1	450	40.2	6.6	6.7	−0.9
45	0.″95	−17.8	−2.1	...	...	...	...	...	....	...	...	....
46	1.″27	−17.4	...	...	...	...	...	210	....	...	6.8	....
47	1.″13	−16.7	−1.7	...	...	0.54	4.6	270	40.6	6.7	6.7	−0.5
48	1.″39	−17.2	−0.7	−0.4	0.3	2.69	1.9	120	40.4	6.8	6.8	−0.7
49	1.″12	−16.9	−1.9	...	...	...	...	...	....	...	...	....
50	1.″66	−18.1	−1.5	−0.9	0.8	0.72	4.1	240	41.0	7.3	6.8	−0.1
51	1.″41	−17.2	−1.7	−2.3	1.6	0.55	4.5	190	40.7	6.9	6.8	−0.4
52	1.″27	−16.2	−0.8	−3.0	3.1	...	...	...	....	...	...	....
53	1.″67	−18.0	−1.8	−1.6	0.8	0.67	4.2	120	40.9	7.2	6.8	−0.2
54	1.″62	−17.1	...	...	...	...	...	310	....	...	6.7	....
55	1.″56	−18.1	−1.4	−0.9	1.0	0.64	4.3	200	40.8	7.3	6.8	−0.3
56	1.″70	−17.9	−1.3	−0.6	0.8	0.65	4.3	420	41.1	7.2	6.7	−0.1
57	2.″01	−17.2	...	...	...	...	...	380	....	...	6.7	....
58	2.″32	−15.8	...	...	...	...	...	410	....	...	6.7	....

6

Conclusions and future work

A system is like the tail of truth,
but the truth is like a lizard.
It leaves it's tail in your fingers,
and runs away... knowing full well
it will grow a new one in a twinkling.

Northern Exposure, "Nothing's Perfect" (1992)

ALONG this thesis we have performed a comprehensive research of the central few parsecs of nearby AGNs. The study is focused on two complementary aspects:

i) Characterisation of the nuclear emission of low-luminosity AGNs ($L_{bol} \lesssim 10^{42}$).

ii) Characterisation of spatially resolved star-forming regions located very close ($\lesssim 500\,$pc) to active nuclei.

We start from a multiwavelength set of high-spatial resolution data for a sample of six active galaxies: NGC 253, NGC 1097, NGC 1386, NGC 1052, NGC 7582 and NGC 7469, sorted by increasing distance. The dataset is described in Chapter 2 and includes: adaptive optics in the NIR (VLT/NaCo), diffraction limited imaging in the MIR (VLT/VISIR) and optical/UV (*HST*), radio maps from VLA and long baseline interferometry (VLBI/VLBA), and X-ray observations from *Chandra*. This permits us to cover almost the whole spectral range (except for the interval between $\sim 10^{11}$–$10^{13}\,$Hz) with a consistent spatial resolution of a few tens of parsecs. The latter is precisely one of the biggest advantages when compared with previous studies, as we are able to determine, with a high accuracy, the nature of the sources of interest and also the ranges where they release most of their energy.

The leading results obtained in this thesis for both the active nuclei and the star formation component, are summarized in Section 6.1. We list the outstanding conclusions in Section 6.2. Finally, in Section 6.3 we present some research scenarios in line with the facilities that will be available in the near future.

6.1 Results

First of all, the morphology of galaxies usually change with wavelength, and thus one should pay a special attention in the alignment among sets of data centred on very different parts of the spectrum, considering that an important part of the subsequent analysis depends on this registration (see Section 2.3.2). That being said, a first look at the central parsecs of each galaxy in Chapter 3 reveals them as complex systems with a number of different components, i.e. an AGN, stellar clusters, dust and gas. Therefore, we performed firstly a carefully analysis to identify the positions of the active nuclei and the stellar clusters, and also define the wavelength ranges in which they are visible. Based on this preliminary work we addressed the two topics of this thesis.

Spectral energy distribution of high and low-luminosity AGNs

Low-luminosity AGNs (LLAGNs) are by far the largest class among AGNs, found in $\gtrsim$ 50–70% of all galaxies (Ho 2008). However, they represent a challenging scenario for current unification theories. First, observations by Ho (1999) and Eracleous et al. (2010) suggest that the big blue bump, i.e. the footprint of the accretion disk in the optical/UV range, is absent in LINERs, a part of the LLAGN population. Second, the obscuring torus, which is a key element in the unified model, is expected to vanish below $L_{bol} \sim 10^{42}\,\mathrm{erg\,s^{-1}}$ (Elitzur & Shlosman 2006; Hönig et al. 2006). Therefore, LLAGNs are considered as radiatively inefficient sources or just lacking an accretion disk. In this context, the thesis studies a small sample of some of the nearest low-luminosity AGNs. As mentioned before, we used the highest-spatial resolution data available nowadays, covering radio, IR, optical, UV and X-ray wavelengths. At the distance of the objects in this work ($\sim$ 16 Mpc), a spatial resolution below $0\farcs5$ represents scales smaller than 40 pc. The use of such fine spatial resolutions has shown to be fundamental in characterising spectral energy distributions of high-luminosity AGNs (Prieto et al. 2010, Chapter 4). In the low-luminosity case the requirement for high resolution is even more critical, as these nuclei are swamped with light of the host galaxy.

Within the sample of seven galaxies, we distinguish four cases of LLAGNs: NGC 253, NGC 1097, NGC 1386 and NGC 1052. The former is the faintest one, the prototypical LINERs NGC 1097 and NGC 1052 are slightly more powerful, while NGC 1386 is a faint Seyfert 2 (see Table 4.1). The limited number of objects is a consequence of the difficulty of compiling subarcsecond data for these faint AGNs

across the electromagnetic spectrum. From this sample, we have built the highest available spatial resolution SED for LLAGNs, comparing it with those derived for the high-luminosity class (Fig. 4.4). The major conclusions of this comparison are:

i) SEDs based on data with apertures larger than $\gtrsim 1''$ are representative, almost exclusively, of the host galaxy, specially in the MIR and the optical/UV (Section 4.4). This applies so far for AGN luminosities of $\lesssim 10^{44}\,\mathrm{erg\,s^{-1}}$ (e.g. Figs 4.6 and 4.7).

ii) SEDs of AGNs with luminosities in the 10^{42}–$10^{44}\,\mathrm{erg\,s^{-1}}$ range unambiguously reflect the presence of a central obscuring structure, less than a few parsecs in size, in both type 1 and type 2 Seyferts, in agreement with the torus considered in unified schemes (Fig. 4.2 and Section 4.2).

iii) SEDs of LLAGNs, with $\lesssim 10^{42}\,\mathrm{erg\,s^{-1}}$ do not show signs for the presence of this structure. The shape of their SED in the MIR to optical/UV range exhibit a gentle fall off towards high frequencies which is not as drastic as the characteristic one in high-luminosity Sy2s. Surprisingly, it cannot be reproduced by moderate reddening of a high-luminosity type 1 AGN (Fig 4.4).

iv) LLAGNs appear slightly different at radio wavelengths when compared with the high-luminosity AGNs studied by us (mostly radio-quiet objects), but remind that seen in radio-loud quasars (Fig. 4.7). These, as Sy1s, show the the characteristic blue bump in their spectra. In contrast, LLAGNs do not (Ho 1999; Eracleous et al. 2010, this work), and this absence is not caused by dust extinction, as shown in this thesis. Thus, we favour the scenario in which LLAGNs only sustain a tenuous, radiatively inefficient disk or even lack this structure (Section 4.3).

v) The case of NGC 253 is of special interest: the bright X-ray source X-1 lacks of a clear optical, IR or radio counterpart, suggesting a strong obscuration (Fig. 4.8). Besides the X-ray emission, the rest of the spectrum claims for a starburst-dominated nuclei (Fig. 4.9). Most surprising of all, X-1 apparently lacks of a counterpart in the MIR, where one would expect a re-emission of the absorbed X-rays. This situation is quite close to the case of NGC 4945 (Marconi et al. 2000, Section 4.6), which is also a well-known starburst galaxy with a core detected only in the hard X-ray band. However, the brightness of this source ($L_{2-10\mathrm{keV}} \sim 10^{45}\,\mathrm{erg\,s^{-1}}$) does not leave any room for doubt about its AGN nature (Iwasawa et al. 1993). We believe that NGC 253 is a low-luminosity ($L_{2-10\mathrm{keV}} \sim 10^{40}\,\mathrm{erg\,s^{-1}}$) member of the same class as NGC 4945. These objects remind to ultraluminous IR galaxies (ULIRGs) in the sense that the starburst

component seems to be hiding or heavily obscuring the AGN. Therefore, nearby objects like NGC 253 or NGC 4945 become excellent laboratories to investigate this type of "embedded AGNs", more common among ULIRGs.

Circumnuclear star formation

Taking advantage of the high-spatial resolution in our study, we have been able to resolve star-forming regions in the central parsecs of all the objects in the sample at different scales from the active nuclei. These clusters are distributed in starburst rings with a diameter of ~ 1 kpc (NGC 1097, NGC 1386, NGC 7469), compact starburst disks within the inner $\lesssim 500$ pc (NGC 253, NGC 7582) or randomly spread clusters within the central $\sim 2 \times 2\,\mathrm{kpc}^2$ (NGC 1052). In each case we have derived the main properties of the resolved star-forming regions, with the aim at providing a genuine characterisation for extragalactic circumnuclear star-formation. However, in all cases there is an AGN in the centre of the galaxy.

In each galaxy, and per each of the star-forming regions found, we obtained a multiwavelength SED and provide estimates for the ages, masses and sizes. A comparative analysis of the properties of these regions as a function of AGN luminosity, galaxy type, and distance to the core is produced. The major contributions are:

i) Most of the clusters appear to be very homogeneous with similar SEDs and very compact sizes ($\lesssim 20$ pc), with ages in the 3–20 Myr range (Section 5.4), regardless of the galaxy type or AGN luminosity. These properties are also similar to those of clusters found in other starbursts and interacting galaxies (Mengel et al. 2005).

ii) We classify them as young stellar clusters (YSCs) in analogy to those in the Milky Way. YSCs in NGC 1386 and NGC 1052 display masses in the range 10^3–$10^4\,\mathrm{M}_\odot$, comparable to the most massive clusters in the Milky Way (Fig. 5.4.5). However, those in NGC 253, NGC 1097, NGC 7582 or NGC 7469 are at least an order of magnitude more massive, and thus comparable to young and massive clusters found in starbursts like NGC 5253 (Vanzi & Sauvage 2004) or interacting galaxies like the Antennae (Zhang et al. 2001).

iii) The cluster mass function in NGC 253, the youngest cluster system with ~ 4.3 Myr in average, follows a power law with an index of $\gamma \approx 1.8$ with no signs of truncation (Fig. 5.27), similar to the case of open clusters and associations in the Milky Way, but also for YSCs found in starbursts and interacting galaxies (see Portegies Zwart et al. 2010, and references therein). In the case of NGC 7469 we find a steeper power law with an index of $\gamma \approx 3.5$,

which is more similar to that of strong star-forming systems. However, in this case we suspect that the clusters are not individually resolved.

iv) NGC 1097 presents a truncated mass function which is very well fitted by a Schechter profile with a characteristic mass of $M_* \sim 2.1 \times 10^5\,M_\odot$ (Fig. 5.28). Interestingly, this galaxy also hosts the oldest clusters in the sample with ~ 10 Myr in average (Section 5.4.4). This value has been pointed out as the typical disruption timescale of YSCs, i.e. the characteristic time at which they begin to dissolve due to disruption by stellar evolution and gravitational shocks (Section 1.2.2). Simulations by Fall & Zhang (2001) suggest that the former affects the high-mass end of the cluster initial mass function (CIMF), while the latter dissolve mostly low massive clusters. As a result, the shape of the theoretical CIMF in Fall & Zhang (2001) changes and develops a turnover around $M_* \sim 2 \times 10^5\,M_\odot$ after ~ 12 Gyr, becoming similar to the lognormal distribution of GCs in the Milky Way (Harris 1991). In this context, Fig. 5.28 suggests that YSCs in NGC 1097 begin to suffer the effects of disruption as a consequence of their evolution.

v) The case of NGC 253 provides us the high-spatial resolution template for YSCs, which could be extended to radio wavelengths due to the proximity (~ 4 Mpc) and thus the sensitivity achieved in this object. We are able to identify the contribution of very young protostellar objects to the SED in the NIR (Figs. 5.2 and 5.3). Thus, the SED template obtained for NGC 253 can be considered as one of the most representative templates for extragalactic young stellar clusters (Section 5.2).

vi) We found a total of 25 clusters in the central $\sim 2 \times 2\,\mathrm{kpc}^2$ of the elliptical NGC 1052 (Section 5.3). Their location around the nucleus is sparse and does not seem to be connected with the radio lobes, H I, ionized gas or dust distributions (Fig. 5.4). A wider FOV map, with high-spatial resolution, of the molecular material is needed in order to check this. Of these clusters, at least 15 present clear signs of star-formation with $L_{\mathrm{H}\alpha} \sim 3.8 \times 10^{36}\,\mathrm{erg\,s^{-1}}$ (Fig. 5.5). Their SED shape can be reproduced by an old population including EHB stars, although these cannot account for the Hα luminosity. In contrast, the SED and Hα emission can be explained in terms of a young population formed in the last ~ 6 Myr (~ 12 Myr for the lowest metallicity) with masses around $\sim 10^4\,M_\odot$ and extinction values of $A_V \sim 3.4$ mag (Fig. 5.6). Thus, we propose that the knots found in the centre of NGC 1052 are YSCs which may have formed in a very recent star formation episode probably related with the merger event that occurred ~ 1 Gyr ago (van Gorkom et al. 1986).

6.2 Conclusions

Here we list the outstanding contributions of this thesis:

- A new alignment is found for NGC 253 and NGC 1386 from radio to optical wavelengths with an accuracy better than $\sim 0\farcs12$, based on our VLT/NaCo data in the NIR. In the former, the extension of the registration to the X-ray range with *Chandra* images completely changes the approach about the nucleus of this galaxy.

- The position of the strong radio source in the nucleus of NGC 253, TH2, is inconsistent with X-1, the bright source discovered in the hard X-ray band. X-1 shows a luminosity and a spectral slope in the X-rays that point to the presence of a hidden AGN in this galaxy.

- We provide a high-spatial resolution SED template for low-luminosity AGNs (LLAGNs) covering the radio, MIR, NIR, optical and X-ray ranges. From its shape in the MIR-to-optical range we confirm that LLAGNs lack of the big blue bump, present in quasars and Sy1s, and conclude that this absence is not a matter of obscuration, as in the case of Sy2s.

- A representative SED template for extragalactic young stellar clusters is derived based on the resolved starburst NGC 253, covering from radio to optical wavelengths. A NIR excess detected in the 1–2 μm range is interpreted in terms of the contribution from hot dust ($\gtrsim 1000$ K) located very close to the protostars inside these clusters.

- For the first time, very young stellar clusters with ages below $\lesssim 10$ Myr have been spatially resolved in the central parsecs of an elliptical galaxy, NGC 1052 in this case. We consider these regions as young stellar clusters produced in the most recent burst of residual star formation, after a merger event occurred ~ 1 Gyr ago.

- In each galaxy, and per each of the star-forming regions spatially resolved, multiwavelength SEDs were produced, together with estimates for the brightness, size, W(Hα), photometric mass, extinction and star-formation rate of each region. We conclude that they are young and compact stellar clusters (YSCs) similar to the most massive ones in the Milky Way, in the cases of NGC 1386 and NGC 1052, and comparable to those found in starburst and merging galaxies in the cases of NGC 253, NGC 1097, NGC 7582 and NGC 7469.

- The cluster mass function for YSCs in NGC 253 and NGC 7469 follows a power-law behaviour, similar to the star-forming regions in the Milky Way –with

an index of $\gamma \sim 2$–, in the former, or more violent star-forming environments ($\gamma > 2$), in the latter.

- The truncation at $\sim 2.1 \times 10^5\,M_\odot$ in the mass distribution of NGC 1097 suggests that the dynamical evolution produces a selective disruption of the less massive clusters in this galaxy ($\lesssim 10^5\,M_\odot$).

6.3 Future work: science with ALMA

In this Section we will discuss briefly the impact of ALMA (Atacama Large Millimeter/submillimetre Array) on some of the topics addressed along this thesis. Another facilities like the European Extremely Large Telescope (E-ELT) or the James Webb Space Telescope (*JWST*) will greatly improve the sensitivity and spatial resolution in the NIR, but we selected ALMA for these examples because it will open, literally, a new "window" of in the spectrum.

Two of the main problems in the study of nuclear regions in galaxies are the presence of several components in the central few hundred parsecs of galaxies and the dust extinction. The former limits those studies based on low-spatial resolution data, while the latter hampers those classic SFR tracers as the UV continuum or Hα emission. One can still use the luminosity in the far-IR (L_{FIR}) to measure the SFR, but this is an integral property over the past starburst history and not a real estimate of the current SFR. Furthermore, if part of the UV photons escape, these are not reprocessed by dust. Finally, the IR luminosity may also include sources not related with star-formation, e.g. an AGN.

ALMA will work on the 84–720 GHz range with an unprecedented sensitivity and high-spatial resolution, the latter in the most extended configuration. The resolutions range from 6 mas at 675 GHz to 38 mas at 110 GHz. With ALMA we will be able to measure: *i)* the thermal free-free emission, *ii)* Hydrogen recombination lines, *iii)* molecular lines, and *iv)* the dust continuum. At wavelengths shorter than ~ 1 cm, the radio continuum emission is expected to be optically thin, with significant or even dominant contribution arising from thermal free-free component. The thermal spectral luminosity of an H II region photoionized by hot stars is proportional to the rate of ionizing photons (Condon 1992). This means that we can estimate the number of massive stars, the age of the cluster and also the SFR. As this emission is not reprocessed, the millimetre/submillimetre range permits us to measure the current SFR. On the other hand, Hydrogen recombination lines are a useful indicator of ionized gas density (Yun 2008). Finally, the dust continuum will provide an estimation for the mass of the dust component. These capacities will also be very useful in the case of active galaxies, specially to resolve the external part of the proposed torus for the nearest galaxies, constraining the models. As an example, we propose three scientific cases for ALMA.

The intriguing nucleus of NGC 253

First of all, the size of the FOV for ALMA (i.e. the primary beam of a single dish antenna) spans the range 9″–56″, thus almost coincident with the FOV of our optical and IR images. One of the scientific cases is about the nature of TH2, the "radio nucleus" of this galaxy. As mentioned in Section 4.5.1, this source resembles more a radio-loud version of Sgr A* rather than an AGN. Fig. 6.1 shows the SED of TH2 (black dots) together with the scaled SED of Sgr A* and the continuum and line sensitivity achieved with ALMA for a 60 sec exposure (solid and dashed-orange lines, respectively). As we can see, one of the uncertainties related with the SED of TH2 is whether its SED will rise up to the IR, as in the case of Sgr A*, or this will become flat as suggested by the value measured at the higher frequency. ALMA will be able to shed light on the nature of this source and determine if it is consistent with being a SMBH or not.

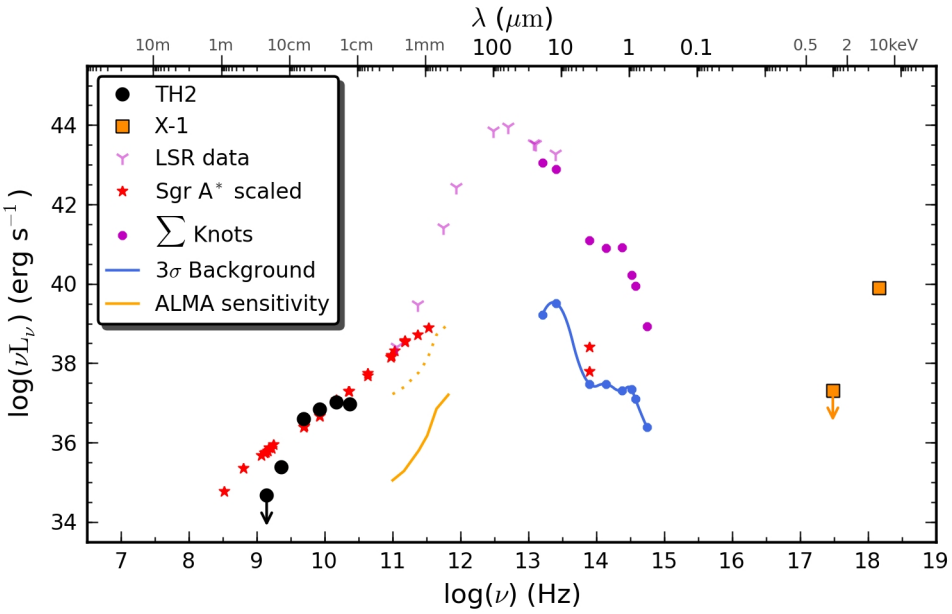

FIGURE 6.1— SEDs for TH2, the strongest radio source in NGC 253 (black dots, Sadler et al. 1995; Ulvestad & Antonucci 1997), X-1, the hardest X-ray source (orange squares), a scaled distribution of Sgr A* (red stars, Falcke et al. 1998; An et al. 2005). We also show the sum of all the star-forming knots found in Section 3.2.1 (purple dots), the 3σ median background distribution (blue dots, see Section 5.4.7) and aperture photometry for the nuclear region based on LSR data (purple spikes). In orange we indicate the ALMA sensitivity for continuum (solid) and line (dashed) emission, for a 60 sec exposure.

Overall, a major contribution of ALMA in the study of AGNs is going to be

the access to the millimetre/submillimetre range with subparsec resolutions, since nowadays we only guess the behaviour of the active nuclei in this part of the spectrum.

Young stellar clusters at light-year scales

The second scientific case is related with the modelling of YSCs in this galaxy. Fig. 6.2 shows the data for knot #5 (green circles), the median SED for the clusters in NGC 253 (purple-shaded area), the stellar cluster model plus dust and non-thermal SNRs (red-solid line), the YSO model (green-solid line) and the ALMA sensitivity (in orange). The 3σ median background is also shown for comparison. The sensitivity of ALMA, even with only 60 sec exposure, is lower than the less optimistic template predictions for the clusters in this galaxy. Thus, observations with ALMA will be able to check the models and templates in the thermal free-free range, providing also estimates for the age, mass and current SFR of the clusters. Moreover, if we consider that these clusters have typical sizes of about 3 pc ($\sim 0\farcs03$ at 20 Mpc), we expect them to be resolved

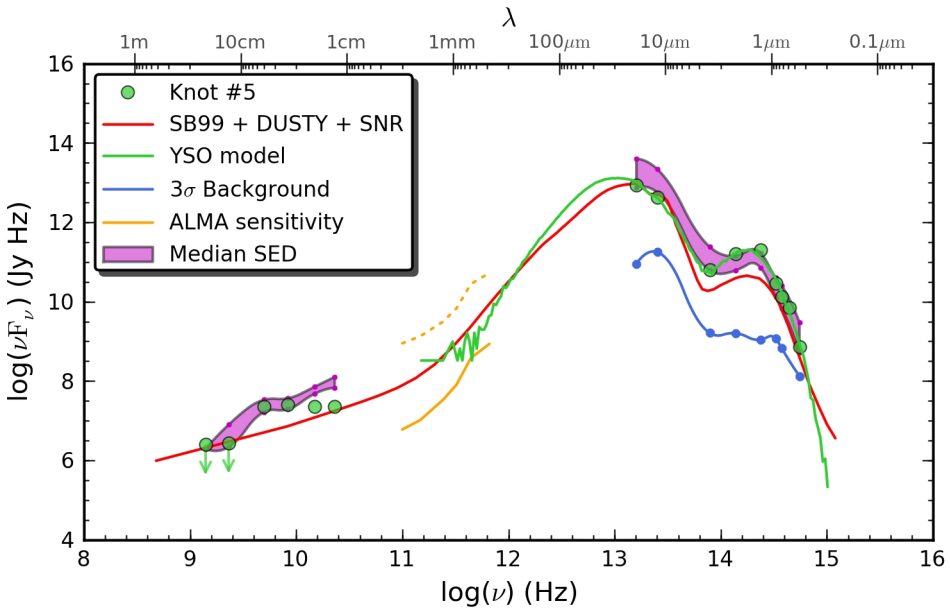

FIGURE 6.2— SED of the representative knot #5 in NGC 253 (green circles), together with the median SED for the cluster in this galaxy (purple-shaded area). For comparison we also show the templates for a stellar cluster model plus dust and non-thermal SNRs (red-solid line) and the YSO model (green-solid line). Blue dots correspond to the 3σ median background. In orange we indicate the ALMA sensitivity for continuum (solid) and line (dashed) emission, for a 60 sec exposure.

with ALMA up to distances of $\lesssim 20$ Mpc. This means that the compact starburst in the nucleus of NGC 7582 will be accessible at almost the same physical scales as we have nowadays for NGC 253 with *HST* or adaptive optics in the NIR.

Star-formation in early-type galaxies

In Section 5.3 we presented the case of NGC 1052, an elliptical galaxy with a recent ($\lesssim 10$ Myr) burst of star formation in the form of YSCs in the inner $2 \times 2\,\mathrm{kpc}^2$. The presence of these clusters has three major implications: *i)* we are looking at the final stage of the residual star-formation (RSF) occurring in the central parsecs of this galaxy, *ii)* the RSF takes place in the form of compact and young stellar clusters similar to those found in starburst galaxies, and *iii)* the reddening predicted by young stellar cluster templates [$\mathrm{E}(B-V) \sim 1.1$ mag] should be explored in future simulations of these systems, which used to assume a lower value as an upper limit.

The case of NGC 1052 is probably one of the best examples for the study of the evolution of early-type galaxies from high redshift to present day, produced mostly via minor mergers with gas-rich satellites. However, high-spatial resolution observations in dynamically younger remnants, for which we expect a larger number of YSCs, are desired to understand in detail the role of minor mergers in the present evolution of elliptical galaxies. In particular, it would be very interesting to investigate the distribution of the molecular material in the centre of NGC 1052 with a spatial resolution comparable to our images in the optical and IR, and check whether the young clusters found are associated with molecular clouds in this galaxy or not. Therefore, ALMA will also be a key instrument in this case to study RSF episodes in early-type galaxies.

Bibliography

Alberdi, A., Colina, L., Torrelles, J. M., et al. 2006, ApJ, 638, 938

Allen, M. G., Koratkar, A. P., & Dopita, M. A. 1999, in Bulletin of the American Astronomical Society, Vol. 31, Bulletin of the American Astronomical Society, 893–+

An, T., Goss, W. M., Zhao, J., et al. 2005, ApJ, 634, L49

Antonucci, R. 1993, ARA&A, 31, 473

Antonucci, R. R. J. & Miller, J. S. 1985, ApJ, 297, 621

Aretxaga, I., Joguet, B., Kunth, D., Melnick, J., & Terlevich, R. J. 1999, ApJ, 519, L123

Baldwin, J. A., Phillips, M. M., & Terlevich, R. 1981, PASP, 93, 5

Barr, P. 1986, MNRAS, 223, 29P

Barth, A. J., Filippenko, A. V., & Moran, E. C. 1999, ApJ, 515, L61

Barth, A. J., Ho, L. C., Filippenko, A. V., & Sargent, W. L. 1995, AJ, 110, 1009

Barth, A. J. & Shields, J. C. 2000, PASP, 112, 753

Barthel, P. D. 1989, ApJ, 336, 606

Barvainis, R. 1987, ApJ, 320, 537

Bastian, N. 2008, MNRAS, 390, 759

Bastian, N. & Gieles, M. 2006, ArXiv Astrophysics e-prints

Bastian, N., Gieles, M., Lamers, H. J. G. L. M., Scheepmaker, R. A., & de Grijs, R. 2005, A&A, 431, 905

Beckert, T., Driebe, T., Hönig, S. F., & Weigelt, G. 2008, A&A, 486, L17

Bennert, N., Jungwiert, B., Komossa, S., Haas, M., & Chini, R. 2006, A&A, 446, 919

Beswick, R. J., Pedlar, A., & McDonald, A. R. 2002, MNRAS, 335, 1091

Bezanson, R., van Dokkum, P. G., Tal, T., et al. 2009, ApJ, 697, 1290

Bianchi, S., Piconcelli, E., Chiaberge, M., et al. 2009, ApJ, 695, 781

Bik, A., Lamers, H. J. G. L. M., Bastian, N., Panagia, N., & Romaniello, M. 2003, A&A, 397, 473

Binette, L., Magris, C. G., Stasińska, G., & Bruzual, A. G. 1994, A&A, 292, 13

Bird, A. J., Malizia, A., Bazzano, A., et al. 2007, ApJS, 170, 175

Blanco, P. R., Ward, M. J., & Wright, G. S. 1990, MNRAS, 242, 4P

Bohlin, R. C. 2007, in Astronomical Society of the Pacific Conference Series, Vol. 364, The Future of Photometric, Spectrophotometric and Polarimetric Standardization, ed. C. Sterken, 315–+

Böker, T. 2010, in IAU Symposium, Vol. 266, IAU Symposium, ed. R. de Grijs & J. R. D. Lépine, 58–63

Bonnell, I. A. & Rice, W. K. M. 2008, Science, 321, 1060

Braatz, J. A., Wilson, A. S., & Henkel, C. 1994, ApJ, 437, L99

Braatz, J. A., Wilson, A. S., & Henkel, C. 1996, ApJS, 106, 51

Braatz, J. A., Wilson, A. S., Henkel, C., Gough, R., & Sinclair, M. 2003, ApJS, 146, 249

Brunthaler, A., Castangia, P., Tarchi, A., et al. 2009, A&A, 497, 103

Bruzual, G. & Charlot, S. 2003, MNRAS, 344, 1000

Burbidge, E. M., Burbidge, G. R., & Prendergast, K. H. 1963, ApJ, 137, 1022

Burtscher, L., Jaffe, W., Raban, D., et al. 2009, ApJ, 705, L53

Cabanac, R. A., Vanzi, L., & Sauvage, M. 2005, ApJ, 631, 252

Caldwell, N., Harding, P., Morrison, H., et al. 2009, AJ, 137, 94

Calzetti, D., Meurer, G. R., Bohlin, R. C., et al. 1997, AJ, 114, 1834

Campbell, M. A., Evans, C. J., Mackey, A. D., et al. 2010, MNRAS, 405, 421

Cappellari, M., Renzini, A., Greggio, L., et al. 1999, ApJ, 519, 117

Cardamone, C. N., Moran, E. C., & Kay, L. E. 2007, AJ, 134, 1263

Cardelli, J. A., Clayton, G. C., & Mathis, J. S. 1989, ApJ, 345, 245

Carter, D., Jorden, P. R., Thorne, D. J., Wall, J. V., & Straede, J. C. 1983, MNRAS, 205, 377

Cenarro, A. J. & Trujillo, I. 2009, ApJ, 696, L43

Cerviño, M. & Valls-Gabaud, D. 2009, Ap&SS, 324, 91

Cervino, M. & Valls-Gabaud, D. 2008, ArXiv e-prints

Chiaberge, M., Capetti, A., & Celotti, A. 1999, A&A, 349, 77

Cid Fernandes, R. J., Storchi-Bergmann, T., & Schmitt, H. R. 1998, MNRAS, 297, 579

Clark, J. S., Negueruela, I., Crowther, P. A., & Goodwin, S. P. 2005, A&A, 434, 949

Claussen, M. J., Diamond, P. J., Braatz, J. A., Wilson, A. S., & Henkel, C. 1998, ApJ, 500, L129+

Claussen, M. J. & Sahai, R. 1992, AJ, 103, 1134

Cohen, A. S., Lane, W. M., Cotton, W. D., et al. 2007, AJ, 134, 1245

Cohen, M., Walker, R. G., Carter, B., et al. 1999, AJ, 117, 1864

Cole, S., Norberg, P., Baugh, C. M., et al. 2001, MNRAS, 326, 255

Colina, L., Alberdi, A., Torrelles, J. M., Panagia, N., & Wilson, A. S. 2001, ApJ, 553, L19

Colina, L., Díaz-Santos, T., Alonso-Herrero, A., et al. 2007, A&A, 467, 559

Collier, S. J., Horne, K., Kaspi, S., et al. 1998, ApJ, 500, 162

Condon, J. J. 1992, ARA&A, 30, 575

Condon, J. J., Cotton, W. D., Greisen, E. W., et al. 1998, AJ, 115, 1693

Condon, J. J., Helou, G., Sanders, D. B., & Soifer, B. T. 1996, ApJS, 103, 81

Cooper, N. J., Lister, M. L., & Kochanczyk, M. D. 2007, ApJS, 171, 376

Corwin, Jr., H. G. 1968, University of Texas Publications in Astronomy, 2

Dahari, O. 1985, AJ, 90, 1772

Dahlem, M. 2005, A&A, 429, L5

Dahm, S. E. & Carpenter, J. M. 2009, AJ, 137, 4024

Dale, D. A., Bendo, G. J., Engelbracht, C. W., et al. 2005, ApJ, 633, 857

Dale, D. A., Gil de Paz, A., Gordon, K. D., et al. 2007, ApJ, 655, 863

D'Alessio, P., Calvet, N., Hartmann, L., Lizano, S., & Cantó, J. 1999, ApJ, 527, 893

Davies, R. I., Maciejewski, W., Hicks, E. K. S., et al. 2009, ApJ, 702, 114

Davies, R. I., Sternberg, A., Lehnert, M. D., & Tacconi-Garman, L. E. 2005, ApJ, 633, 105

Davies, R. I., Tacconi, L. J., & Genzel, R. 2004, ApJ, 602, 148

de Grijs, R., Anders, P., Bastian, N., et al. 2003, MNRAS, 343, 1285

De Rosa, A., Fabian, A. C., & Piro, L. 2002, MNRAS, 334, L21

de Vaucouleurs, G. 1963, ApJS, 8, 31

de Vaucouleurs, G., de Vaucouleurs, A., & Corwin, Jr., H. G. 1976, Second reference catalogue of bright galaxies (University of Texas Press, Austin)

Deo, R. P., Richards, G. T., Crenshaw, D. M., & Kraemer, S. B. 2009, ApJ, 705, 14

Devillard, N. 1999, in Astronomical Society of the Pacific Conference Series, Vol. 172, Astronomical Data Analysis Software and Systems VIII, ed. D. M. Mehringer, R. L. Plante, & D. A. Roberts, 333–+

Dewangan, G. C. & Griffiths, R. E. 2005, ApJ, 625, L31

Díaz-Santos, T., Alonso-Herrero, A., Colina, L., Ryder, S. D., & Knapen, J. H. 2007, ApJ, 661, 149

Disney, M. J. & Wall, J. V. 1977, MNRAS, 179, 235

Dolphin, A. E. & Kennicutt, Jr., R. C. 2002, AJ, 123, 207

Done, C., Gierliński, M., Sobolewska, M., & Schurch, N. 2007, in Astronomical Society of the Pacific Conference Series, Vol. 373, The Central Engine of Active Galactic Nuclei, ed. L. C. Ho & J.-W. Wang, 121–+

Done, C., Madejski, G. M., & Smith, D. A. 1996, ApJ, 463, L63+

Dong, H., Xue, S.-J., Li, C., & Cheng, F.-Z. 2004, Chinese Journal of Astronomy and Astrophysics, 4, 427

Dopita, M. A., Koratkar, A. P., Evans, I. N., et al. 1996, in Astronomical Society of the Pacific Conference Series, Vol. 103, The Physics of Liners in View of Recent Observations, ed. M. Eracleous, A. Koratkar, C. Leitherer, & L. Ho, 44–+

Doroshenko, V. T., Lyutyi, V. M., & Rakhimov, V. Y. 1990, Ap&SS, 171, 55

Dors, Jr., O. L., Storchi-Bergmann, T., Riffel, R. A., & Schimdt, A. A. 2008, A&A, 482, 59

Douglas, J. N., Bash, F. N., Bozyan, F. A., Torrence, G. W., & Wolfe, C. 1996, AJ, 111, 1945

Dultzin-Hacyan, D., Schuster, W. J., Parrao, L., et al. 1992, AJ, 103, 1769

Dunne, L., Eales, S., Edmunds, M., et al. 2000, MNRAS, 315, 115

Ebeling, H., White, D. A., & Rangarajan, F. V. N. 2006, MNRAS, 368, 65

Elitzur, M. & Shlosman, I. 2006, ApJ, 648, L101

Elmegreen, B. G. & Efremov, Y. N. 1997, ApJ, 480, 235

Elmegreen, D. M., Chromey, F. R., McGrath, E. J., & Ostenson, J. M. 2002, AJ, 123, 1381

Elson, R. A. W., Fall, S. M., & Freeman, K. C. 1987, ApJ, 323, 54

Elvis, M., Maccacaro, T., Wilson, A. S., et al. 1978, MNRAS, 183, 129

Elvis, M., Wilkes, B. J., McDowell, J. C., et al. 1994, ApJS, 95, 1

Eracleous, M., Hwang, J. A., & Flohic, H. M. L. G. 2010, ApJS, 187, 135

Falcke, H., Goss, W. M., Matsuo, H., et al. 1998, ApJ, 499, 731

Fall, S. M. 2006, ApJ, 652, 1129

Fall, S. M., Chandar, R., & Whitmore, B. C. 2005, ApJ, 631, L133

Fall, S. M. & Zhang, Q. 2001, ApJ, 561, 751

Fanaroff, B. L. & Riley, J. M. 1974, MNRAS, 167, 31P

Fathi, K., Storchi-Bergmann, T., Riffel, R. A., et al. 2006, ApJ, 641, L25

Faustini, F., Molinari, S., Testi, L., & Brand, J. 2009, A&A, 503, 801

Ferland, G. J. & Netzer, H. 1983, ApJ, 264, 105

Fernández-Ontiveros, J. A., Prieto, M. A., & Acosta-Pulido, J. A. 2009, MNRAS, 392, L16

Ferruit, P., Wilson, A. S., & Mulchaey, J. 2000, ApJS, 128, 139

Figer, D. F. 2008, ArXiv e-prints

Figer, D. F., Kim, S. S., Morris, M., et al. 1999a, ApJ, 525, 750

Figer, D. F., McLean, I. S., & Morris, M. 1999b, ApJ, 514, 202

Figer, D. F., Najarro, F., Gilmore, D., et al. 2002, ApJ, 581, 258

Forbes, D. A., Georgakakis, A. E., & Brodie, J. P. 2001, MNRAS, 325, 1431

Forbes, D. A., Polehampton, E., Stevens, I. R., Brodie, J. P., & Ward, M. J. 2000, MNRAS, 312, 689

Forbes, D. A., Sparks, W. B., & Macchetto, F. D. 1990, NASA Conference Publication, 3098, 431

Fosbury, R. A. E., Mebold, U., Goss, W. M., & Dopita, M. A. 1978, MNRAS, 183, 549

Fosbury, R. A. E., Snijders, M. A. J., Boksenberg, A., & Penston, M. V. 1981, MNRAS, 197, 235

Furlan, E., Hartmann, L., Calvet, N., et al. 2006, ApJS, 165, 568

Gabel, J. R., Bruhweiler, F. C., Crenshaw, D. M., Kraemer, S. B., & Miskey, C. L. 2000, ApJ, 532, 883

Galliano, E., Alloin, D., Pantin, E., et al. 2008, A&A, 492, 3

Galliano, E., Alloin, D., Pantin, E., Lagage, P. O., & Marco, O. 2005, A&A, 438, 803

Gallimore, J. F., Yzaguirre, A., Jakoboski, J., et al. 2010, ApJS, 187, 172

Gaskell, C. M., Goosmann, R. W., Antonucci, R. R. J., & Whysong, D. H. 2004, ApJ, 616, 147

Genzel, R., Weitzel, L., Tacconi-Garman, L. E., et al. 1995, ApJ, 444, 129

Gerin, M., Combes, F., & Nakai, N. 1988, A&A, 203, 44

Ghez, A. M., Wright, S. A., Matthews, K., et al. 2004, ApJ, 601, L159

Gieles, M. 2009a, ArXiv e-prints

Gieles, M. 2009b, MNRAS, 394, 2113

Gieles, M., Larsen, S. S., Bastian, N., & Stein, I. T. 2006a, A&A, 450, 129

Gieles, M., Larsen, S. S., Scheepmaker, R. A., et al. 2006b, A&A, 446, L9

Gil de Paz, A., Boissier, S., Madore, B. F., et al. 2007, ApJS, 173, 185

Gilbert, A. M., Graham, J. R., McLean, I. S., et al. 2000, ApJ, 533, L57

Glass, I. S. 1998, MNRAS, 297, 18

González Delgado, R. M., Heckman, T., & Leitherer, C. 2001, ApJ, 546, 845

González-Martín, O., Masegosa, J., Márquez, I., & Guainazzi, M. 2009a, ApJ, 704, 1570

González-Martín, O., Masegosa, J., Márquez, I., Guainazzi, M., & Jiménez-Bailón, E. 2009b, A&A, 506, 1107

Goudfrooij, P., Mack, J., Kissler-Patig, M., Meylan, G., & Minniti, D. 2001, MNRAS, 322, 643

Graham, A. W. & Spitler, L. R. 2009, MNRAS, 397, 2148

Greggio, L. & Renzini, A. 1990, ApJ, 364, 35

Guainazzi, M., Matt, G., Brandt, W. N., et al. 2000, A&A, 356, 463

Güsten, R., Genzel, R., Wright, M. C. H., et al. 1987, ApJ, 318, 124

Haisch, Jr., K. E., Lada, E. A., & Lada, C. J. 2001, ApJ, 553, L153

Halpern, J. P. & Steiner, J. E. 1983, ApJ, 269, L37

Häring-Neumayer, N., Cappellari, M., Rix, H.-W., et al. 2006, ApJ, 643, 226

Harris, W. E. 1991, ARA&A, 29, 543

Harris, W. E. 1996, AJ, 112, 1487

Heckman, T. M. 1980, A&A, 87, 152

Heeschen, D. S. & Conklin, E. K. 1975, ApJ, 196, 347

Heisler, C. A., Lumsden, S. L., & Bailey, J. A. 1997, Nature, 385, 700

Heisler, C. A. & Vader, J. P. 1994, AJ, 107, 35

Hicks, E. K. S., Davies, R. I., Malkan, M. A., et al. 2009, ApJ, 696, 448

Ho, L. C. 1999, ApJ, 516, 672

Ho, L. C. 2008, ARA&A, 46, 475

Ho, L. C., Filippenko, A. V., & Sargent, W. L. W. 1994, in IAU Symposium, Vol. 159, Multi-Wavelength Continuum Emission of AGN, ed. T. Courvoisier & A. Blecha, 275–278

Ho, L. C., Filippenko, A. V., & Sargent, W. L. W. 1997, ApJS, 112, 315

Hönig, S. F. & Beckert, T. 2007, MNRAS, 380, 1172

Hönig, S. F., Beckert, T., Ohnaka, K., & Weigelt, G. 2006, A&A, 452, 459

Hönig, S. F., Prieto, M. A., & Beckert, T. 2008, A&A, 485, 33

Hsieh, P.-Y., Matsushita, S., Lim, J., Kohno, K., & Sawada-Satoh, S. 2008, ApJ, 683, 70

Hummel, E., van der Hulst, J. M., & Keel, W. C. 1987, A&A, 172, 32

Hunter, D. A., Elmegreen, B. G., Dupuy, T. J., & Mortonson, M. 2003, AJ, 126, 1836

Hwang, N. & Lee, M. G. 2008, AJ, 135, 1567

Hwang, N. & Lee, M. G. 2010, ApJ, 709, 411

Impellizzeri, V., Roy, A. L., & Henkel, C. 2008, in Proceedings of the 9th European VLBI Network Symposium on The role of VLBI in the Golden Age for Radio Astronomy and EVN Users Meeting. September 23-26, 2008. Bologna, Italy. Online at http://pos.sissa.it/cgi-bin/reader/conf.cgi?confid=72, p.33

Iono, D., Yun, M. S., & Ho, P. T. P. 2005, ApJS, 158, 1

Israel, F. P. 2009, A&A, 493, 525

Ivezic, Z., Nenkova, M., & Elitzur, M. 1999, ArXiv Astrophysics e-prints

Iwasawa, K., Koyama, K., Awaki, H., et al. 1993, ApJ, 409, 155

Iyomoto, N., Makishima, K., Fukazawa, Y., Tashiro, M., & Ishisaki, Y. 1997, PASJ, 49, 425

Iyomoto, N., Makishima, K., Fukazawa, Y., et al. 1996, PASJ, 48, 231

Jaffe, W., Meisenheimer, K., Röttgering, H. J. A., et al. 2004, Nature, 429, 47

Jensen, J. B., Tonry, J. L., Barris, B. J., et al. 2003, ApJ, 583, 712

Johnson, K. E. 2004, in Astronomical Society of the Pacific Conference Series, Vol. 322, The Formation and Evolution of Massive Young Star Clusters, ed. H. J. G. L. M. Lamers, L. J. Smith, & A. Nota, 339–+

Johnson, K. E. 2005, in IAU Symposium, Vol. 227, Massive Star Birth: A Crossroads of Astrophysics, ed. R. Cesaroni, M. Felli, E. Churchwell, & M. Walmsley, 413–422

Johnson, K. E., Indebetouw, R., Watson, C., & Kobulnicky, H. A. 2004, AJ, 128, 610

Johnstone, D., Fich, M., Mitchell, G. F., & Moriarty-Schieven, G. 2001, ApJ, 559, 307

Johnstone, D., Matthews, H., & Mitchell, G. F. 2006, ApJ, 639, 259

Jones, D. L., Wrobel, J. M., & Shaffer, D. B. 1984, ApJ, 276, 480

Kadler, M., Kerp, J., Ros, E., et al. 2004, A&A, 420, 467

Kameno, S., Sawada-Satoh, S., Inoue, M., Shen, Z.-Q., & Wajima, K. 2001, PASJ, 53, 169

Karachentsev, I. D., Grebel, E. K., Sharina, M. E., et al. 2003, A&A, 404, 93

Karachentsev, I. D., Tully, R. B., Dolphin, A., et al. 2007, AJ, 133, 504

Kaspi, S., Smith, P. S., Netzer, H., et al. 2000, ApJ, 533, 631

Kaviraj, S., Peirani, S., Khochfar, S., Silk, J., & Kay, S. 2009, MNRAS, 394, 1713

Kaviraj, S., Schawinski, K., Devriendt, J. E. G., et al. 2007, ApJS, 173, 619

Keel, W. C. 1996, ApJS, 106, 27

Kennicutt, Jr., R. C. 1998, ARA&A, 36, 189

Kennicutt, Jr., R. C. & Chu, Y. 1988, AJ, 95, 720

Kennicutt, Jr., R. C., Keel, W. C., & Blaha, C. A. 1989, AJ, 97, 1022

Kenyon, S. J. & Hartmann, L. 1995, ApJS, 101, 117

Khachikian, E. Y. & Weedman, D. W. 1974, ApJ, 192, 581

Kharchenko, N. V., Piskunov, A. E., Röser, S., Schilbach, E., & Scholz, R. 2005, A&A, 440, 403

King, I. R. 1966, AJ, 71, 64

Kinney, A. L., Bohlin, R. C., Calzetti, D., Panagia, N., & Wyse, R. F. G. 1993, ApJS, 86, 5

Kinney, A. L., Calzetti, D., Bohlin, R. C., et al. 1996, ApJ, 467, 38

Klessen, R. S., Krumholz, M. R., & Heitsch, F. 2009, ArXiv e-prints

Kobulnicky, H. A. & Johnson, K. E. 1999, ApJ, 527, 154

Kodaira, K., Vansevičius, V., Bridzius, A., et al. 2004, PASJ, 56, 1025

Koekemoer, A. M., Fruchter, A. S., Hook, R. N., & Hack, W. 2002, in The 2002 HST Calibration Workshop : Hubble after the Installation of the ACS and the NICMOS Cooling System, ed. S. Arribas, A. Koekemoer, & B. Whitmore, 337–+

Kohno, K., Ishizuki, S., Matsushita, S., Vila-Vilaró, B., & Kawabe, R. 2003, PASJ, 55, L1

Koratkar, A. & Blaes, O. 1999, PASP, 111, 1

Koski, A. T. & Osterbrock, D. E. 1976, ApJ, 203, L49+

Kotilainen, J. K., Reunanen, J., Laine, S., & Ryder, S. D. 2000, A&A, 353, 834

Kramer, C., Stutzki, J., Rohrig, R., & Corneliussen, U. 1998, A&A, 329, 249

Kriss, G. A., Peterson, B. M., Crenshaw, D. M., & Zheng, W. 2000, ApJ, 535, 58

Kuraszkiewicz, J., Wilkes, B. J., Schmidt, G., et al. 2009, ApJ, 692, 1180

Lada, C. J. & Lada, E. A. 2003, ARA&A, 41, 57

Lada, C. J., Muench, A. A., Rathborne, J., Alves, J. F., & Lombardi, M. 2008, ApJ, 672, 410

Lagage, P. O., Pel, J. W., Authier, M., et al. 2004, The Messenger, 117, 12

Laine, S., Shlosman, I., Knapen, J. H., & Peletier, R. F. 2002, ApJ, 567, 97

Lançon, A., Gallagher, J. S., Mouhcine, M., et al. 2009, Ap&SS, 324, 241

Large, M. I., Mills, B. Y., Little, A. G., Crawford, D. F., & Sutton, J. M. 1981, MNRAS, 194, 693

Larsen, S. S. 2002, AJ, 124, 1393

Larsen, S. S. 2009, A&A, 494, 539

Lawrence, A. 1991, MNRAS, 252, 586

Leggett, S. K., Hawarden, T. G., Currie, M. J., et al. 2003, MNRAS, 345, 144

Leitherer, C. & Heckman, T. M. 1995, ApJS, 96, 9

Leitherer, C., Robert, C., & Drissen, L. 1992, ApJ, 401, 596

Leitherer, C., Schaerer, D., Goldader, J. D., et al. 1999, ApJS, 123, 3

Lenc, E. & Tingay, S. J. 2006, AJ, 132, 1333

Lenc, E. & Tingay, S. J. 2009, AJ, 137, 537

Lenzen, R., Hartung, M., Brandner, W., et al. 2003, in Society of Photo-Optical Instrumentation Engineers (SPIE) Conference Series, ed. M. Iye & A. F. M. Moorwood, Vol. 4841, 944–952

Levenson, N. A., Weaver, K. A., & Heckman, T. M. 2001, ApJS, 133, 269

Lister, M. L. & Homan, D. C. 2005, AJ, 130, 1389

Lonsdale, C. J., Lonsdale, C. J., Smith, H. E., & Diamond, P. J. 2003, ApJ, 592, 804

Maíz-Apellániz, J. 2001, ApJ, 563, 151

Malin, D. F. & Carter, D. 1983, ApJ, 274, 534

Malkan, M. A. & Sargent, W. L. W. 1982, ApJ, 254, 22

Mamajek, E. E., Meyer, M. R., Hinz, P. M., et al. 2004, ApJ, 612, 496

Maoz, D., Barth, A. J., Ho, L. C., Sternberg, A., & Filippenko, A. V. 2001, AJ, 121, 3048

Maoz, D., Barth, A. J., Sternberg, A., et al. 1996, AJ, 111, 2248

Marconi, A., Oliva, E., van der Werf, P. P., et al. 2000, A&A, 357, 24

Marquez, I. & Moles, M. 1994, AJ, 108, 90

Matthews, T. A. & Sandage, A. R. 1963, ApJ, 138, 30

Mauch, T., Murphy, T., Buttery, H. J., et al. 2003, MNRAS, 342, 1117

McCrady, N. & Graham, J. R. 2007, ApJ, 663, 844

Meisenheimer, K., Tristram, K. R. W., Jaffe, W., et al. 2007, A&A, 471, 453

Mengel, S., Lehnert, M. D., Thatte, N., & Genzel, R. 2005, A&A, 443, 41

Merkulova, N. I. 2000, AJ, 119, 631

Meurer, G. R. 1995, Nature, 375, 742

Meurer, G. R., Heckman, T. M., Lehnert, M. D., Leitherer, C., & Lowenthal, J. 1997, AJ, 114, 54

Miles, J. W., Houck, J. R., Hayward, T. L., & Ashby, M. L. N. 1996, ApJ, 465, 191

Miller, B. W., Whitmore, B. C., Schweizer, F., & Fall, S. M. 1997, AJ, 114, 2381

Miyamoto, S., Kitamoto, S., Iga, S., Negoro, H., & Terada, K. 1992, ApJ, 391, L21

Moffat, A. F. J., Corcoran, M. F., Stevens, I. R., et al. 2002, ApJ, 573, 191

Mohan, N. R., Anantharamaiah, K. R., & Goss, W. M. 2002, ApJ, 574, 701

Morganti, R., de Zeeuw, P. T., Oosterloo, T. A., et al. 2006, MNRAS, 371, 157

Morganti, R., Tsvetanov, Z. I., Gallimore, J., & Allen, M. G. 1999, A&AS, 137, 457

Morris, S., Ward, M., Whittle, M., Wilson, A. S., & Taylor, K. 1985, MNRAS, 216, 193

Motte, F., Andre, P., & Neri, R. 1998, A&A, 336, 150

Müller-Sánchez, F., González-Martín, O., Fernández-Ontiveros, J. A., Acosta-Pulido, J. A., & Prieto, M. A. 2010, ApJ, 716, 1166

Mundell, C. G., Ferruit, P., Nagar, N., & Wilson, A. S. 2009, ApJ, 703, 802

Nagar, N. M., Falcke, H., & Wilson, A. S. 2005, A&A, 435, 521

Nagar, N. M., Wilson, A. S., Mulchaey, J. S., & Gallimore, J. F. 1999, ApJS, 120, 209

Nakai, N., Inoue, M., Miyazawa, K., Miyoshi, M., & Hall, P. 1995, PASJ, 47, 771

Nandra, K., Le, T., George, I. M., et al. 2000, ApJ, 544, 734

Nenkova, M., Sirocky, M. M., Ivezić, Ž., & Elitzur, M. 2008, ApJ, 685, 147

Nicastro, F. 2000, ApJ, 530, L65

O'Connell, R. W. 1999, ARA&A, 37, 603

O'Connell, R. W., Gallagher, III, J. S., Hunter, D. A., & Colley, W. N. 1995, ApJ, 446, L1+

Orienti, M. & Prieto, M. A. 2010, MNRAS, 401, 2599

Osterbrock, D. E. 1989, Astrophysics of gaseous nebulae and active galactic nuclei (University Science Books)

Papadakis, I. E., Nandra, K., & Kazanas, D. 2001, ApJ, 554, L133

Peirani, S., Crockett, R. M., Geen, S., et al. 2009, e-prints (astro-ph: 0912.2629)

Peng, C. Y., Ho, L. C., Impey, C. D., & Rix, H. 2002, AJ, 124, 266

Perez-Olea, D. E. & Colina, L. 1996, ApJ, 468, 191

Perez-Torres, M. A., Alberdi, A., Colina, L., et al. 2009, ArXiv e-prints

Perina, S., Cohen, J. G., Barmby, P., et al. 2010, A&A, 511, A23+

Persson, S. E., Aaronson, M., Cohen, J. G., Frogel, J. A., & Matthews, K. 1983, ApJ, 266, 105

Persson, S. E., Murphy, D. C., Krzeminski, W., Roth, M., & Rieke, M. J. 1998, AJ, 116, 2475

Peterson, B. M. 1993, PASP, 105, 247

Peterson, B. M. 1997, An Introduction to Active Galactic Nuclei (Goméz de Castro, A. I. & Franqueira, M.)

Phillips, M. M. & Frogel, J. A. 1980, ApJ, 235, 761

Piconcelli, E., Bianchi, S., Guainazzi, M., Fiore, F., & Chiaberge, M. 2007, A&A, 466, 855

Pierce, M., Brodie, J. P., Forbes, D. A., et al. 2005, MNRAS, 358, 419

Plana, H. & Boulesteix, J. 1996, A&A, 307, 391

Pogge, R. W., Maoz, D., Ho, L. C., & Eracleous, M. 2000, ApJ, 532, 323

Pogge, R. W. & Martini, P. 2002, ApJ, 569, 624

Polletta, M., Tajer, M., Maraschi, L., et al. 2007, ApJ, 663, 81

Portegies Zwart, S., McMillan, S., & Gieles, M. 2010, ArXiv e-prints

Pott, J., Malkan, M. A., Elitzur, M., et al. 2010, ApJ, 715, 736

Predehl, P. & Schmitt, J. H. M. M. 1995, A&A, 293, 889

Prieto, M. A., Maciejewski, W., & Reunanen, J. 2005, AJ, 130, 1472

Prieto, M. A., Meisenheimer, K., Marco, O., et al. 2004, ApJ, 614, 135

Prieto, M. A., Reunanen, J., Tristram, K. R. W., et al. 2010, MNRAS, 402, 724

Radovich, M., Klaas, U., Acosta-Pulido, J., & Lemke, D. 1999, A&A, 348, 705

Ramos Almeida, C., Levenson, N. A., Rodríguez Espinosa, J. M., et al. 2009, ApJ, 702, 1127

Rampazzo, R., Marino, A., Tantalo, R., et al. 2007, MNRAS, 381, 245

Reid, M. J. 1993, ARA&A, 31, 345

Reines, A. E., Johnson, K. E., & Hunt, L. K. 2008, AJ, 136, 1415

Rejkuba, M., Minniti, D., Silva, D. R., & Bedding, T. R. 2001, A&A, 379, 781

Reunanen, J., Kotilainen, J. K., & Prieto, M. A. 2002, MNRAS, 331, 154

Reunanen, J., Prieto, M. A., & Siebenmorgen, R. 2010, MNRAS, 402, 879

Ricci, R., Prandoni, I., Gruppioni, C., Sault, R. J., & de Zotti, G. 2006, A&A, 445, 465

Ricci, T. V., Steiner, J. E., Menezes, R. B., Garcia-Rissmann, A., & Cid Fernandes, R. 2010, ArXiv e-prints

Rice, W., Lonsdale, C. J., Soifer, B. T., et al. 1988, ApJS, 68, 91

Rickard, J. J. 1975, A&A, 40, 339

Riffel, R. A., Storchi-Bergmann, T., Dors, O. L., & Winge, C. 2009, MNRAS, 393, 783

Risaliti, G., Maiolino, R., & Salvati, M. 1999, ApJ, 522, 157

Robitaille, T. P., Whitney, B. A., Indebetouw, R., & Wood, K. 2007, ApJS, 169, 328

Rodríguez-Ardila, A., Prieto, M. A., Viegas, S., & Gruenwald, R. 2006, ApJ, 653, 1098

Rodríguez-Rico, C. A., Goss, W. M., Zhao, J.-H., Gómez, Y., & Anantharamaiah, K. R. 2006, ApJ, 644, 914

Roman-Lopes, A. & Abraham, Z. 2006, AJ, 131, 951

Rosolowsky, E. 2005, PASP, 117, 1403

Rossa, J., Dietrich, M., & Wagner, S. J. 2000, A&A, 362, 501

Rousset, G., Lacombe, F., Puget, P., et al. 2003, in Society of Photo-Optical Instrumentation Engineers (SPIE) Conference Series, ed. P. L. Wizinowich & D. Bonaccini, Vol. 4839, 140–149

Sadler, E. M., Slee, O. B., Reynolds, J. E., & Roy, A. L. 1995, MNRAS, 276, 1373

Sams, III, B. J., Genzel, R., Eckart, A., Tacconi-Garman, L., & Hofmann, R. 1994, ApJ, 430, L33

Sanders, D. B., Mazzarella, J. M., Kim, D.-C., Surace, J. A., & Soifer, B. T. 2003, AJ, 126, 1607

Sanders, D. B., Phinney, E. S., Neugebauer, G., Soifer, B. T., & Matthews, K. 1989, ApJ, 347, 29

Santiago-Cortés, M., Mayya, Y. D., & Rosa-González, D. 2010, MNRAS, 496

Santos, Jr., J. F. C. & Frogel, J. A. 1997, ApJ, 479, 764

Sawada-Satoh, S., Kameno, S., Nakamura, K., et al. 2008, ApJ, 680, 191

Sazonov, S., Revnivtsev, M., Krivonos, R., Churazov, E., & Sunyaev, R. 2007, A&A, 462, 57

Schachter, J. F., Fiore, F., Elvis, M., et al. 1998, ApJ, 503, L123+

Schartmann, M., Meisenheimer, K., Camenzind, M., et al. 2008, A&A, 482, 67

Schechter, P. 1976, ApJ, 203, 297

Schilbach, E. & Röser, S. 2008, A&A, 489, 105

Schmitt, H. R., Kinney, A. L., Calzetti, D., & Storchi Bergmann, T. 1997, AJ, 114, 592

Schödel, R., Najarro, F., Muzic, K., & Eckart, A. 2010, A&A, 511, A18+

Schulz, H. & Henkel, C. 2003, A&A, 400, 41

Seyfert, C. K. 1943, ApJ, 97, 28

Shapiro, K. L. & et al. 2010, MNRAS, 402, 2140

Shields, G. A. & Wheeler, J. C. 1978, ApJ, 222, 667

Shinozaki, K., Miyaji, T., Ishisaki, Y., Ueda, Y., & Ogasaka, Y. 2006, AJ, 131, 2843

Siebenmorgen, R. & Krügel, E. 2007, A&A, 461, 445

Siebenmorgen, R., Krügel, E., & Spoon, H. W. W. 2004, A&A, 414, 123

Slee, O. B. 1995, Australian Journal of Physics, 48, 143

Slee, O. B., Sadler, E. M., Reynolds, J. E., & Ekers, R. D. 1994, MNRAS, 269, 928

Smith, H. J. & Hoffleit, D. 1963, Nature, 198, 650

Sofue, Y., Yoshida, S., Aoki, T., et al. 1994, PASJ, 46, 1

Sosa-Brito, R. M., Tacconi-Garman, L. E., Lehnert, M. D., & Gallimore, J. F. 2001, ApJS, 136, 61

Stetson, P. B. 1987, PASP, 99, 191

Storchi-Bergmann, T., Baldwin, J. A., & Wilson, A. S. 1993, ApJ, 410, L11

Storchi-Bergmann, T. & Bonatto, C. J. 1991, MNRAS, 250, 138

Storchi-Bergmann, T., Eracleous, M., Livio, M., et al. 1995, ApJ, 443, 617

Storchi-Bergmann, T., Nemmen da Silva, R., Eracleous, M., et al. 2003, ApJ, 598, 956

Strateva, I., Ivezić, Ž., Knapp, G. R., et al. 2001, AJ, 122, 1861

Strickland, D. K., Heckman, T. M., Weaver, K. A., & Dahlem, M. 2000, AJ, 120, 2965

Strickland, D. K., Heckman, T. M., Weaver, K. A., Hoopes, C. G., & Dahlem, M. 2002, ApJ, 568, 689

Sugai, H., Hattori, T., Kawai, A., et al. 2005, ApJ, 629, 131

Tabur, V., Kiss, L. L., & Bedding, T. R. 2009, ApJ, 703, L72

Terashima, Y., Iyomoto, N., Ho, L. C., & Ptak, A. F. 2002, ApJS, 139, 1

Terlevich, R. & Melnick, J. 1985, MNRAS, 213, 841

Terry, J. N., Paturel, G., & Ekholm, T. 2002, A&A, 393, 57

Tingay, S. J. 2004, AJ, 127, 10

Tingay, S. J., Jauncey, D. L., King, E. A., et al. 2003, PASJ, 55, 351

Tristram, K. R. W., Meisenheimer, K., Jaffe, W., et al. 2007, A&A, 474, 837

Tsvetanov, Z. I. & Petrosian, A. R. 1995, ApJS, 101, 287

Tully, R. B. 1988, Nearby galaxies catalog (Cambridge University Press)

Turner, J. L. & Ho, P. T. P. 1985, ApJ, 299, L77

Turner, T. J., Perola, G. C., Fiore, F., et al. 2000, ApJ, 531, 245

Turner, T. J., Weaver, K. A., Mushotzky, R. F., Holt, S. S., & Madejski, G. M. 1991, ApJ, 381, 85

Ueda, Y., Eguchi, S., Terashima, Y., et al. 2007, ApJ, 664, L79

Ulvestad, J. S. & Antonucci, R. R. J. 1997, ApJ, 488, 621

Ulvestad, J. S. & Wilson, A. S. 1984, ApJ, 285, 439

Urry, C. M. & Padovani, P. 1995, PASP, 107, 803

Vacca, W. D., Johnson, K. E., & Conti, P. S. 2002, AJ, 123, 772

van de Ven, G. & Chang, P. 2009, ApJ, 697, 619

van de Ven, G. & Fathi, K. 2009, ArXiv e-prints

van der Bliek, N. S., Manfroid, J., & Bouchet, P. 1996, A&AS, 119, 547

van Gorkom, J. H., Knapp, G. R., Ekers, R. D., et al. 1989, AJ, 97, 708

van Gorkom, J. H., Knapp, G. R., Raimond, E., Faber, S. M., & Gallagher, J. S. 1986, AJ, 91, 791

Vansevičius, V., Kodaira, K., Narbutis, D., et al. 2009, ApJ, 703, 1872

Vanzi, L. & Sauvage, M. 2004, A&A, 415, 509

Vesperini, E. & Heggie, D. C. 1997, MNRAS, 289, 898

Walborn, N. R. & Blades, J. C. 1997, ApJS, 112, 457

Walborn, N. R., Maíz-Apellániz, J., & Barbá, R. H. 2002, AJ, 124, 1601

Ward, M., Penston, M. V., Blades, J. C., & Turtle, A. J. 1980, MNRAS, 193, 563

Weaver, K. A., Heckman, T. M., Strickland, D. K., & Dahlem, M. 2002, ApJ, 576, L19

Weaver, K. A., Wilson, A. S., & Baldwin, J. A. 1991, ApJ, 366, 50

Weaver, K. A., Wilson, A. S., Henkel, C., & Braatz, J. A. 1999, ApJ, 520, 130

Wehrle, A. E., Keel, W. C., & Jones, D. L. 1997, AJ, 114, 115

Weigelt, G. & Baier, G. 1985, A&A, 150, L18

Whitmore, B. C. 2003, in A Decade of Hubble Space Telescope Science, ed. M. Livio, K. Noll, & M. Stiavelli, 153–178

Whitmore, B. C., Zhang, Q., Leitherer, C., et al. 1999, AJ, 118, 1551

Wilson, A. S., Helfer, T. T., Haniff, C. A., & Ward, M. J. 1991, ApJ, 381, 79

Winter, L. M., Mushotzky, R. F., Terashima, Y., & Ueda, Y. 2009, ApJ, 701, 1644

Wold, M. & Galliano, E. 2006, MNRAS, 369, L47

Wold, M., Lacy, M., Käufl, H. U., & Siebenmorgen, R. 2006, A&A, 460, 449

Wolstencroft, R. D., Tully, R. B., & Perley, R. A. 1984, MNRAS, 207, 889

Wrobel, J. M. 1984, ApJ, 284, 531

Xilouris, E. M., Madden, S. C., Galliano, F., Vigroux, L., & Sauvage, M. 2004, A&A, 416, 41

Yang, M. & Phillips, T. 2007, ApJ, 662, 284

Yi, S., Demarque, P., & Oemler, A. J. 1998, ApJ, 492, 480

Yun, M. S. 2008, Ap&SS, 313, 253

Yusef-Zadeh, F., Hewitt, J. W., Arendt, R. G., et al. 2009, ApJ, 702, 178

Zhang, Q. & Fall, S. M. 1999, ApJ, 527, L81

Zhang, Q., Fall, S. M., & Whitmore, B. C. 2001, ApJ, 561, 727